Co-simulation of Electromagnetic Transients and Phasor Models of Electric Power Systems

Frédéric Plumier

Liège, Belgium, November 2015

A dissertation submitted in partial fulfillment of the requirements for the degree of
Doctor of Philosophy (Ph.D.) in Engineering Sciences

Examining Committee

Professor Christophe Geuzaine (*Ph.D. advisor*), Université de Liège, Belgium

Professor Sebastian Schöps, Technische Universität Darmstadt, Germany

Professor Thierry Van Cutsem (*Ph.D. advisor*), FNRS and Université de Liège, Belgium

Professor Dirk Van Hertem, Katholieke Universiteit Leuven, Belgium

Professor Costas Vournas, National Technical University of Athens, Greece

Professor Patricia Rousseaux (*President of Jury*), Université de Liège, Belgium

To my family.

Contents

Acknowledgments

In my opinion, by no means could the research accomplished through a doctoral thesis be done in an isolated way. I would therefore like to express my thanks to the persons that have been on my side throughout this journey.

I would like first to express my thanks to Brother Gonzague De Longcamp CSJ[1] whose advice convinced me to start a doctoral thesis.

Let me express my warm thanks to Professor Patricia Rousseaux (University of Liège), Professor Sebastian Schoeps (Technische Universität Darmstadt), Professor Costas Vournas (National Technical University of Athens) and Professor Dirk Van Hertem (Katholieke Universiteit Leuven), members of the jury, who accepted to spend their time assessing my research. Among those in the jury, there were also my supervisors: Professor Christophe Geuzaine and Professor Thierry Van Cutsem.

I'd like to warmly thank Christophe for helping not only by his advice but also and more especially by his example. His competence in leading was shown throught his leadership, enthousiasm, hard work, creativity and wisdom. I am also grateful for the opportunity he gave me, in parallel with my research, to manage Academic Cooperation with the Faculty of Applied Sciences of the University of Rwanda.

Likewise, I would like to offer my thanks to Thierry for pleasant, highly professional and friendly working athmosphere that he created in our team. More a family than a team, it was a real pleasure to work together with him. I am particularly grateful for his being always available despite a busy schedule and I have been enriched by his dedication to research quality, organisation and attention to detail.

I am also particularly grateful to my former colleague Dr Davide Fabozzi who helped me to design the initial core of the Matlab-EMT solver.

Of course, my gratitude goes to all my colleagues. I will first cite Dr Petros Aristidou who, apart from working with me on some technical part of the coupling, became a friend and accepted

---

[1] Community of Saint John

Nomenclature

Abbreviations

AE	Algebraic Equation
ASEO	Angle-Shifted Energy Operator
AVR	Automatic Voltage Regulator
BC	Boundary Conditions
DAE	Differential Algebraic Equations
DP	Dynamic Phasor
EMF	ElectroMotive Force
EMT	ElectroMagnetic Transients
FAST	Frequency-Adaptive Simulation of Transients
FEMT	Frequency-Adaptive Electromagnetic Transients
FIDVR	Fault-Induced Delayed Voltage Recovery
GS	Gauss-Seidel
HIL	Hardware In the Loop
HVDC	High Voltage Direct Current
KCL	Kirchhoff Current Law
LFE	Low Frequency Equivalent
MTDC	Multi-Terminal Direct Current
ODE	Ordinary Differential Equation
PLL	Phase-Locked Loop
PM	Phasor-Mode
PSRA	Projection on Synchronously Rotating Axes
PSS	Power System Stabilizer
RMS	Root Mean Squares
SFA	Shifted Frequency Analysis
SVC	Static Var Compensator
TVE	Total Vector Error
WR	Waveform Relaxation

Mathematical Symbols

α	damping factor for the PM-EMT dynamic iterations
$\mathbf{I}$	identity matrix
$\mathbf{S}$	complex transformation matrix to convert dio complex signals into abc ones.
$\mathbf{T}$	real transformation matrix to convert abc real signals into $0xy$ ones (also referred to as $0dq$ ones)
ω_s	synchronous frequency of the system (typically here $\omega_s = 2\pi50$ rad/s)
a	rotation operator $a = e^{j\frac{2\pi}{3}}$
H	time step size of PM solver (typically here $H = 20$ ms)
h	time step size of EMT solver (typically here $h = 100$ μs)
N	total number of buses in a given network
n	number of boundary buses between the PM and the EMT sub-systems
T_x	Time interval considered for the positive-sequence phasor extraction
$\boldsymbol{L}_{pm}$	positive-sequence inductance matrix (of size $n \times n$) of the PM sub-system, seen from its n boundary buses
$\boldsymbol{L}_{pm}^{abc}$	three-phase inductance matrix (of size $3n \times 3n$) of the PM sub-system, seen from its n boundary buses
$\boldsymbol{R}_{pm}$	positive-sequence resistance matrix (of size $n \times n$) of the PM sub-system, seen from its n boundary buses
$\boldsymbol{R}_{pm}^{abc}$	three-phase resistance matrix (of size $3n \times 3n$) of the PM sub-system, seen from its n boundary buses
$\boldsymbol{Z}_{pm}$	positive-sequence Thévenin impedance matrix (of size $n \times n$) of the PM sub-system, seen from its n boundary buses

Introduction

1.1 A glance at previous works

The term *co-simulation* refers to the combination of (at least) two different tools for performing a multi-physics or multi-model simulation. This research deals specifically with the co-simulation of ElectroMagnetic Transients (EMT) models and Phasor-Mode (PM) models[1]. The main motivation behind this work is to combine the accuracy of EMT with the computational efficiency of PM simulations. Today there is no widely accepted approach for such a co-simulation. While mature software exist for both models, further investigations and developments are needed for their efficient and accurate coupling.

Coupled PM-EMT solvers have been proposed initially in 1981 in the context of the simulation of an Alternating Current (AC) grid comprising a Direct Current (DC) link with its two current-source High Voltage Direct Current (HVDC) converters [HTAA81]. The EMT sub-system was relatively small, comprising the DC cable and the HVDC converters at both ends (with their transformers and harmonic filters). The PM sub-system included single-point Thévenin equivalents, varying with time. The development was oriented towards incorporating a detailed EMT model inside a PM simulation, to gain accuracy for components inaccurately represented under PM model under all possible events. Time interpolation was used to convert PM variables into EMT ones at the interface, although the exact procedure was not described. In order to pass from EMT variables to PM ones, the Fast Fourier Transform was used to derive the boundary voltage while real power was evaluated numerically.

Later on, [RA88b] proposed, for accuracy reasons, to extend the EMT sub-system to include parts of the surrounding AC network around the HVDC link. Two different interface locations were tested [RA88c]: (i) interface located directly at the converter AC buses, and (ii) interface placed one bus further away from the converter. The simulation results showed, as expected, that it was beneficial to extend the interface to reduce the distortion ratio at the interface between PM and

---

[1]PM models are also referred to as "models under the quasi-sinusoidal approximation" or "RMS models".

EMT sub-systems. A least-squares curve fitting approach for fundamental frequency waveform extraction replaced the FFT and real power methods of [HTAA81].

In the PhD thesis [And95], the author extended the application area of PM-EMT co-simulations, claiming that the inclusion of multiple and independent detailed EMT islands was possible, with application to Static Var Compensators (SVCs) and Flexible AC Transmission Systems (FACTS) devices. The author validated the PM-EMT coupling on a 5-machine, 10-bus test system, where the EMT sub-system was composed of a point-to-point HVDC link with twelve-pulse converters. The work focused on transient stability PM studies, using full transient EMT model of HVDC converters during significant transient disturbances. The use of a *frequency dependent equivalent* of the AC network made it possible to set the boundary at the terminals of the HVDC converters.

Some authors have worked on improving the *boundary conditions* (e.g. [ZFA14, CS⁺02]). In this context, in [SSCZ03, SCS05, SCSS05, FLCW06], several studies were performed on a 39-bus test system [Kun94]. The EMT sub-system, included a fixed capacitor-thyristor controlled reactor SVC and had one bus in common with the PM sub-system. Tentative improvements have been made to the model of the PM sub-system used in the EMT simulation. In particular in [FLCW06], the frequency of the current source of the Norton equivalent (PM sub-system model in the EMT simulation) is updated with the estimated frequency at each boundary bus, with however relatively few theoretical basis supporting this technique. In [ZGW⁺13], the authors focus on the implementation of a frequency dependent network equivalent of the PM sub-system in the EMT simulation. It appears that this type of equivalent makes it possible to place the boundary very near an HVDC converter.

Reference [IFHI03] mentionned the possibility to *predict in time* the value of the PM sub-system to improve the convergence of the co-simulation procedure. In that reference, the authors reported on tests with an interface including up to two boundary buses.

An interesting work, more of theoretical nature, on *iterative* PM-EMT simulations was presented in [KK00]. An average number of iterations below two per co-simulation time step was reported, on a small test system (one machine, one transformer and one transmission line). In the more recent references [AF14, AF13, AF12, Abh11], the authors assess the need to iterate between the PM and EMT solvers to get accurate results, in particular in short-term voltage stability studies. They conclude that in unstable cases, a non-iterative PM-EMT simulation does not give accurate results. A single solver handling the two different models is used. In this context, it is proposed to start with a PM simulation, to switch to the PM-EMT hybrid simulation after disturbances, and to come back to PM simulation after the disturbances have died out. The following application areas for PM-EMT simulators are quoted by these authors:

- Identification of local voltage collapse and voltage collapse cascade,

- wide-area protection analysis,

- modeling of power electronics in wind farms.

However there are still some limitations in that work. In particular, a mere current injector is used to model the EMT sub-system, which is not optimal for the convergence of the iterative process between PM and EMT solvers. Furthermore the coupling in the presence of multiple boundary buses is not considered in detail.

Other authors have worked on the inclusion of Multi-Terminal DC (MTDC) grids in the EMT sub-system [vdMGvdM$^+$14, vHGK11, vdMRK10], reviewing also PM-EMT co-simulation techniques, and proposing improved protocols and boundary conditions. It has been found that a non-iterative PM-EMT co-simulation is more accurate when solving the EMT sub-system first. Faults in the PM sub-system were also considered in [zLxHT$^+$11], the representation of the non-EMT part being not just an equivalent, but a sub-system *per se*. The reported work also involves DC links.

Very recently, hybrid PM-EMT simulations have been used to simulate Fault-Induced Delayed Voltage Recovery (FIDVR) [Ope15, HV15]. This work is interesting in several respects: (i) a three-sequence solver is used on the PM side, which allows handling imbalances at the boundary; (ii) the application to FIDVR; (iii) the detection of fast dynamics inside the EMT network to switch from a parallel to a serial protocol. Some aspects leave room for improvements, in our opinion, including the co-simulation protocol, the boundary conditions on the PM sub-system side, the prediction before iterating, the handling of transient events in the PM sub-system, and the PM-to-EMT and EMT-to-PM conversion techniques.

1.2 Thesis objectives

Until recently, some authors were challenging the theoretical basis supporting the PM-EMT co-simulation [FD12]. It is true that the literature review presented in the previous section raises many questions:

1. How is the simulation impacted if a *static Thévenin equivalent* is used to represent the PM sub-system over the whole simulation? What is the error made with a static Thévenin equivalent, and what is the added value of PM-EMT co-simulation?

2. Is it necessary to *iterate* between the PM and the EMT solvers, and if yes, how many iterations are generally required for a sufficient accuracy of the PM-EMT co-simulation?

3. How to interface the PM and EMT solvers? As regards passing the EMT results to the PM simulation, how to avoid introducing a delay due to the processing of past values of the EMT simulation outputs? Is the PM time step size restricted to a particular value, for instance related to the fundamental period (i.e. submultiple, equal or multiple of the fundamental period)? What is the accuracy of the EMT-to-PM conversion techniques?

4. How far is it advantageous to extend the EMT sub-system, considering the computational power available nowadays? What is the impact of increasing the number of *boundary buses*

on the number of PM-EMT co-simulation iterations needed for a given accuracy? Is there a limit on the maximum number of boundary buses between the PM and EMT sub-systems?

5. What is the most efficient and accurate interaction protocol between the PM and the EMT solvers? To which cases are the serial or the parallel protocol best suited? What solver should be called first (in a serial protocol)?

6. How should the PM sub-system be modeled when performing the EMT simulation, and conversely, how should one model the EMT sub-system in the PM simulation? These equivalent models will be called *boundary conditions.* Is a first-order (Thévenin or Norton) dynamically updated equivalent on one side sufficient? How is the convergence rate impacted when changing the type of boundary conditions used?

7. In view of its limitations, what are the main areas of application of PM-EMT hybrid simulations?

These are many and various issues that we have tried to address in this research work, building on a number of proposed techniques, and bringing our own enhancements.

1.3   Thesis outline

Chapter 2 offers a brief overview of the dynamic phenomena occuring in a power system. The main power system modeling approaches, spanning from the most precise EMT models to the simplified PM ones, are presented. By way of illustration, the derivation of the EMT and PM models of a three-phase lumped parameter overhead line is presented. The obtained models are compared in terms of computational efficiency and accuracy. The Nordic test system used throughout the whole thesis is also introduced with a comparison of dynamic models.

Chapter 3 is devoted to a review of the techniques to efficiently couple the PM and EMT solvers. Model partitioning is first discussed and the main iterative coupling schemes are presented. The boundary conditions to be used in each of the EMT and PM solvers are discussed and compared in terms of accuracy and convergence properties. The extrapolation techniques, in time and inside the co-simulation iterations, are also considered. A relaxation algorithm, incorporating the best suited techniques for PM-EMT coupling, is presented. The chapter is concluded with a convergence study.

An early version of the relaxation algorithm was published in [PGV13]. An improved version of the latter, showing the importance of first-order boundary conditions was presented in [PAGV14]. In parallel, a paper focusing on the convergence properties obtained with different boundary conditions was published in [PGV14]. Finally, a more complete algorithm,

including frequency update in the boundary conditions, single-iteration accuracy evaluation, and prediction in time, has been submitted for publication [PAGV15].

Chapter 4 presents the interface between PM and EMT simulations. The chapter is subdivided in two parts devoted to the PM-to-EMT and the EMT-to-PM conversion, respectively. Both sections include a literature review and a comparison of the main performances of the techniques used.

The PM-to-EMT conversion was described mathematically in [PGV13], and further elaborated in [PAGV14], stressing the relevance of linear interpolation in PM-EMT coupled simulations.
For what concerns the EMT-to-PM conversion, an original technique was proposed in [PGV13]. An improvement was brought to the latter in [PAGV14] regarding the extraction under disturbed conditions. In [PAGV15], a measure of the extraction quality was proposed. Unpublished, improved techniques are presented in this thesis.

Chapter 5 offers a sample of simulation results for a single and for multiple interface buses between the PM and the EMT sub-systems. The case where a single EMT sub-system evaluation is allowed (e.g. for hardware-in-the-loop simulations) is also assessed.

The cases involving a single interface bus and related results were presented in [PGV13] and [PAGV14]. The extension to multiple interface buses was presented in [PAGV15].

Chapter 6 summarizes contributions and suggests some directions for future work.

Overall, this thesis expands the following material which has been published or submitted, in various journals and at conferences:

Under preparation:

[10] J. Nshimiyimana, **F. Plumier**, P. Dular J. Gyselinck, and C. Geuzaine. Comparison of Co-simulation schemes for Field/Circuit coupled problems. To be submitted to —, 2016.

Under review:

[9] J. Nshimiyimana, **F. Plumier**, J. Gyselinck, P. Dular and C. Geuzaine. Co-simulation of Finite Element and Integrated Circuit Solvers using an Optimized Waveform Relaxation Method. Submitted to *IEEE Energycon 2016 (under 2nd review)*, Leuven, 2016.

[8] **F. Plumier**, P. Aristidou, C. Geuzaine, T. Van Cutsem, "Co-simulation of Electromagnetic Transients and Phasor Models: a Relaxation Approach", Submitted to *IEEE Transactions on Power Delivery (under 2nd review)*, 2015.

Published:

[7] **F. Plumier**, P. Aristidou, C. Geuzaine, and T. Van Cutsem. A relaxation scheme to combine phasor-mode and electromagnetic transients simulations. In *Proceedings of the 18th Power System Computational Conference (PSCC)*, Wroclaw, August 2014. Available at: http://hdl.handle.net/2268/168630

[6] **F. Plumier**, C. Geuzaine, and T. Van Cutsem. On the convergence of relaxation schemes to couple phasor-mode and electromagnetic transients simulations. In *Proceedings of the IEEE PES General Meeting*, Washington DC, July 2014. This paper was selected as one of the four "Best of the Best" Conference Papers submitted to the 2014 PES General Meeting. Available at: http://hdl.handle.net/2268/163099

[5] **F. Plumier**, C. Geuzaine, and T. Van Cutsem. Coupled boundary conditions for co-simulation of power system dynamics. In *Proceedings of the 6th International Conference on Advanced Computational Methods in Engineering*, Gent, June 2014.

[4] J. Nshimiyimana, **F. Plumier**, P. Dular and C. Geuzaine. Optimized Waveform Relaxation Methods for Modeling Electromagnetic Field-Circuit Problems. *In Proceedings of the 16th Biennal IEEE Conference on Electromagnetic Field Computation*, Annecy, April 2014.

[3] **F. Plumier**, C. Geuzaine, and T. Van Cutsem. Boundary impedance adaptation for the acceleration of hybrid simulations of power systems. In *Proceedings of the 22nd International Conference on Domain Decomposition Methods (DD22)*, Lugano, September 2013.

[2] **F. Plumier**, C. Geuzaine, and T. Van Cutsem. A multirate approach to combine electromagnetic transients and fundamental-frequency simulations. In *Proceedings of the 10th International Power System Transients conference (IPST)*, Vancouver, July 2013. Available at: http://hdl.handle.net/2268/149354

[1] **F. Plumier**, D. Fabozzi, C. Geuzaine, and T. Van Cutsem. Combining Full Transients and Phasor Approximation Models in Power System Time Simulation. In *Proceedings of the 21th International Conference on Domain Decomposition Methods (DD21)*, Rennes, June 2012.

Power system dynamic models

Having introduced in Chapter 1 the context and historical background of PM and EMT coupled simulations, we will enter now into more detail about EMT, PM and intermediate models. The main dynamic models for power system simulation will be introduced. The chapter will end with a comparison between the presented modeling approaches.

To derive a dynamic model of a power system, a possible way consists in modeling every power system component and the interactions between all components. This is not the only approach to deriving a dynamic model of a power system (one may use a measurements based approach to model the whole power system as a black- or gray-box; see for instance [SS04]), but it is the approach chosen in this thesis. Our choice is to make use of physics-based models. This approach tries to reproduce the actual time-domain evolution of state variables at any location in the system. The clear interest of physics-based models is to give inherent physical insight into power system simulation and to give access to any variable in the system.

A generic power system is represented in Figure 2.1. It includes components that we refer to as "injectors", represented by dashed circles. The injectors are connected to bus bars. The injectors include production units injecting power into the network (e.g. synchronous generators), loads drawing power from the network as well as (synchronous or static) compensators, power-electronics converters, etc. The network is mainly composed of overhead power lines, cables and transformers, not shown in Figure 2.1. The main symbols used for power system representation are summarized in Figure 2.2.

In this chapter, we will present the main families of power system modeling approaches for dynamic simulations. Dynamic phenomena occuring in a power system will be detailed in Section 2.1.

The most accurate representation, for which the model is refined depending on the level of detail needed for the phenomenon under study, is called EMT model [Dom69, WA03, MV15]. These models will be presented in Section 2.2. An example of derivation of the typical pi-section model of an overhead line will be given in Section 2.2.2. The test system used and the EMT solver implemented in our research will be presented in Section 2.2.3.
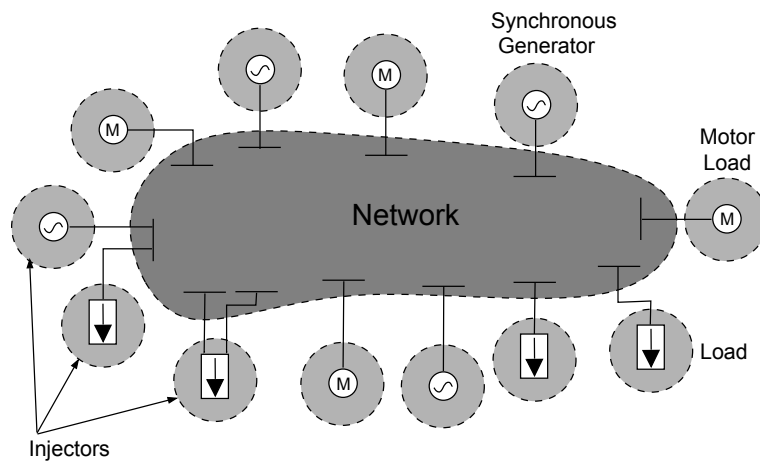
Figure 2.1: Schematic view of a power system.
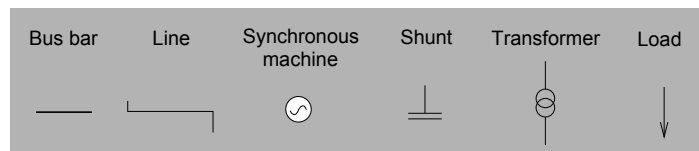
Figure 2.2: Power system symbols.

Section 2.3 will introduce intermediate accuracy models. Section 2.3.1 will present a family of techniques gathered together under the name of Dynamic Phasor (DP) techniques. These modeling approaches basically consist in studying the dynamic behavior of the complex coefficients of the main terms of a Fourier series decomposition of the variables over a sliding time window. The second approach presented (Section 2.3.2) to simulate large power systems consists in equivalencing a subset of the whole system.

The second proposed simplification (Section 2.3.3) consists in performing a coupled PM-EMT simulation. In this approach, rather than equivalencing a chosen subset of the power system, this subset is simulated, but with a simplified modeling approach (namely the PM approximation), while the domain of greater interest is simulated under full precision EMT models.

Section 2.4 will present positive-sequence phasor-mode simplified models [Kun94], named here PM models. For comparison purposes with EMT models, the PM model of a three-phase overhead power line will be derived in Section 2.4.4 while the complexity of the PM model of the Nordic test system will be described in Section 2.4.5. A brief description of the PM solver will end the section.

Section 2.5 will conclude the chapter with a comparison of the presented modeling methods.
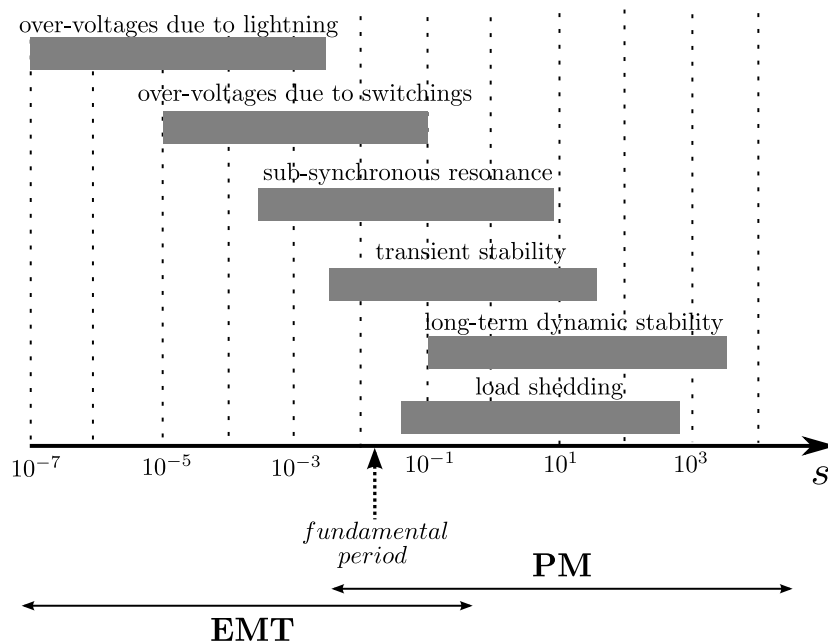
Figure 2.3: Classification of dynamic phenomena. (inspired from [AAALM02])

2.1 Dynamic phenomena occuring in a power system

An introduction to the dynamic phenomena occurring in a power system is now necessary. Dynamic phenomena can be roughly classified in the following two categories:

- Low frequency transients, abusively called electromechanical transients,

- High frequency transients, referred to as electromagnetic transients.

Low frequency transients are phenomena which are slow compared to the fundamental period. The period of oscillatory phenomena is long compared to one fundamental period of the voltages, at least 10 periods. On the other hand, high frequency oscillations have a period which cannot be considered long compared to the fundamental period, i.e. less than 10 fundamental periods. The main dynamic phenomena occuring in a power system are summarized in Figure 2.3. Lightning striking overhead lines induces very fast waves whose time constant ranges from $0.1\,\mu$s to 1ms. Switching operations concern the connection or disconnection of transmission lines or other components to or from the network. Switching can be planned or not. Planned switching operations include maintenance or addition of a new component to the network, while unplanned switchings generally concerns the disconnection of a faulted segment from the rest of the network. Over-voltages due to switching are characterized by time constants ranging from $10\,\mu$s to 100 ms. Sub-synchronous resonance is a condition where the electric network exchanges significant energy with a turbine-generator at one or more frequencies below the synchronous frequency. It originates from the interaction between turbine-generators and a series capacitor compensated network or
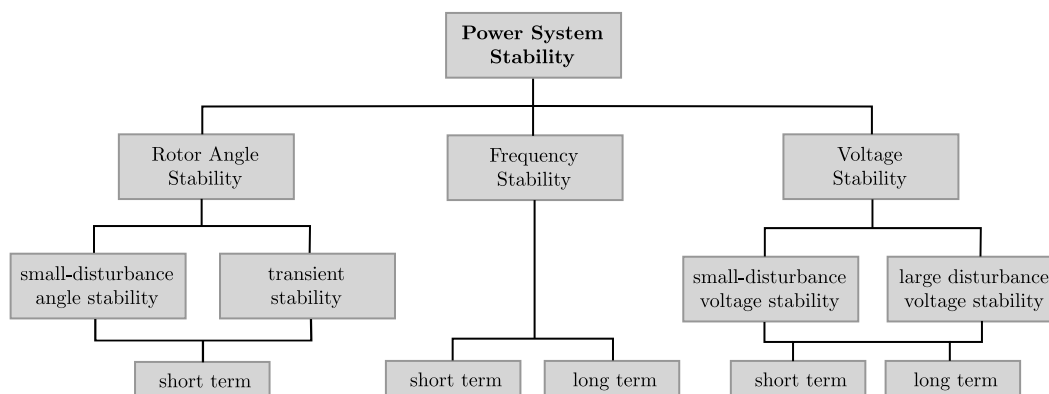
Figure 2.4: Classification of power system stability [KPA$^+$04].

with other components, such as Power System Stabilizers (PSS), HVDC converter controls, static var compensators, high speed governor controls, and variable speed drives converters [19992]. Sub-synchronous resonance phenomena involve dynamics in the range $[0.5\,\mathrm{ms}$ - $10\,\mathrm{s}]$.

The slower phenomena occuring in a power system can be classified as shown in Figure 2.4. Power systems transient stability phenomena [KPA$^+$04] are associated with the operation of synchronous machines in parallel. Transient stability becomes important in the presence of long distance heavy power transmissions. From a physical point of view, transient stability is defined as the ability of a power system to maintain the synchronous operation of the machines when subjected to large disturbances. It depends on the ability to maintain/restore equilibrium between electromagnetic torque and mechanical torque of each synchronous machine in the system. Frequency stability refers to the ability of a power system to maintain steady frequency following a severe system upset resulting in a significant imbalance between generation and load. It can be both a short-term issue (e.g. severe power imbalance after a network split) or a long-term one (e.g. unsatisfactory boiler control in power plants). Voltage stability refers to the ability of the power system to maintain steady voltages at all buses in the system after being subjected to a disturbance. It also decomposes into short- and long-term categories [VCV98]. To support this classification, the link with recent events in power systems is shown in Figure 2.5. A blackout generally results from the successive combination of two or more kinds of power system instability [ES13].

2.2   Electromagnetic transients models

2.2.1   Introduction to electromagnetic transients models

In the EMT modeling approach the three-phase voltages and currents are represented as three separate time-varying variables, without any assumption on their respective waveform. In Figure 2.6,
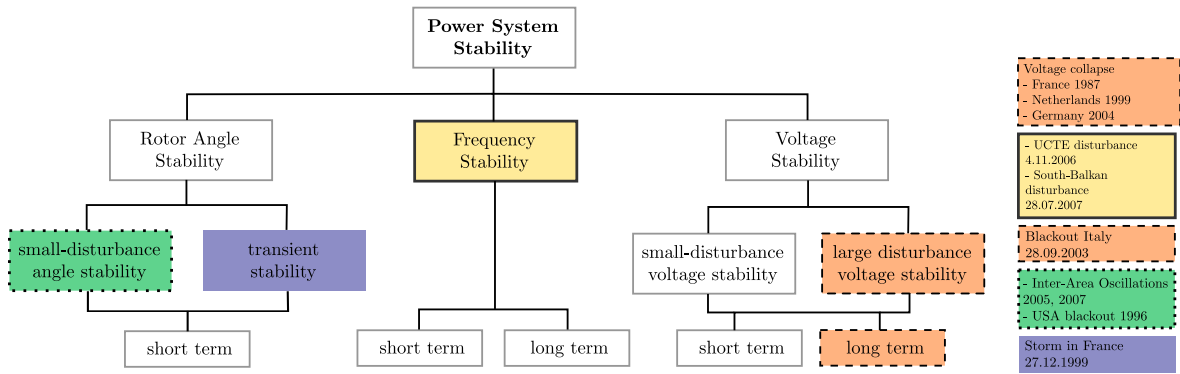
Figure 2.5: Classification of power system stability with examples [ENT11].

the i-th injector is connected to a bus characterized by the voltages

$$v_{abc} = \begin{cases} v_a(t) \\ v_b(t) \\ v_c(t) \end{cases} ,$$

and the injector itself, with a level of detail that depends of the required accuracy of the model, is represented through a set of Differential Algebraic Equations (DAEs):

$$\mathbf{\Gamma}_i \dot{\mathbf{x}}_i = \mathbf{\Phi}_i\left(\mathbf{x}_i\right) ,$$

where $\mathbf{\Gamma}_i$ is a diagonal matrix composed of zeros and ones, and $\mathbf{x}_i$ is a vector containing the algebraic and differential state variables of the injector. A one for a diagonal component of $\mathbf{\Gamma}_i$ corresponds to a differential equation for the corresponding component of $\mathbf{x}_i$ while a zero gives an algebraic equation.

The network is also modeled through a set of DAEs:

$$\mathbf{\Gamma} \dot{\mathbf{x}} = \mathbf{\Phi}\left(\mathbf{x}\right) ,$$

where $\mathbf{\Gamma}$ again is a diagonal matrix composed of zeros and ones, and $\mathbf{x}$ is a vector containing all algebraic and differential state variables of the network, including the bus voltages v_{abc}.

By way of illustration we derive in Section 2.2.2 the equations of an overhead power line to show a typical example of EMT model. The majority of the other EMT models implemented in our EMT solver (Section 2.2.3) are detailed in Appendix A.1. Some models, for which EMT and PM models are identical (e.g. controllers), are grouped in Appendix A.3.

2.2.2 Electromagnetic transients model of an overhead line with lumped parameters

The lumped element model represented in Figure 2.7 is used to model short overhead transmission lines connecting two buses [WA03]. Each bus includes three abc nodes. This model, called PI
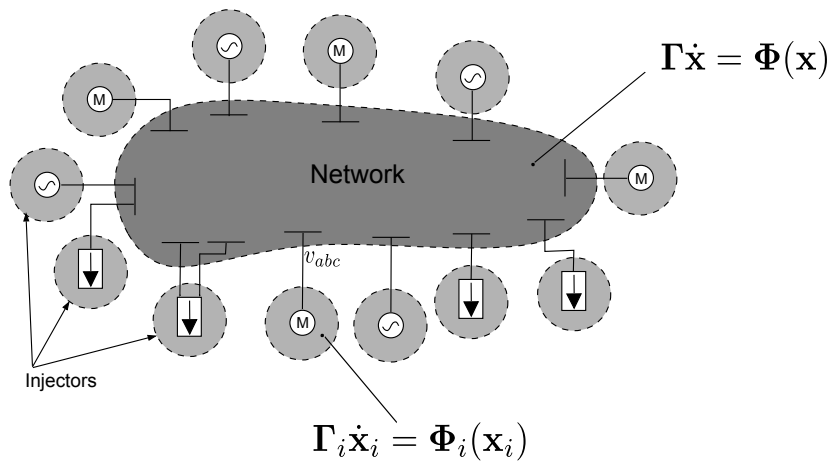
Figure 2.6: EMT representation of the power system.
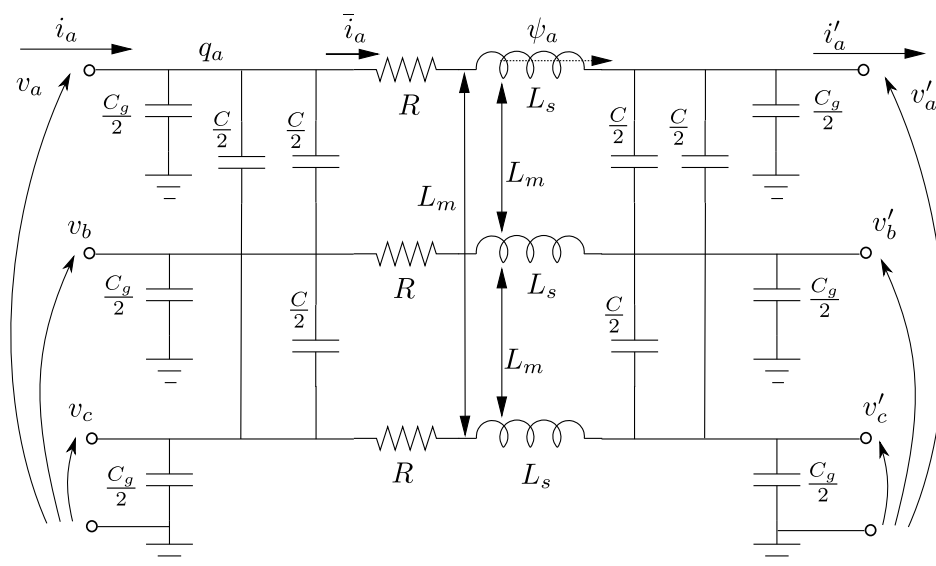
Figure 2.7: Model of a power line, as implemented in our EMT solver.

section model, thus connects the three nodes on one side to the three nodes on the other side. In this model, for simplicity and without lack of generality, the line is assumed to have the same voltage reference on the left and right hand sides. It is also assumed here that the line parameters are constant. The line is supposed to obey a perfect three-phase symmetry, again for the simplicity of the presentation.

Consider the capacitor and inductor equations on the left hand side of the line. First writing the capacitor charge equations:

$$0 = -q_a + \frac{C_g}{2} v_a + \frac{C}{2} (v_a - v_b) + \frac{C}{2} (v_a - v_c) , \tag{2.1}$$

$$0 = -q_b + \frac{C_g}{2} v_b + \frac{C}{2} (v_b - v_c) + \frac{C}{2} (v_b - v_a) , \tag{2.2}$$

$$0 = -q_c + \frac{C_g}{2} v_c + \frac{C}{2} (v_c - v_a) + \frac{C}{2} (v_c - v_b) , \tag{2.3}$$

where C_g is the total equivalent capacitance of the full length of a wire with respect to ground, C is the total equivalent capacitance between two wires, q_{abc} are the charges on abc wires respectively, and v_{abc} are the potentials of abc wires with respect to the ground.

According to Kirchhoff's current law the currents $\bar{i}_a$, $\bar{i}_b$ and $\bar{i}_c$ entering the series part of the PI section model (see Figure 2.7) are given by:

$$\bar{i}_a = i_a - \frac{dq_a}{dt} , \tag{2.4}$$

$$\bar{i}_b = i_b - \frac{dq_b}{dt} , \tag{2.5}$$

$$\bar{i}_c = i_c - \frac{dq_c}{dt} . \tag{2.6}$$

The flux linkages in the various phases are given by:

$$\psi_a = L_s \bar{i}_a + L_m \bar{i}_b + L_m \bar{i}_c ,$$

$$\psi_b = L_m \bar{i}_a + L_s \bar{i}_b + L_m \bar{i}_c ,$$

$$\psi_c = L_m \bar{i}_a + L_m \bar{i}_b + L_s \bar{i}_c .$$

Solving for the currents yield:

$$\bar{i}_a = A\psi_a - B (\psi_b + \psi_c) , \tag{2.7}$$

$$\bar{i}_b = A\psi_b - B (\psi_c + \psi_a) , \tag{2.8}$$

$$\bar{i}_c = A\psi_c - B (\psi_a + \psi_b) , \tag{2.9}$$

where

$$A = \frac{L_m + L_s}{L_s^2 + L_s L_m - 2L_m^2} ,$$

$$B = \frac{L_m}{L_s^2 + L_s L_m - 2L_m^2} .$$

The voltage drop along the phase wires can be written as:

$$v_a - v'_a = R\bar{i}_a + \frac{d\psi_a}{dt} \,, \tag{2.10}$$

$$v_b - v'_b = R\bar{i}_b + \frac{d\psi_b}{dt} \,, \tag{2.11}$$

$$v_c - v'_c = R\bar{i}_c + \frac{d\psi_c}{dt} \,, \tag{2.12}$$

where $\bar{i}_a$, $\bar{i}_b$ and $\bar{i}_c$ can be replaced by their expressions (2.7)-(2.9).

Similarly, on the right side of the line, one has:

$$0 = -q'_a + \frac{C_g}{2}v'_a + \frac{C}{2}\left(v'_a - v'_b\right) + \frac{C}{2}\left(v'_a - v'_c\right) \,, \tag{2.13}$$

$$0 = -q'_b + \frac{C_g}{2}v'_b + \frac{C}{2}\left(v'_b - v'_c\right) + \frac{C}{2}\left(v'_b - v'_a\right) \,, \tag{2.14}$$

$$0 = -q'_c + \frac{C_g}{2}v'_c + \frac{C}{2}\left(v'_c - v'_a\right) + \frac{C}{2}\left(v'_c - v'_b\right) \,, \tag{2.15}$$

$$\frac{dq'_a}{dt} = \bar{i}_a - i'_a \,, \tag{2.16}$$

$$\frac{dq'_b}{dt} = \bar{i}_b - i'_b \,, \tag{2.17}$$

$$\frac{dq'_c}{dt} = \bar{i}_c - i'_c \,. \tag{2.18}$$

where again $\bar{i}_a$, $\bar{i}_b$ and $\bar{i}_c$ can be replaced by their expressions (2.7)-(2.9).

Replacing (2.7)-(2.9) in (2.4)-(2.6), (2.16)-(2.18) and (2.10)-(2.12), finally gives:

$$\frac{dq_a}{dt} = i_a - A\psi_a + B\left(\psi_b + \psi_c\right) \,, \tag{2.19}$$

$$\frac{dq_b}{dt} = i_b - A\psi_b + B\left(\psi_c + \psi_a\right) \,, \tag{2.20}$$

$$\frac{dq_c}{dt} = i_c - A\psi_c + B\left(\psi_a + \psi_b\right) \,, \tag{2.21}$$

$$\frac{dq'_a}{dt} = -i'_a + A\psi_a - B\left(\psi_b + \psi_c\right) \,, \tag{2.22}$$

$$\frac{dq'_b}{dt} = -i'_b + A\psi_b - B\left(\psi_c + \psi_a\right) \,, \tag{2.23}$$

$$\frac{dq'_c}{dt} = -i'_c + A\psi_c - B\left(\psi_a + \psi_b\right) \,, \tag{2.24}$$

$$\frac{d\psi_a}{dt} = -v'_a + v_a - AR\psi_a + BR\left(\psi_b + \psi_c\right) \,, \tag{2.25}$$

$$\frac{d\psi_b}{dt} = -v'_b + v_b - AR\psi_b + BR\left(\psi_c + \psi_a\right) \,, \tag{2.26}$$

$$\frac{d\psi_c}{dt} = -v'_c + v_c - AR\psi_c + BR\left(\psi_a + \psi_b\right) \,. \tag{2.27}$$

Equations (2.1)-(2.3), (2.13)-(2.15), (2.19)-(2.27), constitute the final set of 15 equations (9 linear Ordinary Differential Equations (ODEs) and 6 linear Algebraic Equations (AEs)) of the line model. Note that when deriving this model, no assumption was made concerning the expected time evolution of the various charges, voltages, currents and flux linkages.

2.2.3 Electromagnetic transients model of the Nordic test system

The test system that has been used in this research is the 74-bus, 102-branch, 23-machine Nordic system, version B, documented in [IEE15]. The one-line diagram is shown in Figure 2.8. This system is fictitious but inspired of the Swedish system (at the time of setting up the system). It is composed of four areas:

- "North" with hydro generation and some load,

- "Central" with much load and thermal power generation,

- "Equiv" connected to the "North" ; it includes a very simple equivalent of an external system,

- "South" that contains thermal generation, rather loosely connected to the rest of the system.

Without lack of generality, power-electronics based components such as static var compensators, wind parks or HVDC links have not been added, since the focus of the work was on a correct and efficient coupling between EMT and PM models, and not on particular components. We believe the proposed method is general enough to allow incorporating such components in the future.

The system has a 400-kV backbone, whose structure is shown in Figure 2.9, with rather long transmission lines, compensated with series capacitors. The percentage of series compensation[1] is indicated on the lines of concern in Figure 2.9.

The system is heavily loaded with large power transfer from North to Central areas. Secure system operation is limited by transient (angle) and long-term voltage instability (see Figure 2.4).

The models used in this test system are presented in Appendix A.

The size of the EMT model, in terms of number of ODEs and AEs, is detailed in Table 2.1. The AEs are classified in column "lin." if they are linear, and in the column "n.-lin." if at least one equation in the set is non-linear. Similarly, ODEs are all of the type "lin." since all non-linearities have been put into the AEs for the models under study here. Other models may of course also include non-linear ODEs.

---

[1]The degree of series compensation (DsC) is defined as the ratio of the capacitive reactance of the series capacitor to the inductive reactance of the transmission line, i.e.

$$DsC \triangleq \frac{|X_C|}{X_L} \times 100\%$$
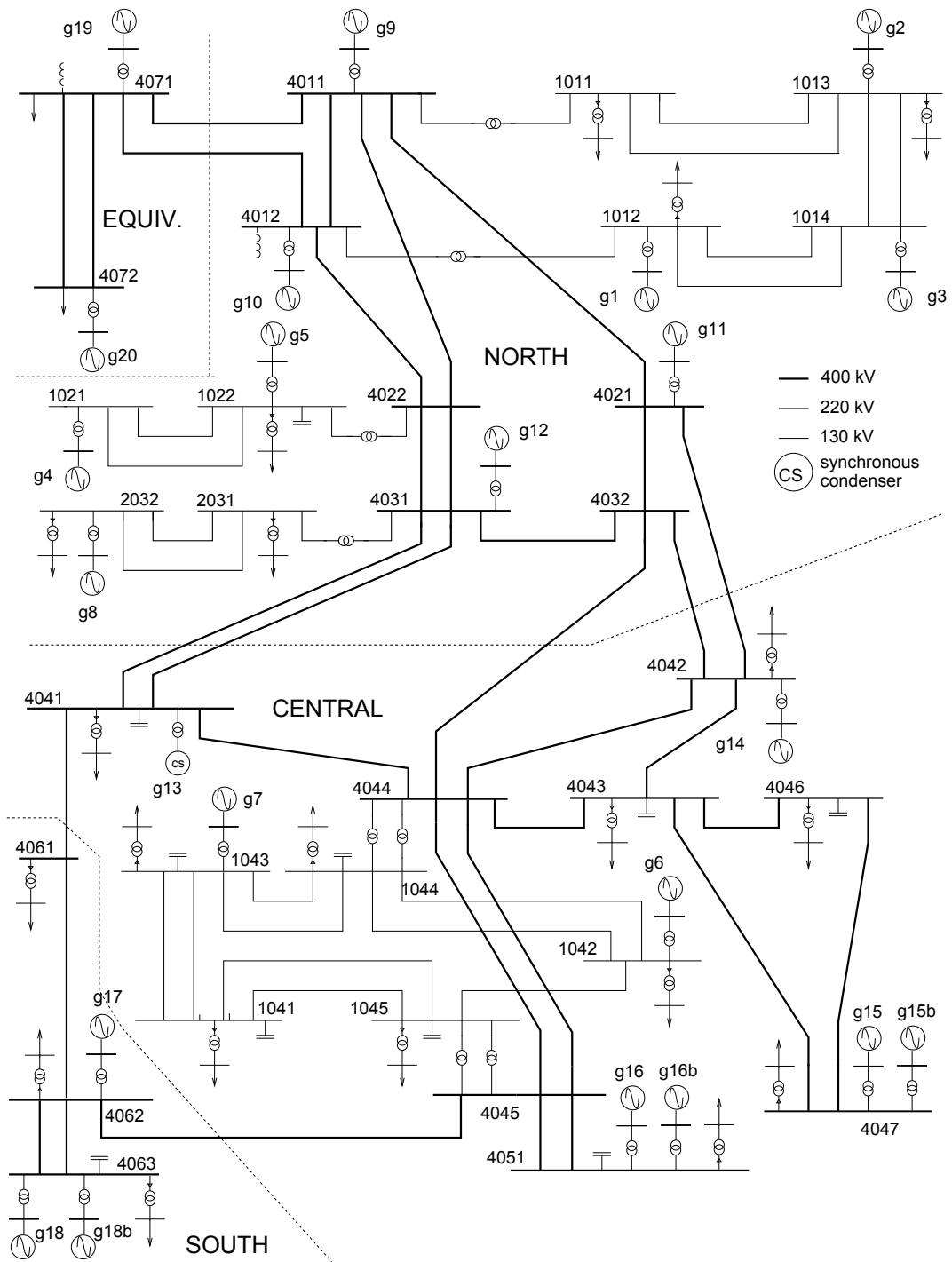
Figure 2.8: Nordic system, version B. [IEE15]
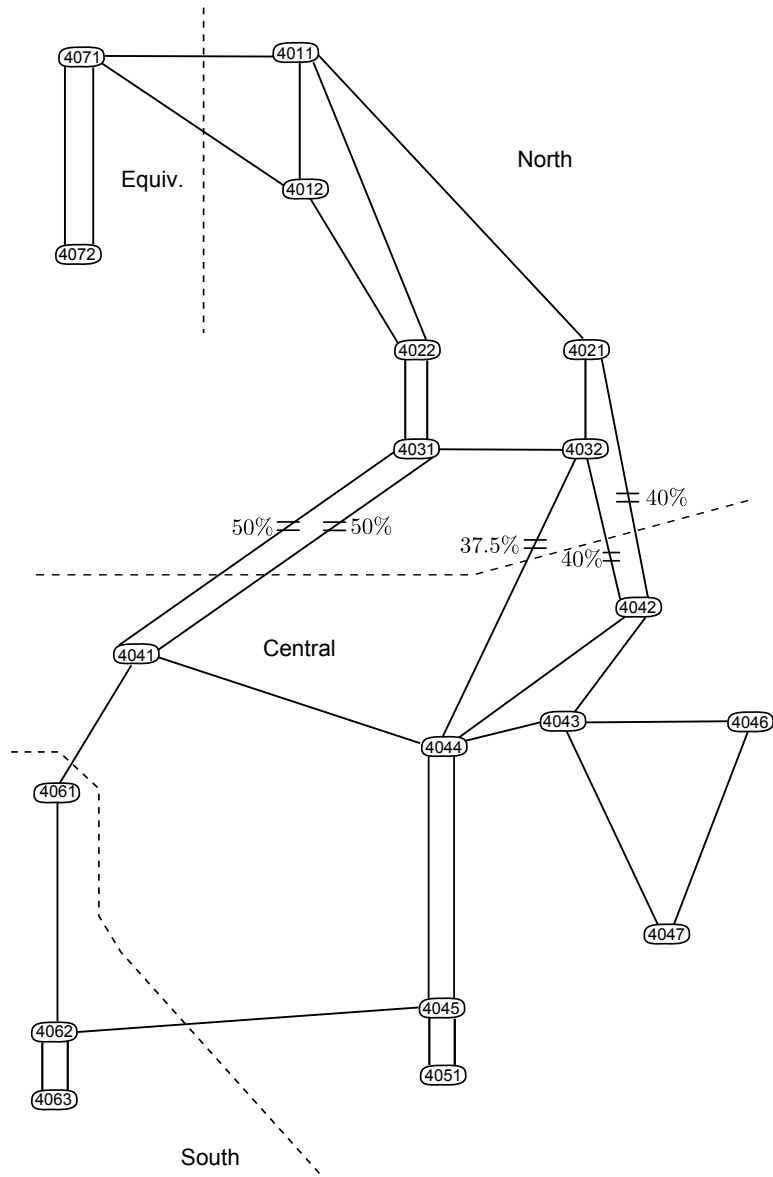
Figure 2.9: Backbone 400-kV system.

element	eqs per component				number of elts.	number of eqs.
	ODEs	AEs		Tot.		
	lin.	lin.	n.-lin.			
lines	9	6		15	52	780
transformers	3	5		8	53	424
shunts	3			3	11	33
impedance loads	3	3		6	22	132
buses (for KCLs[2])		3		3	79	237
synchronous machines	8		12	20	23	460
AVR[3]+exciters[4]	1 - 2	1 - 0		2	23	46
speed governors+turbines	4		2	6	12	72
constant torques		1		1	11	11
power system stabilizers	3	1		4	23	92
Total equations count:						**2287**

Table 2.1: EMT equations count for the test system.

It was not possible to use the well-known commercial EMTP-RV software [emt] for the PM-EMT co-simulation with the PM solver (see Section 2.4.6), since it was not possible in the commercial version of EMTP-RV to iterate on the simulation at every time-step, which was needed in development of a co-simulation solution. Instead, a solver was developed and implemented in MATLAB to perform the dynamic simulation of the above outlined EMT models. It is briefly presented in Appendix B. The equations are written in state-space form and solved with a "dishonnest" Newton method, where the sparse Jacobian matrix is not updated at every iteration. Both Backward Euler and Trapezoidal integration methods were implemented. The system is implemented in a decomposed way, allowing parts of the Jacobian to be kept constant throughout the whole simulation while other parts of the Jacobian may be updated at every time step or every Newton iteration if needed. The Jacobian matrix obtained when simulating the Central-South part of the Nordic system is presented in Appendix B.

As a preliminary step, the EMT solver implemented in MATLAB was validated, on a sub-domain of the Nordic system, comparing its output results with those given by EMTP-RV. In this test, the remaining of the system (i.e. the non-shaded part in Figure 2.10) was replaced by a constant voltage source at fundamental frequency. A single-phase fault was assumed on line 4046-4047, near bus 4047 (see Figure 2.10), cleared by opening the three phases of the faulted line.

Figure 2.11 shows the current in phase a received by the above mentioned voltage source, before, during and after the fault. The evolutions do not show any significant difference between the MATLAB-based EMT solver and the benchmark EMTP-RV. Thus, for the level of detail expected

---

[2]Kirchhoff Current Law
[3]Automatic Voltage Regulator.
[4]One out of the two equations is an ODE. The second equation is an AE or an ODE depending on whether an integrator in the model is limited or not.
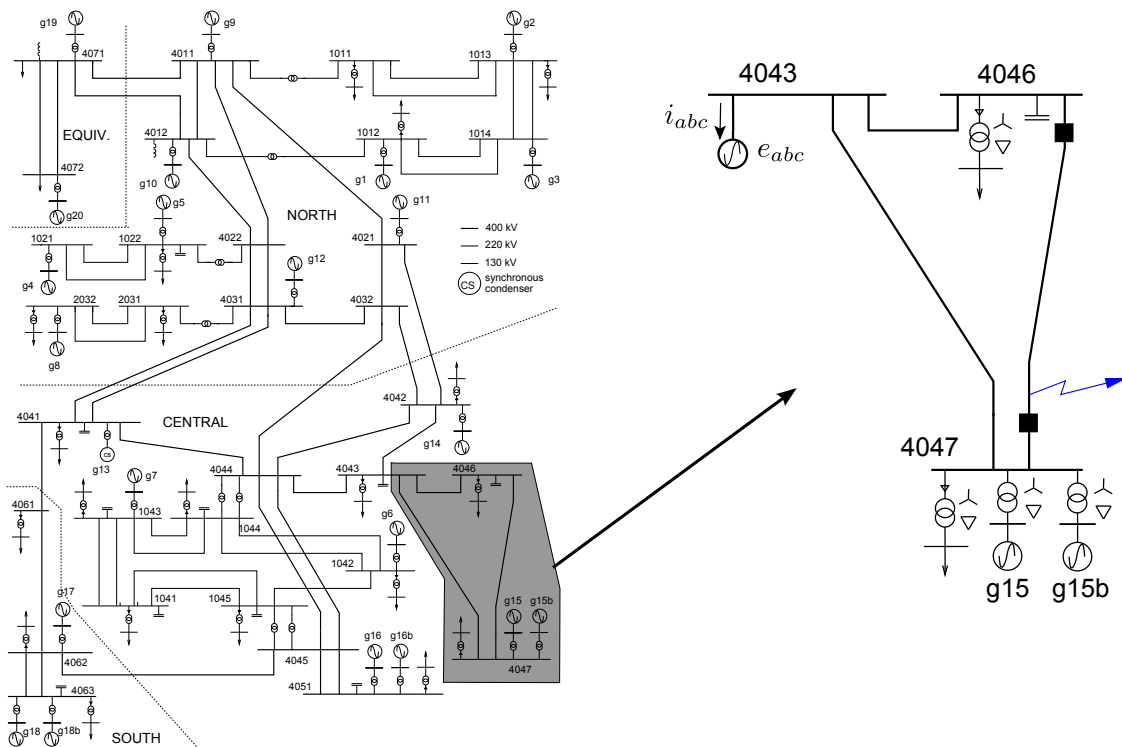
Figure 2.10: Sub-system of the Nordic test system used for validation of implemented MATLAB-EMT solver.

from the hybrid PM-EMT simulation, the EMT solver can be considered equivalent to EMTP-RV.

2.3 From electromagnetic transients to phasor models

2.3.1 Dynamic phasors family

As mentionned in the introduction of this chapter, several techniques can be grouped into the family of Dynamic Phasor (DP) modeling techniques. This section introduces the general principles of DP modeling techniques.

2.3.1.1 Shifted-frequency analysis, frequency-adaptive simulation of transients and frequency-adaptive electromagnetic transients

The idea of Shifted Frequency Analysis (SFA) [ZMD07, ZMD09, MDBB14] is that it is generally useless to simulate in detail the carrier waveform of the abc signals, because their envelopes generally give sufficient information, while avoiding the requirement of using small time step sizes compared to the carrier period. The basic operations proposed by SFA are shown in Figure 2.12. SFA proposes to transform the real signals $s(t)$ (instantaneous signals as observed in reality) into
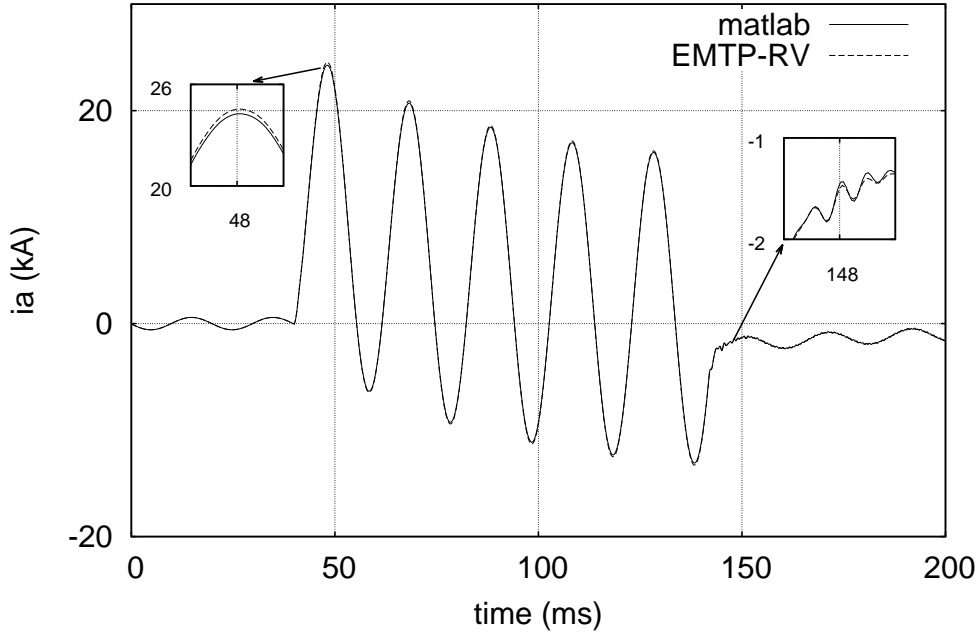
Figure 2.11: Current in phase a received by voltage source at bus 4043, obtained from MATLAB-based EMT solver and EMTP-RV, respectively.
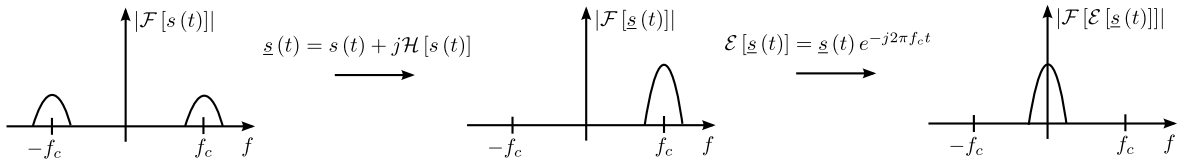
Figure 2.12: Hilbert transform and carrier frequency shifting.

analytic signals $\underline{s}(t)$:

$$\underline{s}(t) = s(t) + j\mathcal{H}[s(t)] \ . \tag{2.28}$$

While the Fourier spectrum of the real signal $s(t)$ extends to negative frequencies, this is not the case for the Fourier spectrum of the corresponding analytic signal $\underline{s}(t)$. In (2.28), $\mathcal{H}[\bullet]$ is the notation for Hilbert transform[5]. The effect of the Hilbert transform on a real signal is to phase shift it by $-90°$. The analytic signal $\underline{s}(t)$ is then shifted by a shift frequency f_s according to:

$$\mathcal{E}[\underline{s}(t)] = \underline{s}(t)\, e^{-j2\pi f_s t} \ . \tag{2.29}$$

If the shift frequency f_s is chosen equal to the carrier frequency f_c, the carrier is eliminated from the signal, and only the envelope remains. This allows for a larger time step size to be used in the EMT simulation of the shifted analytic signal $\mathcal{E}[\underline{s}(t)]$ in (2.29).

References [SSG06, GS09] proposed an extension of SFA, called Frequency-Adaptive Simulation of Transients (FAST). While in SFA, the shift frequency f_s in (2.29) is fixed, FAST makes the shift

---

[5]$\mathcal{H}[s(t)] = \frac{1}{\pi}\int_{-\infty}^{\infty}\frac{s(\xi)}{t-\xi}d\xi.$
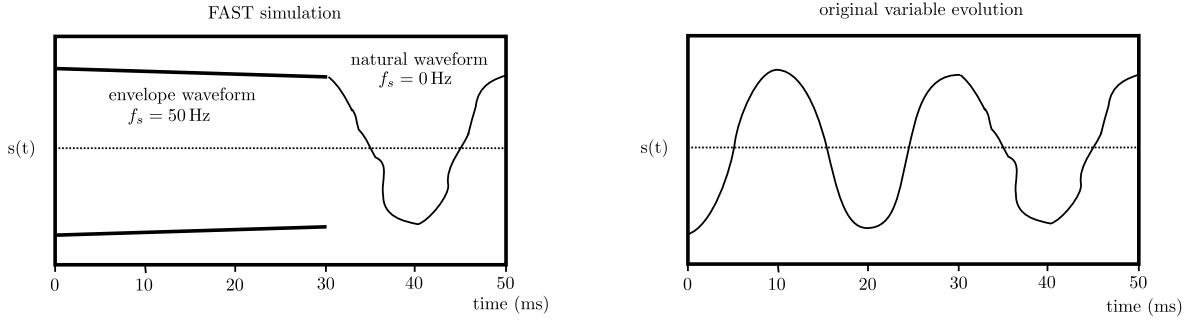
Figure 2.13: FAST simulation.
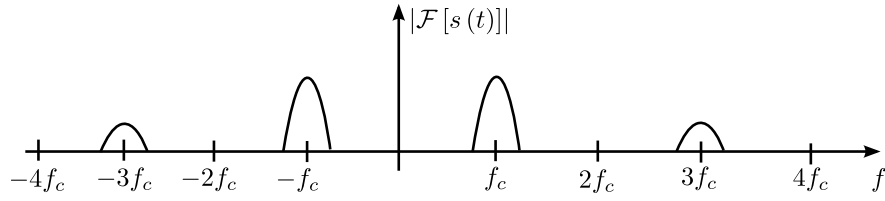
Figure 2.14: Signal with non-negligible harmonic content.

frequency a simulation parameter in addition to time step size. In FAST, while the shift frequency could take any value, there are two basic cases, easy to understand:

- if f_s is set to the carrier frequency - say - $f_c = 50\,\text{Hz}$, FAST reduces to the fixed-carrier frequency dynamic phasor approach, outlined above,

- if f_s is set to zero, FAST reduces to classical EMT model.

The advantage of FAST over SFA is that FAST can switch from $f_s = 0$ to track an electromagnetic transient signal for a short period, and then use $f_c = 50$ Hz to reduce the computational burden when the envelope gives sufficient information on the simulated signal. An illustrative example (inspired from [GS09]) is shown in Figure 2.13. Modeled elements using FAST include transformers, synchronous machines and transmission lines.

Recently, some authors [FD12] proposed a method, called Frequency-Adaptive EMT (FEMT), similar to FAST in the sense that the shift frequency is adaptive.

2.3.1.2 Dynamic phasors

In the case where the simulated signal contains harmonics (e.g. Figure 2.14), the SFA and FAST techniques (Section 2.3.1.1) have to be extended. A time-domain waveform $x(\tau)$ can be represented in the interval $[t - T,\ t]$ using a Fourier series of the form

$$x(\tau) \quad = \quad \sum_{k=-\infty}^{\infty} X_k(t)\, e^{jk\omega_s \tau}, \tag{2.30}$$
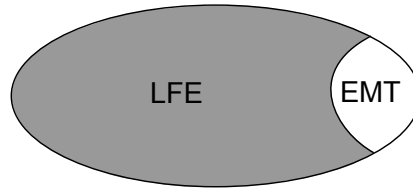
Figure 2.15: Part of the power system is represented through a LFE.

where $\omega_s = \frac{2\pi}{T}$ and $X_k(t)$, the complex Fourier coefficients, called dynamic phasors [Hen99, SLA99, SSA02, Dem08, YBA11], are given by:

$$X_k(t) = \frac{1}{T} \int_{t-T}^{t} x(\tau) e^{-jk\omega_s \tau} d\tau \ . \tag{2.31}$$

The waveform $x(\tau)$ can be approximated on the given interval $[t - T, \, t]$ and to an arbitrary accuracy, by using equations (2.30)-(2.31), with an appropriate number of Fourier coefficients kept in the model.

2.3.2   Low frequency equivalent of a part of the system

A simplified way to simulate a large power system consists in deriving a Low Frequency Equivalent (LFE) of a part of the latter while simulating in detail the remaining part [CA70, SDS14]. This leads to perform a coupled LFE-EMT simulation, as illustrated in Figure 2.15.

2.3.2.1   Low frequency equivalent derivation techniques

A survey on proposed techniques for calculating dynamic system equivalents and in particular LFEs is offered in [ANL+12]. The main techniques for LFE can be categorized into the following families:

- Modal methods,

- Coherency methods,

- Measurement or simulation based methods.

In transient stability analysis, the dynamic models of a power system are nonlinear. Hence, to be applicable, model reduction methods must either be applied directly to the nonlinear system, or reduce the linearized model of the system.

Modal methods [UT71, EKS02] are based on the linearized state space model:

$$\dot{\mathbf{X}} = \mathbf{A}\mathbf{X} + \mathbf{B}\mathbf{u} \, ,$$

where the eigenvalues of the system matrix $\mathbf{A}$ give the modes of the dynamic system. The principle of modal methods is to extract the relatively less damped modes (eigenvalues of $\mathbf{A}$ closer
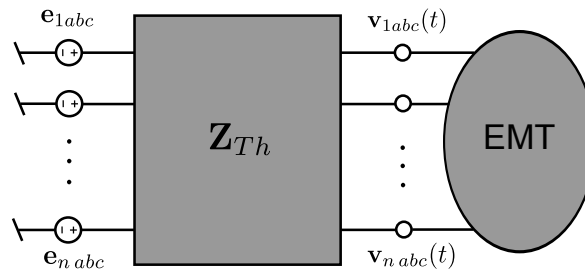
Figure 2.16: Multiport EMT Thévenin equivalent.

to the imaginary axis) while ignoring the highly damped modes. These methods belong to the family of Proper Orthogonal Decomposition (POD) methods [Ast04]. The main drawback of these methods is that, being based on a linearized state space model, they do not take into account the discrete events (such as for instance transformer tap changing, load shedding, ..) occuring in the equivalenced sub-system.

Coherency methods or "similarity" methods involve grouping of "similar" machines [LS73, MV11]. The groups are obtained by analysis of the system response to a perturbation. The LFE is then obtained by replacing such groups by a large equivalent machine.

Other methods rely on the response of the external system, measured or simulated [ANL$^+$12]. Curve fitting techniques are used to determine the model parameters, based on the system response.

2.3.2.2 Low frequency equivalent implementation

Regardless of the way the LFE is derived, it needs to be implemented in the EMT solver. There are several options, but the simplest equivalent one can think of is a multiport Thévenin equivalent as shown in Figure 2.16.

The model derived from the Thévenin equivalent is written as:

$$\mathbf{v} = \mathbf{e_{Th}} + \mathbf{R}_{\mathbf{Th}}^{abc}\mathbf{i} + \mathbf{L}_{\mathbf{Th}}^{abc}\frac{d}{dt}\mathbf{i}\,, \tag{2.32}$$

with

$$
\begin{aligned}
\mathbf{v} &= \begin{bmatrix} v_{1\,abc} & \cdots & v_{n\,abc} \end{bmatrix}^T, \\
\mathbf{e_{Th}} &= \begin{bmatrix} e_{1\,abc} & \cdots & e_{n\,abc} \end{bmatrix}^T, \\
\mathbf{i} &= \begin{bmatrix} i_{1\,abc} & \cdots & i_{n\,abc} \end{bmatrix}^T,
\end{aligned}
$$

where the general form of $\mathbf{R_{Th}^{abc}}$ is:

$$
\mathbf{R_{Th}^{abc}} =
\begin{bmatrix}
R_1 & 0 & 0 & & R_{1n} & 0 & 0 \\
0 & R_1 & 0 & \cdots & 0 & R_{1n} & 0 \\
0 & 0 & R_1 & & 0 & 0 & R_{1n} \\
& \vdots & & \ddots & & \vdots & \\
R_{1n} & 0 & 0 & & R_n & 0 & 0 \\
0 & R_{1n} & 0 & \cdots & 0 & R_n & 0 \\
0 & 0 & R_{1n} & & 0 & 0 & R_n
\end{bmatrix},
\tag{2.33}
$$

where the off-diagonal terms are zero because of the negligible resistive coupling between abc phases.

$\mathbf{L_{Th}^{abc}}$ is generally of the form:

$$
\mathbf{L_{Th}^{abc}} =
\begin{bmatrix}
L_{1a} & L_{1ab} & L_{1ac} & & L_{1na} & L_{1nab} & L_{1nac} \\
L_{1ab} & L_{1b} & L_{1bc} & \cdots & L_{1nab} & L_{1nb} & L_{1nbc} \\
L_{1ac} & L_{1bc} & L_{1c} & & L_{1nac} & L_{1nbc} & L_{1nc} \\
& \vdots & & \ddots & & \vdots & \\
L_{1na} & L_{1nab} & L_{1nac} & & L_{na} & L_{nab} & L_{nac} \\
L_{1nab} & L_{1nb} & L_{1nbc} & \cdots & L_{nab} & L_{nb} & L_{nbc} \\
L_{1nac} & L_{1nbc} & L_{1nc} & & L_{nac} & L_{nbc} & L_{nc}
\end{bmatrix},
\tag{2.34}
$$

where the off-diagonal terms are non-zero to take into account the magnetic coupling between abc phases.

2.3.3   Simulating a part of the system with a simplified model

While the equivalencing methods presented in the previous section lead to a speed up in computation speed, they inherently lack precision because the LFE is computed once for all. If the LFE needs to be updated, then the LFE-EMT solution may become cumbersome due to the successive recomputations of the equivalents. Another interesting possibility, which is the one chosen in this thesis, consists of simulating one part of the network with simplified models. Among them, the PM model routinely used for power system stability analysis is attractive due to its ability to retain some nonlinearity as well as a significant subset of the power system dynamics (see Figure 2.4). The derivation of PM models is recalled in the next section.
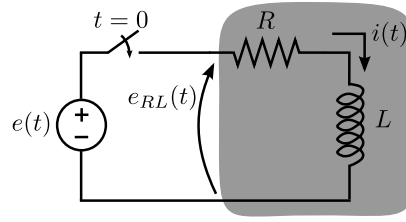
Figure 2.17: RL circuit with equivalent source e(t).

2.4 Phasor models

2.4.1 Phasor model of a simple RL circuit

In order to give insight into the approximation underlying PM models, we consider the very simple RL circuit shown in Figure 2.17, with $R = 1\,\Omega$ and $L = 20\,mH$, characterized by a time constant $\tau = L/R = 20\,ms$. The RL circuit is connected through a switch to the voltage source $e(t)$ with a varying Root Mean Squares (RMS) value $E(t)$. The voltage $e(t)$ is thus of the form:

$$e(t) = \sqrt{2}E(t)\cos\left(\omega_s t + \phi_0\right)\,,\tag{2.35}$$

where ω_s is the synchronous frequency of the system, chosen here as:

$$\omega_s = 2\pi 50\text{ rad/s}\,.\tag{2.36}$$

The phase angle of the voltage source $e(t)$ at $t = 0$ is $\phi_0 = -\pi/4$. The evolution of $E(t)$ is given by the following ODE:

$$\frac{dE(t)}{dt} = \frac{E_0 - E(t)}{T_E}\,, E\left(0^+\right) = 0.5\tag{2.37}$$

where $T_E = 300\,ms$.

The voltage $e_{RL}(t)$ is given by:

$$e_{RL}(t) = \begin{cases} e(t) & \forall t \geq 0 \\ 0 & \forall t < 0 \end{cases}\,,$$

The time evolutions of the voltage source $e_{RL}(t)$ and of its RMS value $E_{RL}(t)$ are shown in Figures 2.18b and 2.18a respectively.

For $t \geq 0$, the equation of the circuit of Figure 2.17 is:

$$L\frac{di}{dt} = e(t) - Ri(t)\,.\tag{2.38}$$

The solution $i(t)$ of this ODE is shown in Figure 2.19.

The current $i(t)$ is a modulated cosine at fundamental frequency ω_s. EMT simulation of this circuit requires a minimum of 20 time steps per fundamental period to correctly represent the cosine and its distorsions, i.e. $h_{EMT} \leq 1\,ms$.

(a) Evolution of $E_{RL}(t)$.

(b) Evolution of $e_{RL}(t)$
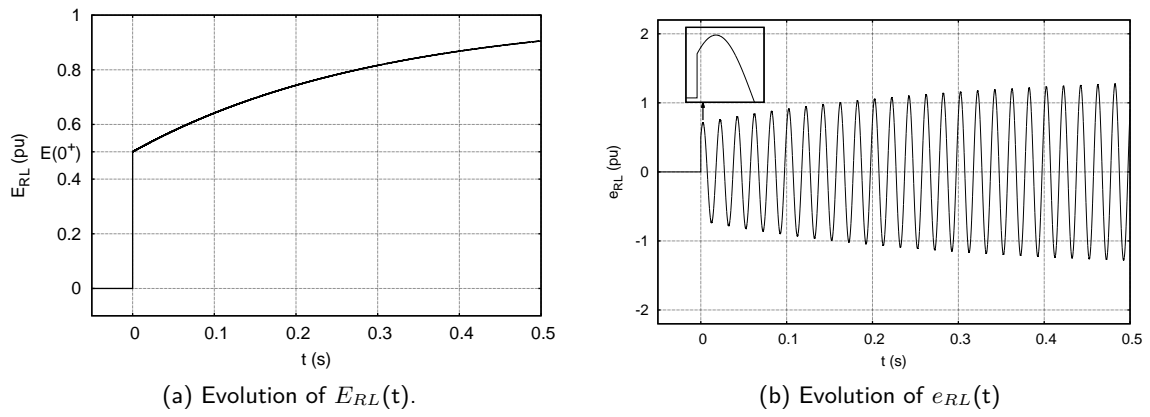
Figure 2.18: Applied voltage e_{RL}.
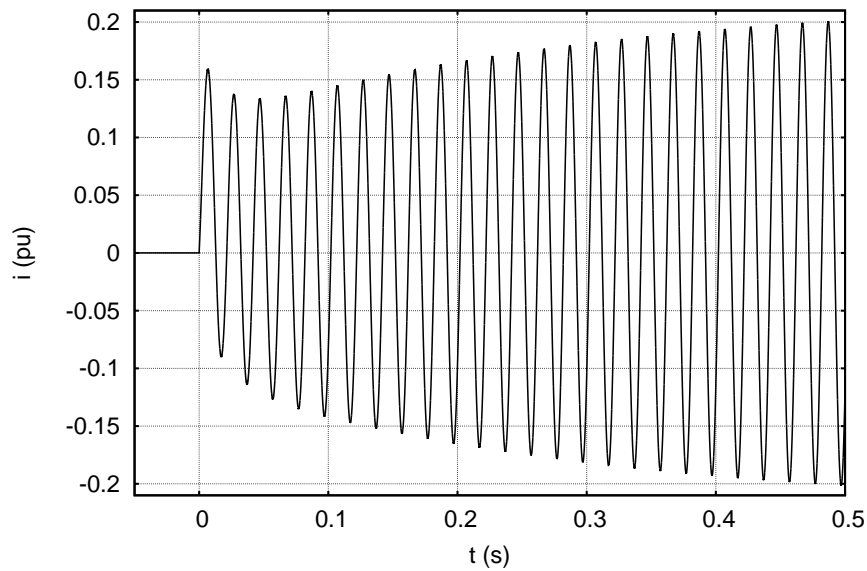
Figure 2.19: EMT solution for i(t).
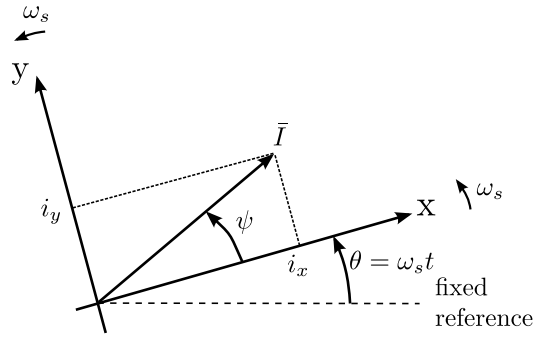
Figure 2.20: Synchronous reference frame.

Without lack of generality, let us assume that the solution $i(t)$ is of the form:

$$i(t) = \sqrt{2} \ real \left[(i_x + ji_y) \, e^{j\omega_s t} \right] , \tag{2.39}$$

where the following complex number:

$$\bar{I} = i_x + ji_y ,$$

is an extension of the standard *phasor*. i_x and i_y can be interpreted as the projection of $\bar{I}$ on rotating axes, usually referred to as Synchronous Reference Frame (SRF) such as represented in Figure 2.20. The following relations are easily derived:

$$L\frac{di}{dt} = \sqrt{2} \, L \, real \left[\frac{d}{dt} \left[(i_x + ji_y) \, e^{j\omega_s t} \right] \right] , \tag{2.40}$$

$$Ri = \sqrt{2} \, R \, real \left[(i_x + ji_y) \, e^{j\omega_s t} \right] , \tag{2.41}$$

$$e = \sqrt{2} \, real \left[(e_x + je_y) \, e^{j\omega_s t} \right] . \tag{2.42}$$

Definition (2.42) and voltage source equation (2.35) then simply give for $e_x(t)$ and $e_y(t)$:

$$e_x(t) = E(t) \cos \phi_0$$
$$e_y(t) = E(t) \sin \phi_0$$

Replacing (2.40), (2.41) and (2.42) into (2.38), and simplifying the expression yields the following two equations:

$$L\frac{d}{dt}i_x - \omega_s L i_y + Ri_x = e_x , \tag{2.43}$$

$$L\frac{d}{dt}i_y + \omega_s L i_x + Ri_y = e_y . \tag{2.44}$$

Equations (2.43) - (2.44) can be solved numerically in place of (2.38) to obtain the time evolution of $i_x(t)$ and $i_y(t)$. The latter are shown in Figure 2.21. From them, the current $i(t)$ is obtained using (2.39). This gives exactly the same solution as the one represented in Figure 2.19. Let us remark that (2.43) - (2.44) are also the DP model of the RL network of Figure 2.17 when
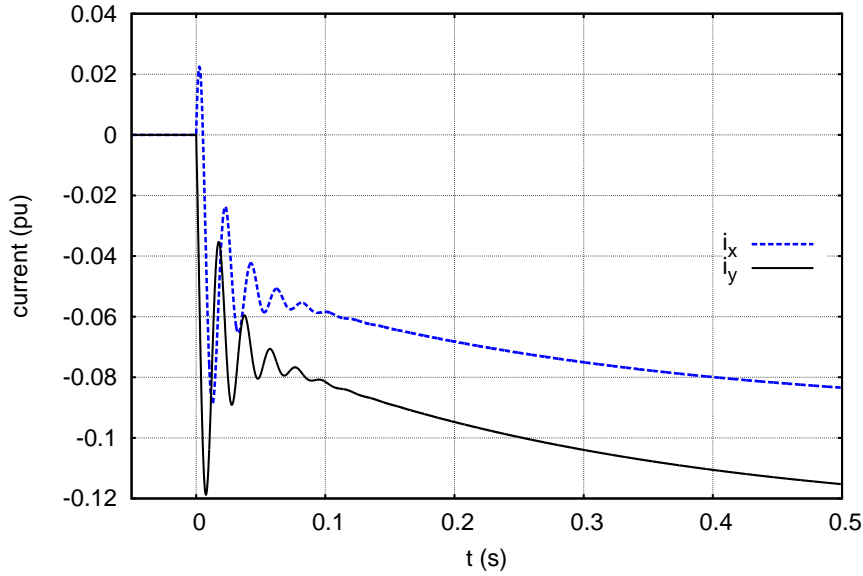
Figure 2.21: EMT solution for $i_x(t)$ and $i_y(t)$.

considering only the fundamental (this simple circuit does not contain any higher-order harmonic and there is no interest to use the DP model for it).

Now, if the derivatives are neglected in (2.43) - (2.44)[6], these equations become the following algebraic equations:

$$-\omega_s L i_y + R i_x \;\; = \;\; e_x \,, \tag{2.45}$$

$$+\omega_s L i_x + R i_y \;\; = \;\; e_y \,, \tag{2.46}$$

where $e_x(t)$ and $e_y(t)$ derive from their definition through (2.42). The two real equations (2.45) and (2.46) can be combined into a single complex equation:

$$(R + j\omega_s L)\,\bar{I} = \bar{E} \,, \tag{2.47}$$

where

$$\bar{E} \;\; \triangleq \;\; e_x + je_y \,.$$

Equation (2.47) is nothing but the phasor equation of the RL circuit in steady-state sinusoidal operation. It is very important to note that the RL network obtained after neglecting the derivatives can be described by AEs, neglecting its own dynamics which is fast compared to the slower evolution of $E(t)$ ($\tau = 20\,\mathrm{ms} \ll T_E = 300\,\mathrm{ms}$). Equations (2.37), (2.45) and (2.46) make up the PM model of the RL circuit with the time-varying source. A solver that can handle DAEs is needed to solve

---

[6]Neglecting the derivatives of the currents reminds the power system reader of the phasor approximation of the synchronous machine where the transformation ElectroMotive Force (EMF) $\frac{d\psi_{dqo}}{dt}$ are neglected in the stator Park equations, as noted in Appendix A.2.3. In phasor approximation, stator fluxes changes instantaneously following a perturbation, while in EMT model, stator flux dynamics are included.
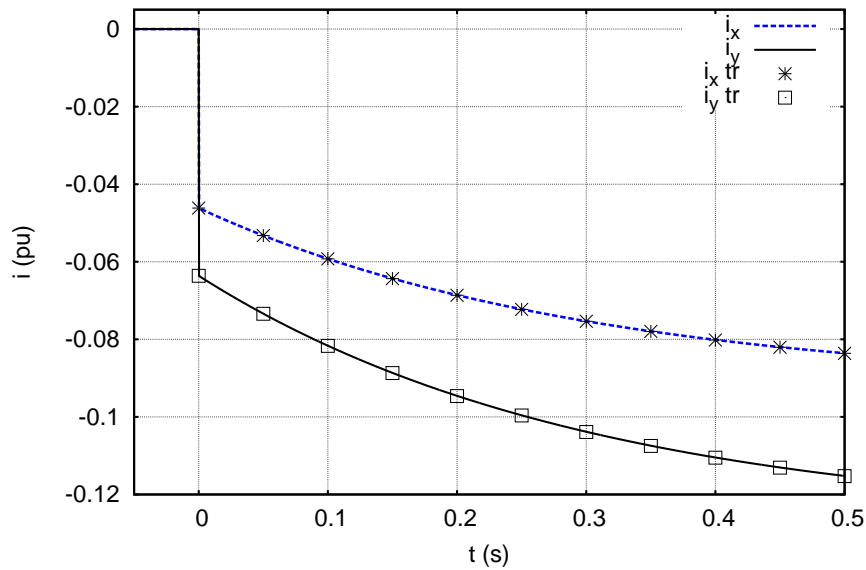
Figure 2.22: Integration of PM currents with $H = 50\,ms$.

such a system. While a maximum time step size of $h = 1\,\text{ms}$ had to be used for solving EMT model, a time step size $H = 50\,\text{ms}$ is small enough to accurately solve the PM equations with the trapezoidal rule. This is confirmed by Figure 2.22 where the crosses indicate the time steps.

A comparison of the solutions obtained by EMT and PM models is shown in Figure 2.23. In fact, it is very uncommon in PM simulation to rebuild the "full-wave" evolution of currents, voltages, etc. It is done in Figure 2.23b for comparison purposes only. As can be seen, the EMT transients are not reproduced by the PM model. In particular, the current $i(t)$ obtained from the PM model experiences a non-physical discontinuity at $t = 0$ due to the jump in the amplitude of the source voltage $e(t)$. After a very short time however, the EMT and PM approximations are so close to each other that it is impossible to distinguish both curves.

The simple example presented in this section assumed a constant phase angle ϕ_0 for the voltage source $e(t)$, as explicited by (2.35). Note that in PM simulation, we also deal with variable phase angles (see (2.48)).

Figure 2.24 shows a comparison of EMT and PM models of single-phase electrical components. We note that a derivative (respectively integral) in EMT corresponds to a $+90°$ (respectively $-90°$) phase shift in the PM model. Let us also note that while the PM models of Figure 2.24 are much simpler than the EMT ones (and more computationally efficient), they are also restrictive since they assume quasi-sinusoidal waveforms of angular frequency ω_s. The angular frequency ω_s of concern here is the frequency of the current through the self-inductance L or the frequency of the voltage accross the capacitance C.
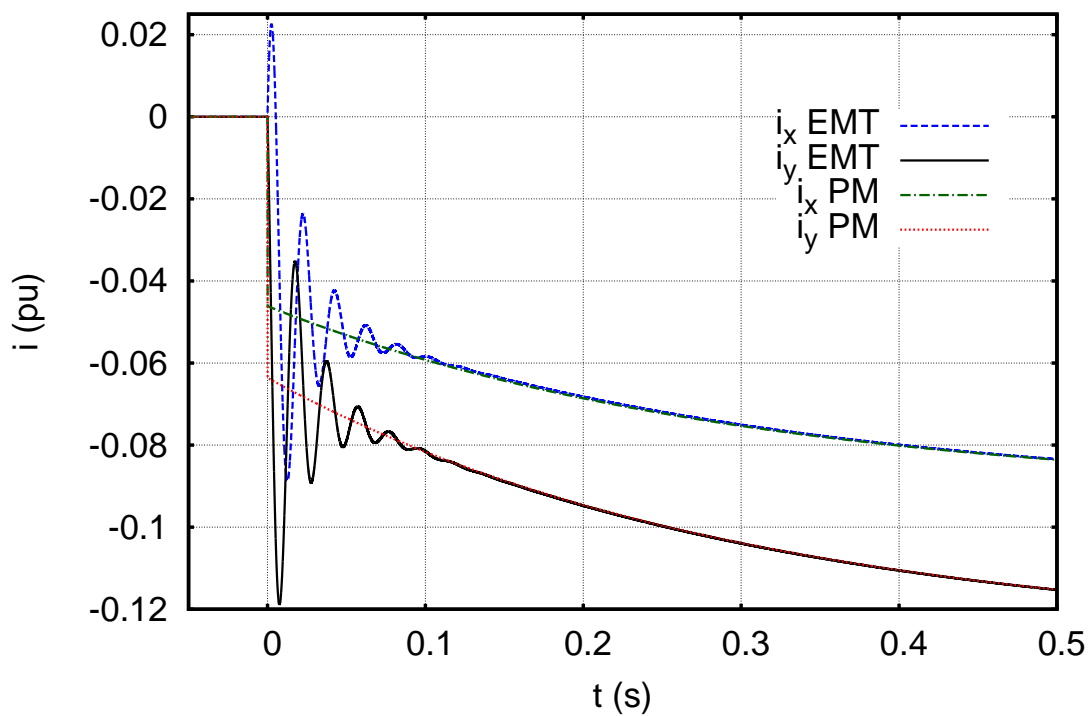
(a) $i_x(t)$ and $i_y(t)$.
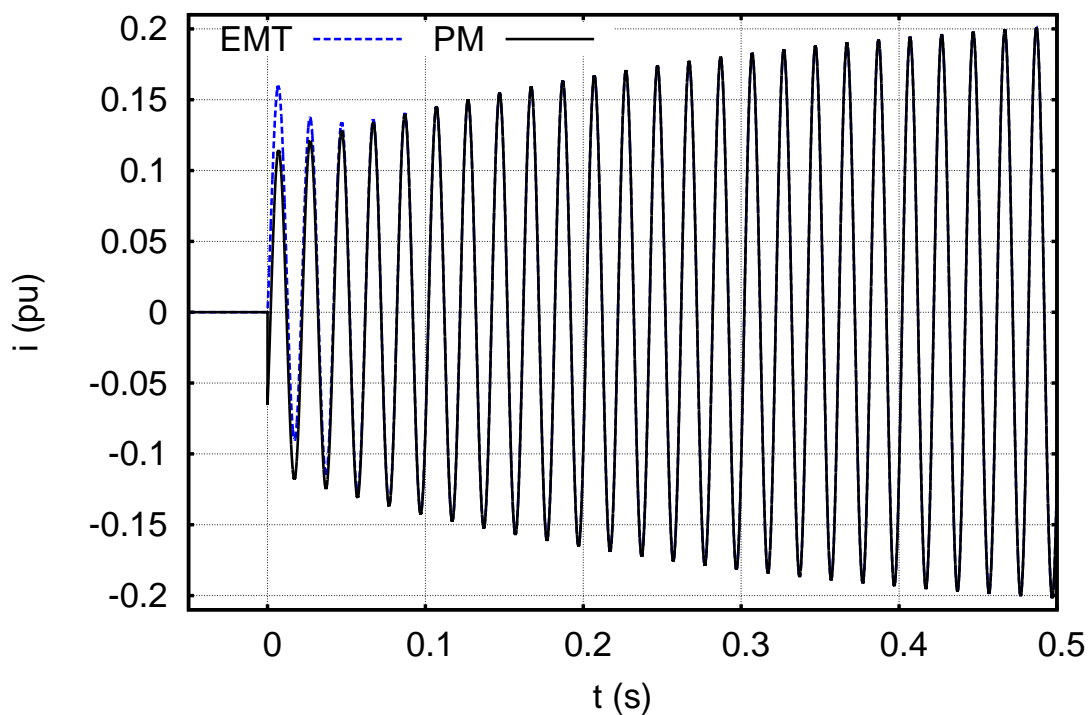
(b) $i(t)$.

Figure 2.23: Comparison of EMT and PM solutions.
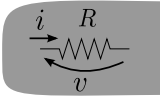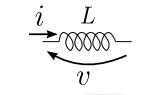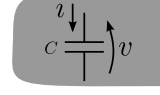
Figure 2.24: EMT and PM models of single-phase components.
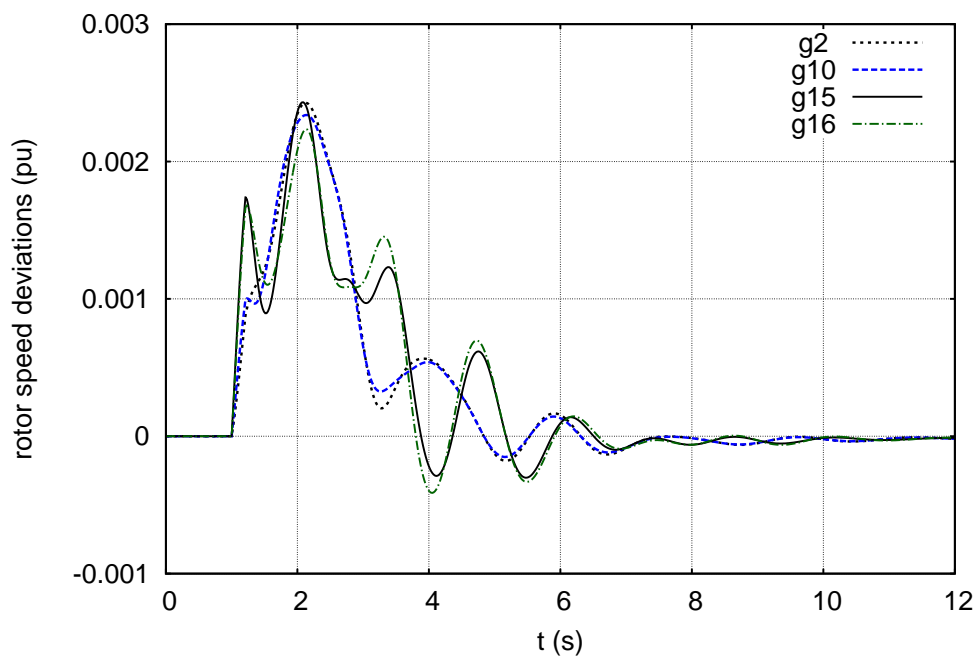
Figure 2.25: Evolution of rotor speeds in a power system.

2.4.2 What is (what are) the frequency (the frequencies) in a power system?

The presence of the angular frequency ω_s in (2.45) and (2.46) raises the following question: *what is or what are the frequencies in a power system?* In general a power system is not a perfectly synchronous system characterized by a single frequency ω_s. The frequency of the voltages at a bus is influenced by the rotation speeds of the nearest synchronous machines. Figure 2.25 shows the rotor speed deviations (with respect to synchronous speed and in per unit) of some machines in the Nordic system presented in Section 2.2.3, after a $210\,\text{ms}$ short-circuit applied at $t = 1\,\text{s}$ on bus 1042, very near machine g6 (this test case will be detailed in Section 5.2.2.1). We observe a speed deviation in the order of 0.1 percent with respect to the synchronous angular frequency ω_s. This deviation may seem negligible at first glance, but it is mandatory to take it into account in the PM-EMT coupling algorithm, as will be explained in Section 3.8.

2.4.3   Phasor models of three-phase networks

The example of Section 2.4.1 considered a single-phase RL circuit. However, transmission networks are three-phase circuits. In this section, we introduce PM models of three-phase networks. In transmission networks, voltages and currents are generally close to pure cosine wave phase shifted of $\frac{2\pi}{3}$ between them. By extension of (2.35) of the simple example, such variables can be written:

$$\mathbf{v}_{abc} = \left[\begin{array}{c} v_a \\ v_b \\ v_c \end{array} \right] = \left[\begin{array}{c} \sqrt{2}V_a\left(t\right)\cos\left(\omega_s t + \phi_a\left(t\right)\right) + \epsilon_a \\ \sqrt{2}V_a\left(t\right)\cos\left(\omega_s t + \phi_a\left(t\right) - \frac{2\pi}{3}\right) + \epsilon_b \\ \sqrt{2}V_a\left(t\right)\cos\left(\omega_s t + \phi_a\left(t\right) - \frac{4\pi}{3}\right) + \epsilon_c \end{array} \right], \tag{2.48}$$

where ϵ_a, ϵ_b and ϵ_c express the small deviations from the phase-shifted cosine waves. The reason why voltages and currents obey such time evolutions is because they are produced by synchronous generators with a three-phase stator, built to produce voltages such as (2.48).

The PM approximation neglects ϵ_a, ϵ_b and ϵ_c by assuming $\epsilon_a \approx \epsilon_b \approx \epsilon_c \approx 0$. This approximation expresses the fact that:

- each of the three evolutions obey a cosine wave description, with varying amplitudes and phase angles,

- each waveform has the same effective value $V_a\left(t\right)$,

- the waveforms are phase shifted with respect to each other by $\frac{2\pi}{3}$.

The RMS value V_a and phase angle ϕ_a are supposed to vary slowly compared to the period $2\pi/\omega_s$ ($20\,\text{ms}$ in Europe and $16.67\,\text{ms}$ in North America, for instance). The frequency spectrum of the amplitude and phase angle modulation is generally limited to $[0 - 5\text{Hz}]$. It is clear from (2.48) that a single-phase (or "per-phase" [Kun94]) equivalent representation is sufficient. One can also write

$$\left[\begin{array}{c} \bar{V}_a \\ \bar{V}_b \\ \bar{V}_c \end{array} \right] = \left[\begin{array}{c} \bar{V}_a \\ a^2\bar{V}_a \\ a\bar{V}_a \end{array} \right], \tag{2.49}$$

where a has been defined as:

$$a = e^{j\frac{2\pi}{3}}. \tag{2.50}$$

The sequence (2.48) is called positive-sequence and is represented in Figure 2.26 together with the so-called negative- and zero-sequence. It can be shown that any sequence of phasors such as:

$$\left[\begin{array}{c} \bar{V}_a \\ \bar{V}_b \\ \bar{V}_c \end{array} \right] = \left[\begin{array}{c} V_a e^{j\phi_a} \\ V_b e^{j\phi_b} \\ V_c e^{j\phi_c} \end{array} \right], \tag{2.51}$$

Figure 2.26: Positive-, negative- and zero-sequence phasors.
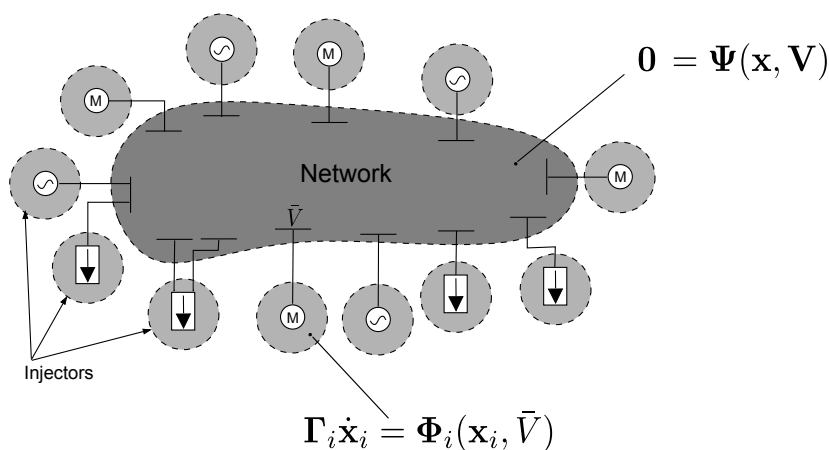
Figure 2.27: Power system representation in PM approximation.

can be decomposed into a sum of positive-, negative- and zero-sequence phasors:

$$
\begin{bmatrix} \bar{V}_a \\ \bar{V}_b \\ \bar{V}_c \end{bmatrix} = \begin{bmatrix} \bar{V}_{a1} + \bar{V}_{a2} + \bar{V}_{a0} \\ \bar{V}_{b1} + \bar{V}_{b2} + \bar{V}_{b0} \\ \bar{V}_{c1} + \bar{V}_{c2} + \bar{V}_{c0} \end{bmatrix}.
\tag{2.52}
$$

A sequence containing negative- and/or zero-sequence in addition to positive-sequence yields imbalanced phasors.

The most typical PM solvers deal with the positive sequence only [Kun94]. Some PM solvers include positive-, negative- and zero-sequence [Eur], but this is not very common. There exists correction techniques to account for imbalances when simulating the positive sequence model only [Kun94]. Most stability studies in PM consider three-phase faults, which are the most dangerous for stability. Such faults involve mainly positive sequence.

PM solvers deal with a model of the type shown in Figure 2.27. Compared to the corresponding representation in EMT models (Figure 2.6), the PM approximation is characterized by algebraic equations for the network, while the network under EMT representation is described by a set
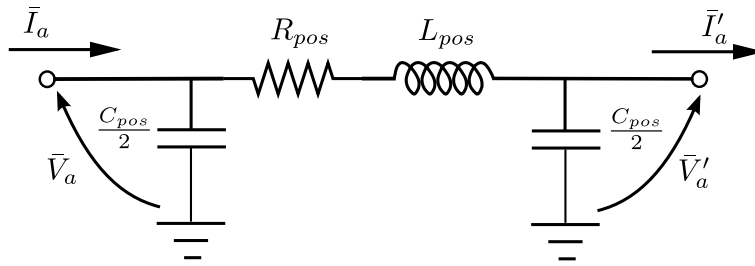
Figure 2.28: Implemented line PM model.

of DAEs. This means that the PM approximation neglects the network dynamics by assuming these dynamics to be infinitely fast (compared to the other phenomena under study, especially electromechanical transients). This point is further illustrated in the next section by getting back to the transmission line model.

2.4.4 Phasor model of an overhead line

Let us assume that the three input and output voltages as well as the currents in the three-phase line of Figure 2.7 are balanced. In this case, a single-phase (or "per-phase") model is sufficient to represent the line. The model is shown in Figure 2.28. Compared to Figure 2.7, the line-to-line C and line-to-ground C_g capacitances on each side have been combined into a single capacitance $\frac{C_{pos}}{2}$ accounting for the effects of the couplings. The series resistance R_{pos} is equal to R since resistive coupling between phases had been neglected in Figure 2.7. The series inductance L_{pos} accounts for self and mutual inductances in Figure 2.7.

For further illustration let us derive the charge equation (2.1) in PM approximation:

$$
\begin{aligned}
\bar{Q}_a &= \frac{1}{2}\left(C_g + 2C\right)\bar{V}_a - \frac{C}{2}\left(\bar{V}_b + \bar{V}_c\right) \\
&= \frac{1}{2}\left(C_g + 2C\right)\bar{V}_a - \frac{C}{2}\left(a^2\bar{V}_a + a\bar{V}_a\right) \\
&= \frac{1}{2}\left(C_g + 2C\right)\bar{V}_a + \frac{C}{2}\bar{V}_a \\
&= \frac{1}{2}\left(C_g + 3C\right)\bar{V}_a .
\end{aligned}
\tag{2.53}
$$

In the circuit of Figure 2.28, the charge-voltage relation is written as:

$$
\bar{Q}_a = \frac{1}{2}C_{pos}\bar{V}_a .
\tag{2.54}
$$

By comparing (2.53) with (2.54), the per-phase capacitance C_{pos} is found to be:

$$
C_{pos} = \frac{1}{2}\left(C_g + 3C\right) .
$$

A similar development for the inductances yields:

$$
L_{pos} = L_s - L_m .
$$

The equations of the PM model can be written in matrix form as:

$$
\begin{aligned}
\begin{bmatrix} \bar{I}_a \\ \bar{I}'_a \end{bmatrix} &= \mathbf{Y} \begin{bmatrix} \bar{V}_a \\ \bar{V}'_a \end{bmatrix} \\
&= \begin{bmatrix} \frac{1}{Z_{pos}} + jB_{pos} & -\frac{1}{Z_{pos}} \\ -\frac{1}{Z_{pos}} & \frac{1}{Z_{pos}} + jB_{pos} \end{bmatrix} \begin{bmatrix} \bar{V}_a \\ \bar{V}'_a \end{bmatrix} ,
\end{aligned}
\tag{2.55}
$$

where $\mathbf{Y}$ is the nodal admittance matrix [GS94] of the two-port of Figure 2.28 and

$$
\begin{aligned}
Z_{pos} &= R_{pos} + j\omega L_{pos} , \tag{2.56} \\
B_{pos} &= \omega C_{pos} . \tag{2.57}
\end{aligned}
$$

The PM model (2.55) depends on the fixed (or slowly varying) angular frequency ω through its parameters Z_{pos} and B_{pos} given by (2.56) and (2.57) respectively.

To summarize, the PM model (2.55) of a transmission line includes only 4 (real) linear AEs, to be compared to the 15 equations (9 linear ODEs and 6 linear AEs) of the corresponding EMT model.

2.4.5 Complexity of phasor model of the Nordic test system

For comparison purposes with the EMT model (see Table 2.1), the equation count of the PM model is presented in Table 2.2. The ratio of the equation count in the EMT model to the equation count in the PM model is $2287/609 \approx 3.76$. Moreover, since in EMT, the $50\,\mathrm{Hz}$ (or $60\,\mathrm{Hz}$) waveform is simulated, a maximum time step size of $h = 100\,\mu\mathrm{s}$ has to be used, while a $H = 20\,\mathrm{ms}$ is sufficient for the PM solution. The time step size ratio is $H/h = 200$. The overal speed-up ratio between PM and EMT models for Nordic test system can be roughly estimated as:

$$
\frac{eqs_{EMT}}{eqs_{PM}} \cdot \frac{H_{PM}}{h_{EMT}} \cong 770 .
$$

In reality, however, detailed EMT models are even more time-consuming due to the switching events, detailed control and protection schemes, etc., a fact which emphasizes even more the attractiveness of co-simulation.

2.4.6 Phasor-mode solver used

In this work we used the solver named RAMSES (for RApid Multiprocessor Simulation of Electric power Systems) developed at University of Liège. It is a positive-sequence PM solver. RAMSES solver is open to extensions needed for the co-simulation.

This solver implements a parallel algorithm for dynamic PM simulation of large-scale electric power systems based on the Schur complement domain decomposition method [AFV14]. A non-overlapping, topology-based, decomposition scheme is applied exploiting a star-shaped sub-domain

element	eqs per component				number of elts.	number of eqs.
	ODEs	AEs		Tot.		
	lin.	lin.	n.-lin.			
lines transfos shunts imp. loads buses } admittance matrix [7] Y		2N		2N	79	158
synchronous machines	6		4	10	23	230
AVR+exciters[8]	1 - 2	1 - 0		2	23	46
speed governors+turbines	4		2	6	12	72
constant torques		1		1	11	11
power system stabilizers	3	1		4	23	92

Total equations count: 609

Table 2.2: Count of PM equations for the test system.

layout. The decomposition is reflected to a separation of the DAEs describing the system. The non-linear DAE system describing each sub-domain is solved independently by discretization and using a Newton method with infrequent matrix update and factorization. The interface variables shared between sub-domains are updated using a Schur-complement-based method [GTD08, Saa03].

The above algorithm improves the simulation performance in two ways: first, the independent calculations of the sub-systems (such as formulation of DAE system, discretization, formulation of linear systems for Newton methods, solution of linear system, check of convergence, etc.) are parallelized, thus providing computational acceleration. Second, it exploits the locality of the decomposed sub-systems to avoid many unnecessary computations.

Further details about the solver implementation can be found in [AFV14] and related references.

2.5   Comparison of power system dynamic models

Table 2.3 is a tentative comparison between the main single-model and combined-model approaches of power system transient simulations including EMT phenomena of interest. Let us note that if the DP approaches need to be compared to PM-EMT co-simulation, they are not really concurrent approaches, since some DP techniques can be considered as innovative approaches to EMT simulation. DP may also be combined to PM through coupled PM-DP solutions. To our best knowledge, this combination has not been considered in the literature yet.Concerning computational speed, EMT is the slowest technique while the fastest ones are LFE-EMT, PM-EMT[9] and, of course,

---

[7]N is the number of buses

[8]One out of the two equations is an ODE. The second equation is an AE or an ODE depending on whether an integrator in the model is limited or not.

[9]the computing speed of LFE-EMT and PM-EMT solution may be moderate due to the small time step size requirement for the EMT sub-system solution, and depending on the size of the EMT sub-system.

	EMT	DP	LFE/EMT	PM/EMT	PM
computational speed	--	+	+/-	+/-	++
accuracy[10]	++	++	+	++	--
existing commercial tools	yes	no	no	no	yes

Table 2.3: Comparison of transient models of power systems. (A "+" indicates that the method of the corresponding column can be characterized by the attribute of the corresponding line. A "++" expresses the high correspondance between the attribute and the method. A "-" or a "−" express the opposite. The notation "+/-" indicates a mixed positive and negative correspondance to the attribute of the corresponding line.)

PM due to its simpler model. On the other hand, PM simulations are not accurate enough if precision is needed to reproduce EMT phenomena (for instance for some controllers sensitive to EMT phenomena [BH14]). The required accuracy in this case can be obtained from EMT, DP, and PM-EMT solutions. LFE-EMT simulations can give the required accuracy for what concerns the zone of interest. However, as previously said, LFE-EMT simulations gives sufficient precision in the low frequency range only, provided that the equivalent is updated frequently enough throughout the simulation. The line entitled "existing commercial tool" concerns the availability of widespread industrial tools, using the specified modeling approach.

---

[10]for phenomena containing non-negligible EMT information

Coupling phasor-mode and electromagnetic transients simulations

After introducing in Chapter 2 the EMT and PM models, we will discuss in this chapter the coupling between PM and EMT simulations. In Section 3.1 we will discuss the number of sub-systems to be envisaged when performing PM-EMT co-simulation. Section 3.2 will then introduce iterative schemes, including fixed-point algorithms, Jacobi and Gauss-Seidel (GS) variants, and finally Waveform Relaxation (WR). Boundary conditions will be discussed in Section 3.3, detailing boundary impedance matrix computation. Section 3.4 will introduce extrapolation techniques. Finally, Section 3.6 will present the proposed coupling method, whose convergence will be analyzed in Section 3.7.

3.1 How many coupled sub-systems?

Let us first examine the main configurations of coupled PM and EMT sub-systems. The configurations may be classified in four cases:
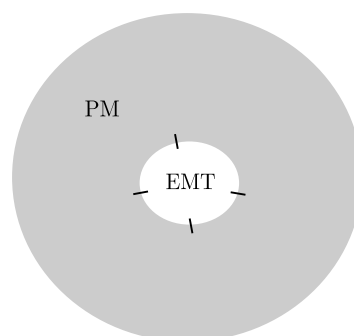
Figure 3.1: Case A: one EMT connected to one PM sub-system.
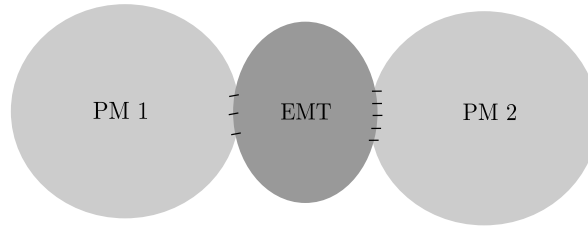
Figure 3.2: Case B: one EMT connected to several (two) PM sub-systems.

Case A: one EMT sub-system connected to one PM sub-system   The simplest configuration possible is shown in Figure 3.1. It may be characterized by several three-phase boundary buses between EMT and PM sub-systems, represented here by small lines crossing the boundaries. This is the configuration chosen in this thesis, as will be seen for example on the test-case of Figure 5.10.

Case B: one EMT sub-system connected to several PM sub-systems   The second configuration is shown in Figure 3.2. A practical example of application is shown in Figure 3.3, inspired from [PGV15]. In that example, a Multi-Terminal HVDC (MTDC) grid connects two asynchronous AC power systems. The MTDC with some neighbouring parts of the AC networks could be simulated with an EMT software, for accuracy reasons or for simulation of a single-phase fault on the AC side. The rest of the two AC asynchronous power systems could be simulated with a PM solver.

Some PM simulators give the ability to simulate in the same PM sub-system several asynchronous AC areas. It is the case for RAMSES, presented in Section 2.4.6 and used in this thesis. With such a PM solver, case B reduces to case A, since all the asynchronous PM sub-systems will be simulated in the same run (see Figure 3.3).

Case C: Several EMT sub-systems connected to one PM sub-system   This case may arise for example when some wind parks are connected to a large synchronous power system. We may want to simulate the wind parks in EMT and the remaining power system in PM. If it is possible to simulate all the EMT sub-systems in one EMT simulation run, case C reduces to case A.

Case D: Several EMT sub-systems connected to several PM sub-systems   Considering the ability to simulate in the same run all the PM sub-systems (see explanation in case B), this last case reduces from an algorithmic point of view to case C, and subsequently to case A (see explanation in case C).

3.2   Iterative schemes

The main iterations performed in PM-EMT co-simulation are represented in Figure 3.4. The PM sub-system simulated with a PM solver is considered as a process $\mathcal{S}_{PM}$ which, given the input vector $\mathbf{x}_1$ and its internal variables $\mathbf{y}_{PM}$, outputs the vector $\mathbf{x}_2$. Similarly, the process $\mathcal{S}_{EMT}$
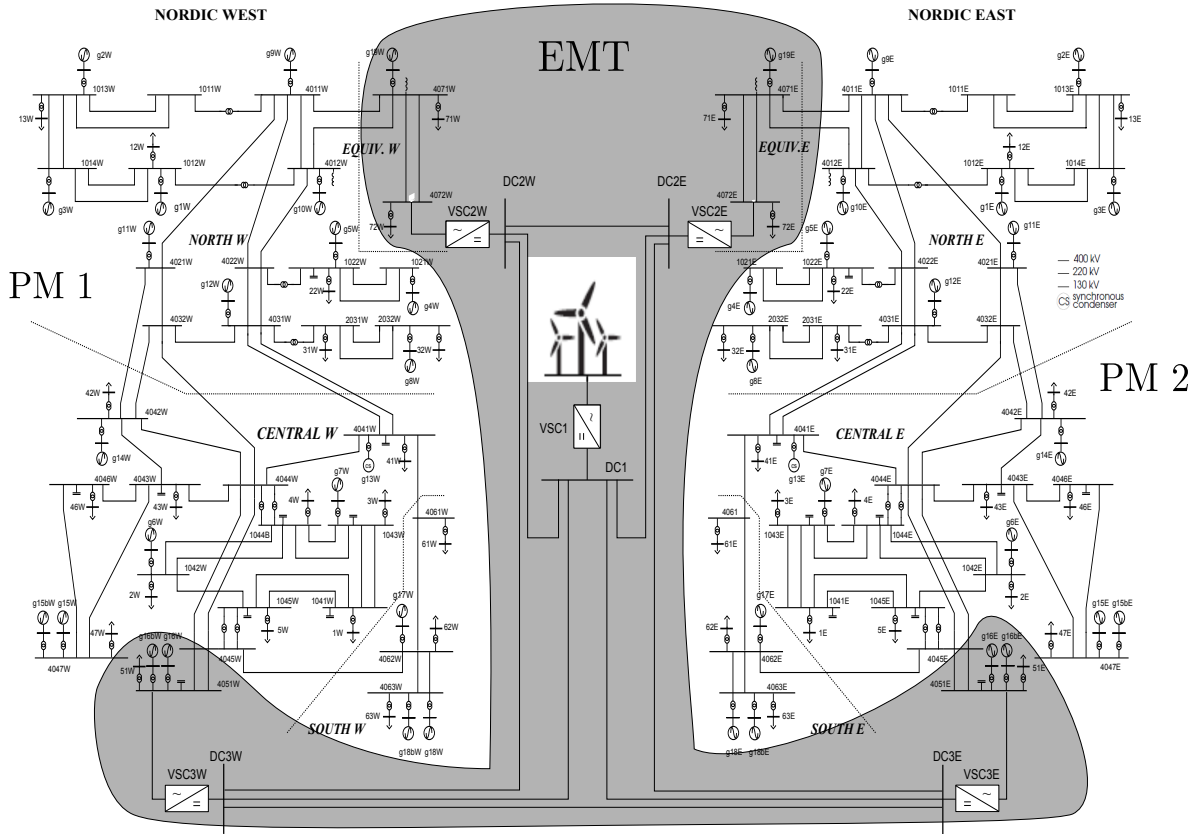
Figure 3.3: Example of application of case B, inspired from [PGV15].

represents the EMT simulation of the EMT sub-system. Given the input vector $\mathbf{x}_2$ and its internal variables $\mathbf{y}_{EMT}$, $\mathcal{S}_{EMT}$ produces the output vector $\mathbf{x}_1$. Vectors $\mathbf{x}_1$ and $\mathbf{x}_2$ may be combined in a single vector $\mathbf{x}$ as:

$$\mathbf{x} = \left[\begin{array}{c} \mathbf{x}_1 \\ \mathbf{x}_2 \end{array} \right] .$$

Throughout this manuscript, the $\mathbf{x}$ variables will interchangeably be called *interface* or *boundary variables*. The iterations between the $\mathcal{S}_{PM}$ and $\mathcal{S}_{EMT}$ processes will interchangeably be called *dynamic iterations* [BBGS13, MN87] or *co-simulation iterations* [THW09] or simply *iterations*. The time step size used in $\mathcal{S}_{PM}$, denoted H, will generally be higher than the one used in $\mathcal{S}_{EMT}$, denoted h .

At a given time step, the solution of the co-simulation process is attained when $\mathbf{x}$ reaches an equilibrium value, i.e. when $\mathbf{x}_2 = \mathcal{S}_{PM}\left(\mathcal{S}_{EMT}\left(\mathbf{x}_2\right)\right)$ or equivalently when $\mathbf{x}_1 = \mathcal{S}_{EMT}\left(\mathcal{S}_{PM}\left(\mathbf{x}_1\right)\right)$. In a numerical process, this equilibrium will be reached within some specified tolerance. It may be necessary to perform multiple dynamic iterations to reach the solution with a given tolerance. A major assumption made in this work is to accept those multiple dynamic iterations if needed for a given co-simulation time step. Now, in a second phase, the precision obtained when restricting the number of EMT sub-system simulations to one and only one will be evaluated.
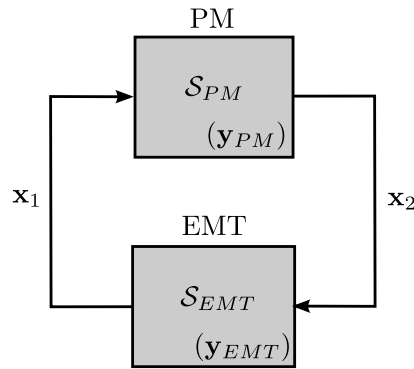
Figure 3.4: PM-EMT coupled processes.
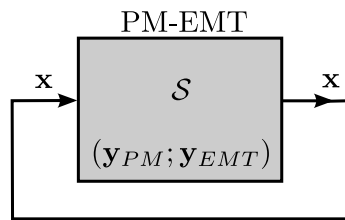
Figure 3.5: PM-EMT viewed as a fixed-point problem.

Variables $\mathbf{x}_1$ in $\mathbf{x}$ are input variables for process $\mathcal{S}_{PM}$ and output variables for process $\mathcal{S}_{EMT}$. Similarly, variables $\mathbf{x}_2$ in $\mathbf{x}$ are input variables for process $\mathcal{S}_{EMT}$ and output variables for process $\mathcal{S}_{PM}$. Both processes $\mathcal{S}_{PM}$ and $\mathcal{S}_{EMT}$ can be represented as a single process $\mathcal{S}$ with internal variables $\mathbf{y}_{PM}$ and $\mathbf{y}_{EMT}$, where the interface variables $\mathbf{x}$ have been externalized (see Figure 3.5). The rest of this section uses this simplified presentation with a single process $\mathcal{S}$.

3.2.1   Fixed-point algorithms and functional iterations

Principle   Let us consider the fixed-point iterations given by the following equation:

$$\mathbf{x}^{k+1} = \mathcal{S}\left(\mathbf{x}^k\right) , \tag{3.1}$$

for which our goal is to find the fixed-point $\mathbf{x}_*$ satisfying:

$$\mathbf{x}_* = \mathcal{S}\left(\mathbf{x}_*\right) .$$

$\mathcal{S}\left(\mathbf{.}\right)$ is sometimes called *mapping function*. Figure 3.6 shows how, for a one-dimensional mapping function $\mathcal{S}$, the convergence depends on the slope of $\mathcal{S}$ (or equivalently on the value of its derivative $\mathcal{S}' = \frac{d\mathcal{S}}{dx}$) on a certain interval close to the solution, where the iterates should stay. The starting value being x_0, the functional iteration gives $x_1 = \mathcal{S}\left(x_0\right)$ as second iterate. In Figure 3.6a, the slope of $\mathcal{S}$ with respect to x is positive and lower than 1. It is easily checked that the successive iterates get progressively closer to the fixed point x_*. The iterative process is converging. The case of a negative slope lower than one in absolute value is represented in Figure 3.6b. Again in this

(a) Positive slope.   (b) Negative slope.
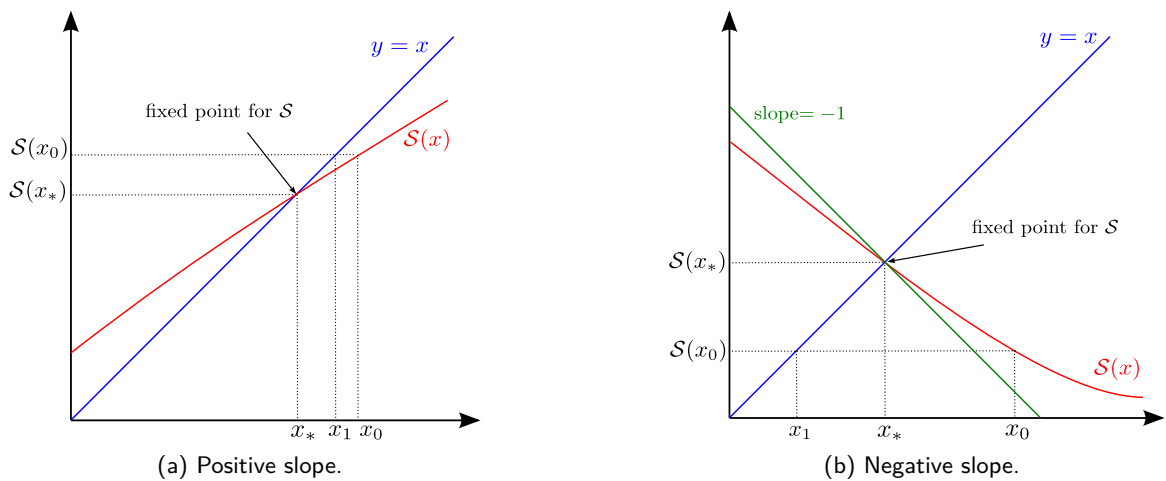
Figure 3.6: Converging functional iterations.
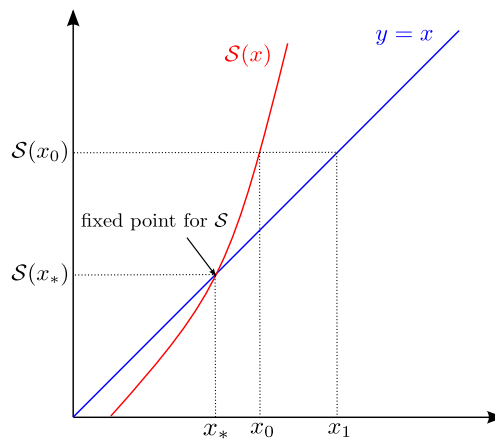
Figure 3.7: Diverging functional iterations.

case, the iterative process will converge towards the fixed-point solution. Figure 3.7 however shows a case where the iterative process diverges from the fixed-point x_*. We observe that the slope of $\mathcal{S}$ is higher than 1 in that case. This single-dimensional example intends to give an intuitive view of the contracting or not-contracting characteristic of the mapping function $\mathcal{S}$.

According to Banach's fixed point principle, the iterative process (3.1) will converge if the operator $\mathcal{S}$ is contracting; i.e. if it satisfies the condition:

$$\|\mathcal{S}(x) - \mathcal{S}(y)\| \leq q \|x - y\| \ , \tag{3.2}$$

where $0 < q < 1$. The smaller the contraction constant q, the faster the convergence of the iterative process (3.1). On the examples shown in Figure 3.6, we observe that the smallest the absolute value of the slope of $\mathcal{S}$, the fastest the convergence (or equivalently the slowest the divergence) of the iterative process.

Damping factor α It is generally necessary to introduce a relaxation or damping factor α into (3.1) to achieve convergence (see e.g. [IC96]). Equation (3.1) is then rewritten as follows:

$$\tilde{\mathbf{x}}^{k+1} = \alpha \mathbf{x}^{k+1} + (1 - \alpha) \mathbf{x}^k \ , \tag{3.3}$$

which means that, instead of taking a full step from $\mathbf{x}^k$ to $\mathbf{x}^{k+1}$ at the $(k+1)$th iteration, according to (3.1), we take a fraction α of this step, reaching $\tilde{\mathbf{x}}^{k+1}$ rather than $\mathbf{x}^{k+1}$. The case where $\alpha < 1$ is called *under-relaxation*; the case $\alpha > 1$ is called *over-relaxation*. The goal of this relaxation parameter is to create a mapping function $\tilde{\mathcal{S}}$, characterized by the same fixed point $\mathbf{x}_*$ while being more contractive than $\mathcal{S}$. Equation (3.3) is useful for stabilization and/or acceleration of the fixed point iterations. Parameter α is said to be optimal when it is adjusted to get the smallest possible contraction coefficient q in (3.2). Ideally, the damping should be consistently optimal, i.e. the damping coefficients should be optimal at every iteration.

A PM-EMT approach making use of adaptive damping factors was proposed in [KK00]. The latter approach assume the coupling to be diagonally dominant at the boundary buses, which is generally not the case. Due to this rectriction, this approach may not be general enough to be applied to any test-case.

3.2.2   Interface Jacobian: tangent or Newton's method

In Figure 3.5, the iterative process $\mathcal{S}$ expressed in (3.1) was solved by functional iterations. Let us rewrite the fixed-point equation (3.1) in the following form, dropping the iteration index k and putting all terms in the right hand side of the equality sign:

$$\begin{aligned} \mathbf{0} \ &= \ \mathbf{x} - \mathcal{S}\left(\mathbf{x}\right) \ , \\ &= \ \mathcal{I}\left(\mathbf{x}\right) \ , \end{aligned} \tag{3.4}$$

where we defined $\mathcal{I}\left(\textbf{.}\right)$ as the *interface constraint operator*:

$$\mathcal{I}\left(\mathbf{x}\right) \triangleq \mathbf{x} - \mathcal{S}\left(\mathbf{x}\right) \ .$$

The derivative of the interface constraint with respect to the interface variables is:

$$\frac{d\mathcal{I}}{d\mathbf{x}} = \mathbf{I} - \frac{d\mathcal{S}}{d\mathbf{x}} \ ,$$

where $\dfrac{d\mathcal{S}}{d\mathbf{x}}$ is the *interface Jacobian matrix*, i.e. the matrix of partial derivatives of $\mathcal{S}$ with respect to each component of the interface vector $\mathbf{x}$. Applying Newton's method [AP98] to solve the interface constraint (3.4) we solve

$$\left(\frac{d\mathcal{I}}{d\mathbf{x}}\right) \boldsymbol{\Delta} \ = - \ \mathcal{I}\left(\mathbf{x}^k\right) \ , \tag{3.5}$$

where the Jacobian matrix $\dfrac{d\mathcal{I}}{d\mathbf{x}}$ is evaluated at $\mathbf{x}^k$ and where $\boldsymbol{\Delta}$ is used to update the boundary variables:

$$\boldsymbol{\Delta} = \mathbf{x}^{k-1} - \mathbf{x}^k \ .$$

Equivalently to (3.5), we write:

$$\left(\mathbf{I} - \frac{d\mathcal{S}}{d\mathbf{x}} \right) \mathbf{\Delta} = - \left(\mathbf{x}^k - \mathcal{S}\left(\mathbf{x}^k \right) \right) \ .$$

The next Newton iterate is obtained by

$$\mathbf{x}^{k+1} = \mathbf{x}^k + \mathbf{\Delta} \ .$$

The advantage of this method is the fast convergence obtained by Newton's method. The drawback of the latter method is the need to evaluate the Jacobian matrix $\dfrac{d\mathcal{S}}{d\mathbf{x}}$ at $\mathbf{x}^k$. If the size of the interface vector $\mathbf{x}$ is m and if the Jacobian cannot be derived analytically, the evaluation of the Jacobian matrix requires evaluating

$$\mathcal{S}\left(\mathbf{x}^k + \begin{bmatrix} 0 \\ \vdots \\ \epsilon \\ \vdots \\ 0 \end{bmatrix} \right) = \mathcal{S}\left(\mathbf{x}^k + \epsilon \mathbf{e}_i \right) \ ,$$

where ϵ is small compared to the ith component of vector $\mathbf{x}^k$ and $\mathbf{e}_i$ is a vector containing zeros at all places and a one at position i. We perturb by ϵ_i the i-th component only $(i = 1, \ldots, m)$ of vector $\mathbf{x}^k$. The i-th column of the Jacobian matrix $\dfrac{d\mathcal{S}}{d\mathbf{x}}$ is then given by

$$\frac{\mathcal{S}\left(\mathbf{x}^k + \epsilon_i \mathbf{e}_i \right) - \mathcal{S}\left(\mathbf{x}_i^k \right)}{\epsilon_i} \ .$$

Let us note that we described here Newton's method to accelerate fixed-point iterations when considering one system $\mathcal{S}$ only. It is possible to apply Newton to more than one systems, e.g. the $\mathcal{S}_1$ and $\mathcal{S}_2$ sub-systems in Figure 3.9, as proposed in [SBE+14]. Again the drawback of the method is the additional computational cost required for the interface Jacobian computation. Other methods were proposed, elaborating on the original paper of Chan [Cha84], out of which we point out the review paper [YLD09]. All these methods give a dramatically improved convergence compared to block Gauss-Seidel methods, but to the cost of extra sub-systems' evaluations.

3.2.3   Jacobi and Gauss-Seidel schemes

In this work, we are interested to PM-EMT co-simulation schemes where the PM sub-system and the EMT sub-system may be evaluated several times per time step. The Jacobi and the Gauss-Seidel schemes are classical schemes to iteratively solve partitioned problems. In what follows, the main time step size used by the PM solver will be denoted by H while the main time step size for the EMT solver will be written h.
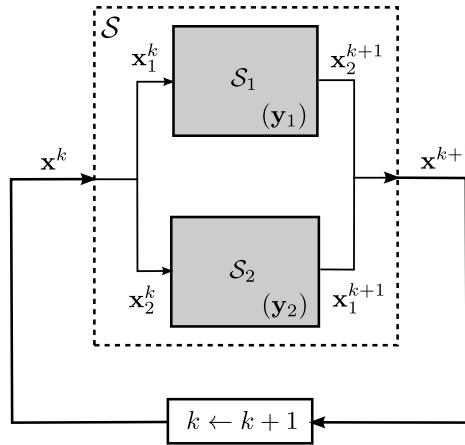
Figure 3.8: Coupled sub-systems, solved in parallel.

3.2.3.1   Jacobi variant

Two coupled systems, represented by their mapping functions $\mathcal{S}_1$ and $\mathcal{S}_2$ can be solved in parallel, as sketched in Figure 3.8. Each sub-system has internal variables, $\mathbf{y}_1$ and $\mathbf{y}_2$ respectively, in addition to common boundary[1] variables $\mathbf{x}$. In this scheme, the boundary vector $\mathbf{x}^k$ is splitted into $\mathbf{x}_1^k$ and $\mathbf{x}_2^k$. The vector $\mathbf{x}_1^k$ is input to sub-system $\mathcal{S}_1$ which outputs $\mathbf{x}_2^{k+1}$. Similarly, the complementary vector $\mathbf{x}_2^k$ is input to the coupled sub-system $\mathcal{S}_2$ which outputs $\mathbf{x}_1^{k+1}$:

$$
\begin{aligned}
\mathbf{x}_2^{k+1} &= \mathcal{S}_1\left(\mathbf{x}_1^k\right), \\
\mathbf{x}_1^{k+1} &= \mathcal{S}_2\left(\mathbf{x}_2^k\right).
\end{aligned}
$$

In this scheme, called Jacobi[2], each sub-system is solved with an input from iteration k. The advantage of this scheme is that systems $\mathcal{S}_1$ and $\mathcal{S}_2$ can be solved in parallel, which may be beneficial if they are of similar sizes. As shown by the dashed rectangle in Figure 3.8, the Jacobi iterative scheme can be viewed as a fixed-point iterative scheme with a mapping function $\mathcal{S}$ such as the one of (3.1).

3.2.3.2   Gauss-Seidel variant

Principle   Rather than solving $\mathcal{S}_1$ and $\mathcal{S}_2$ in parallel, we may solve them in sequence, as sketched in Figure 3.9. This is called a Gauss-Seidel (GS) scheme[3]. After performing one full GS step, the interface vector is updated from $\mathbf{x}^k$ to $\mathbf{x}^{k+1}$:

$$
\mathbf{x}^{k+1} = \mathcal{S}_2\left(\mathbf{x}^{k+\frac{1}{2}}\right) = \mathcal{S}_2\left(\mathcal{S}_1\left(\mathbf{x}^k\right)\right), \tag{3.6}
$$

---

[1]Some authors (e.g. [SBE+14, EOBE14]) classify the boundary variables as input or output ones. Input variables exist when a control device imposes a certain value to one of the sub-systems. In this thesis, variables are not considered to be inputs or outputs, but boundary variables only. Indeed the control sub-systems are not isolated in the splitting considered.

[2]to refer to the German mathematician Carl Gustav Jacob Jacobi, 1804-1851. One of his most important contribution is the so-called Jacobian matrix.

[3]from Carl Friedrich Gauss, 1777-1855, and Philipp Ludwig von Seidel, 1821-1896, German mathematicians.
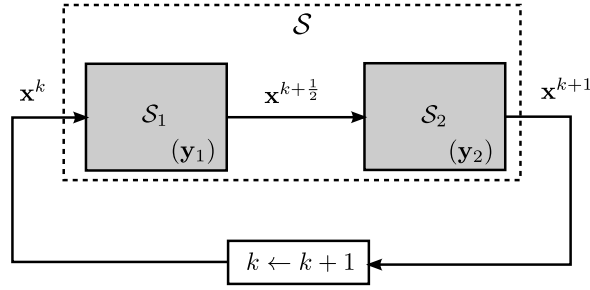
Figure 3.9: Coupled sub-systems, solved sequentially.

where the $k + \frac{1}{2}$ index indicates that half of the Gauss-Seidel iteration has been performed, as shown in Figure 3.9. By comparison to the scheme presented in Figure 3.8, sub-system $\mathcal{S}_2$ is solved here with updated input values. The convergence of this scheme is expected to be better than the Jacobi one. The series combination of the two sub-systems $\mathcal{S}_1$ and $\mathcal{S}_2$ gives mapping function $\mathcal{S}$ and (3.6) reduces to the fixed point equation (3.1).

Sequence of computation   The sequence of computation of the sub-systems may influence the rate of convergence. Furthermore, [BBGS13] showed that in some cases, the order in which the sub-systems are treated can be crucial for convergence or divergence. While the following sequences:

$$\mathbf{x}^{k+1} \; = \; \mathcal{S}_2\left(\mathcal{S}_1\left(\mathbf{x}^k\right)\right) , \tag{3.7}$$

$$\mathbf{x}^{k+1} \; = \; \mathcal{S}_1\left(\mathcal{S}_2\left(\mathbf{x}^k\right)\right) , \tag{3.8}$$

share the same fixed point solution $\mathbf{x}_*$ given by:

$$\mathbf{x}_* = \mathcal{S}_2\left(\mathcal{S}_1\left(\mathbf{x}_*\right)\right) = \mathcal{S}_1\left(\mathcal{S}_2\left(\mathbf{x}_*\right)\right) ,$$

the numerical process of fixed point iterations may not converge as fast in (3.8) as in (3.7). The choice of the sequence of computations may even lead to divergence in one case and convergence in the other [AG01, MNS06, JDP09, BBGS13].

In this thesis, for practical purpose, since the PM solver used is much faster than the EMT one, it was chosen to solve the PM sub-system first for every time step. The EMT sub-system is solved next. The sub-systems are solved successively until a convergence criterion is met. Since in practice, the convergence showed to be very good, another sequence of computation has not been investigated.

In cases where PM-EMT co-simulation is to be used for Hardware-In-the-Loop (HIL) testing, the number of evaluations of the EMT sub-system will be limited to one, since in that case the EMT sub-system is no longer represented by a piece of code, but by some hardware. There exists three "protocols" for the computation sequence of the sub-systems, represented in Figure 3.10.

In Figure 3.10a, information from the last accepted time step H is first passed to the EMT solver (step 1), the EMT sub-system is then solved (step 2) and gives updated information to the PM solver (step 3). The PM sub-system is finally solved (step 4) before proceeding to the next time step (steps 5 and following). Figure 3.10b shows a similar procedure, but the order of execution of the solvers is interchanged. Protocols (a) and (b) are described for instance in references [vdMGvdM$^+$14, JMDS$^+$09]. The third procedure (c) is without a doubt the most interesting, since it allows a second evaluation of the PM sub-system and brings the accuracy to a maximum for such a non-iterative procedure [PAGV15]. In protocol (c), after solving the PM sub-system a first time, the EMT sub-system is solved and then, the PM sub-system is solved again before proceeding to the next time step.

3.2.4   Waveform relaxation

The waveform relaxation[4] method was proposed for time-domain simulations in 1982 in the context of integrated-circuits simulation [LRSV82]. Waveform relaxation methods are iterative methods to solve time dependent problems. They start with an initial guess of the solution over the entire time interval of interest, and produce iteratively better and better approximation of the solution over the entire time interval at once. A schematic representation of a Gauss-Seidel waveform relaxation process over two non-overlapping sub-systems A and B of the system under study is given in Figure 3.11a. At iteration $k+\frac{1}{2}$, sub-system A is solved over the time-window $[t_0, t_0 + T]$. The updated time evolution of its boundary vector is given by $\mathbf{x}^{k+\frac{1}{2}}(t)$, where the index $k + \frac{1}{2}$ indicates that half of the iteration was performed (in the Gauss-Seidel sense). Taking into account the updated boundary vector evolution, sub-system B can now be solved. It produces the updated values of the boundary variables over the considered time-window: $\mathbf{x}^{k+1}(t)$, $t \in [t_0, t_0 + T]$.

The convergence of WR methods for Initial Value Problems was studied in [MN87]. The study of WR convergence for DAEs was initiated in [Mie89] and extended in [AG01] with the use of a preconditioner. The idea described in [AG01] consists in applying relaxation to the system of non-linear DAEs describing the circuit under study. The system is splitted into decoupled sub-systems of DAEs corresponding to the decoupled dynamical subcircuits. For convergence of the waveform relaxation process to be possible, each sub-system $\mathcal{S}_1$ and $\mathcal{S}_2$ must be solved with an accuracy at least equal to the accuracy required by the dynamic iterations of (3.1) (see Figure 3.12a):

$$tol_A \;\; \leq \;\; tol_{dyn\,iter}\,,$$
$$tol_B \;\; \leq \;\; tol_{dyn\,iter}\,.$$

In general, if the equations are normalized, we may set:

$$tol_A = tol_B\,.$$

Waveform relaxation was proposed for power system PM simulation [CI90] but it has not been

---

[4]Let us remark that we are talking here about iterative methods of relaxation, which should not be confused with the concept of relaxation in mathematical optimization, which approximate a difficult problem by a simpler one whose solution provides information about the solution of the original problem.
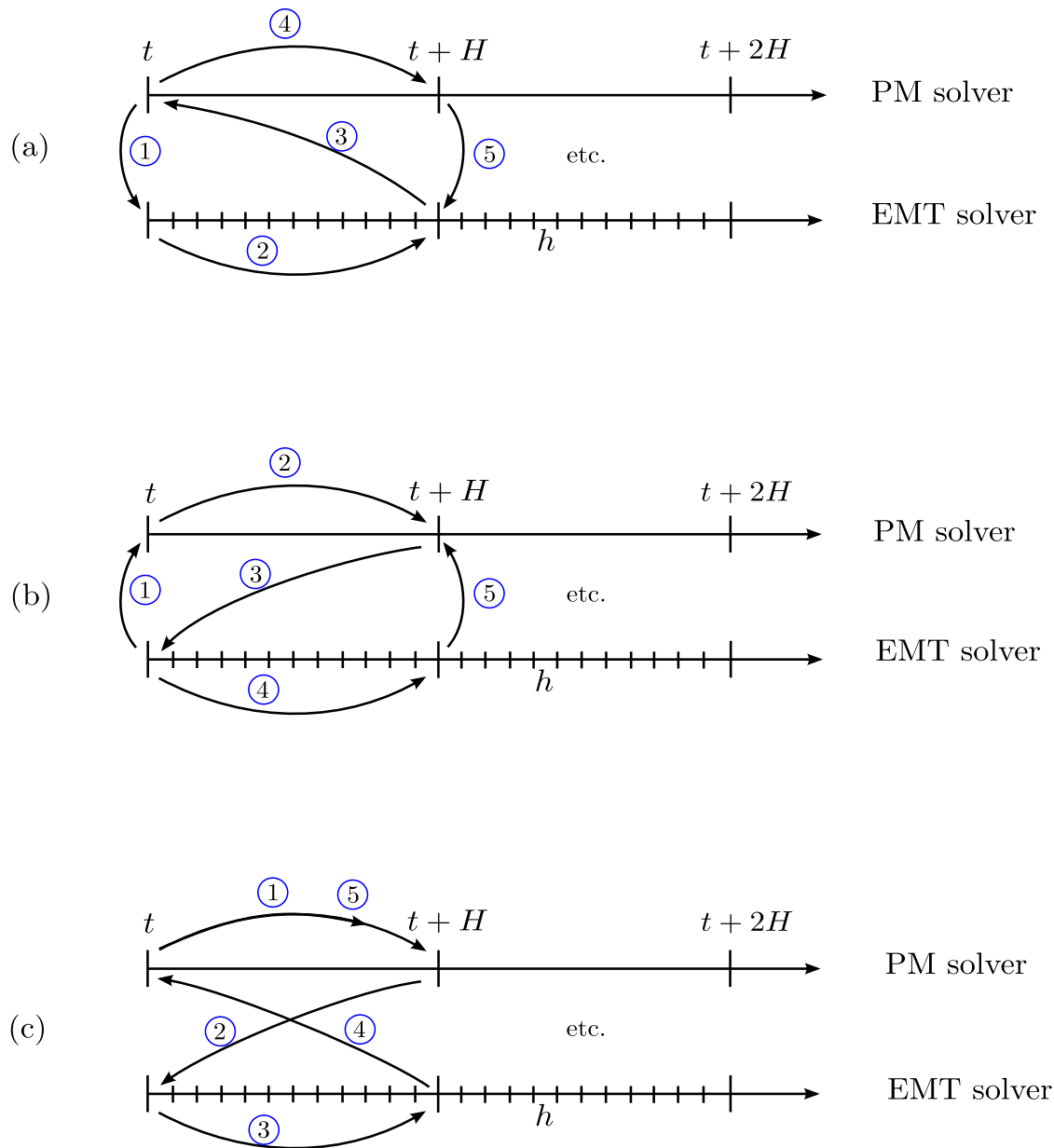
Figure 3.10: Three protocols of computation involving a single evaluation of the EMT sub-system. (a) EMT sub-system is computed first (b) PM sub-system is computed first and only once (c) PM sub-system is computed first, but is solved once more after having solved the EMT sub-system.
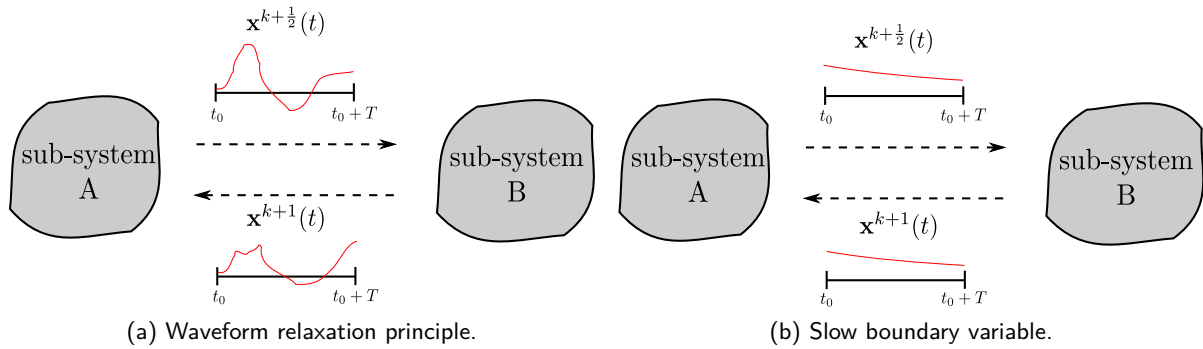
(a) Waveform relaxation principle.   (b) Slow boundary variable.

Figure 3.11: Subdivision into sub-systems A and B.

(a) Required accuracy.   (b) Multirate process.
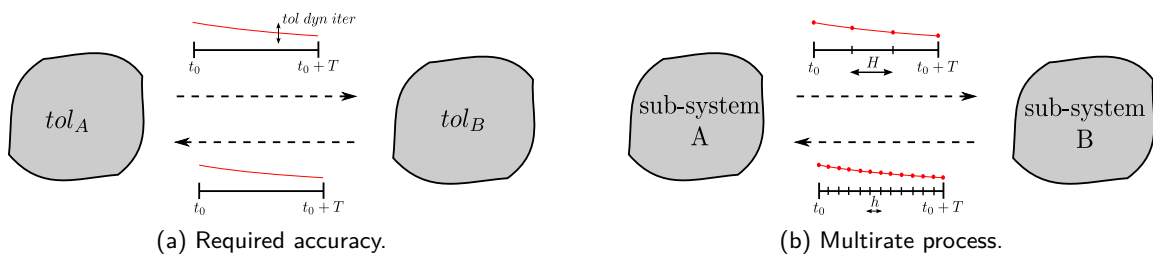
Figure 3.12: Accuracy and multirate characteristics of WR.

much used, due to probably weak convergence properties. Reference [JMD09] also proposed a possible use of waveform relaxation in the context of power system simulations for real-time studies. Waveform relaxation may in some cases be also a multirate process, as illustrated by Figure 3.12b. A *multirate ratio* can be defined as the ratio between the main time step size used in solver A and the main time step size used in solver B, i.e $multirate\ ratio = \dfrac{H}{h}$. The latter ratio characterizes the gain obtained in using a multirate technique to solve a given problem.

The case of PM-EMT co-simulation, which is the focus of this research, is a particular case of WR due to the multiple time steps h performed in the EMT simulation, while a simple time step H is performed on PM solver side, as shown in Figure 3.13. This is beneficial for the convergence. Indeed, in WR methods, it has been shown that for ODEs, the smaller the length T of the time window, the faster the convergence [MN96], and the convergence rate of dynamic iteration is not affected whether we deal with a DAE system or an equivalent ODE system[5] [Mie89].

3.3 Boundary conditions

3.3.1 Which model for the other sub-system?

The communication of the updated boundary vector provides a degree of freedom on the way the sub-systems are modeled. This degree of freedom is often called *Boundary Conditions* (BC)

---

[5]The technique to reduce a DAE system into an ODE system is described in [GP84].
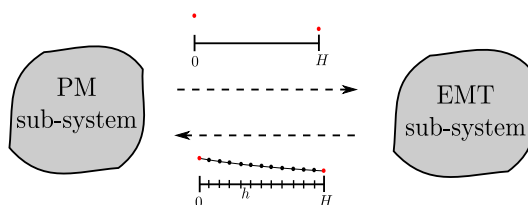
Figure 3.13: PM-EMT co-simulation as a particular case of WR.
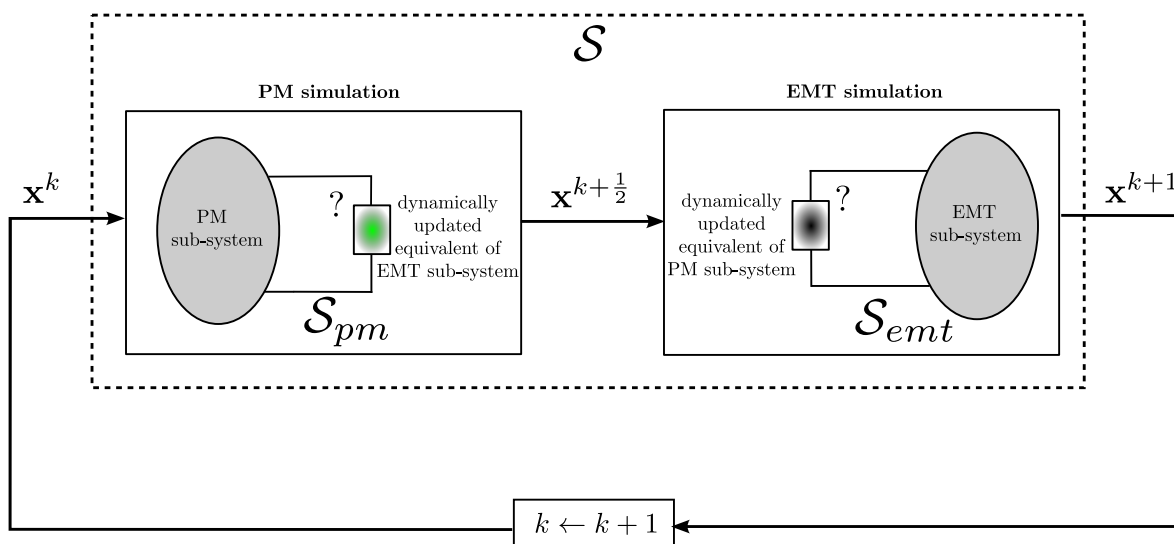
Figure 3.14: Model of one sub-system when dealing with the other.

[SBG04]. Figure 3.14 represents the two degrees of freedom coming from the necessity to use some model for each sub-system when communicating its updated information to the other. The choice and the computation of a dynamically updated equivalent can be viewed as preconditioning the problem. The better the quality of the equivalents, the larger the time step H can be chosen without meeting convergence problems [SDGB10].

Figure 3.15 shows a graphical representation of different kinds of boundary conditions in the simplified case of a single boundary bus and DC networks (involving real voltages and currents). In this figure, $\left(V^k, I^k\right)$ are the boundary voltage and current respectively, at iteration k of the present time step computation. Four possible models of a given sub-system are shown:

- a current source J^k, equal to the last computed iterate of the boundary current I^k,

- a voltage source E^k, equal to the last computed iterate of the boundary voltage V^k,

- an impedance Z^k, equal to the ratio $\dfrac{V^k}{I^k}$,

- a Thévenin (or a Norton) equivalent, for which the Thévenin impedance $\hat{Z}_{th}$ must be pre-computed, in order to dynamically update the Thévenin voltage source (or equivalently the
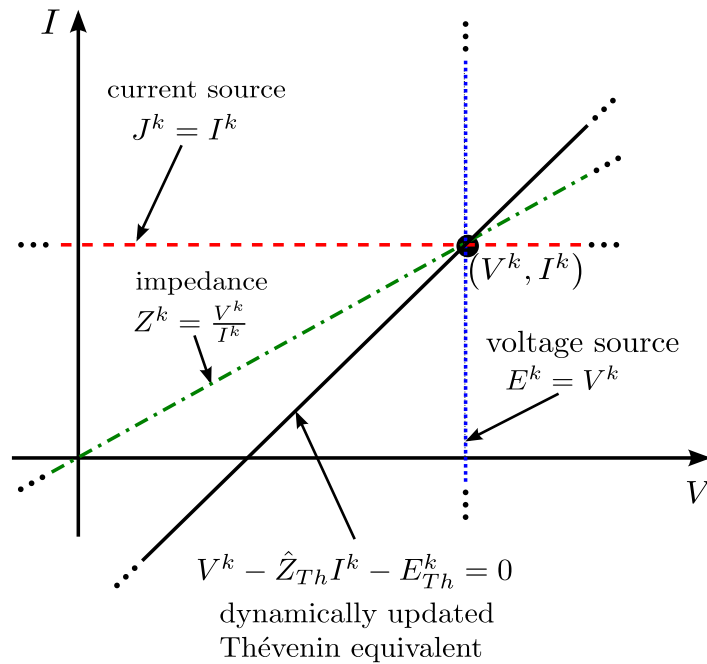
Figure 3.15: Four types of boundary conditions.

Norton current source)[6].

Table 3.1 summarizes how to compute the equivalent model involved in the various kinds of boundary conditions.

Figure 3.15 clearly shows that voltage or current source boundary conditions contain less information, since they take into account only a part of the boundary information. Only the boundary currents or the boundary voltages are considered. Their advantage is that they are very simple to evaluate and to implement. In the waveform relaxation literature, this kind of boundary conditions are referred to either *zero-order boundary conditions* [PGV14, LL11, LCL09] because, at the boundary between both sub-systems, the current (resp. voltage) source is constant when performing the PM (resp. the EMT) simulation. It does not depend on the voltage (resp. current) being computed by the PM (resp. EMT) simulation, and will be updated only at the next iteration of the relaxation process. This kind of boundary conditions are also referred to constant boundary conditions [AK02] or source coupling [BBS13].

Impedance boundary conditions are easy to compute and implement in a single interface bus case. However, their use in the presence of n interface buses is difficult. Indeed, let us assume that the

---

[6]The dynamic update of the Thévenin and Norton equivalents will be discussed in Section 3.6 (see Figure 3.23).
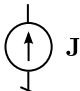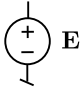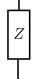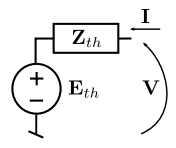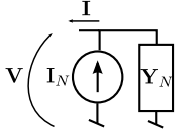
Chosen model	Needed parameter	How to compute BCs for boundary vectors $\mathbf{V}$ and $\mathbf{I}$
$\mathbf{J}$	-	$\mathbf{J} = \mathbf{I}$
$\mathbf{E}$	-	$\mathbf{E} = \mathbf{V}$
z	-	$Z_i = \frac{V_i}{I_i} \quad i = 1, \dots, n$
$\mathbf{Z}_{th}$, $\mathbf{E}_{th}$, $\mathbf{I}$, $\mathbf{V}$	$\mathbf{Z}_{th}$	$\mathbf{E}_{th} = \mathbf{V} - \mathbf{Z}_{th}\mathbf{I}$
$\mathbf{I}$, $\mathbf{V}$, $\mathbf{I}_N$, $\mathbf{Y}_N$	$\mathbf{Y}_N$	$\mathbf{I}_N = \mathbf{I} + \mathbf{Y}_N\mathbf{V}$

Table 3.1: Zero-order and first-order boundary conditions.

impedance at each bus is computed as follows:

$$
\begin{aligned}
Z_1 &= \frac{V_1}{I_1}, \\
&\vdots \\
Z_i &= \frac{V_i}{I_i}, \\
&\vdots \\
Z_n &= \frac{V_n}{I_n},
\end{aligned}
$$

where $i = 1, \dots, n$ refers to the interface bus of concern. While very simple, these boundary conditions do not take into account the coupling between the various boundary buses. This will generally lead to a degraded convergence.

Finally Thévenin (or equivalently Norton) boundary conditions are easy to compute. However, they require the reduced impedance matrix to be determined beforehand for all the topologies appearing during the simution. This operation is presented in Section 3.3.3. These conditions are more sophisticated than the zero-order ones since they attempt to match the voltages and the currents at the interface between the PM and EMT sub-systems already during the iteration [AK02]. In

other words, instead of exchanging updated values of voltages or currents at the interface, updated relations (e.g. first-order) between boundary voltages and currents are exchanged.

Figure 3.16 summarizes the combinations of representations documented in the literature of PM-EMT hybrid simulations while Table 3.2 summarizes the type of boundary conditions used and the related publications (including our contributions). Some references were not included when we were not sure about the boundary conditions used.

In [PGV13, HCSC14], it was chosen to use an ideal current source to represent the EMT sub-system in the PM simulation, and an ideal voltage source to represent the PM sub-system in the EMT simulation, as shown in Figure 3.16a. While this configuration offers the advantage of simplicity, it requires to have, at the boundary, three-phase voltages and currents with negligible imbalance and distortion since this is the usual assumption taken in PM simulation. In turn, this requires to place the boundary far enough from the location of the disturbance, i.e. to have a large enough EMT sub-system. With the increasing computational power available nowadays, it should generally not be a problem to increase the size of the EMT sub-system until fundamental-frequency positive-sequence currents are observed at the boundary with the PM sub-system.

The approach shown in Figure 3.16b. still relies on a current source to represent the EMT sub-system, but uses a Frequency Dependent Network Equivalent (FDNE) which consists of an admittance in parallel with an ideal current source to represent the PM sub-system. This more accurate representation, valid over a wide frequency range, allows putting the boundary closer to the disturbance location without degrading accuracy.

The third approach, represented in Figure 3.16c, was used to include an EMT-model of a Static Var Compensator (SVC) in PM simulation. This is probably the reason why the authors of the related papers [CS[+]02, FLCW06, ZDKS09] represented by an dynamically updated impedance the EMT-modeled device in the PM solver.

The fourth representation, considered in [And95, TYZZ05, PAGV14, XyHTPH14, vdMGvdM[+]14, PAGV15], resorts to Norton or Thévenin equivalents for both sides, as shown in Figure 3.16d. Note that choosing between a Norton or a Thévenin representation is free; the shown combination is convenient for incorporation in the usual PM and EMT models. Ideally, the Thévenin matrix $\mathbf{Z}_{th}$ and the Norton matrix $\mathbf{Y}_n$ should be full matrices, to take into account the coupling between different boundary buses. It is also possible to use diagonal matrices, but the convergence (or equivalently the accuracy) is degraded.

3.3.2   Overlapping sub-systems

The splitting of a power system into two sub-systems can be made with adjacent or overlapping systems. An example of overlapping sub-systems in PM-EMT simulations is shown on Figure 3.17.

---

[7]EMT modeled in PM by updated constant P and Q injections are considered here too.

[8]These references concerned a SVC, which helps understanding why the authors decided to use an impedance model to represent the SVC in the PM solver.
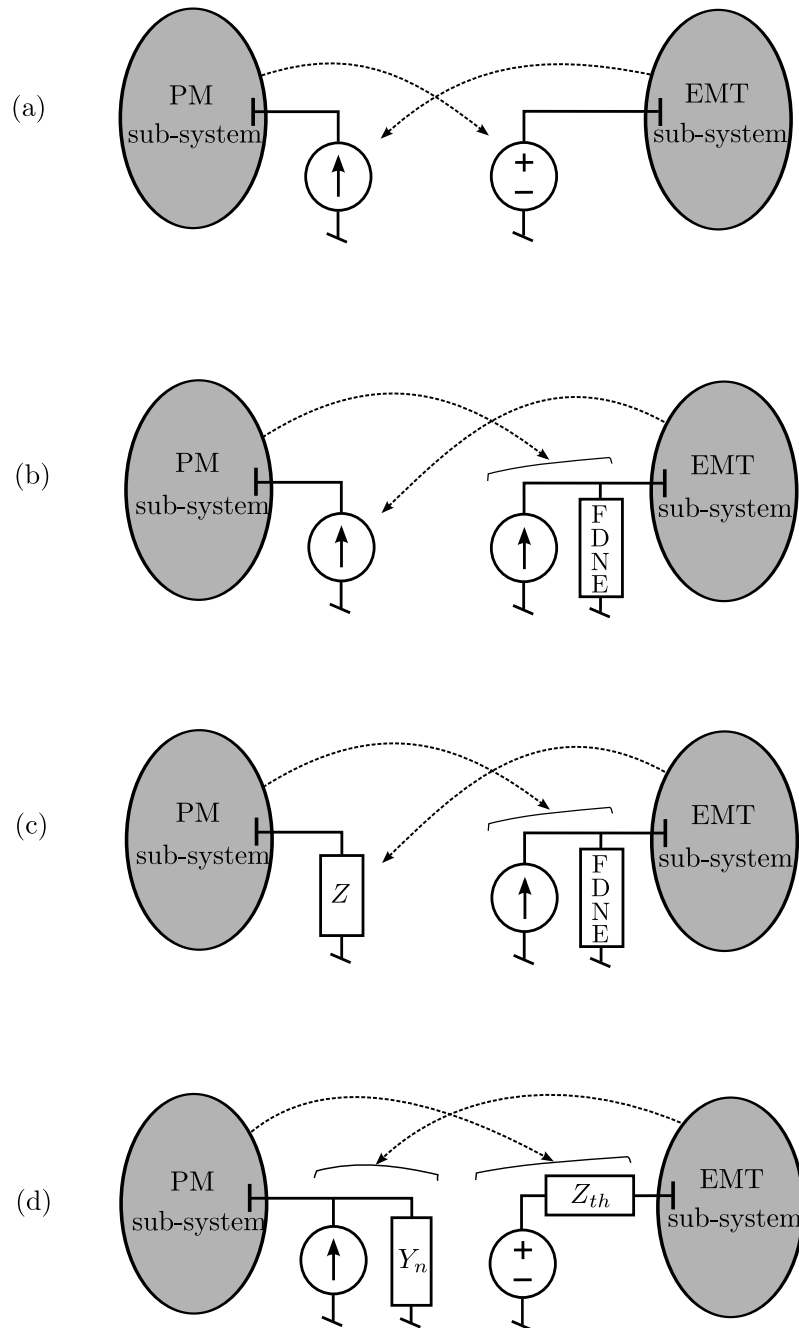
Figure 3.16: Proposed boundary conditions in PM-EMT literature.

Dynamically updated equivalent of PM in EMT	of EMT in PM	References
		-
		[PGV13, HCSC14]
		-
		-
		[SRA98, SSCZ03, SCS05, HKLS05, LGY09, zLxHT+11, vHGK11, AF12, AF13, ZGW+13, AF14, Lou14, ZFA14, HV15][7]
		[CS+02, FLCW06, ZDKS09][8]
		[ZFLZ14]
		-
		[And95, TYZZ05, PAGV14, XyHTPH14, vdMGvdM+14, PAGV15]

Table 3.2: Boundary conditions used in PM-EMT literature.
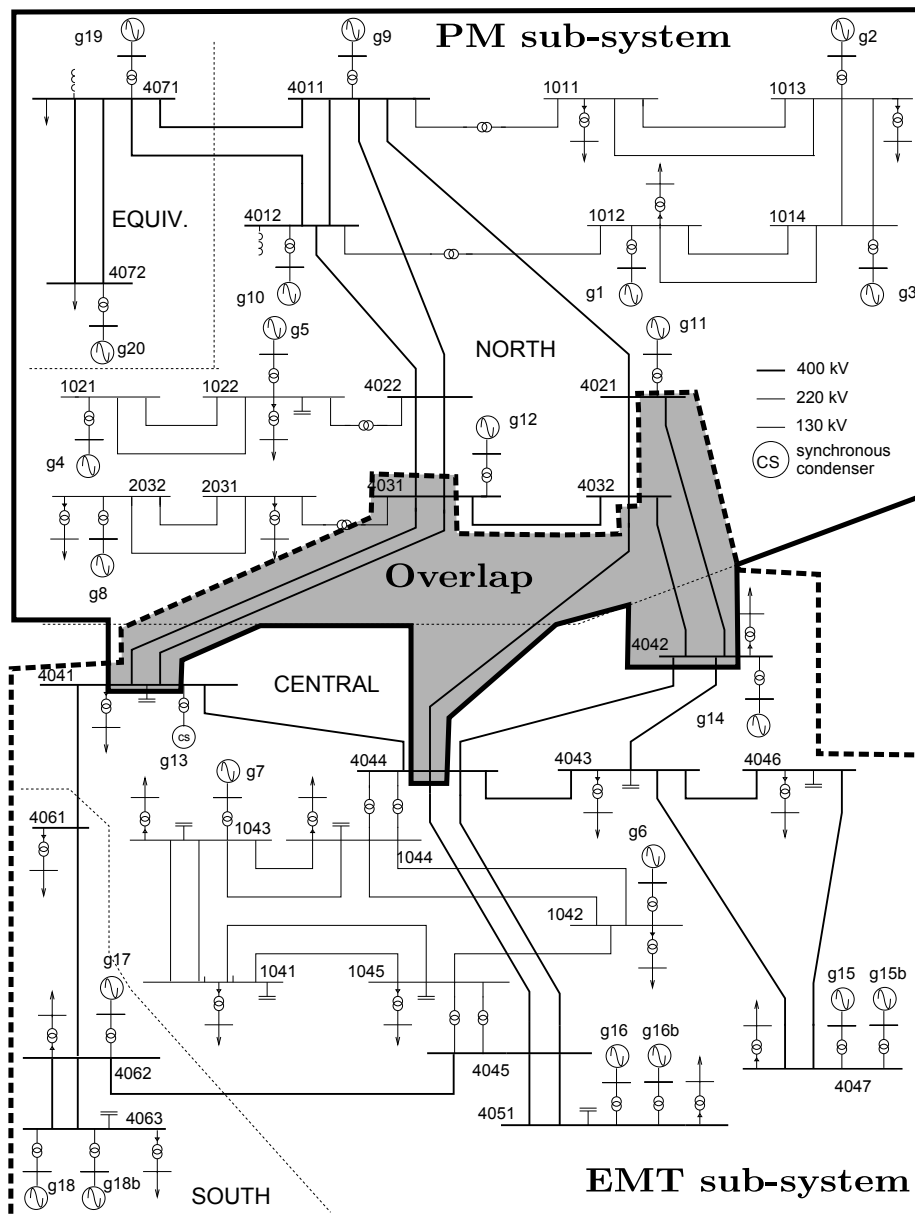
Figure 3.17: Overlapping sub-systems.

Figures 3.18a and 3.18b show a possible implementation of overlapping PM-EMT simulation, with zero-order boundary conditions. A better implementation would require to use coupled Thévenin equivalent instead of voltage sources. A reference introducing overlapping PM-EMT simulation can be found in [IFHI03]. Overlapping PM and EMT sub-systems were not tested in this work. However, the non-overlapping PM-EMT simulations yielded so good results in terms of convergence speed (and solution) that overlapping PM-EMT simulations may be of reduced interest. However, overlapping PM-EMT simulations could be studied as a textbook case and compared to non-overlapping simulations.

(a) EMT simulation.   (b) PM simulation.
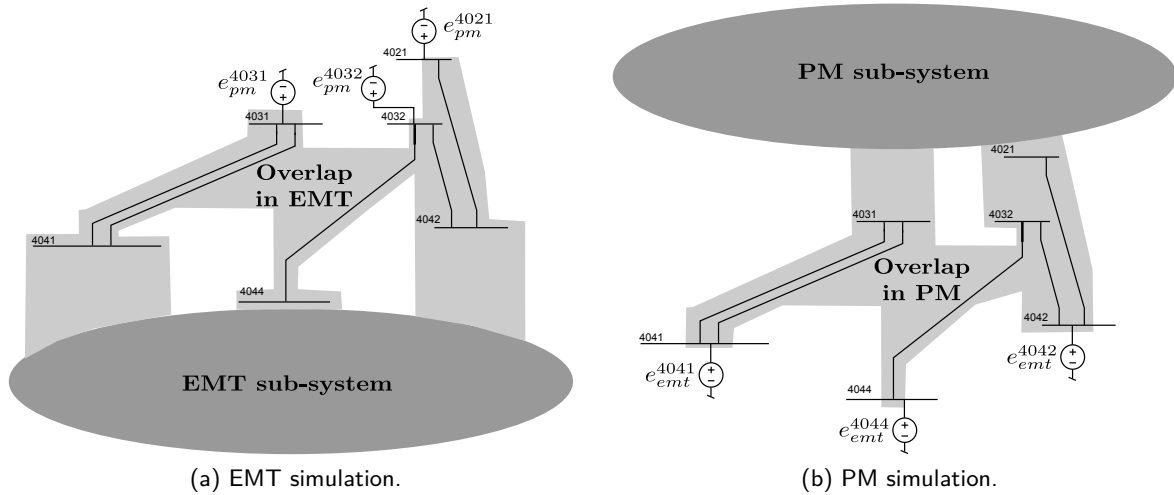
Figure 3.18: Overlapping PM-EMT co-simulation.

3.3.3   Boundary impedance matrix computation

First-order boundary conditions require to have an estimate of the boundary impedance matrix $\mathbf{Z}_{bb}$ (or equivalently, the boundary admittance matrix $\mathbf{Y}_{bb}$) seen from the n boundary buses of the PM and EMT sub-systems (see Figure 3.19). The matrix will vary depending on the topology of the replaced sub-system. Considering for instance a fault that takes place in the sub-system, there will be three configurations:

- before-fault,

- on-fault,

- post-fault.

For a given topology, to derive the boundary admittance matrix $\mathbf{Y}_{bb}$, we start from the *nodal admittance matrix* (or simply, admittance matrix) $\mathbf{Y}$ of the sub-system. The concept of nodal admittance matrix was introduced in Section 2.4.4 dedicated to the derivation of the PM model of an overhead line. The admittance matrix, given by (2.55), relates node voltages to currents injected into the same nodes. For a general N-bus network, the voltage-current relation is:

$$\mathbf{I} = \mathbf{Y}\mathbf{V}\,,$$

where $\mathbf{V}$ and $\mathbf{I}$ are vectors containing bus voltages and injected currents respectively.

The computation of matrix $\mathbf{Y}$ for a given network is summarized in Appendix C, detailing the contribution of every network component. In this work, for simplicity and without lack of generality, all loads have been considered to be constant admittances. The sub-synchronous reactance of the synchronous machines has been considered in their contribution to the nodal admittance matrix.
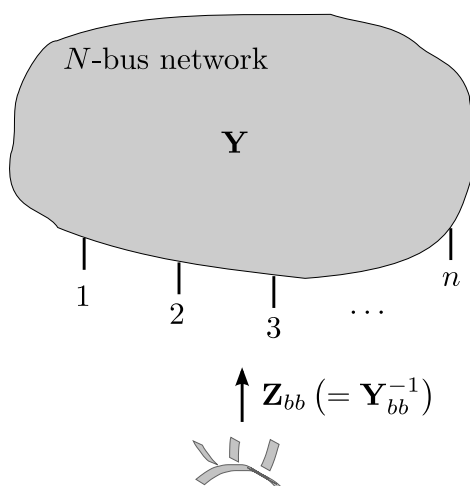
Figure 3.19: Boundary impedance matrix seen from n chosen buses of an N-bus network.

The detailed contribution of loads and synchronous machines to the nodal admittance matrix is given in Section C.3.1.

To derive the reduced admittance matrix $\mathbf{Y}_{bb}$ seen from the boundary buses of a network from the admittance matrix of the whole network, the following scheme can be used:

1. *Build the nodal admittance matrix of the concerned sub-system* (i.e. PM or EMT).

2. *Reduce that matrix to its boundary buses* through a Schur reduction [Hay68]:

   Given "$bb_{indices}$", the indices of the boundary buses in the nodal admittance matrix and "$all\_but\_bb_{indices}$", the remaining indices, the following sub-matrices are extracted:

$$
\begin{aligned}
\mathbf{Y}_{11} &= \mathbf{Y}\left(bb_{indices},\ bb_{indices}\right), \\
\mathbf{Y}_{12} &= \mathbf{Y}\left(bb_{indices},\ all\_but\_bb_{indices}\right), \\
\mathbf{Y}_{21} &= \mathbf{Y}\left(all\_but\_bb_{indices},\ bb_{indices}\right), \\
\mathbf{Y}_{22} &= \mathbf{Y}\left(all\_but\_bb_{indices},\ all\_but\_bb_{indices}\right).
\end{aligned}
$$

   The reduced nodal admittance matrix $\mathbf{Y}_{bb}$ is given by:

$$
\mathbf{Y}_{bb} = \mathbf{Y}_{11} - \mathbf{Y}_{12}\mathbf{Y}_{22}^{-1}\mathbf{Y}_{21},
$$

   where $\mathbf{Y}_{22}^{-1}$ is the inverse of matrix $\mathbf{Y}_{22}$.

3. *If needed, compute the boundary impedance matrix $\mathbf{Z}_{bb}$*:

$$
\mathbf{Z}_{bb} = \mathbf{Y}_{bb}^{-1}. \tag{3.9}
$$

   $\mathbf{Z}_{bb}$ generally is complex, with a real part of the form (2.33) and an imaginary part of the form (2.34).

The boundary admittance matrix $\mathbf{Y}_{bb}$ relates input bus voltages and currents:

$$\mathbf{I}_{bb} = \mathbf{Y}_{bb}\mathbf{V}_{bb} \, , \tag{3.10}$$

where $\mathbf{V}_{bb}$ (resp. $\mathbf{I}_{bb}$) is the vector of boundary bus voltages (resp. currents). Similarly for the boundary impedance matrix:

$$\mathbf{V}_{bb} = \mathbf{Z}_{bb}\mathbf{I}_{bb} \, .$$

"On-the-fly" computation of the Thévenin equivalent parameters is also possible and may be needed in some real-time applications [SJ13]. Thévenin equivalent re-computation was not implemented in this work since the convergence obtained with the offline pre-computation of the Thévenin equivalent parameters was satisfactory in terms of number of iterations. In practice, unforeseen changes in the Thévenin equivalent may arise from automatic devices (such as protections tripping devices, load tap changers, etc.) or loads.

3.4 Extrapolation techniques

3.4.1 Extrapolation in time

To speed up the convergence of the relaxation process, when starting the computations of a new time step $t + H$, the interface variables can be initialized to predicted values obtained from the previous time steps. For instance, with a first-order (linear) prediction, the predicted value of variables $\boldsymbol{x}$ is given by:

$$\begin{aligned}
\tilde{\boldsymbol{x}}(t + H) &= \boldsymbol{x}(t) + \frac{\boldsymbol{x}(t) - \boldsymbol{x}(t - H)}{H} H \\
&= 2\boldsymbol{x}(t) - \boldsymbol{x}(t - H) \, ,
\end{aligned} \tag{3.11}$$

where the slope at time t has been approximated by finite differences (see Figure 3.20). A second-order prediction can also be used, which relies on three points in the past. Just after a large disturbance, such as fault inception and clearing, a zero-order prediction is used for a sufficient number of steps (3 to 5) before resorting to a higher-order prediction.

3.4.2 Extrapolation through iterations

Aitken accelerator [IT69] or similar methods (e.g. [JS68]) may be used to further improve the convergence of the co-simulation scheme. The principle of the Aitken accelerator is shown in Figure 3.21 for a single variable case. The principle is similar to extrapolation in time represented in Figure 3.20, but applied to the successive dynamic iterations instead of to the successive time steps. Let us consider the convergent sequence $(x_k)_{k\in\mathbb{N}}$ defined by

$$x_{k+1} = f\left(x_k\right) \, ,$$

converging to the solution x^* such that:

$$f\left(x^*\right) = x^* \, .$$
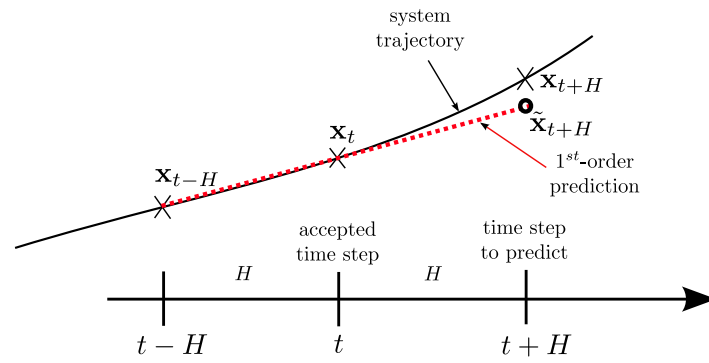
Figure 3.20: Prediction of the interface variables at the next time step.
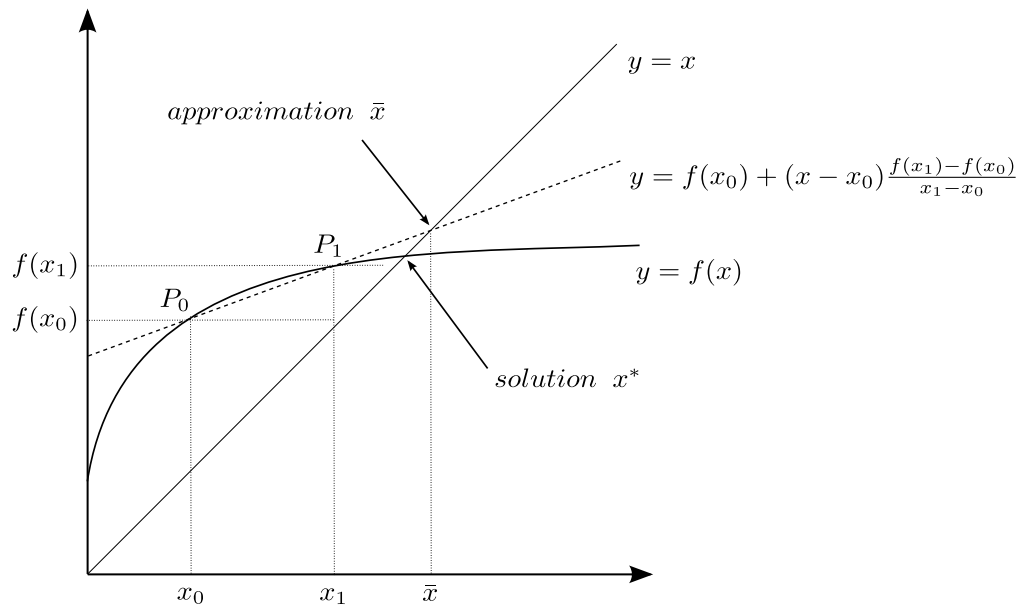
Figure 3.21: Aitken accelerator principle.

Given an initial point x_0, we can construct the sequence $(x_k)_{k \in \mathbb{N}}$ graphically, as already explained in Section 3.2.1. Figure 3.21 shows the principle of Aitken acceleration: knowing two successive iterates x_0 and x_1, and assuming f is linear in the vicinity of its solution, one can compute at a negligible cost an approximation $\bar{x}$ of the solution, which is closer to the latter than the most recent iterate x_1:

$$\bar{x} = f(x_0) + (\bar{x} - x_0) \frac{f(x_1) - f(x_0)}{x_1 - x_0} \; .$$

Function f is applied to approximation $\bar{x}$ rather than to the last iterate x_1, giving:

$$x_2 = f(\bar{x}) \; ,$$

which should be closer to the solution x^* than $f(x_1)$.

Aitken and similar acceleration methods are interesting when at least 3 to 5 iterations are needed to satisfy the convergence tolerance, which is not the case in our co-simulation scheme. For this reason, we did not include Aitken or similar acceleration schemes in the final co-simulation algorithm. Moreover, most such acceleration methods work for scalar variables, or multiple but decoupled variables, i.e. with at least a diagonally dominant matrix $\mathbf{Z}_{bb}$, which would neglect the coupling between boundary buses, which reduces their interest.

Implementation schemes for acceleration methods are provided in Figures B.6 and B.7.

3.5 Summary of presented coupling techniques

Table 3.3 summarizes the various techniques presented in Sections 3.2-3.4. The coupling techniques are classified according to the chosen characteristics for the iterative schemes, the chosen boundary conditions and the extrapolation techniques.

Iterative schemes: A damping factor $\alpha = 1$ (or no damping factor, to express it differently) is chosen for PM-EMT co-simulation iterations (see Section 3.2.1). The relevance of this choice, leading to a reduced number of co-simulation iterations (confirmed by the tests further presented in Section 3.7.2.7). For what concerns the choice between parallel Jacobi and sequential Gauss-Seidel evaluation schemes, our preference went to the second to take advantage of its faster convergence (Section 3.2.3). Another reason in favour of this choice comes from the different simulation times for the PM and EMT sub-systems, as discussed in Section 2.4.5. Therefore, a parallel co-simulation scheme, such as the Jacobi one, is of lower interest. The choice of solving the PM sub-system first is related to the particular case of a single EMT sub-system evaluation (as detailed in Section 3.2.3.2). The size of the relaxation time window in our application is equal to the PM time step size H, which is typically in the order of a period at fundamental frequency. This leads to the multirate ratio (Section 3.2.4) typically equal to 200.

Boundary conditions: First-order conditions are chosen on both sides of the PM-EMT boundary to improve convergence speed to the utmost. Overlapping PM and EMT sub-systems (see Section 3.3.2) were not tested in this work. Overlapping sub-systems may bring more difficulty for automatic boundary selection, and are here of reduced interest since non-overlapping sub-systems were found to provide a very good convergence. Note that in column "Number of dyn. iter", the word "reference" means that the line of concern is the reference for the comparison of the average number of dynamic iterations per time step.

Extrapolation: A second-order extrapolation of the PM-EMT co-simulation iterations is used when starting a new time-step to further reduce the number of co-simulation iterations needed per time step. The observed number of co-simulation iterations per time step is too small to gain any benefit from extrapolating the co-simulation iterations of a particular time step. Aitken (see Section 3.4.2) or interface Jacobian schemes (see Section 3.2.2) are thus not used.

Table 3.4 summarizes the main possible co-simulation implementation choices and proposes a comparison between them. In order to give the greatest flexibility and generality to the proposed co-simulation procedure, it was chosen to communicate updated information to the PM solver outside its internal Newton iterative process, rather than to update the EMT model inside the Newton iterations of the PM solver. Communication between both solvers is implemented through network sockets, since this technique was available between the FORTRAN 2003 code of the PM solver and the MATLAB code of the EMT solver. The coupling code is implemented in MATLAB, for simplicity (the EMT solver being also written in this language).

Iterative schemes			Number of dyn. iter	Additional cost (in dyn iter.)	Our choice
1. Damping factor	- parameter α		not reduced	negligible	$\alpha = 1$
2. Gauss-Seidel	- Gauss-Seidel	PM first	reduced	negligible	✓
or		EMT first	reduced	negligible	
Jacobi	- Jacobi		not reduced	negligible	
3. Wavef. Relax.	Particular case: Time window size = PM time step size H				
4. Multirate ratio	typically $20\text{ms}/100\mu\text{s} = 200$				

Boundary Conditions

		Number of dyn. iter	Additional cost	Our choice
1. First order	- on EMT-side	reduced	negligible	
	- on PM-side	reduced	negligible	
	- on both EMT and PM sides	much reduced	negligible	✓
2. Overlap	- without overlap	reference	negligible	✓
	- with overlap	not tested	negligible	

Extrapolation

		Number of dyn. iter	Additional cost	Our choice
1. In time	- zero-order	reference	negligible	
	- first-order	reduced	negligible	
	- second-order	reduced	negligible	✓
2. In dyn. iter.	- zero-order	reference	negligible	✓
	- Aitken	reduced from 3rd or 4th it.	negligible	
	- Boundary Jacobian	much reduced	significant	

Table 3.3: Summary of relaxation techniques.

Point of coupling	Advantages	Drawbacks	Our choice
- inside Newton iterations	-	-	
- outside Newton iterations	-	-	✓
Communication through...			
- shared memory	fast	more complicate	
- network sockets	network-enabled	slower	✓
- file	easiest	slowest	
Programming language			
- MATLAB	easier to implement	slower to execute	✓
- python	easier to implement	slowerto execute	
- C	faster to execute	slower to implement	
- FORTRAN 2003	fasterto execute	slower to implement	

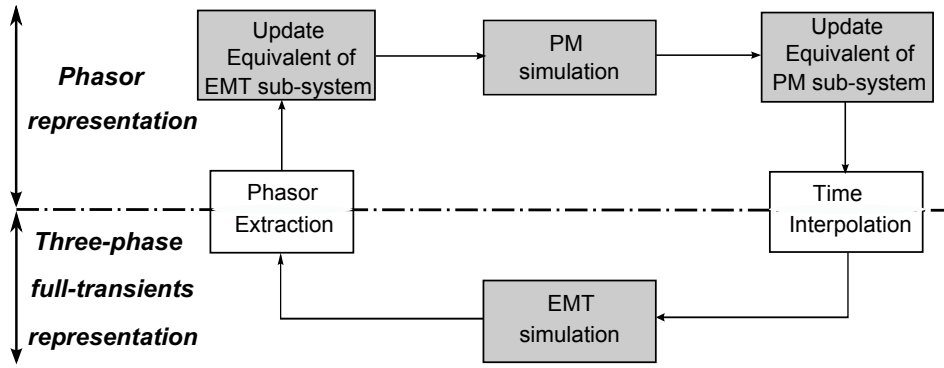Table 3.4: Summary of co-simulation implementation choices.

Figure 3.22: Overview of relaxation process.

3.6 Relaxation algorithm

Coupled PM-EMT simulations are not multi-physics simulations (as is the case for fluid-structure or circuit-field simulations [SDGB10]) but rather multi-models coupling of the same phenomena. It could be said that EMT simulations are time-domain while PM simulations are (a particular kind of) frequency-domain simulations. Coupling PM with EMT simulations requires some care because at the boundary between the two (or more) sub-systems, both sides need to receive an information compatible with their modeling assumptions. This requires performing time interpolation and phasor extraction, as sketched in Figure 3.22. In this section, a perfect conversion from PM to EMT models, and conversely, is assumed. Conversion techniques between PM and EMT models will be treated in Chapter 4.

The overall relaxation process is shown in Figure 3.23, together with the dynamically updated equivalents. In this figure, equation (2.32) of the multiport Thévenin equivalent has been recalled. Note, however, that the Thevenin equivalent *is not static but refreshed at every iteration of every time step* as explained next.

Assuming that the PM simulation is performed first (relying on the last updated equivalent of the EMT sub-system), the intermediate values of the boundary bus voltages and currents $\boldsymbol{V}^{k+\frac{1}{2}}$ and $\boldsymbol{I}^{k+\frac{1}{2}}$ are passed to the EMT simulation.

First, they are used to compute the vector of Thévenin voltage phasors:

$$\bar{\boldsymbol{E}}_{pm} = \bar{\boldsymbol{V}}^{k+\frac{1}{2}} - \boldsymbol{Z}_{pm}\bar{\boldsymbol{I}}^{k+\frac{1}{2}} \; , \tag{3.12}$$

with:

$$\boldsymbol{Z}_{pm} = \boldsymbol{R}_{pm} + j\omega_s\boldsymbol{L}_{pm} \; , \tag{3.13}$$

where $\boldsymbol{Z}_{pm}$ is an estimate of the Thévenin impedance matrix of the PM sub-system, as seen from its boundary buses, and $\boldsymbol{R}_{pm}$ (resp. $\boldsymbol{L}_{pm}$) is the corresponding resistance (resp. inductance) matrix, computed prior to the simulation, and ω_s is the synchronous frequency of the system. Next, the components of $\bar{\boldsymbol{E}}_{pm}$ are interpolated (this step will be detailed in Section 4.1.1) to
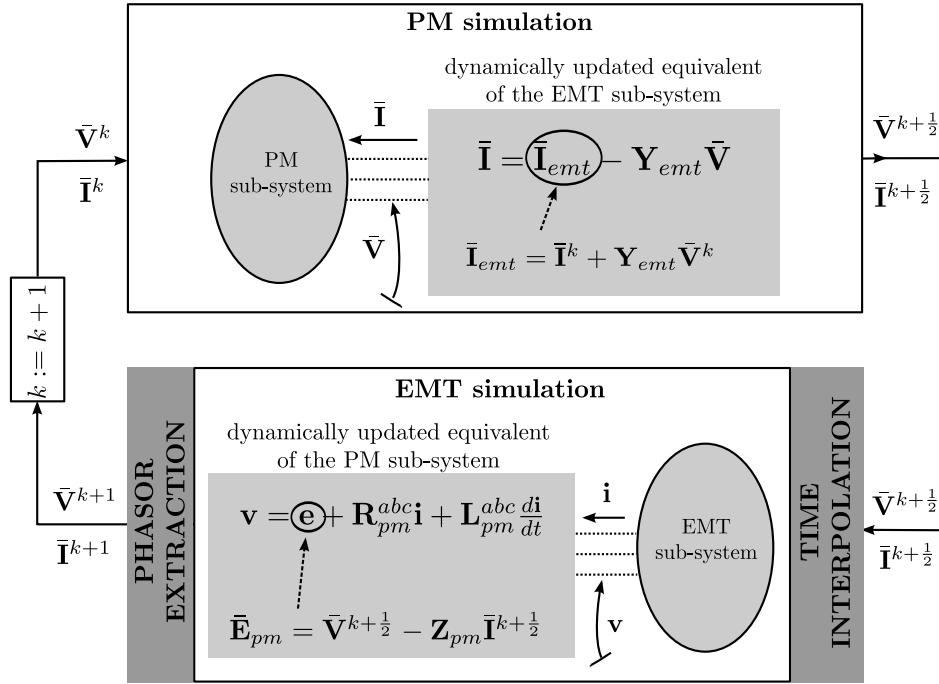
Figure 3.23: Co-simulation algorithm.

obtain the voltage vector e at each discrete time $t + mh$ $(m = 0, \ldots, \rho)$, where for simplicity of presentation, H has been assumed to be a multiple of h, i.e. $H = \rho h$ where ρ is an integer. Finally, the Thévenin equivalent is replaced by the differential equations of the corresponding RL circuit:

$$\boldsymbol{v} = \boldsymbol{e} + \boldsymbol{R}_{pm}^{abc}\,\boldsymbol{i} + \boldsymbol{L}_{pm}^{abc}\,\frac{d}{dt}\boldsymbol{i}\,, \tag{3.14}$$

where $\boldsymbol{v}$, $\boldsymbol{e}$ and $\boldsymbol{i}$ are vectors of dimension $3n$ relative to the three phases of the n boundary buses, and $\boldsymbol{R}_{pm}^{abc}$ (resp. $\boldsymbol{L}_{pm}^{abc}$) is the $3n \times 3n$ three-phase resistance (resp. inductance) matrix derived from $\boldsymbol{Z}_{pm}$ (and, hence, accounting for the coupling between boundary buses).

After the EMT simulation is completed and the phasors extracted (this step will be detailed in Section 4.2), the updated boundary values $\boldsymbol{V}^{k+1}$ and $\boldsymbol{I}^{k+1}$ are available, which are in turn involved in the updated Norton equivalent used by the PM simulation. That equivalent is represented with standard models of current injectors, impedance loads, and branches with pi-equivalents.

Figure 3.24 shows the overall flowchart of the proposed method. A detailed version is provided in Appendix B.

3.7   Convergence study

In this section, we will principally focus on assessing the convergence of PM-EMT co-simulation for various boundary conditions (see Section 3.3). After presenting the test-case used, we will introduce the key notion of *iteration factor* w that will help us to characterize the convergence of
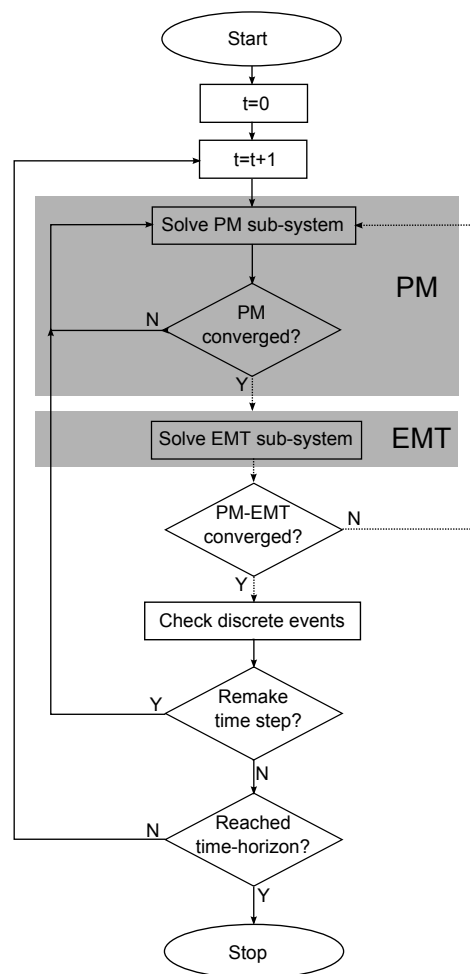
Figure 3.24: Proposed relaxation.

the co-simulation process. We will also show the effect of the damping parameter α, explained in Section 3.2.1, on the number of co-simulation iterations. In Section 3.7.3, we will show that the use of specific boundary conditions does not modify the solution of the iterative process.

3.7.1   Simplified test-case

To illustrate the convergence properties discussed in this section, a simple example will be used throughout the various cases. The one-line diagram of the simple system considered is shown in Figure 3.25. The PM sub-system only consists of a voltage source $\bar{E}_{pm}$ in series with an impedance $Z_{pm} = j0.01$ pu (on 100-MVA base). Bus 1 is the boundary. The EMT sub-system includes a $1,200$-MVA round-rotor synchronous machine modeled with four rotor windings and a simple excitation and voltage regulation system. This sub-system has a three-phase, full-transients model of the EMTP type, involving 56 differential and 63 algebraic states.

A three-phase fault takes place on line 2-4. It is eliminated by opening the breakers at both ends of the line.
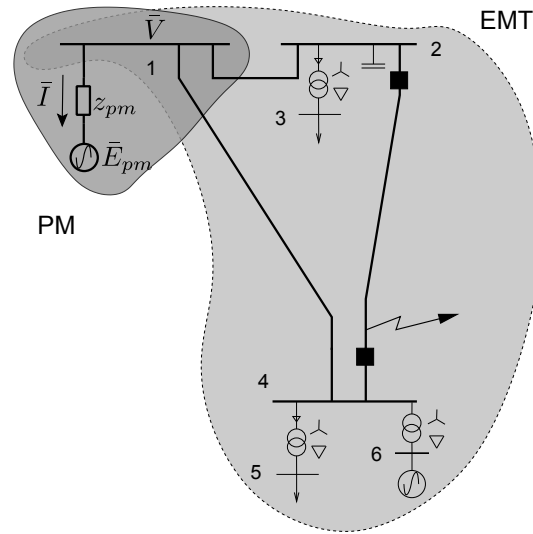
Figure 3.25: System used to test the convergence of the relaxation process.

This simple test system is used to illustrate the derivations of Section 3.7.2, in particular under large disturbances and nonlinear effects, not considered in the theoretical derivations of Section 3.7.2. The focus here is on the convergence of various PM-EMT coupling schemes. Of course, it does not allow assessing the computational efficiency of the proposed hybrid simulation versus a full EMT simulation.

3.7.2   Theoretical study of convergence properties

3.7.2.1   Iteration factor

In general, the PM-EMT co-simulation is an iterative way for solving, for the boundary variables, the system composed of both the PM and the EMT sub-systems. In particular, assuming a single interface bus for simplicity, the iterative process can be written:

$$x^{k+1} = wx^k + c \quad k = 0, 1, 2, \ldots \tag{3.15}$$

where all numbers are complex and c is a constant independent of x^k and x^{k+1}. w is called the *iteration factor*.

Of course, w is not chosen directly, but through the choice of the boundary conditions that will impact the convergence of the iterative process. The lower the norm of w, denoted $||w||$, the lower the number of iterations for the sequence (x^k) to reach convergence, detected for instance from the norm $||x^{k+1} - x^k||$ being smaller than some tolerance. If $||w||$ is much smaller than one, the convergence will take place rapidly, while if $||w||$ is larger than one, the sequence will not converge [WSV87].

In what follows, various equivalents used in the PM-EMT relaxation process will be brought into the form (3.15).
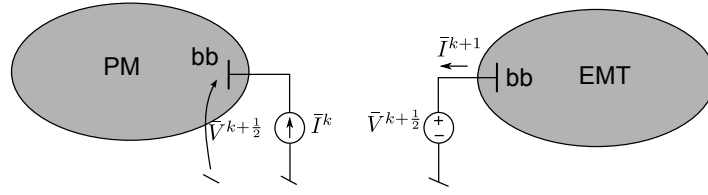
Figure 3.26: Zero-order boundary conditions ("bb" denotes the boundary bus, common to both PM and EMT sub-systems).

3.7.2.2 PM sub-system equivalenced by voltage source and EMT by current source

The simplest equivalent, used in particular in [PGV13], to model one sub-system when simulating the other is through voltage and current sources as shown in Figure 3.26. Note that the phasor representation is used to comply with the phasor model, but the equivalents are converted into time-varying sources and differential equations in the EMT simulation, as detailed in Section 3.6. Let us consider the iterations performed when passing from time t to time $t + H$, i.e. over one step of the PM simulation.

At a given iteration, the PM simulation (assumed to be carried out first) determines the evolution of the PM sub-system over a single step H, with the EMT sub-system replaced by a current source. The value $\bar{I}^k$ of the boundary current has been extracted from the EMT simulation performed at the previous iteration. This PM simulation yields the new estimate $\bar{V}^{k+\frac{1}{2}}$ of the boundary bus voltage, where the upperscript $k + \frac{1}{2}$ indicates that half of the iteration has been performed.

Next, using this voltage, the EMT simulation is carried out to obtain the EMT sub-system evolution from t to $t + H$, using time steps h, and interpolating the evolution of the boundary bus voltage. This simulation yields the updated current $\bar{I}^{k+1}$.

Convergence is checked by comparing $||\bar{V}^{k+1} - \bar{V}^k||$ and $||\bar{I}^{k+1} - \bar{I}^k||$ to some tolerances. If the latter are satisfied, the simulation proceeds with the next time interval $[t + H \ t + 2H]$. Otherwise, an additional relaxation iteration is performed.

In order to assess the speed of convergence, an approximation of the PM and EMT sub-systems must be assumed. Let us suppose that, in the vicinity of the solution point, they can be linearized in respectively a Thévenin and a Norton equivalent, as shown in Figure 3.27. From this figure, one easily obtains:

$$\bar{V}^{k+\frac{1}{2}} = \bar{E}_{pm} + z_{pm}\bar{I}^k \,, \tag{3.16}$$

$$\bar{I}^{k+1} = \bar{I}_{emt} - y_{emt}\bar{V}^{k+\frac{1}{2}} \,. \tag{3.17}$$

Introducing (3.16) into (3.17) yields the recursive relation:

$$\bar{I}^{k+1} = -z_{pm}y_{emt}\,\bar{I}^k + (\bar{I}_{emt} - y_{emt}\bar{E}_{pm}) \,, \tag{3.18}$$

from which the iteration factor is easily identified as:

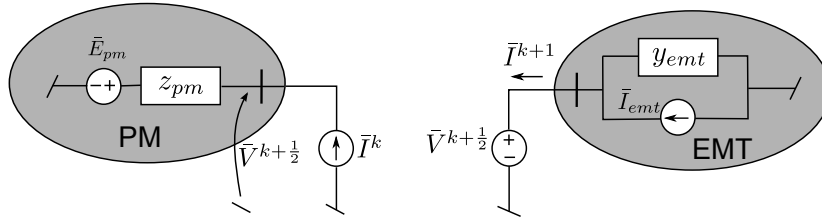$$w_1 = -z_{pm}y_{emt} \,. \tag{3.19}$$

Figure 3.27: Configuration of Fig. 3.26 with the PM and EMT sub-systems replaced by Thévenin and Norton equivalents.

Thus, for fast convergence, $||w_1||$ should be small. This is the case, for instance, if z_{pm} tends to zero, i.e. if the PM sub-system behaves as a pure voltage source. In this case, its representation by the $\bar{V}^{k+\frac{1}{2}}$ voltage comes closer to its real behavior, and convergence will be fast. However, in all other cases (for instance if the PM sub-system behaves more like a current source) convergence is expected to be slow, or even divergence may take place. Similar considerations hold true for the EMT sub-system behaving as a current source.

This is illustrated in Figure 3.28, obtained with the simple system introduced in Section 3.7.1. The PM (resp. EMT) simulation uses a current (resp. voltage) source as shown in Figure 3.26. The plot shows the successive values of the complex current (in Cartesian coordinates) during the relaxation process over the time step H that follows the fault inception. It is easily seen that oscillations around the solution take place during the iterations. It takes as many as 64 iterations to converge, which clearly shows that zero-order boundary conditions do not yield satisfactory convergence of hybrid PM-EMT simulations. The value of the current to which the process converges is $\bar{I} = 19.6124 + j7.3114$ pu.

For the system of concern, replacing the generator (see bus 6 in Figure 3.25) by a constant e.m.f. behind subtransient reactance, the value of y_{emt} computed from the reduced nodal admittance matrix is $y_{emt}^{\star} = 10.4083 - j88.8711$ pu. This leads to $w_1 = -0.8887 + j0.1041$. The magnitude $||w_1|| = 0.8948$, being close to unity, explains the slow convergence. Also, w_1 is close to a real negative number, which explains the oscillatory behavior of the successive iterates around the solution.

3.7.2.3   PM sub-system equivalenced by Thévenin and EMT by Norton

First-order boundary conditions, involving a linear relation between voltage and current are now considered. They consist of Thévenin and Norton equivalents as shown in Figure 3.29. An early version of this configuration was proposed in [And95] and it has also been used in [PAGV14]. Note that Norton or Thévenin equivalents can be used interchangeably.

The PM simulation is performed with the EMT sub-system replaced by a Norton equivalent, involving an admittance $\hat{y}_{emt}$ and the Norton current $\bar{I}^k + \hat{y}_{emt}\bar{V}^k$ updated with the latest available boundary voltage and current. In case a fault is simulated in the EMT sub-system, $\hat{y}_{emt}$ can be
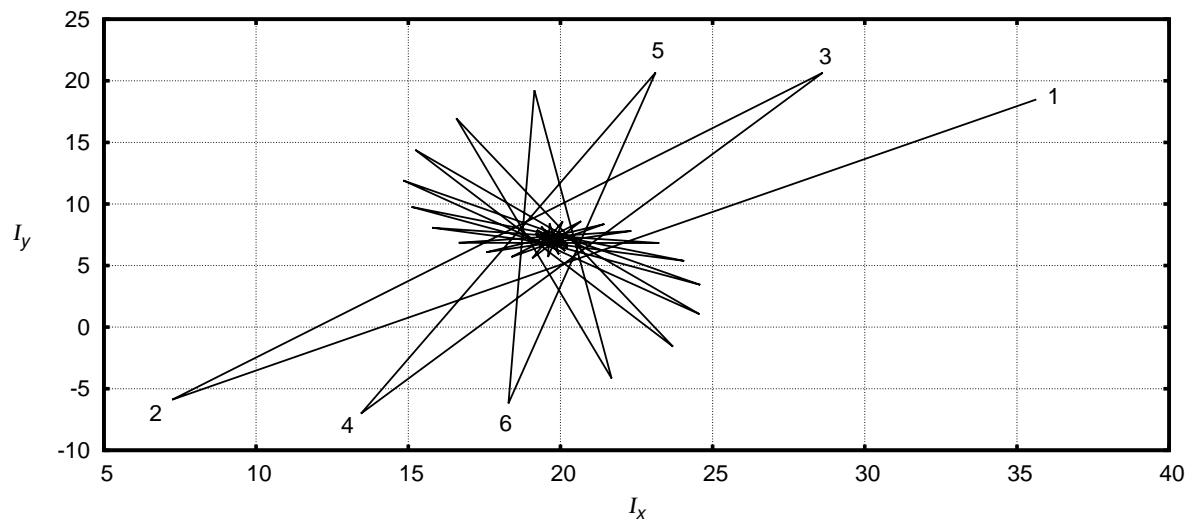
Figure 3.28: Example of iterations performed with the equivalents of Fig. 3.26. The first six iterations are identified with numbers.
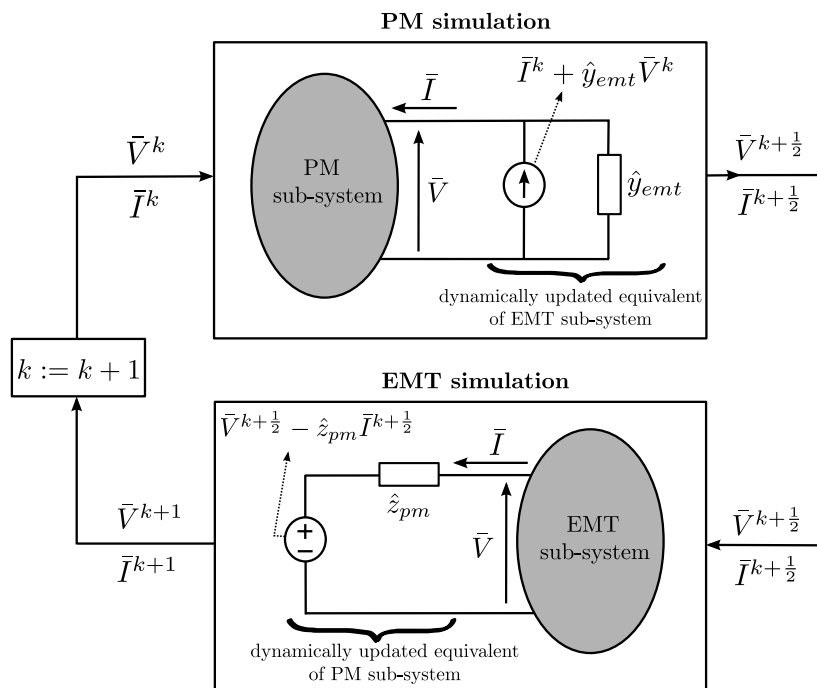

Figure 3.29: First-order boundary conditions.

computed beforehand for the pre-fault, during-fault and post-fault situations. Alternatively, it could be estimated numerically, from the previous values of the boundary voltage and current.

Similarly, the EMT simulation is performed with the PM sub-system replaced by a Thévenin equivalent, involving an impedance $\hat{z}_{pm}$ (also determined beforehand or numerically), and the Thévenin voltage $\bar{V}^{k+\frac{1}{2}} - \hat{z}_{pm}\bar{I}^{k+\frac{1}{2}}$ also updated with the latest available boundary voltage and current.

The following relations are easily derived from Figure 3.29:

$$\bar{I}^{k+\frac{1}{2}} = \bar{I}^k + \hat{y}_{emt}\bar{V}^k - \hat{y}_{emt}\bar{V}^{k+\frac{1}{2}} , \tag{3.20}$$

$$\bar{V}^{k+1} = \bar{V}^{k+\frac{1}{2}} - \hat{z}_{pm}\bar{I}^{k+\frac{1}{2}} + \hat{z}_{pm}\bar{I}^{k+1} . \tag{3.21}$$

As for the zero-order boundary conditions, we assume at this point that the PM and EMT sub-systems can be linearized in respectively a Thévenin and a Norton equivalent, as shown in Figure 3.27, with the following equations:

$$\bar{V}^{k+\frac{1}{2}} = \bar{E}_{pm} + z_{pm}\bar{I}^{k+\frac{1}{2}} , \tag{3.22}$$

$$\bar{I}^{k+1} = \bar{I}_{emt} - y_{emt}\bar{V}^{k+1} , \tag{3.23}$$

which can be compared to Equations (3.16) and (3.17). From equations (3.20) - (3.23), the iteration factor is obtained as:

$$w_2 = \underbrace{-z_{pm}y_{emt}}_{w_1} \frac{1 - \dfrac{\hat{z}_{pm}}{z_{pm}}}{1 + \hat{z}_{pm}y_{emt}} \frac{1 - \dfrac{\hat{y}_{emt}}{y_{emt}}}{1 + z_{pm}\hat{y}_{emt}} . \tag{3.24}$$

This result shows that $\hat{z}_{pm}$ and $\hat{y}_{emt}$ can be used as degrees of freedom to make the iteration factor w_2 smaller in magnitude than w_1. More precisely, the iteration factor w_2 can be decreased by choosing $\hat{z}_{pm} \simeq z_{pm}$, i.e. by using a Thévenin impedance $\hat{z}_{pm}$ close to the exact value z_{pm}. It can also be decreased by choosing $\hat{y}_{emt} \simeq y_{emt}$, i.e. by using a Norton admittance $\hat{y}_{emt}$ close to y_{emt}. In principle, only one of two choices is sufficient.

3.7.2.4 PM sub-system equivalenced by Thévenin and EMT by current source

Variants combining voltage/current sources with Thévenin/Norton equivalents (i.e. mixed zero- and first-order boundary conditions) can be also contemplated. In Figure 3.30, for instance, the PM sub-system is represented by a Thévenin equivalent in the EMT simulation, while the EMT sub-system is represented by a current source in the PM simulation. Formally, this corresponds to setting $\hat{y}_{emt}$ to zero, and involving $\bar{I}^k$ instead of $\bar{I}^{k+\frac{1}{2}}$ in the Thévenin equivalent (indeed, the current injected in the PM sub-system is not updated by the PM simulation). This configuration (or improved variants of the latter) has been used in [zLxHT+11, vHGK11, AF13, ZGW+13, ZFA14, Lou14].
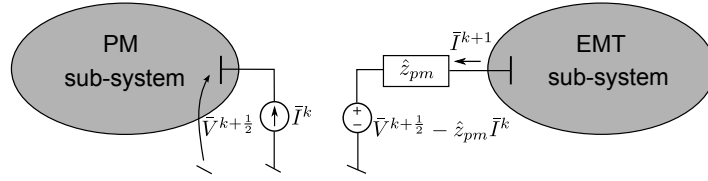
Figure 3.30: Mixed zero- and first-order boundary conditions - first variant.
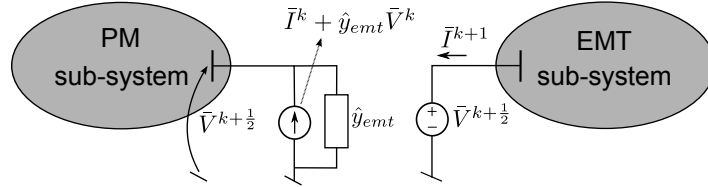

Figure 3.31: Mixed zero- and first-order boundary conditions - second variant.

Through derivations similar to the ones in Sections 3.7.2.2 and 3.7.2.3 the following iteration factor is found:

$$w_3 = \underbrace{-z_{pm}y_{emt}}_{w_1} \; \frac{1 - \dfrac{\hat{z}_{pm}}{z_{pm}}}{1 + \hat{z}_{pm}y_{emt}} \; . \tag{3.25}$$

No result is given for this configuration since the PM part of the test system is already modeled by a simple Thévenin equivalent (see Figure 3.25).

3.7.2.5 PM sub-system equivalenced by voltage source and EMT by Norton

This variant is shown in Figure 3.31, with the PM sub-system represented by a voltage source in the EMT simulation, and the EMT sub-system by a Norton equivalent in the PM simulation. Formally, this corresponds to setting $\hat{z}_{pm}$ to zero.

To the authors' knowledge, this configuration has not been considered in the literature. The reason is that most publications (e.g. [ZGW$^+$13]) consider the possibility for the PM-EMT sub-system boundary to be close to the disturbance location, and use a shunt admittance to approximate the response of the PM sub-system to harmonics generated by the EMT model.

The following iteration factor is obtained:

$$w_4 = \underbrace{-z_{pm}y_{emt}}_{w_1} \; \frac{1 - \dfrac{\hat{y}_{emt}}{y_{emt}}}{1 + z_{pm}y_{emt}\dfrac{\hat{y}_{emt}}{y_{emt}}} \; . \tag{3.26}$$

To assess the impact of using an estimated Norton admittance $\hat{y}_{emt}$ that significantly departs from the exact (but unknown) value y_{emt}, Figure 3.32 shows the evolution of $||w_4||$ with $||\dfrac{\hat{y}_{emt}}{y_{emt}}||$, for two values of the product $z_{pm}y_{emt}$ corresponding to respectively ($z_{pm} = j0.01$, $y_{emt} = -j100$) and ($z_{pm} = j0.01$, $y_{emt} = -j1000$). Note the logarithmic scale used in abscissa. This plot suggests
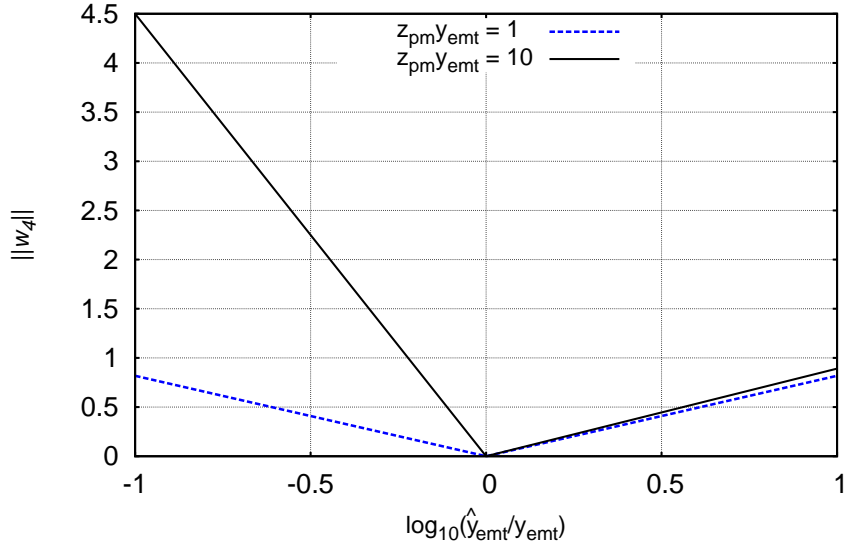
Figure 3.32: Variation of $||w_4||$ with $||\dfrac{\hat{y}_{emt}}{y_{emt}}||$ for two values of $z_{pm}y_{emt}$.

that $||w_4||$ remains small (i.e. convergence remains fast) even when $\hat{y}_{emt}$ significantly departs from y_{emt}, except when $z_{pm}y_{emt} = 10$ if $\hat{y}_{emt}$ was significantly smaller than y_{emt}. Furthermore, when $z_{pm}y_{emt} = 10$, $||w_4||$ remains reasonably small on a large range of $\dfrac{\hat{y}_{emt}}{y_{emt}}$, while $w_1 = -z_{pm}y_{emt} = -10$, indicating that the equivalent of Figure 3.26 would lead to severely diverging iterations.

Getting back to the system of Section 3.7.1, the scenario already considered in Figure 3.28 has been simulated with the equivalent of Figure 3.31. Figure 3.33 shows the successive values of the complex current (in Cartesian coordinates) during the relaxation process over the time step H that follows the fault inception. It takes only four iterations for the relaxation process to converge in these constraining conditions. Compared to Figure 3.28, the number of iterations is drastically reduced when using a first-order boundary condition, which is thus recommended for hybrid PM-EMT simulation. Note that the final value of the current is found to be $\bar{I} = 19.6128 + j7.3115$ pu, i.e. the same value as in Figure 3.28.

The results of Figure 3.33 have been obtained with $\hat{y}_{emt} = y^{\star}_{emt}$, the Norton admittance estimated from a simple linear approximation of the EMT sub-system (see Section 3.7.2.2). Figure 3.34 shows the variation of the number of relaxation iterations for various values of $\hat{y}_{emt}$ obtained by multiplying $\hat{y}^{\star}_{emt}$ by a real, positive number. The number of iterations is the lowest for $\hat{y}_{emt} = y^{\star}_{emt}$. The shape of the curve is remarkably similar to the one of Figure 3.32.
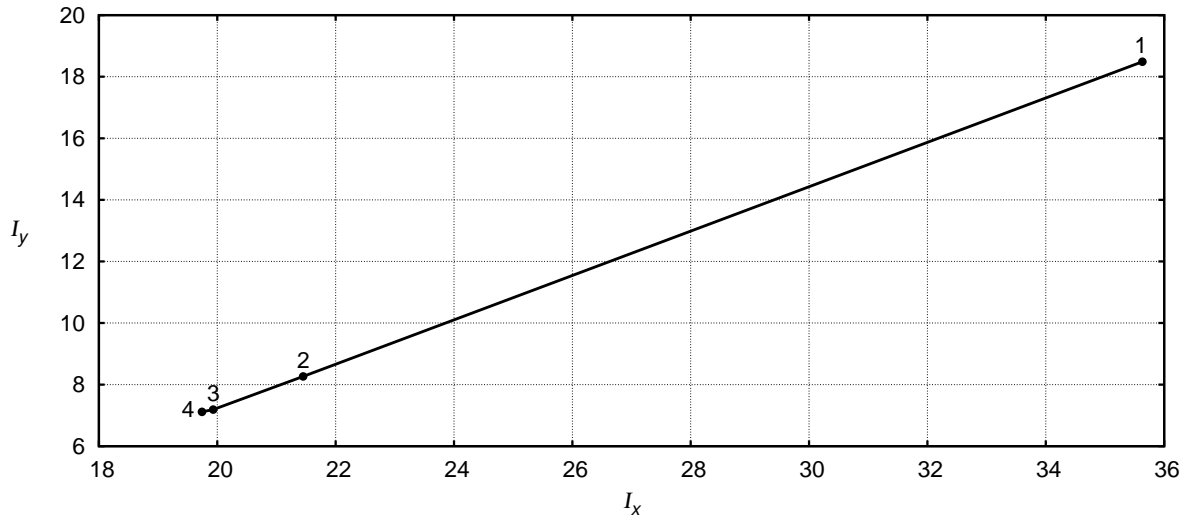
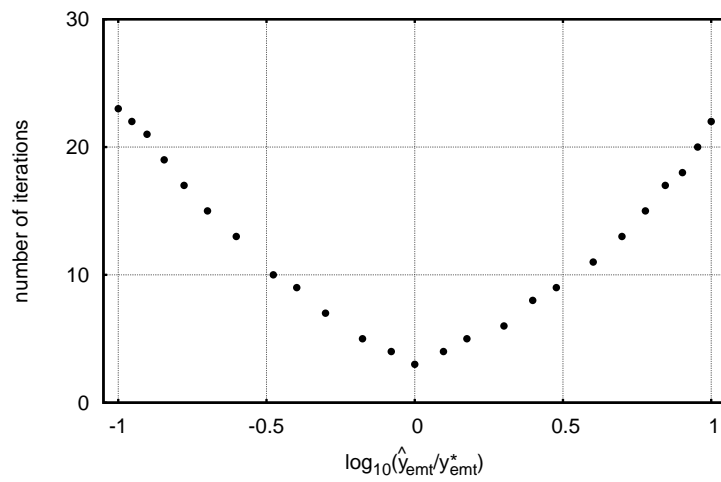Figure 3.33: Example of iterations performed with the equivalents of Figure 3.31.

Figure 3.34: Number of relaxation iterations for various values of $\dfrac{\hat{y}_{emt}}{y_{emt}^{\star}}$.
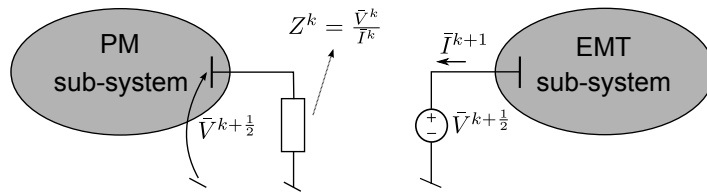
Figure 3.35: Mixed zero- and first-order boundary conditions - third variant.
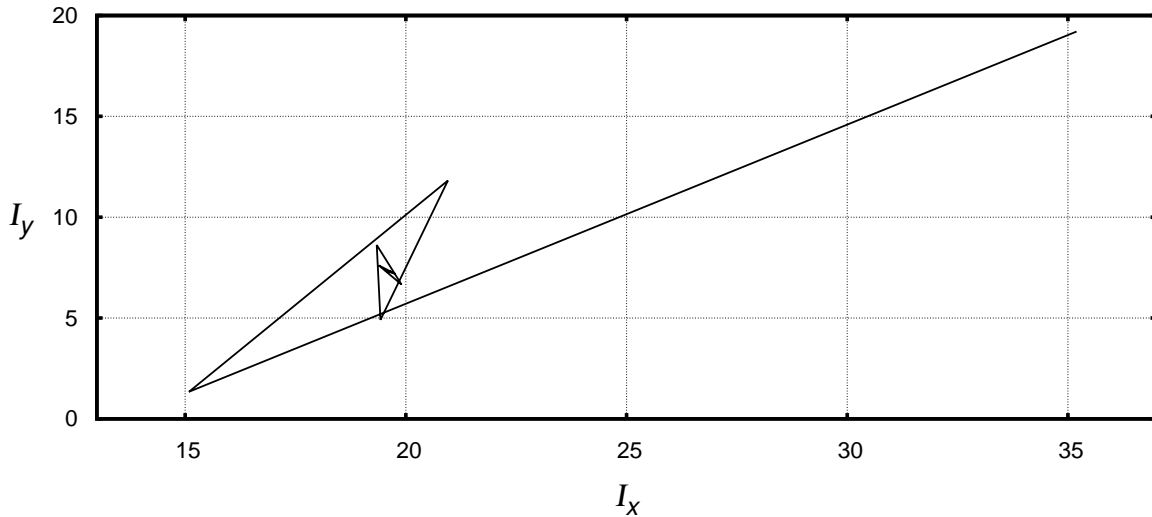

Figure 3.36: Example of iterations performed with the equivalents of Figure 3.35.

3.7.2.6 PM sub-system equivalenced by voltage source and EMT by impedance

The last variant is shown in Figure 3.35. The following iteration factor is obtained:

$$w_5 \approx \frac{1}{1 + 2\frac{\bar{I}_{emt}}{\bar{E}_{pm}/z_{pm}}}$$

Again, getting back to the system of Section 3.7.1, the scenario considered in Figure 3.28 has been simulated with the equivalent of Figure 3.35. Figure 3.36 shows the successive values of the complex current (in Cartesian coordinates) during the relaxation process over the time step H that follows the fault inception. Here it takes 11 iterations for the relaxation process to converge. Compared to Figure 3.28, the number of iterations is reduced when using a first-order boundary condition, but higher than in Figure 3.33. The final value of the current is found to be also $\bar{I} = 19.6128 + j7.3115$ pu, i.e. the same value as in Figure 3.28.

3.7.2.7 Influence of damping parameter α

A damping parameter α different from 1 (introduced in Section 3.2.1) can be used whatever the chosen boundary conditions. An example of the influence of the damping parameter on the number of iterations is shown in Figure 3.37, derived experimentally from the test case considered in Section 3.7.1, with zero-order boundary conditions. Overrelaxation with $\alpha = 1.03$ destabilizes the

Figure 3.37: Influence of damping parameter on the number of dynamic iterations for zero-order boundary conditions.
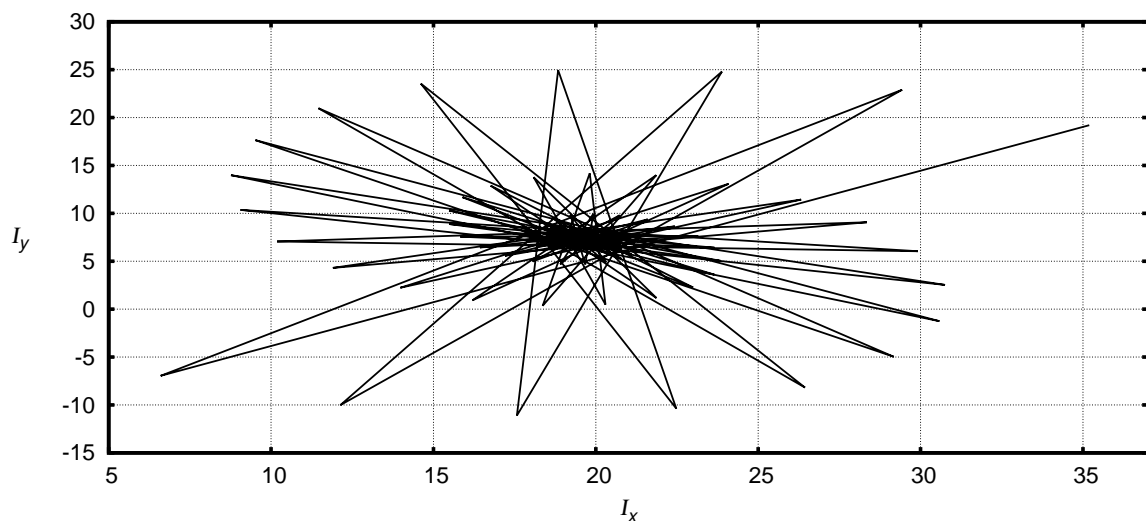
Figure 3.38: Example of iterations performed with the equivalents of Figure 3.26, making use of a damping parameter $\alpha = 1.03$.

iterating process, leading to 152 iterations (see Figure 3.38), to be compared to the 64 iterations obtained with $\alpha = 1$. Underrelaxation with $\alpha = 0.95$ somewhat improves convergence, leading to "only" 32 iterations (see Figure 3.39). However, two small a damping parameter again leads to increasing the number of iterations, since the corrections brought by each iteration will be too small (see Figure 3.40 with 16 iterations for $\alpha = 0.15$).

The influence of the damping parameter on the number of iterations for the same case, but with single-sided first-order boundary conditions, is shown in Figure 3.41. Since the initial number of iterations was already very low, the use of a damping coefficient does not improve much the performance. Again, too small a damping coefficient degrades the performance of the iterative
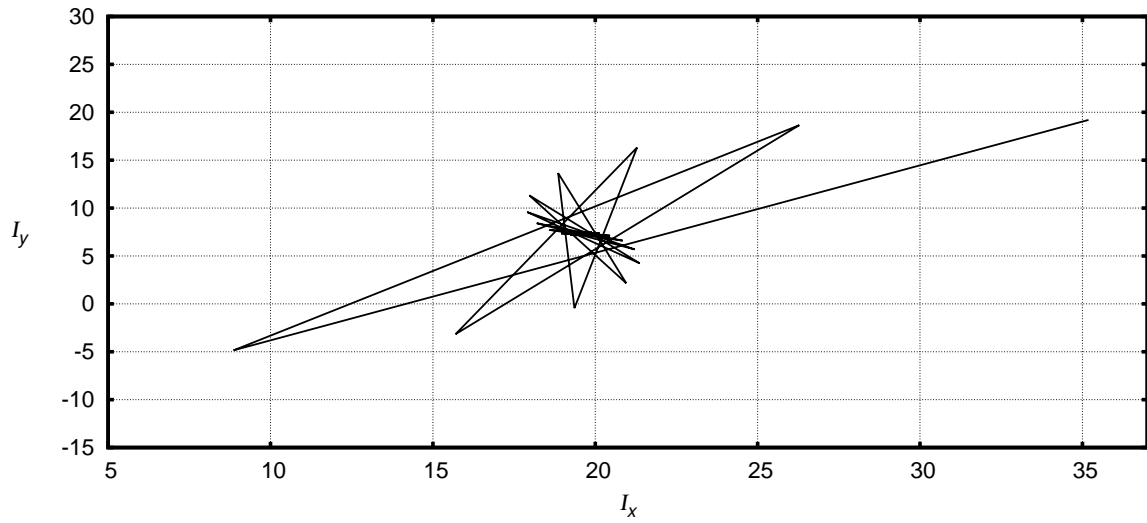
Figure 3.39: Example of iterations performed with the equivalents of Figure 3.26, making use of a damping parameter $\alpha = 0.95$.
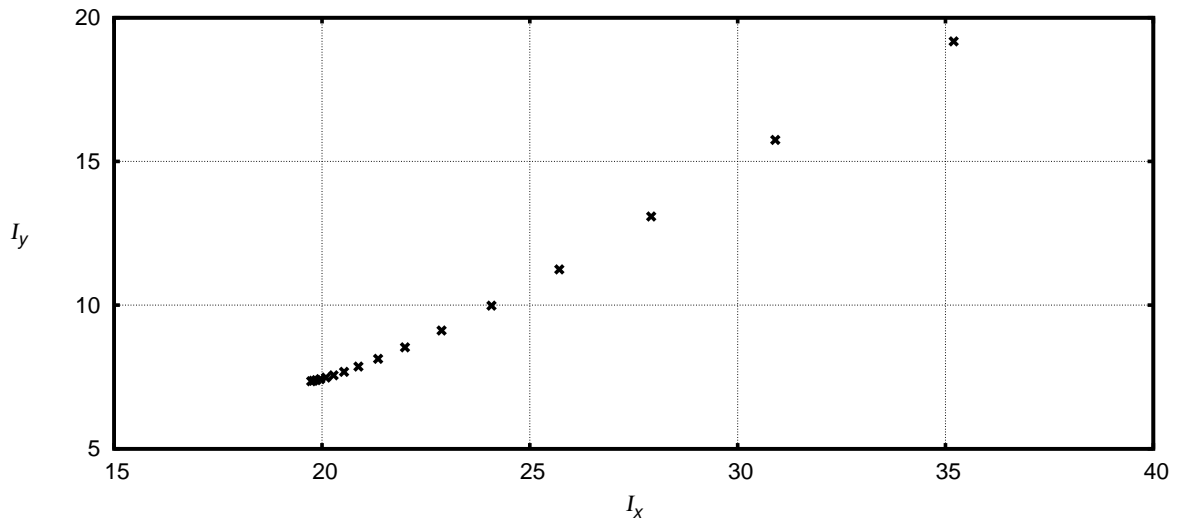
Figure 3.40: Example of iterations performed with the equivalents of Figure 3.26, making use of a damping parameter $\alpha = 0.15$.
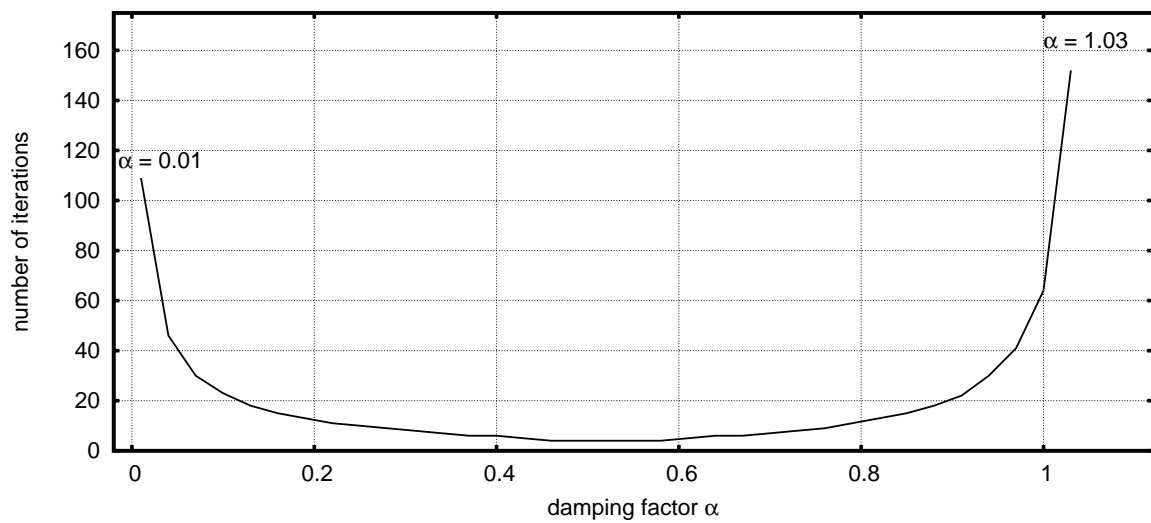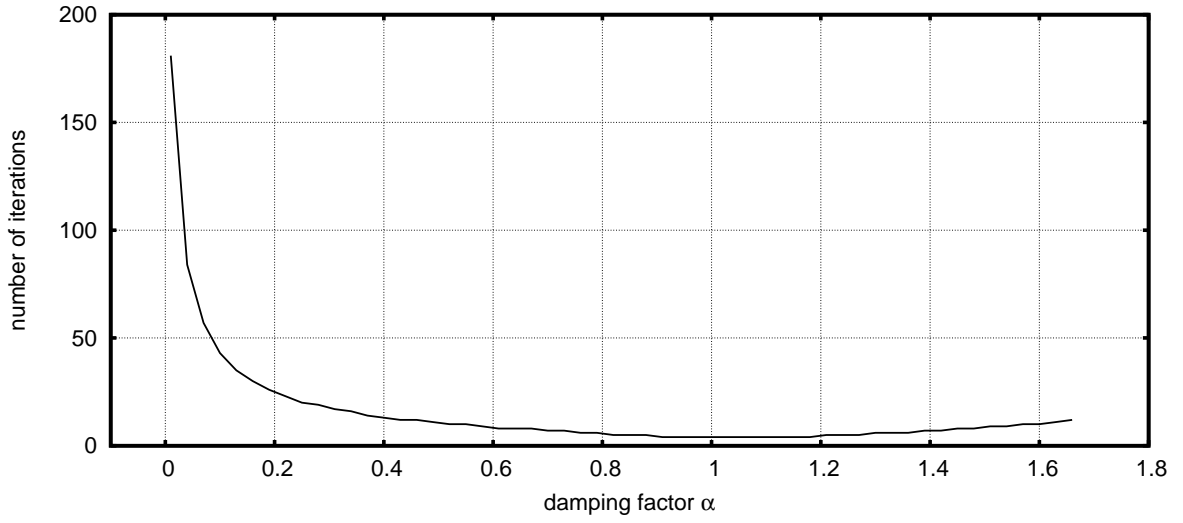
Figure 3.41: Influence of damping parameter on the number of dynamic iterations for single-sided first-order boundary conditions.
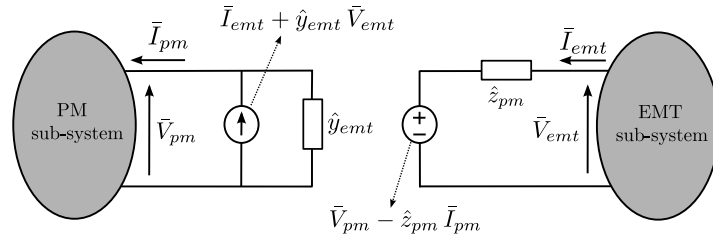
Figure 3.42: Situation reached when the relaxation process has converged.

process because of too small corrections at every iteration.

3.7.3 Solution of the PM-EMT simulation

Let $\bar{V}_{pm}$ and $\bar{I}_{pm}$ (resp. $\bar{V}_{emt}$ and $\bar{I}_{emt}$) be the values of the boundary voltage and current, provided by PM (resp. EMT) simulation, once convergence has taken place. At convergence, the circuits in Figure 3.29 operate as shown in Figure 3.42, where intermediate values have been replaced by final ones. The following equations are easily derived from Figure 3.42:

$$\bar{I}_{pm} = \bar{I}_{emt} + \hat{y}_{emt}\bar{V}_{emt} - \hat{y}_{emt}\bar{V}_{pm} , \tag{3.27}$$

$$\bar{V}_{emt} = \bar{V}_{pm} - \hat{z}_{pm}\bar{I}_{pm} + \hat{z}_{pm}\bar{I}_{emt} . \tag{3.28}$$

Introducing (3.28) into (3.27) and rearranging the terms yields:

$$(1 + \hat{z}_{pm}\hat{y}_{emt})\bar{I}_{pm} = (1 + \hat{z}_{pm}\hat{y}_{emt})\bar{I}_{emt} \iff \bar{I}_{pm} = \bar{I}_{emt} , \tag{3.29}$$

where it has been assumed that the parenthesis is nonzero. Hence, Eq. (3.27) becomes:

$$\bar{V}_{pm} = \bar{V}_{emt} . \tag{3.30}$$

From equations (3.29) and (3.30) it is concluded that, *whatever the values of $\hat{y}_{emt}$ and $\hat{z}_{pm}$, the converged solution reached by the PM and EMT simulations is such that the boundary bus has the same voltage in both of them, and the current injected by one is the current received by the other.* Thus, there is a perfect match between the PM and EMT simulations. On the other hand, the values of $\hat{y}_{emt}$ and $\hat{z}_{pm}$ influence the convergence of the relaxation process. For instance, if $\hat{y}_{emt}$ was set to zero, at the k-th iteration the PM simulation would be performed with the boundary current set to $\bar{I}^k$; hence, the current change induced by the change of voltage $\bar{V}^k$ would be accounted for at the $(k+1)$-th iteration only. The Norton equivalent (with $\hat{y}_{emt} \neq 0$) yields a linear approximation of that variation of the current with the voltage. Similar considerations apply to the Thévenin equivalent and $\hat{z}_{pm}$.

The PM and EMT simulations match for any choice of $\hat{y}_{emt}$ and $\hat{z}_{pm}$, provided the PM and EMT models are iterated until convergence. The same does not hold true if a single iteration is performed, i.e. a single PM simulation followed by a single EMT simulation when passing from t to $t + H$. This case is of interest when hybrid simulation is used to test "hardware in the loop" [Mos13], as discussed in Section 3.2.3.2. In that application, $\hat{y}_{emt}$ and $\hat{z}_{pm}$ should be as accurate as possible to preserve the solution accuracy.

3.8 Taking into account the instantaneous frequency of the boundary currents

PM simulations are usually performed with constant network and machine impedances, computed at nominal frequency. In the EMT simulation, on the other hand, no such approximation is made, since current and voltage waveforms are computed by solving equations of the type (3.14).

Hence, using $\boldsymbol{Z}_{pm}$ at nominal frequency ω_s (as in (3.13)) to compute $\bar{\boldsymbol{E}}_{pm}$ and there from obtaining (by interpolation) the voltage source e used in (3.14) introduces some inconsistency. An expectedly more accurate approach, in case of large frequency deviations, consists in updating $\boldsymbol{Z}_{pm}$ with frequency before computing the Thévenin voltage $\bar{\boldsymbol{E}}_{pm}$.

Because frequency differs from one boundary bus to another, the following approximation is considered:

$$\boldsymbol{Z}_{pm} \simeq \boldsymbol{R}_{pm} + j\,\boldsymbol{L}_{pm}\,diag\left(\omega_1, \ldots, \omega_n\right). \tag{3.31}$$

Thus, the i-th column of $\boldsymbol{L}_{pm}$ is multiplied by the angular frequency ω_i of the current at the i-th boundary bus ($i = 1, \ldots, n$). The latter frequency is evaluated numerically at discrete time $t + H$ as:

$$\omega_i(t + H) \simeq \omega_s + \frac{\psi_i(t + H) - \psi_i(t)}{H}\,, \tag{3.32}$$

where $\psi_i(t)$ is the phase angle of the extracted current at the previous discrete time t and $\psi_i(t+H)$ the corresponding phase angle obtained from the last EMT simulation of the current time $t + H$. An illustration of the estimation of the current frequencies is shown in Figure 3.44a. The latter estimated frequencies may be compared to the curves in Figure 3.44b, showing the rotor speed
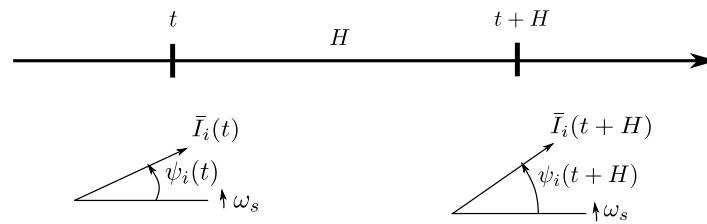
Figure 3.43: Phase angle variations of boundary current $\bar{I}_i$.

of three machines close to the boundary bus of concern. As can be seen there is a very good agreement between both sets of curves.

$\boldsymbol{Z}_{pm}$ is updated at every co-simulation iteration, and used to compute $\bar{\boldsymbol{E}}_{pm}$ according to (3.12).

The instantaneous frequency computation of the boundary currents can be done at every time step and every dynamic iteration. Note that the boundary current phasors are readily available, since they are needed to update the equivalent of the PM sub-system (see Fig. 3.23). Hence, the computation of the instantaneous frequencies of the boundary currents is made at negligible cost. The influence of this frequency update in the boundary conditions will be illustrated by test case 5 in Section 5.2.4.
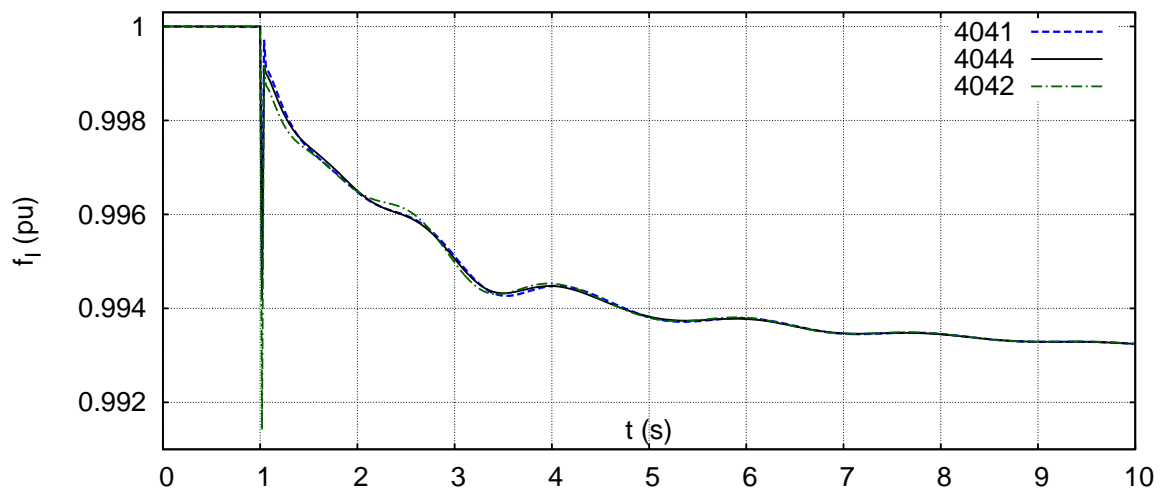
(a) Estimated frequencies of the currents at three boundary buses.
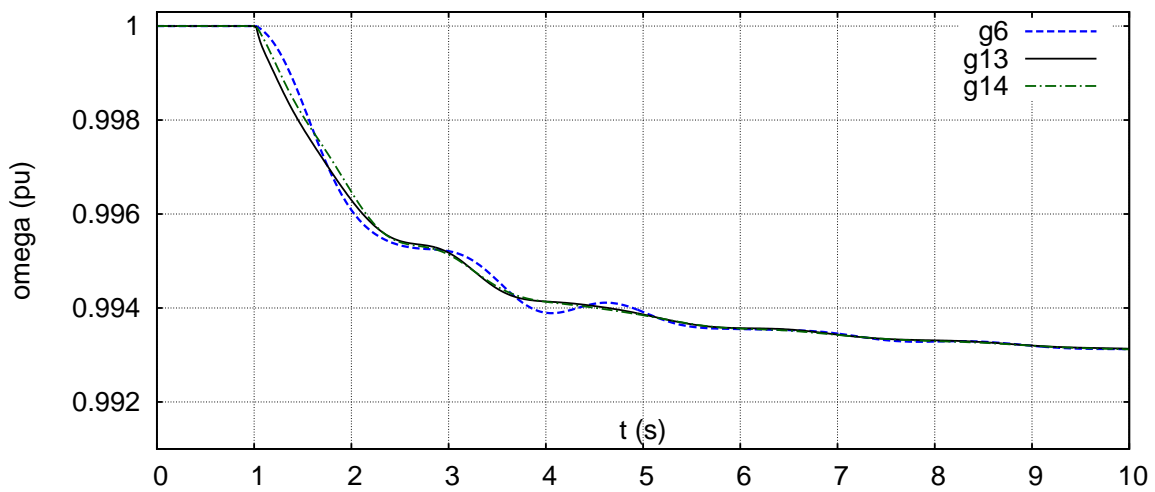
(b) Rotor speed of three machines located close to the boundary buses considered in the upper plot (a).

Figure 3.44: Case 5: Estimated frequencies and rotor speeds.

Interfacing phasor and electromagnetic transients models

The proposed relaxation algorithm, presented in the last chapter, is depicted in Figure 3.23. Details will be given in this Chapter concerning the implementation of the PM-to-EMT and EMT-to-PM conversion blocks.

The PM-to-EMT conversion, referred to as "*time interpolation*", is a simple (however nontrivial) operation. It consists in the interpolation of the Thévenin voltage source phasors. The literature about time interpolation in PM-EMT hybrid simulations is limited (maybe due to the fact that this topic is considered trivial) and non-comprehensive. The aspects of interpolation to be carefully considered, for an accurate and robust implementation, will be detailed in Section 4.1.

The reverse EMT-to-PM conversion, referred to as "*phasor extraction*", is more complex and there is an extensive literature about it. Existing and original phasor extraction techniques will be presented and compared in Section 4.2.

4.1 Passing from phasor to electromagnetic transient models

Some works about PM-EMT hybrid simulations, documented in [ZGW$^+$13, SCS05, SCSS05, SSCZ03, SRA98, RA88b], did not consider[1] any time interpolation of the PM sub-system equivalent, assuming a very small PM time step size H. In this case, the amplitude and phase angle variations over H of the voltages and currents relative to the PM sub-system can be assumed negligible. In some other works [FLCW06, SCS05], the authors observed discontinuities in the EMT boundary voltages and currents coming from the fact they did not interpolate the equivalent (Norton or Thévenin) of the PM sub-system. In some references (see for instance [vdMGvdM$^+$14, vHGK11, FLCW06]) the authors considered a time interpolation of the phase angles (or equivalently the frequency) but not of the amplitudes. In our opinion, the computational

---

[1]to our best understanding of the work presented in the cited references.

linear interpolation		References
phase angles	amplitudes	
-	-	[ZGW$^+$13, SCS05, SCSS05, SSCZ03, SRA98, RA88b]
✓	-	[vdMGvdM$^+$14, vHGK11, FLCW06]
✓	✓	[PAGV15, PAGV14, AF12, HTAA81]

Table 4.1: Classification of co-simulation publications according to the kind of PM sub-system equivalent interpolation.

procedure being simple, it is appropriate if not essential to interpolate both phase angles and RMS values of the phasors produced by PM simulation.

A linear interpolation of both amplitudes and phase angles was mentionned in [AF12, HTAA81]. However, the exact procedure was not described. Table 4.1 classifies references on PM-EMT co-simulation according to the kind of time interpolation performed. In this section, we explain and further extend what was presented in our references [PAGV15, PAGV14] about time interpolation of the first-order equivalent of the PM sub-system.

4.1.1 How to interpolate Thévenin voltage sources?

Let us consider an EMT simulation over the time interval $[t \quad t + H]$. The values of all states at time t have been computed and accepted; the ones at time $t + H$ are being computed. The most recent PM simulation provides the estimates $\bar{\mathbf{V}}^{k+\frac{1}{2}}(t+H)$ and $\bar{\mathbf{I}}^{k+\frac{1}{2}}(t+H)$ of the boundary voltages and currents (see Figure 3.23). The corresponding estimated Thévenin voltages are given by:

$$\bar{\mathbf{E}}_{pm}(t + H) = \bar{\mathbf{V}}^{k+\frac{1}{2}}(t + H) - \mathbf{Z}_{pm}\bar{\mathbf{I}}^{k+\frac{1}{2}}(t + H) \,. \tag{4.1}$$

A linear interpolation of respectively the magnitudes and the phase angles of $\bar{\mathbf{E}}_{th}$ is considered, as shown in Figure 4.1 for a chosen boundary bus. For simplicity of presentation, H is assumed to be a multiple of h, i.e. $H = \rho h$ where ρ is an integer. Thus, at the discrete time $t + mh$ ($m = 0, \ldots, \rho$), the interpolated Thévenin voltage magnitude is given by:

$$\left\| \bar{E}_{pm}(t + mh) \right\| = ||\bar{E}_{pm}(t)|| + \frac{m}{\rho} \left(||\bar{E}_{pm}(t + H)|| - ||\bar{E}_{pm}(t)|| \right) \,,$$

where $|| \; ||$ denotes the magnitude. The interpolated phase angles is given by:

$$\angle\bar{E}_{pm}(t + mh) = \angle\bar{E}_{pm}(t) + \frac{m}{\rho} \left(\angle\bar{E}_{pm}(t + H) - \angle\bar{E}_{pm}(t) \right) \,.$$

The discretized Thévenin voltage are obtained as ($m = 0, \ldots, \rho$):

$$e_a(t + mh) = \sqrt{2} \left\| \bar{E}_{pm}(t + mh) \right\| \cos\left(\omega_s(t + mh) + \angle\bar{E}_{pm}(t + mh) \right) \,,$$

$$e_b(t + mh) = \sqrt{2} \left\| \bar{E}_{pm}(t + mh) \right\| \cos\left(\omega_s(t + mh) + \angle\bar{E}_{pm}(t + mh) - \frac{2\pi}{3} \right) \,,$$

$$e_c(t + mh) = \sqrt{2} \left\| \bar{E}_{pm}(t + mh) \right\| \cos\left(\omega_s(t + mh) + \angle\bar{E}_{pm}(t + mh) - \frac{4\pi}{3} \right) \,,$$
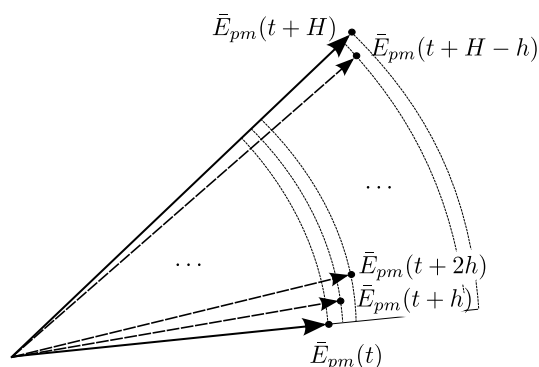
Figure 4.1: Interpolation of amplitude and phase of one Thévenin voltage phasor.

where ω_s is the nominal angular speed of the system.

Note that for the interpolation of phase angles, special care must be taken in order for angles to remain continuous when crossing the π value. Not managing this correctly would lead to a wrong PM-EMT co-simulation (with more frequent errors for the simulations stabilizing at an off-nominal frequency, leading to phase angles drifting continuously and to more frequent π value crossings).

For illustration purposes, an example of correct interpolation versus two wrong ones is shown in Figure 4.2. In this example, the cosine waveform $\cos(\omega_s t + \phi(t))$ is represented over three successive 20 ms time windows, thus spanning from 0 to 60 ms. The phase angle ϕ evolves linearly with time with a slope of $\pi/180$ rad/ms. The initial phase angle at $t = 0$ is $\phi_0 = 5\pi/6$ rad. The phase angle ϕ crosses the π value at $t = 30$ ms, in the second time window. An interpolation error occurs when a $\pm 2\pi$ jump is added to only one of the two phase angles being interpolated over a given time window. This leads to two possible errors, depending on whether the $\pm 2\pi$ jump is added at the start or at the end of the considered time window. In one case, the cosine will have double frequency over one fundamental period, while in the other case, a constant value will be observed, as represented in Figure 4.2.

4.1.2   How to handle discontinuities occurring in the EMT sub-system?

The simulation of large disturbances, typically faults, in the EMT sub-system calls for some comments. In such a case, the amplitude and phase of boundary voltages are expected to undergo a fast and significant change (although this can be somewhat attenuated by setting the PM-EMT boundary far enough from the fault location). This is represented, for what concerns the amplitude and for a single boundary bus, by the gray-shaded curve in Figure 4.3. The issue is whether a linear interpolation of the equivalent of the PM sub-system is sufficient to reproduce this fast change in the boundary voltages.

Three possibilities can be considered. Solution (a) in Figure 4.3 suggests to simply keep using linear interpolation the same way for the time window following an event, as we proposed in [PAGV14]. Figure 4.3 (b), suggested in [AF12], consists in using the latest computed value at time $t + H$. This is implemented by using the voltage $\bar{V}^{k+\frac{1}{2}}(t + H)$ over the whole time interval $[t, t + H]$
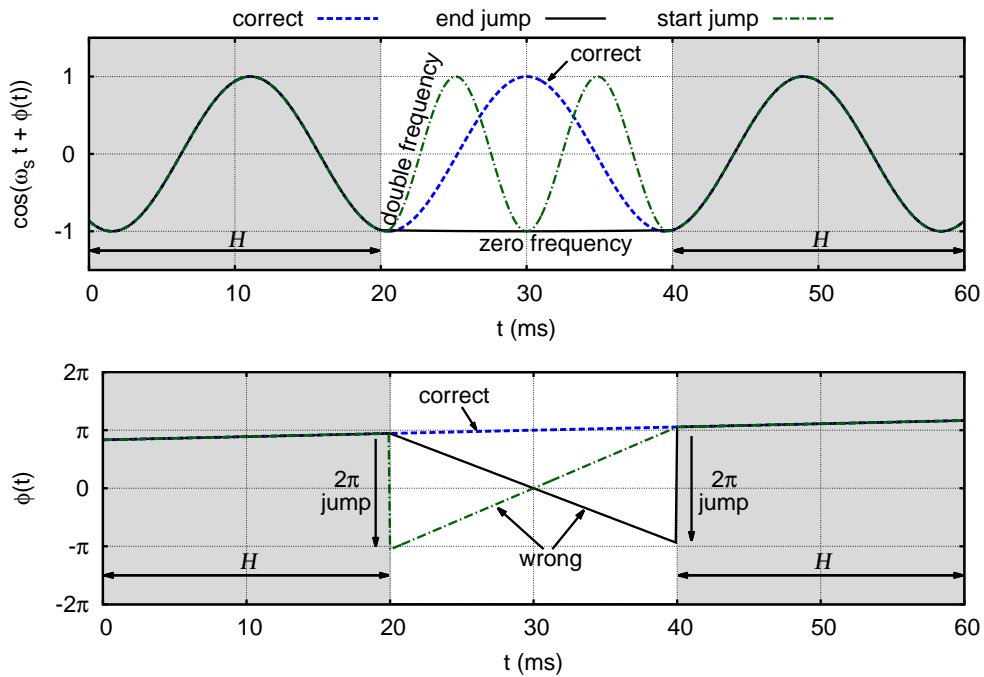
Figure 4.2: The correct versus some wrong phase angle interpolations when the phase angle crosses the π value.

to compute the Thévenin voltage source $\bar{E}_{pm}$. The third possibility, represented in Figure 4.3 (c), consists in performing a small time step right after the event. While it seems attractive, this solution is difficult to implement because it requires to extract the phasors of the disturbed signals over a very small time window (see Section 4.2).

Owing to the presence of the Thévenin impedance, the scheme of Figure 4.3 (a) gives good enough accuracy, as illustrated in Figure 4.4 showing the evolution of a boundary bus voltage in response to a three-cycle fault applied at $t = 1$ s and cleared at $t = 1.1$ s. It can be observed in Figure 4.4 that the use of a linearly interpolated Thévenin equivalent reproduces the sharp drop in the voltage evolutions from the EMT benchmark (see Figure 4.5). In the case of Figure 4.4, it was possible to use steps of 20 ms in the PM simulation, as shown by the curve labelled "Thévenin voltage magnitude $||\bar{E}_{pm}||$" in the figure. This case is similar to case 1, which will be presented in the next chapter (see Section 5.1.2).

Note that apart from the sharp drop, the high frequency transients for the periods following the fault inception and after the fault elimination are not perfectly reproduced by the PM-EMT co-simulation, compared to the EMT simulation. However this is not due to interpolation but rather to the fact that boundary impedance (used in the boundary conditions) is correct at fundamental frequency only. An improved implementation could use a more elaborated representation of the Thévenin impedance at the boundary to better represent it at high frequencies. Remark also that in general the variables of interest will not be located at the boundary bus since we decided to extend the boundary buses further away from the disturbance.
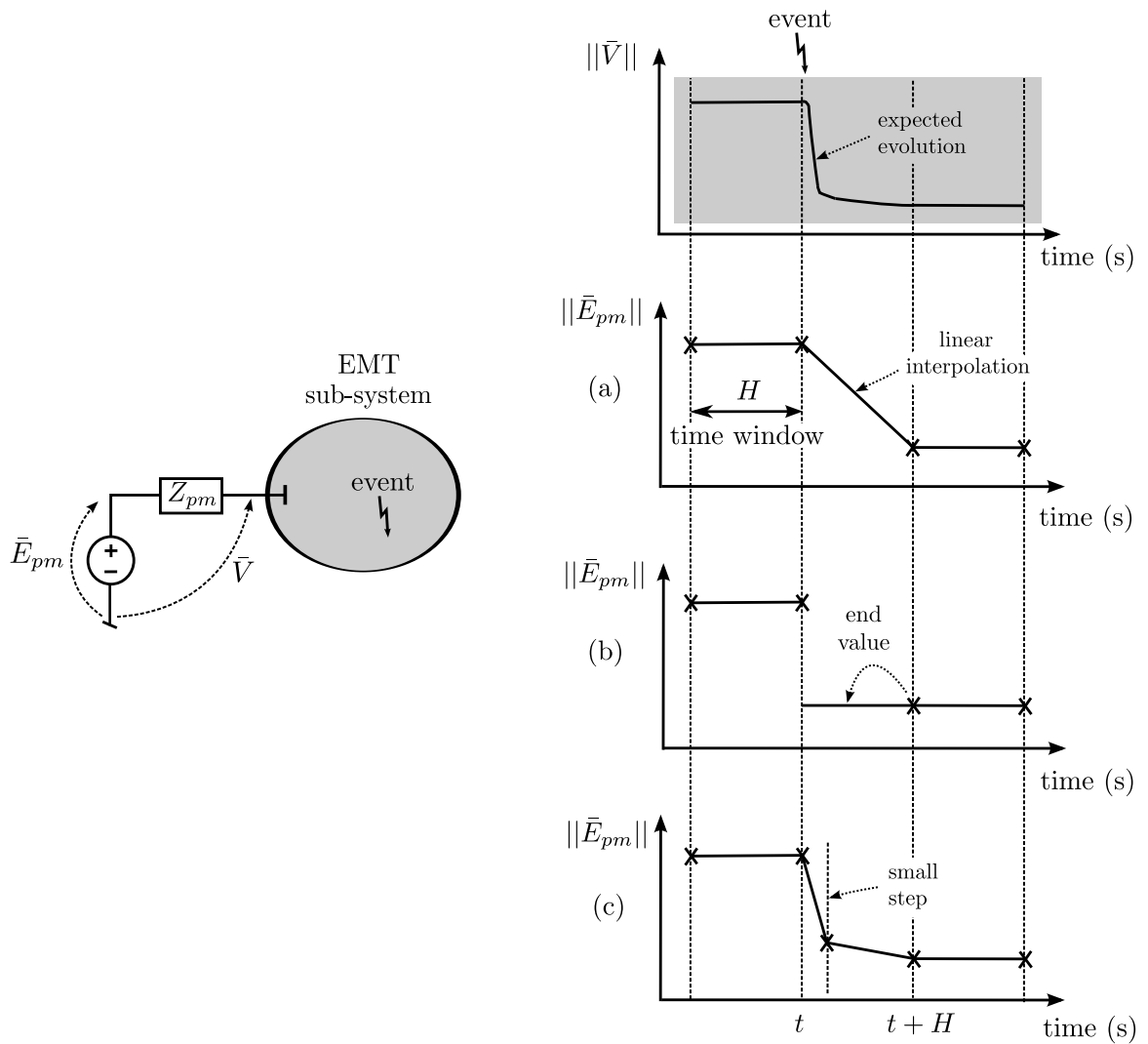
Figure 4.3: Grey-shade: Time evolution of the boundary voltage magnitude $||\bar{V}||$ right after a disturbance. (a)-(c): Interpolation of the Thévenin voltage source magnitude $||\bar{E}_{pm}||$: (a) linear interpolation (b) $||\bar{E}_{pm}||$ is set to the end value of the currently computed time window for its duration (c) small time step (e.g. 1 ms) performed right after the application of the discontinuity.
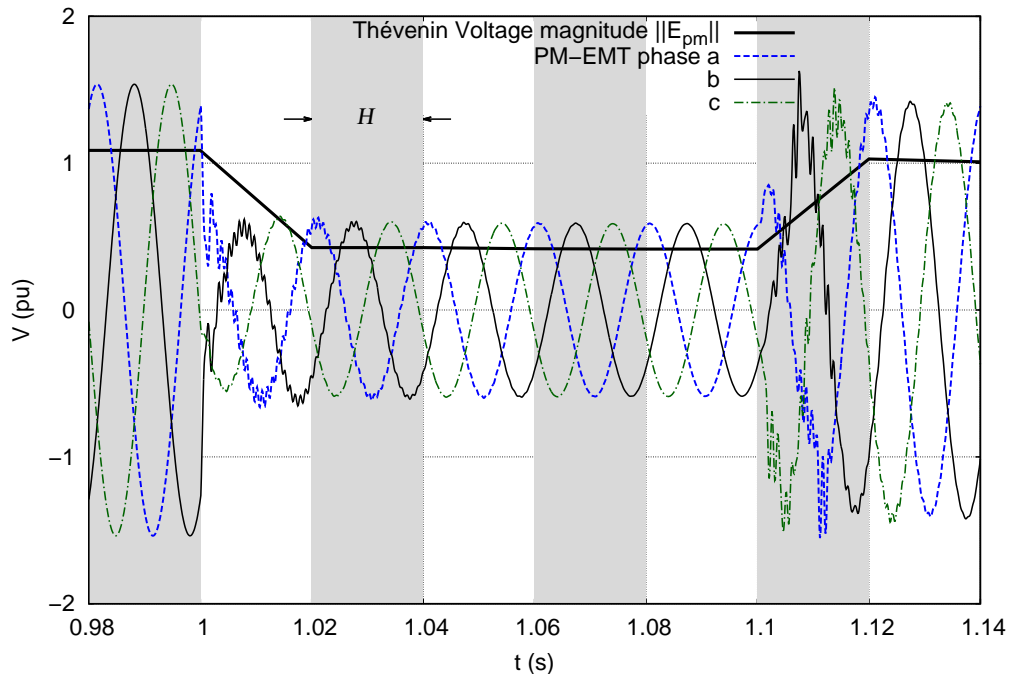
Figure 4.4: Example of evolution of voltage at boundary bus during a fault, when a linear interpolation of the Thévenin voltage source is used. (Case 1)
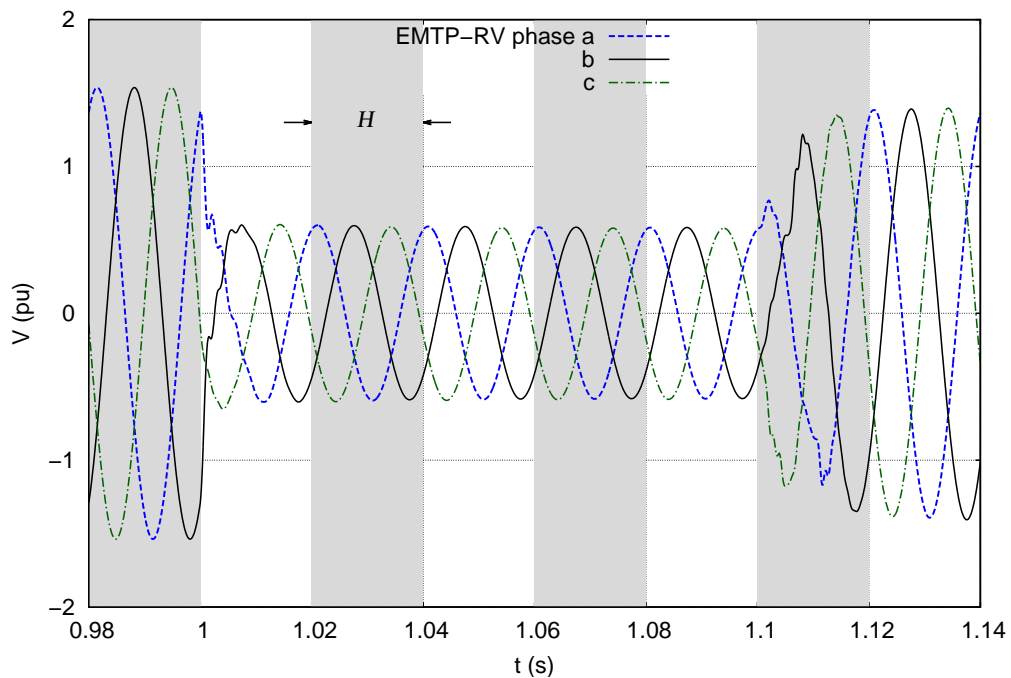
Figure 4.5: Case 1. EMT computed evolution of the three-phase voltages at the boundary bus.

4.2 Passing from electromagnetic transients to phasor models

The main characteristics of the needed phasor extraction method are depicted in Figure 4.6. The considered waveforms are quasi-sinusoidal, three-phase waveforms of the type (2.48), containing harmonics and decaying DC components. A time interval T_x for the extraction, approximately equal to one fundamental period T_s of the waveforms, is considered here. In case the PM time-step size H is bigger than T_x, the extraction methods presented in the following sections can be used as such. In the case where $H < T_x$, previous PM time steps have to be considered to perform the extraction (see Figure 4.7). Let us note that choosing H significantly smaller than T_s reduces the interest of performing PM-EMT co-simulation since it will increase the number of PM sub-system evaluations.

Another characteristic of the needed phasor extraction technique is that the phasor extraction process must give the value of the amplitude and phase of the positive-sequence component at a precise instant of time, without any delay.

The quantitative performance index for phasor extraction is the Total Vector Error (TVE) recommended by IEEE Std. C37. 118 [20111], the IEEE synchronized phasor measurement standard. The principle is shown in Figure 4.8. The TVE can be computed as
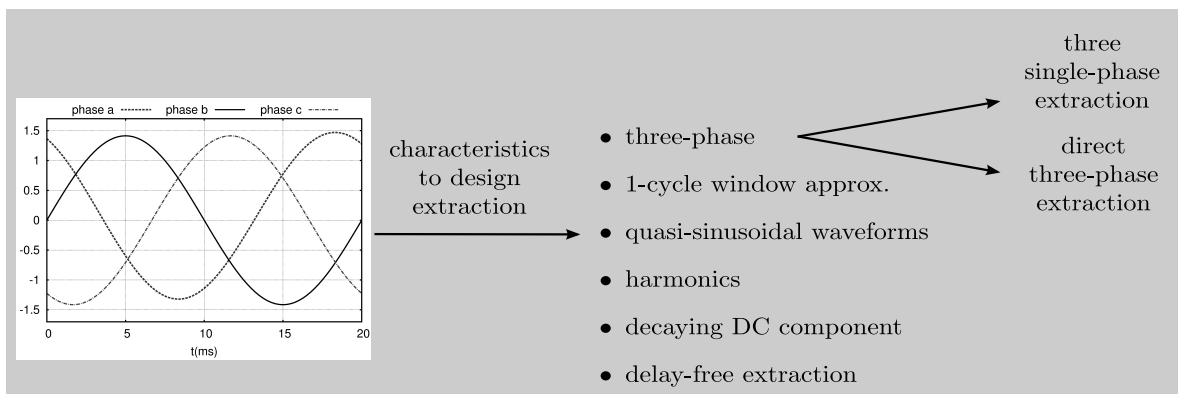
Figure 4.6: Characteristics of waveforms to which extraction is applied.
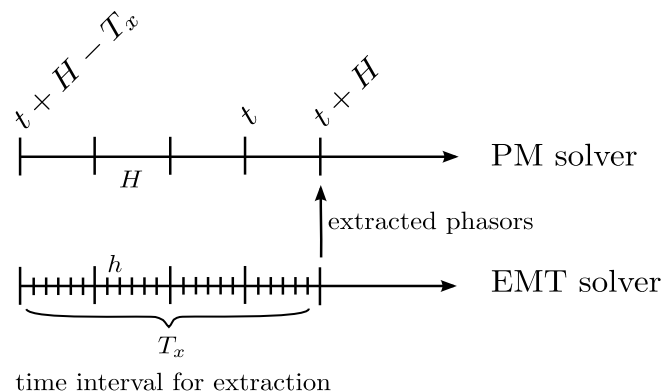
Figure 4.7: Extraction over several PM time steps.
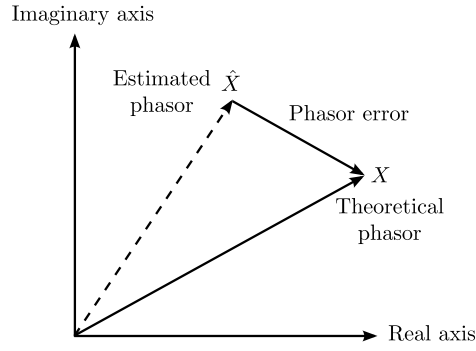
Figure 4.8: Principle of TVE.
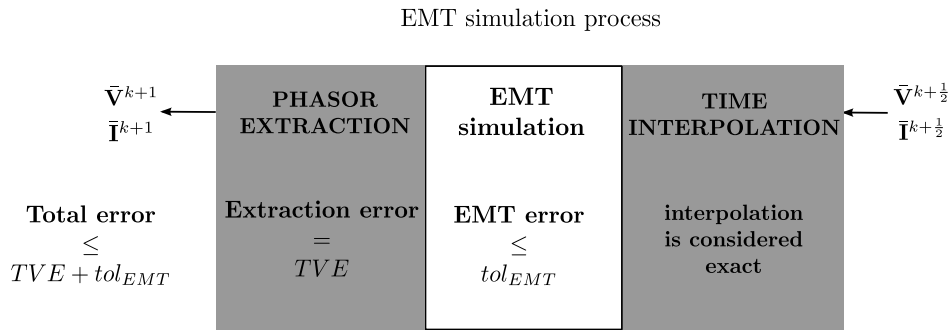
Figure 4.9: Precision of the EMT simulation with time interpolation and phasor extraction blocks.

$$TVE = \sqrt{\frac{\left(\hat{X}_R - X_R\right)^2 + \left(\hat{X}_I - X_I\right)^2}{X_R^2 + X_I^2}} \, ,$$

where $\hat{X}_R$, $\hat{X}_I$ are the real and imaginary parts of the estimated phasor, and X_R, X_I are the real and imaginary parts of the exact phasor. A small TVE value indicates better performance of phasor extraction. Figure 4.9 illustrates the precision of an EMT simulation, including the effect of time interpolation and phasor extraction. In order not to degrade the accuracy yielded by the EMT simulation itself, it is appropriate to have:

$$TVE \leq tol_{EMT} \, ,$$

in order the global error to be of the same order of magnitude as the precision of the EMT solution.

4.2.1   Literature review

Techniques for positive-sequence phasor extraction (referred here as "*extraction*") are numerous and used in many different fields. Some extraction methods have been developed for the needs of Phase-Locked Loops (PLL) [Gup75, HH96, Chu00]. Some others are used in Phasor Measurement Units [PBN11, PT08]. Extraction techniques have been also developed in other fields, such as for instance speech or signal processing.
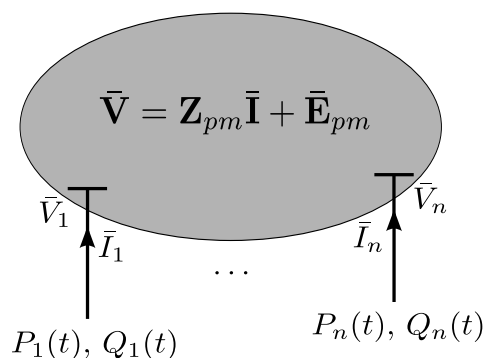
Figure 4.10: Active and reactive power injection in a n-port network.

Phase-locked loops are generally classified into single-phase or three-phase, depending on the device or grid type considered. First used in communication systems from the 1920s, PLLs have been applied since the 1970s in electronic applicances involving servomotors [Gup75]. More recently, PLLs have been used in three-phase inverters to synchronize the power electronic interfaces with the system voltage at the point of coupling. The PLL called Double-Decoupled Synchronous Reference Frame (DDSRF) PLL [RPB$^+$07], for instance, is a typical three-phase PLL.

Phasor measurement units were invented in 1988 by Arun Phadke and James Thorp. Their purpose is to synchronize with an absolute time reference, provided by the Global Positioning System (GPS), the real time phasor measurements.

Fast Fourier Transform using one-cycle running window has been used in many references [HV15, ZFA14, ZFLZ14, AF12, IAKW12]. While this technique is well known, easy to use and accurate, two major drawbacks need to be overcome. The first disadvantage of the method is the need to estimate the fundamental frequency of the signal of concern. A second drawback is the fact that the obtained phasor is an average over a one-cycle window rather that an instantaneous phasor value.

A technique based on instantaneous active and reactive powers estimation was proposed in reference [LGY09] and used in [ZGW$^+$13]. It consists in computing the instantaneous active and reactive powers at each boundary bus, as schematically represented in Figure 4.10. This gives $2n$ equations only, to determine $4n$ unknowns: the amplitudes and phase angles of the n boundary voltages and currents. To solve this, the method assumes the PM time step to be small (for instance smaller or equal to $2\,\mathrm{ms}$) compared to the transients of interest in PM simulation, which are roughly speaking in the frequency range of $0 \sim 5\,\mathrm{Hz}$ (period larger than $200\,\mathrm{ms}$), hence allowing to "freeze" the PM sub-system from one step to the next, assuming the boundary voltage phasors to be the same as the ones of the previous time step. In that case, only $2n$ unknowns remain: the amplitudes and phase angles of the n boundary currents. The assumption that the PM time step size is so small is not requested in our approach where H is generally chosen equal to one period at fundamental frequency. For instance $H = 20\,\mathrm{ms}$ allows tracking dynamics with a time constant of $0.1\,\mathrm{s}$. Of course it would possible to use smaller time steps in the PM solver to meet
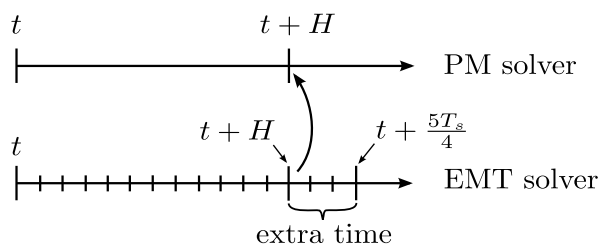
Figure 4.11: Additional simulation time needed for ASEO extraction.

the requirement of a very small H; however, the advantage of co-simulation would be partly lost.

An interesting and very accurate extraction method, called Angle-Shifted Energy Operator (ASEO), has been proposed in [JWW13]. This method is an adaptation of the so-called Teager Energy Operator [MKQ93b, MKQ93a], consisting of processing a longer time interval for the extraction to be more robust to noise. In PM-EMT coupled simulations, this would require to simulate the EMT sub-system over an additional time interval (typically one fourth of a fundamental period T_s), as sketched in Figure 4.11. For that reason, this method was not further considered since an extended simulation time interval means an additional computing cost and a higher implementation complexity.

In the following two sections, we will focus in particular on two methods. The first one, presented in Section 4.2.2, consists in a Projection on Synchronously Rotating Axes (PSRA). The second technique, developed in Section 4.2.3, is the least-squares curve-fitting and was used in many references [vdMGvdM$^+$14, Lou14, vHGK11, zLxHT$^+$11, FLCW06, SCS05, SCSS05, SSCZ03, CS$^+$02, SRA98, RA88a]. We will propose some modifications to extend the range of applications of least-squares fitting.

4.2.2 Projection on synchronously rotating axes

As shown in Figure 3.23, the phasor extraction follows the EMT simulation and aims at providing the updated estimates $\left(\bar{V}^{k+1}, \bar{I}^{k+1}\right)$ of the boundary voltages and currents. The positive-sequence phasor of each current and voltage is extracted.

The phasor extraction considered in this work consists of three steps: (i) projection on synchronously rotating axes [PGV13], (ii) post-processing using a low-pass filter, and (iii) scaling of the boundary currents.

4.2.2.1 Positive-sequence extraction

The amplitude and the phase angle of the positive-sequence component of the currents are computed from the three time-varying current waveforms by projecting the latter on (x, y) reference axes[2], using a Park-type transform. This technique, inspired of the principle of PLL systems [Chu00], is free from any delay associated with processing of the current waveforms.

---

[2]often referred to as (d, q) axes, particularly in the case of synchronous machines.
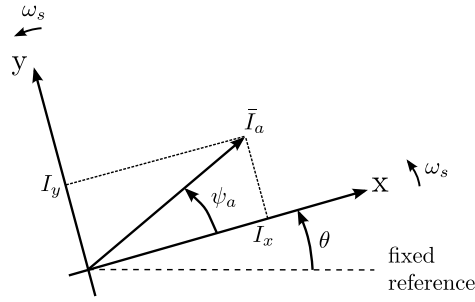
Figure 4.12: Reference axes and phasors involved in the extraction of the positive-sequence component of a boundary current.

More precisely, (x, y) are the orthogonal axes used in the PM simulation to project the rotating vectors associated with quasi-sinusoidal variables, and obtain their corresponding rectangular components. As shown in Figure 4.12, these axes rotate at the nominal angular speed ω_s and, at time t, the x axis is at an angular position

$$\theta = \omega_s t \tag{4.2}$$

with respect to a fixed reference, where the position of the x-axis at $t = 0$ has been arbitrarily set to zero.

The current waveforms to process can be written as:

$$\mathbf{i}_{abc} = \begin{bmatrix} i_a \\ i_b \\ i_c \end{bmatrix} = \begin{bmatrix} \sqrt{2}I_a \cos\left(\omega_s t + \psi_a\right) + \epsilon_a \\ \sqrt{2}I_a \cos\left(\omega_s t + \psi_a - \frac{2\pi}{3}\right) + \epsilon_b \\ \sqrt{2}I_a \cos\left(\omega_s t + \psi_a - \frac{4\pi}{3}\right) + \epsilon_c \end{bmatrix}, \tag{4.3}$$

where ϵ_a, ϵ_b and ϵ_c are noise terms accounting for deviations with respect to three-phase, balanced, positive-sequence components. The current in $\mathbf{i}_{abc}$ are projected on the above mentioned axes by applying the linear transform [Paa00]:

$$\mathbf{i}_{0xy} = \mathbf{T}\,\mathbf{i}_{abc} \tag{4.4}$$

with:

$$\mathbf{T} = \frac{\sqrt{2}}{3} \begin{bmatrix} 1/\sqrt{2} & 1/\sqrt{2} & 1/\sqrt{2} \\ \cos\left(\theta\right) & \cos\left(\theta - \frac{2\pi}{3}\right) & \cos\left(\theta - \frac{4\pi}{3}\right) \\ -\sin\left(\theta\right) & -\sin\left(\theta - \frac{2\pi}{3}\right) & -\sin\left(\theta - \frac{4\pi}{3}\right) \end{bmatrix}. \tag{4.5}$$

In the ideal case where the three currents make up a balanced, positive sequence, i.e. $\epsilon_a = \epsilon_b = \epsilon_c = 0$, the projected currents are easily obtained as:

$$\mathbf{i}_{0xy} = \begin{bmatrix} i_0 \\ i_x \\ i_y \end{bmatrix} = \begin{bmatrix} 0 \\ I_a \cos\psi_a \\ I_a \sin\psi_a \end{bmatrix} \tag{4.6}$$
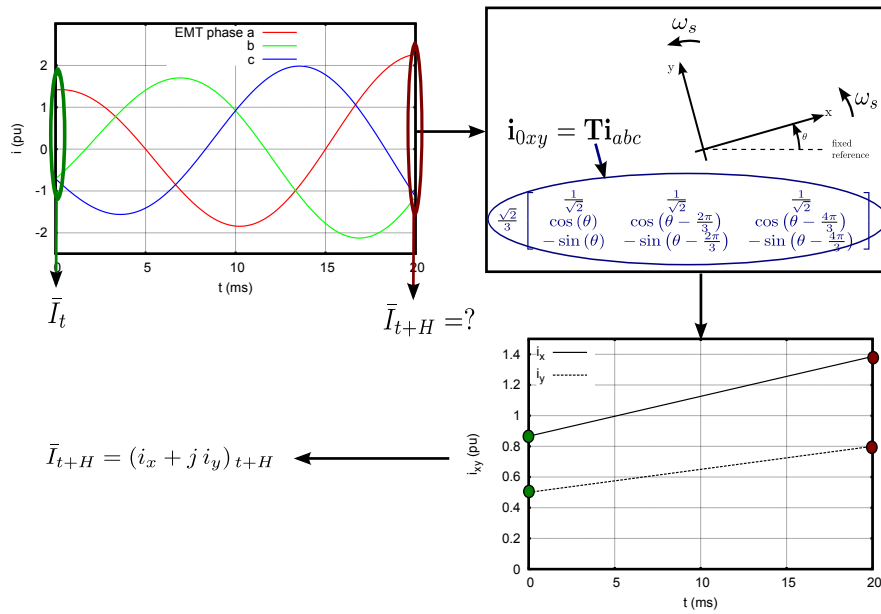
Figure 4.13: Summary of the phasor extraction method.

The last two components are the projections on x and y of a vector rotating at angular speed ω_s, representing the current in phase a, having an amplitude I_a and a phase angle ψ_a with respect to the x axis (see Figure 4.12). Its magnitude and phase angle are easily obtained as:

$$I_a = \sqrt{i_x^2 + i_y^2}, \tag{4.7}$$

$$\psi_a = \arctan\left(\frac{i_y}{i_x}\right). \tag{4.8}$$

At this point of the procedure, equations (4.4)-(4.5) are applied only to the currents $\mathbf{i}_{abc}$ obtained at time $t + H$ of the EMT simulation.

The procedure can be summarized as shown in Figure 4.13.

4.2.2.2   Negative-sequence, DC and harmonics cancellation

Low-pass filtering   Because the effects of a fault located in the EMT sub-system are expected to be still felt at the boundary between PM and EMT sub-systems, the boundary current waveforms contain noise terms. The latter stem from aperiodic, negative- and zero-sequence components, as well as harmonics, whose effect must be filtered out.

While three-phase, balanced, positive-sequence currents are converted into constant i_x and i_y, aperiodic (resp. negative-sequence) components present in the phase currents will be transformed into sinusoidal components at nominal (resp. double nominal) frequency. Thus, the filter must:

- preserve the amplitude of components with frequencies between 0 and 5 Hz. This covers the frequency spectrum of concern in PM simulation;
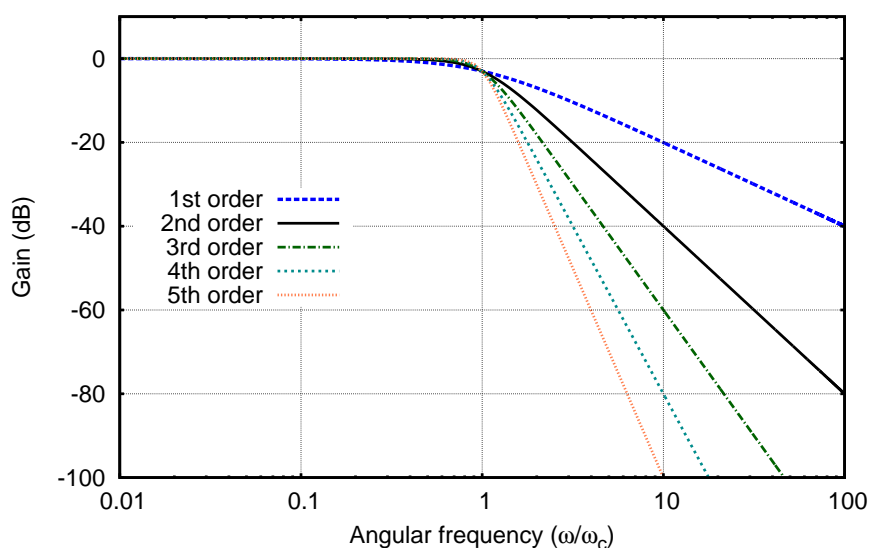
Figure 4.14: Magnitude response of Butterworth filter.

- filter out the fundamental-frequency, double-fundamental-frequency and higher frequency components;

- not affect the phase of the initial signal in the $[0\ 5]$ Hz frequency range, to avoid introducing any delay between the EMT and PM simulations.

This low-pass numerical filter processes sampled i_x and i_y values obtained by applying (4.4) at equidistant discrete times in $[t + H - T_x \quad t + H]$. The sampling period can be h, the small time step size used in EMT simulation. Re-sampling may be necessary in case the discrete times of the EMT simulation are not equidistant, for instance because it was necessary to reduce the time step size during the simulation. The width T_x of the time interval processed by the filter is usually no smaller than one half cycle at nominal frequency, and most often closer to one cycle. It may be occasionally reduced, for instance at fault application and clearing. The time interval processed by the filter should not become too narrow, for accuracy reasons.

Satisfactory results have been obtained with a Butterworth low-pass filter [But30]. In its continuous-time version, the magnitude-squared transfer function takes on the form:

$$\left\| H_c\left(j\omega\right) \right\|^2 = \frac{1}{1 + \left(j\omega/j\omega_c\right)^{2N}}, \tag{4.9}$$

where ω_c is the cutoff frequency. This filter is characterized by a magnitude response maximally flat in the passband. This means that the first $2N - 1$ derivatives of the function (4.9) are zero at $\omega = 0$ [OS89]. For instance, the magnitude response of Butterworth filters of orders 1 to 5 are shown in Figure 4.14.

However, the phase response must also be considered. As shown in Figure 4.15, the filter introduces a non-negligible phase shift in the pass-band, which in turn creates group and phase delay.
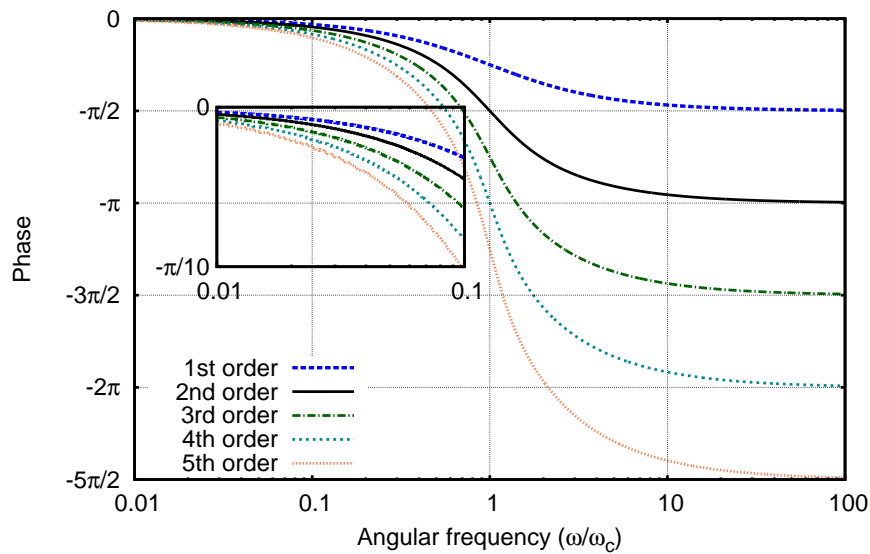
Figure 4.15: Phase response of Butterworth filter.

Group and phase delay are precisely what we want to avoid. Consider a linear time-invariant filter with transfer function $H(s)$, driven by the following quasi-sinusoidal signal:

$$x(t) = a(t) \cos(\omega t + \phi(t)),$$

where $a(t)$ and $\phi(t)$ are the slowly varying amplitudes and phase angles. The output of the filter is approximated by:

$$y(t) = |H(j\omega)| \, a(t - \tau_g) \cos(\omega(t - \tau_\phi) + \phi(t)),$$

where τ_g is the group delay, representing the shift in time of the amplitude a, and τ_ϕ is the phase delay.

For a filter with transfer function $H(s)$ the group delay τ_g and the phase delay τ_ϕ can be computed as follows from the phase angle $\phi(\omega)$ of $H(j\omega)$:

$$
\begin{aligned}
\tau_g(\omega) &= -\frac{d\phi(\omega)}{d\omega}, \\
\tau_\phi(\omega) &= -\frac{\phi(\omega)}{\omega}.
\end{aligned}
$$

The filter is applied twice, once with increasing and once with decreasing times. Doing so should almost cancel the phase shift introduced by the filter in the pass-band. The order of the filter has been taken to two. However, applying the filter twice yields globally a fourth-order filter, which is expected to give sufficient cut-off band attenuation for most systems.

The procedure can be summarized as shown in Figure 4.16.
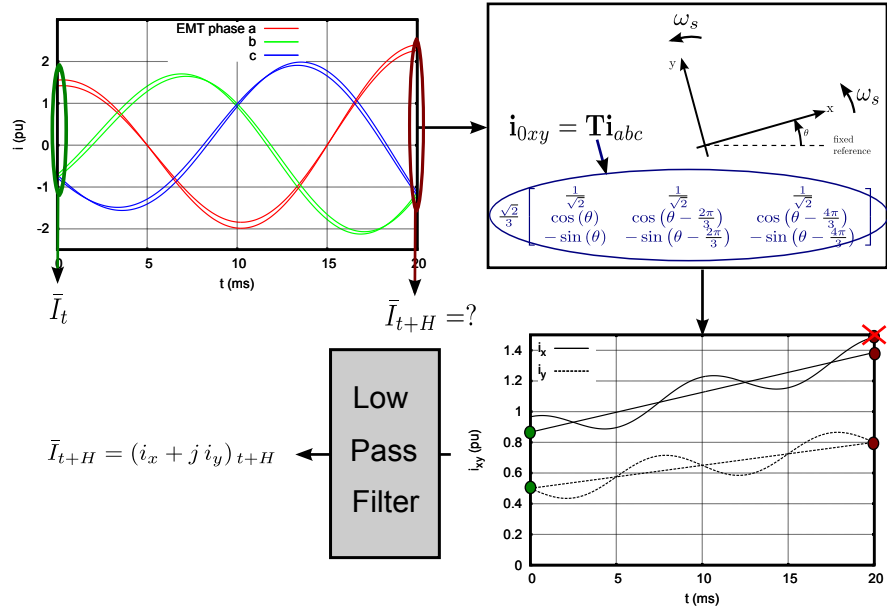
Figure 4.16: Summary of the phasor extraction method with a smoother.

4.2.2.3   Scaling of the boundary currents

The three-phase instantaneous power at a boundary bus is given by:

$$p(t) = v_a(t)i_a(t) + v_b(t)i_b(t) + v_c(t)i_c(t), \tag{4.10}$$

where (v_a, v_b, v_c) are the phase-to-ground voltages, and (i_a, i_b, i_c) the phase currents. If the currents were perfectly three-phase balanced, at fundamental frequency only, the above power would be equal to the three-phase active power given by:

$$P = 3\, real\left(\bar{V}_a \bar{I}_a^*\right), \tag{4.11}$$

where $\bar{V}_a$ and $\bar{I}_a$ are the extracted voltage and current phasors in phase a, and * denotes the complex conjugate.

A comparison between the above two powers can serve as a measure of quality of the phasor extraction. In practice, since $p(t)$ is affected by noise, as previously explained, the same Butterworth filter is applied to the sampled values of p to obtain the filtered value $\bar{p}(t+H)$ at time $t+H$. The quality index is the relative discrepancy:

$$J(t+H) = \left|\frac{\bar{p}(t+H) - P(t+H)}{\bar{p}(t+H)}\right|, \tag{4.12}$$

where $P(t+H)$ is computed from Eq. (4.11) using the phasors relative to time $t+H$.

Furthermore, the ratio between $\bar{p}(t+H)$ and $P(t+H)$ can be used to scale the extracted current, with the objective of having the same active power transfer seen from both sides of the boundary. The magnitude I_a of the previously extracted current is corrected into I_a^{cor} according to:

$$\frac{I_a^{cor}}{I_a} = \frac{\bar{p}(t+H)}{P(t+H)}. \tag{4.13}$$

4.2.3   Least-squares curve-fitting

4.2.3.1   Principle

An alternative extraction method consists in performing least-squares curve-fitting of the three signals of which we want to determine the positive-sequence component. Given the computed signals $x(k)$ over the interval $[0 \; k_{max}]$, the objective is to find the corresponding set of parameters Γ minimizing the following expression over the given interval $[0 \; k_{max}]$:

$$\varepsilon = \sum_{k=1}^{k_{max}} \left\{ x(k) - f(k, \Gamma) \right\}^2 \; , \tag{4.14}$$

where $k = 0, \ldots, k_{max}$ is used to index the samples ($k_{max} = f_s T_x$, where f_s is the sampling frequency).

From the set of parameters Γ we will be able to determine the effective value $A(t + H)$ and the phase angle $\phi(t + H)$ of the fitted (pseudo-)sinusoidal signal, of the type $A(t) \cos(\omega_s t + \phi(t))$, at time $t + H$, i.e. at the end of the EMT simulation interval. Note that the procedure is going to be applied to each of the three phases separately. This yields the effective values $A_a(t + H)$, $A_b(t + H)$ and $A_c(t + H)$ as well as the phase angles $\phi_a(t + H)$, $\phi_b(t + H)$ and $\phi_c(t + H)$.

The positive, negative and zero-sequence values at $t + H$ are then obtained as:

$$\begin{bmatrix} S_{pos} \\ S_{neg} \\ S_{zero} \end{bmatrix} = \frac{1}{3} \begin{bmatrix} 1 & a & a^2 \\ 1 & a^2 & a \\ 1 & 1 & 1 \end{bmatrix} \begin{bmatrix} \dfrac{A_a(t + H)}{\sqrt{2}} e^{j\phi_a(t+H)} \\ \dfrac{A_b(t + H)}{\sqrt{2}} e^{j\phi_b(t+H)} \\ \dfrac{A_c(t + H)}{\sqrt{2}} e^{j\phi_c(t+H)} \end{bmatrix} \quad , \; where \; a = e^{j\frac{2\pi}{3}}.$$

4.2.3.2   Choice of the curve f to fit the data

Several choices are possible for the function f in (4.14) to fit the sampled values coming from EMT simulation. In this section, we consider four possible choices, by increasing order of complexity.

In the literature about hybrid PM-EMT simulations, the choice is most generally oriented towards a cosine waveform f_1 characterized by a constant amplitude and a constant phase angle , which are the parameters to be determined. Thus, this choice consists in using a cosine waveform to fit data samples coming from a quasi-cosine waveform, i.e. to find the closest constant amplitude and phase angle to fit over the time interval $[t + H - T_x \; t + H]$ a waveform characterized by slowly varying amplitude and phase angle. The amplitude and the phase angle obtained will be mean values over $[t + H - T_x \; t + H]$. Assuming linearly varying amplitude and phase angle, the mean values determined by the optimization process can be assigned to the middle of the time interval, i.e. to $t + H - T_x/2$. An additional step is then necessary to estimate the phasor at time $t + H$. We have not found in the literature a description of this additional step; we use a linear extrapolation relying on the previously extracted phasor values.

Furthermore we have treated several extensions of the above fitting by choosing:
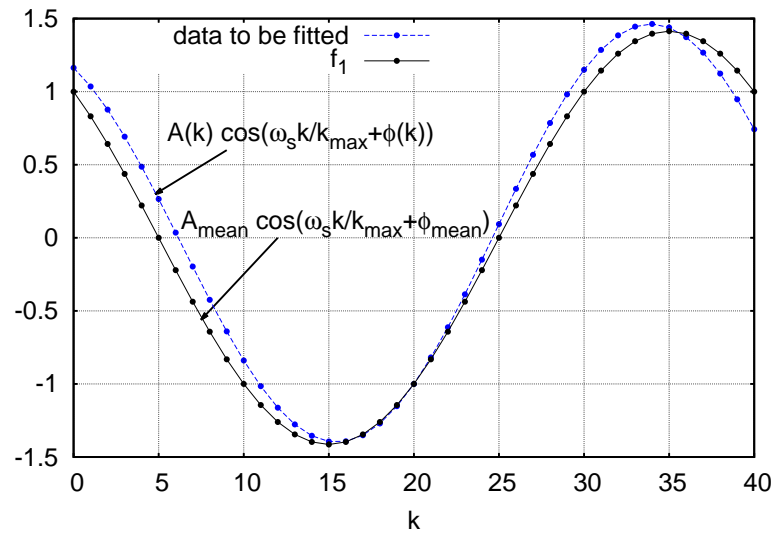
Figure 4.17: Fitting a quasi-cosine wave with a pure cos.

- $f = f_2$: a quasi-cosine waveform, whose amplitude and phase angle are linearly varying with time,

- $f = f_3$: a quasi-cosine waveform of the type f_2, with the addition of a linearly varying DC component,

- $f = f_4$: a quasi-cosine waveform of the type f_2, with the addition of an exponentially decaying DC component.

Fitting a cosine waveform with constant amplitude and phase angle The following function is used for the least squares curve-fitting:

$$f_1\left(k,\ A_{mean},\ \phi_{mean}\right) \quad = \quad A_{mean}\cos\left(\omega_s\frac{k}{k_{max}}H + \phi_{mean}\right). \tag{4.15}$$

The optimization provides the values of A_{mean} and ϕ_{mean} which best fit the sampled points over the interval $[t + H - T_x\ t + H]$.

By way of example, Figure 4.17 illustrates the fitting of the quasi-cosine wave f_1 to points obtained in fact by sampling the (unknown) signal:

$$x\left(t\right) = A\left(t\right)\cos\left(\omega_s t + \phi\left(t\right)\right),$$

where the amplitude $A\left(t\right)$ was varied linearly from $A\left(t\right) = 0.95 \cdot \sqrt{2}$ to $A\left(t + H\right) = 1.05 \cdot \sqrt{2}$ and the phase angle $\phi\left(t\right)$ was varied linearly from $\phi\left(t\right) = \pi/6$ to $\phi\left(t + H\right) = 2\pi/6$. After the least squares fitting, the values obtained are $A_{mean} = 1$ and $\phi_{mean} = \pi/4$ as expected. This example shows some limitation of using function f_1 which is not very accurate.

Knowing the value $A\left(t + H - T_x\right)$ and $\phi\left(t + H - T_x\right)$ at time $t + H - T_x$, the values at time $t + H$ are determined by linear extrapolation according to:

$$A_{t+H} = A_{t+H-T_x} + 2\left(A_{mean} - A_{t+H-T_x}\right), \tag{4.16}$$

$$\phi_{t+H} = \phi_{t+H-T_x} + 2\left(_{mean} - \phi_{t+H-T_x}\right). \tag{4.17}$$

Fitting a quasi-cosine waveform with linearly varying amplitude and phase angle   To improve the accuracy obtained with the f_1 function, let us try now:

$$f_2\left(k,\ A_1,\ \phi_1\right) = \left(A_0 + \frac{\left(A_1 - A_0\right)k}{k_{max}}\right)\cos\left(\omega_s\frac{k}{k_{max}}H + \phi_0 + \frac{\left(\phi_1 - \phi_0\right)k}{k_{max}}\right), \tag{4.18}$$

where $(A_0,\ \phi_0)$ are the amplitude and phase angle, respectively, at time $t + H - T_x$, and similarly for $(A_1,\ \phi_1)$ at time $t + H$. The values of $(A_0,\ \phi_0)$ can be retrieved from the fitting performed over the previous time window, or can be added to the unknowns of the least-squares optimization.

Fitting a quasi-cosine waveform including a linearly varying DC component   This corresponds to:

$$f_3\left(k,\ A_1,\ \phi_1,\ DC_1\right) = \left(A_0 + \frac{\left(A_1 - A_0\right)k}{k_{max}}\right)\cos\left(\omega_s\frac{k}{k_{max}}H + \phi_0 + \frac{\left(\phi_1 - \phi_0\right)k}{k_{max}}\right)$$
$$+ \left(DC_0 + \frac{\left(DC_1 - DC_0\right)k}{k_{max}}\right), \tag{4.19}$$

where the parameters $(A_0,\ \phi_0,\ DC_0)$ are the amplitude, the phase angle and the offset, respectively, at time $t + H - T_x$, and similarly for $(A_1,\ \phi_1,\ DC_1)$ at time $t + H$. Again, the parameters $(A_0,\ \phi_0,\ DC_0)$ can be retrieved from the optimization performed at the previous time window, or can be included as variables of the new optimization.

Fitting a quasi-cosine waveform including an exponentially decaying DC component   This corresponds to:

$$f_4\left(k,\ A_1,\ \phi_1,\ DC,\ \tau\right) = \left(A_0 + \frac{\left(A_1 - A_0\right)k}{k_{max}}\right)\cos\left(\omega_s\frac{k}{k_{max}}H + \phi_0 + \frac{\left(\phi_1 - \phi_0\right)k}{k_{max}}\right)$$
$$+ \left(DC\ \exp\left(-\frac{kH}{k_{max}\tau}\right)\right), \tag{4.20}$$

where the parameters $(A_0,\ \phi_0)$ are the amplitude and phase angle respectively, at time $t + H - T_x$, and similarly for $(A_1,\ \phi_1)$ at time $t + H$. Again, the parameters $(A_0,\ \phi_0)$ can be used from the optimization performed at the previous time window, or can be computed into a new optimization process.
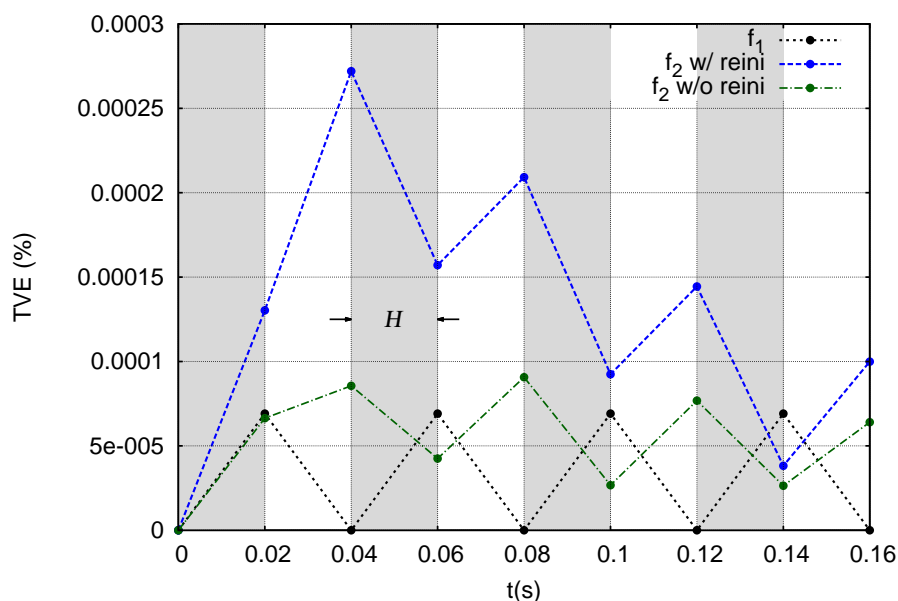
Figure 4.18: Exact amplitude and phase angle.

4.2.4 Numerical Tests

4.2.4.1 Influence of precision of the extracted values at the last time step on the newly extracted phasors

Amongst extraction methods, some techniques rely on the phasors extracted at previous time steps for the estimation of phasors at time $t + H$, as mentionned in Section 4.2.3.2. Such techniques include Fourier transform, least-squares fitting f_1, and least-squares fitting f_2, f_3 and f_4 (when parameters (A_0, ϕ_0) are not computed in the new optimization process). Equations (4.16) and (4.17) can be used to compute the phasors at time $t + H$. We examine in this section the propagation of an error in the phasors at a given time step.

For simplicity, let us choose a time step H and a time interval for extraction T_x both equal to one fundamental period T_s of the signal:

$$T_x = H = T_s \,,$$

where $T_s = 20$ ms will been assumed. In general, for the extraction of the phasors to be computed at time $t + H$, the previously extracted phasor (at time t) is assumed to be accurate. However, we have to examine the case where the previous phasors contain some errors.

Exact initial amplitudes and phase angles The Total Vector Error obtained when the initial amplitude and phase angle are exact are shown in Figure 4.18. A high accuracy is obtained for f_1 as well as for f_2. In this figure, "f_2 w/ reini" refers to the case where (A_0, ϕ_0) have been added to the unknowns of the least-squares optimization. On the contrary, "f_2 w/o reini" refers to the case where (A_0, ϕ_0) are assumed to be given by the extraction at the last time step.
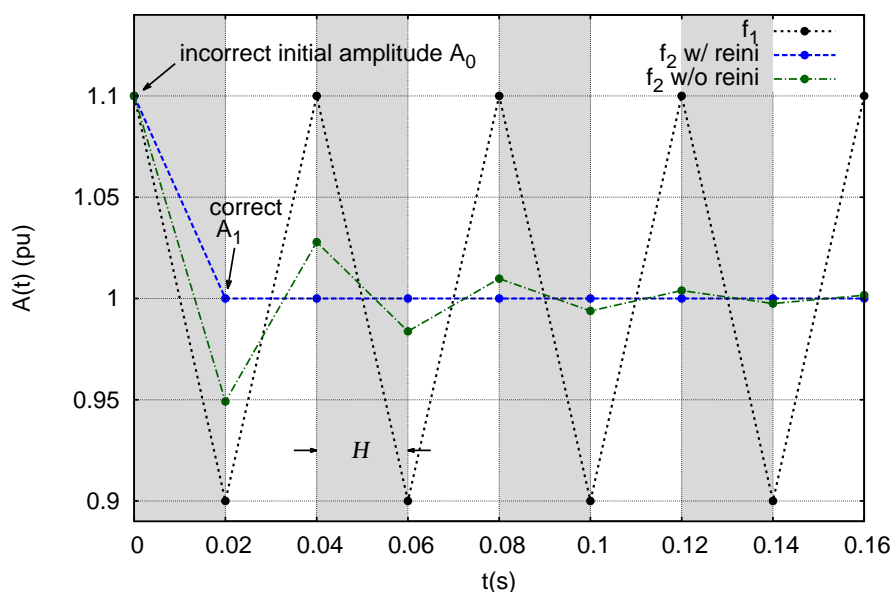
Figure 4.19: Oscillations observed with curve fitting methods with wrong initial value of amplitude.

Inexact initial amplitudes and phase angles   Figure 4.19 shows the extracted amplitude of a constant amplitude cosine signal over several successive $20-$ms time interval starting from a wrong initial value, characterized by a 10 percents error on the amplitude. It is observed that a simple cosine curve-fitting with f_1 cannot resolve the initial mistake, while quasi-cosine curve-fitting f_2 based on previous phasors ("f_2 w/o reini") is impacted by the mistake for a couple of periods only. The proposed quasi-cosine f_2 curve-fitting including (A_0, ϕ_0) in the unknowns of the least-squares optimization (i.e. "f_2 w/ reini") directly gives the correct extracted phasor from the time interval. From the results shown in Figure 4.20 the same conclusions can be drawn when the initial phase angle extracted value was mistaken by 10 percents.
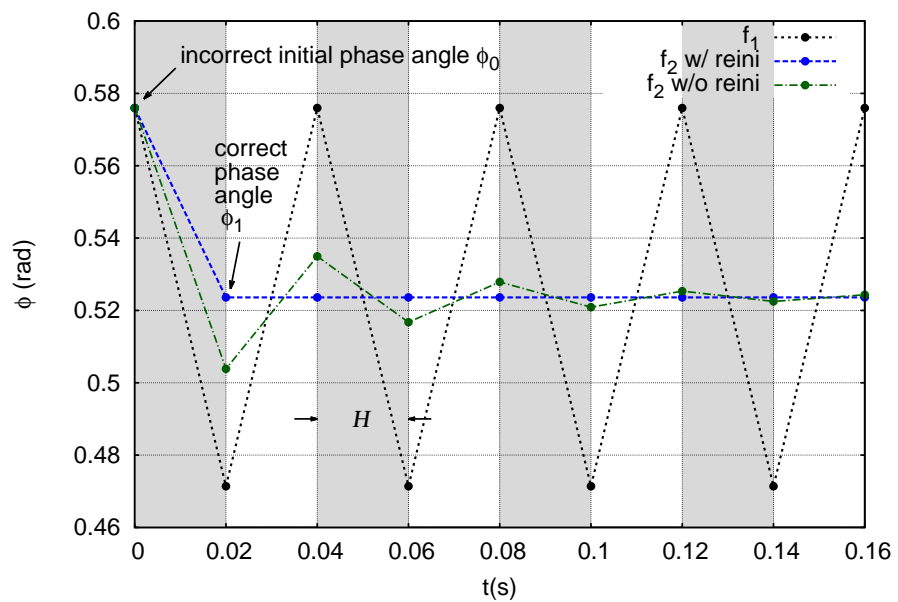
Figure 4.20: Oscillations observed with curve fitting methods with wrong initial value of phase angle.
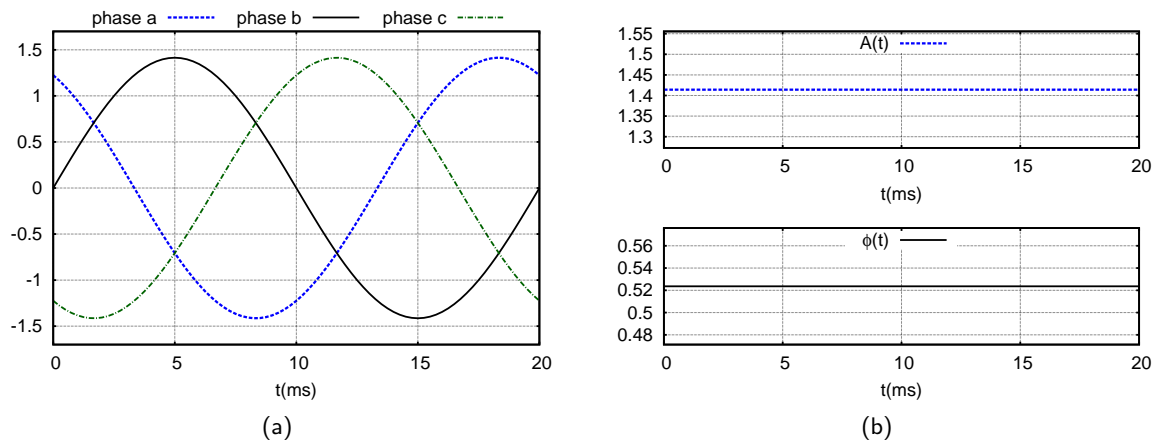
Figure 4.21: Waveforms a. Constant amplitudes and phase angles.

4.2.4.2 Test waveforms

Eight three-phase waveforms (type-a to type-g) have been generated to test and compare the PSRA and the curve-fitting extraction techniques presented in Sections 4.2.2 and 4.2.3 respectively. They were chosen as follows.

a. Constant amplitudes and phase angles The signals merely consist of three-phase positive-sequence cosine waveforms with a constant amplitude and phase angle. The amplitude of every cosine wave is $A = \sqrt{2}$ and the phase angle of phase a at $t = 0$ is $\phi_0 = \pi/6$. Figure 4.21.a shows the corresponding three-phase abc time evolutions. Figure 4.21.a has been obtained by making a PSRA without filtering. It shows the evolution of the amplitude $A(t)$ and the phase angle $\phi(t)$ of the projection, given by (4.7) and (4.8) respectively, before any filtering. In the case of constant amplitudes and phase angles, the PSRA simply gives a constant amplitude and phase angle, equal to the ones assigned to each cosine wave.

b. Linear change in amplitude For waveforms of type b, the phase angle of phase a is kept constant to the value $\phi_0 = \pi/6$ over the time window of interest and the amplitudes of the cosine waves are linearly increased by 10 percent over the time window, i.e. from $A = \sqrt{2}$ to $A = 1.1\sqrt{2}$. The three-phase abc time evolutions for these type-b waveforms are presented in Figures 4.22.a, while the amplitude and phase angle of 4.22.b result from the PSRA. Figure 4.22 shows that the initial amplitude change is correctly retrieved by PSRA technique in this case.

c. Linear change in phase angle Waveforms of type c are characterized by a constant amplitude of every cosine wave $(A = \sqrt{2})$. On the other hand, the phase angle of phase a is linearly increased from $\phi_0 = \pi/6$ to $\phi_0 = 2\pi/6$ over the time window of interest. Phases b and c are shifted by $-2\pi/3$ and $+2\pi/3$ with respect to phase a. The three-phase abc time evolutions for type-c waveforms
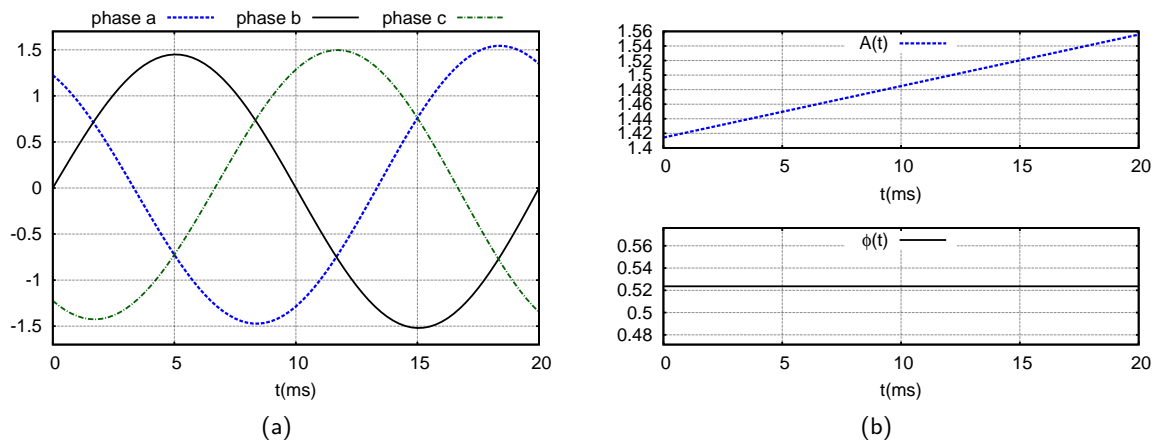
Figure 4.22: Waveforms b. Linear change in amplitude.
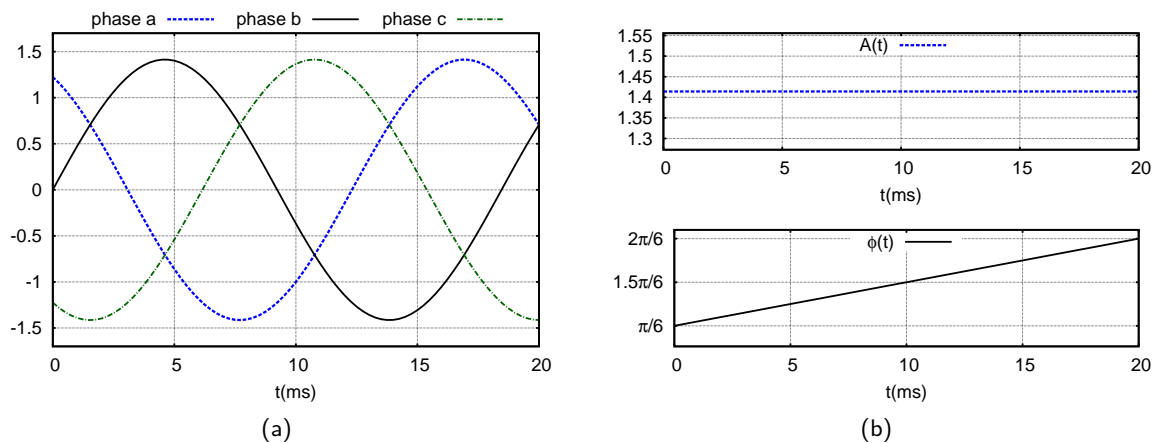
Figure 4.23: Waveforms c. Linear change in phase angle.

are shown in Figure 4.23.a. Figure 4.23.b shows the amplitude and phase angle derived from the PSRA. The initial increase of the phase angle is directly retrieved from the PSRA.

d. Linear change in amplitude and phase angle Type-d waveforms combine a linear evolution of amplitudes together with a linear evolution of phase angles of abc waveforms. Amplitudes are interpolated from $A = \sqrt{2}$ to $A = 1.1\sqrt{2}$ and the phase angle of phase a waveform increases linearly from a starting value $\phi_0 = \pi/6$ to a final value $\phi_0 = 2\pi/6$ at the end of the time window of interest. Phase b and c are shifted by $-2\pi/3$ and $+2\pi/3$ with respect to phase a. The three-phase abc and xy time evolutions for waveform d. are shown in Figures 4.24.a and 4.24.b respectively. The conclusions are similar than those given for waveforms of type a, b, and c.

e. Inverse Sequence Rejection For type-e waveforms a phase imbalance is considered. Namely, a constant 10 percent negative sequence ($A_{neg} = 0.1\sqrt{2}$ and $\phi_{0\,neg} = 0$) is added to the waveforms of type-a ($A_{pos} = \sqrt{2}$ and $\phi_{0\,pos} = \pi/6$), yielding the curves shown in Figures 4.25.a and 4.25.b.
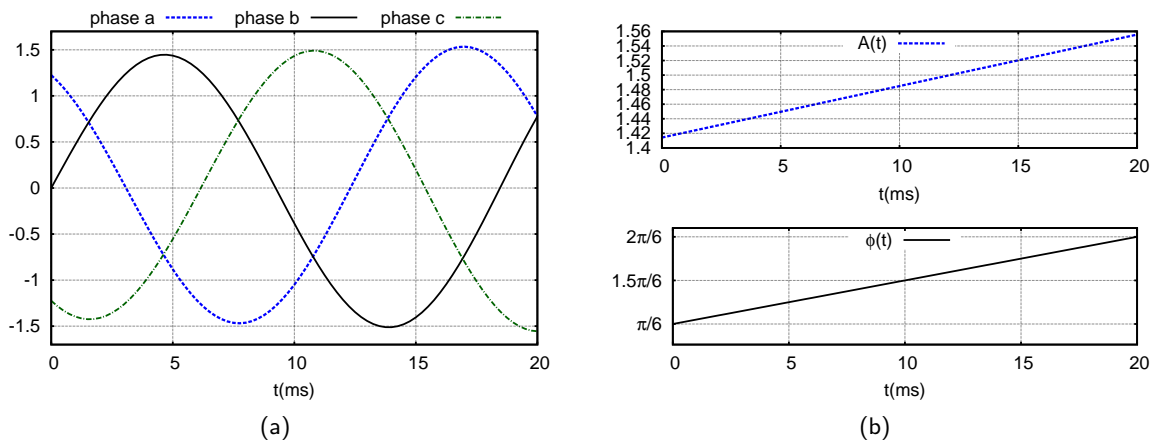
Figure 4.24: Waveforms d. Linear change in amplitude and phase angle.
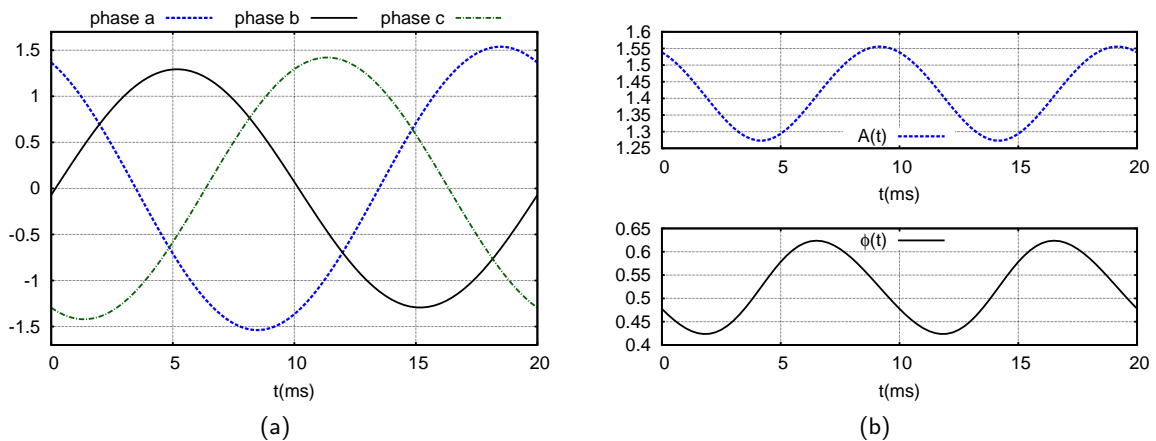
Figure 4.25: Waveforms e. Inverse sequence.

The presence of negative sequence in the waveforms is visible in the PSRA projections as a double-fundamental frequency signal superimposed on the time evolutions of the amplitude and the phase angle observed for type-a waveforms. The PSRA technique will need filtering to give an accurate result in the presence of imbalance.

f. Harmonic Rejection   Provided that the PM-EMT boundary is placed far enough from the disturbance location, the harmonic content at the PM-EMT boundary is supposed to be negligible. However, to test the phasor extraction methods in non ideal situations, type-f waveforms containing 2 percents fifth harmonic ($A_{H5} = 0.02\sqrt{2}$ and $\phi_{0\,H5} = \pi/6$) together with type-a waveforms ($A = \sqrt{2}$ and $\phi_0 = \pi/6$) are considered. The three-phase abc time evolutions for waveform f., are shown in Figure 4.26.a. The time evolutions of the amplitude and the phase angle obtained by PSRA are shown in 4.26.b. In the synchronous reference axes representation of Figure 4.26.b, the presence of fifth harmonics is observed through harmonics at six times the fundamental frequency in both the amplitude and phase angle evolutions. This is due to the fact that a positive-sequence
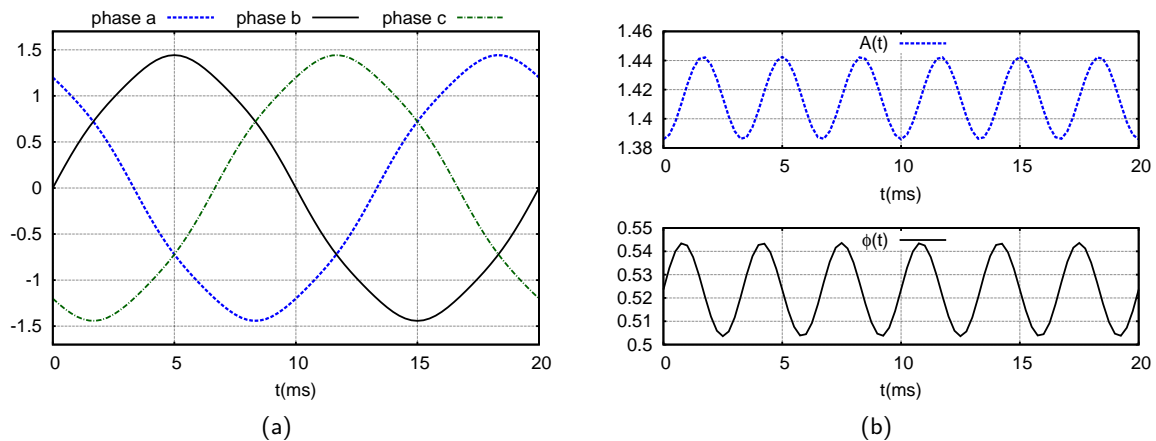
Figure 4.26: Waveforms f. Harmonic H5.
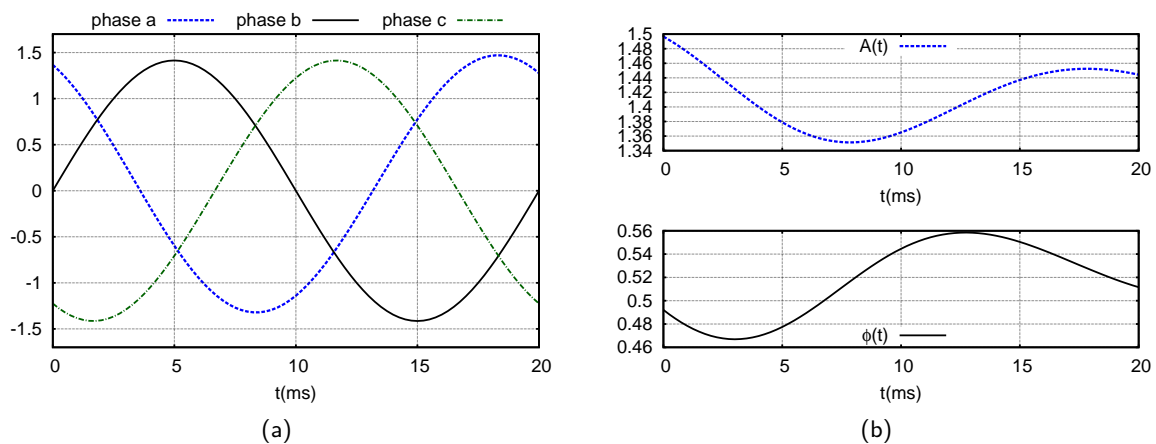
Figure 4.27: Waveforms g. DC component.

produces at the fifth-harmonic a negative sequence of signals. The projection on a rotating frame at synchronous frequency then increases by one the order of the observed harmonic.

g. DC component Rejection Finally, type-g waveforms contain an exponentially decaying DC component characterized by an initial value of 0.1 and a time constant τ_{DC} equal to 10 fundamental periods. The three-phase abc and PSRA amplitude $A(t)$ and phase angle $\phi(t)$ time evolutions for waveform g. are shown in Figures 4.27.a and 4.27.b respectively. In synchonous reference axes, a DC component becomes a fundamental frequency waveform, as expected

4.2.5 Results of extraction with PSRA or least-squares fitting

Table 4.2 summarizes the TVEs obtained with the methods presented in Section 4.2, i.e. the PSRA method, with and without filter, and the curve-fitting methods obtained with the four f functions detailed in Section 4.2.3. The time interval used was a single $20\,\text{ms}$ time window, and

Waveform		PSRA		Least-square Curve-fitting			
nb	Characteristic	w/o filter	w/ filter	f_1	f_2	f_3	f_4
a.	cst pos-seq.	7.4e-14	5.1e-13	6.9e-5	6.9e-5	1.9e-4	6.9e-7
b.	A_{pos} chg.	8.6e-14	0.53	3.4e-2	6.9e-5	9.8e-5	6.9e-7
c.	ϕ_{pos} chg.	8.9e-14	3.1	4.1	6.9e-5	6.4e-5	6.9e-7
d.	A_{pos} & ϕ_{pos} chg.	8.1e-14	3.1	4.2	6.9e-5	7.9e-5	7.3e-7
e.	10% neg. seq.	9.2	4.5	6.9e-5	6.9e-5	1.4e-4	6.8e-7
f.	2% H5	2.0	8.1e-2	1.0e-2	0.17	3.4	0.97
g.	$\tau = 10T_s$ dec.DC	30.8	26.6	1.8	18.3	0.02	1.3e-5

Table 4.2: TVE (in %) on the estimation of the positive-sequence phasor at the end of a given time-window.

the comparison has been made between the positive-sequence phasor obtained from the considered extraction technique and the positive-sequence phasor from which the three-phase signal had been initially produced.

As could be expected, the PSRA without filter gives poor results when negative-sequence, harmonics or decaying DC are present in the signals (waveforms e., f. and g.). These results are improved by adding a filter to the PSRA projections. However, the quality of the extraction remains rather poor for waveforms e. and g., with a TVE of a few percents. For what concerns curve-fitting techniques, a pure cosine waveform (f_1) fails to accurately represent a phase change, leading to a TVE of a few percents for the phasor extraction from waveforms c. and d. The quasi-cosine curve-fitting (f_2) gives good results, except as expected when a DC component is present (waveform g). The best results are consistently given by fitting a quasi-cosine waveform including an exponentially decaying DC component (f_4) to each of the abc signals. Let us observe that this technique gives poor results in the presence of harmonics in the signals from which to extract the boundary phasors. As previously explained, harmonic content at the boundary buses should be low enough for the co-simulation to be accurate.

4.2.6   Discussion

At fault elimination, the time interval on which it is needed to extract the positive-sequence phasor will comprise two segments of (quasi-)cosine waveforms with different amplitudes and phase angles, as shown in Figure 4.28 (coming from case 1 in Chapter 5). This phenomenon will be less critical if the boundary buses are located far from the faulted bus, which is another reason to somewhat extend the EMT sub-system. To our best knowledge, this problem has not been mentionned in the PM-EMT co-simulation literature. Coming back to the figure, the breakers open the various phases at different times after $t = 1.10$ s. The time window from which we want to extract the phasor is marked in shaded grey. The two cosines, for each phase, are separated by a dash-dotted vertical line. The phasors are needed at time $t = 1.12$ s.

It is obvious that extraction methods relying on the whole time interval, such as Fourier analysis or least-squares fitting techniques are not well suited for extracting the phasor from such waveforms.
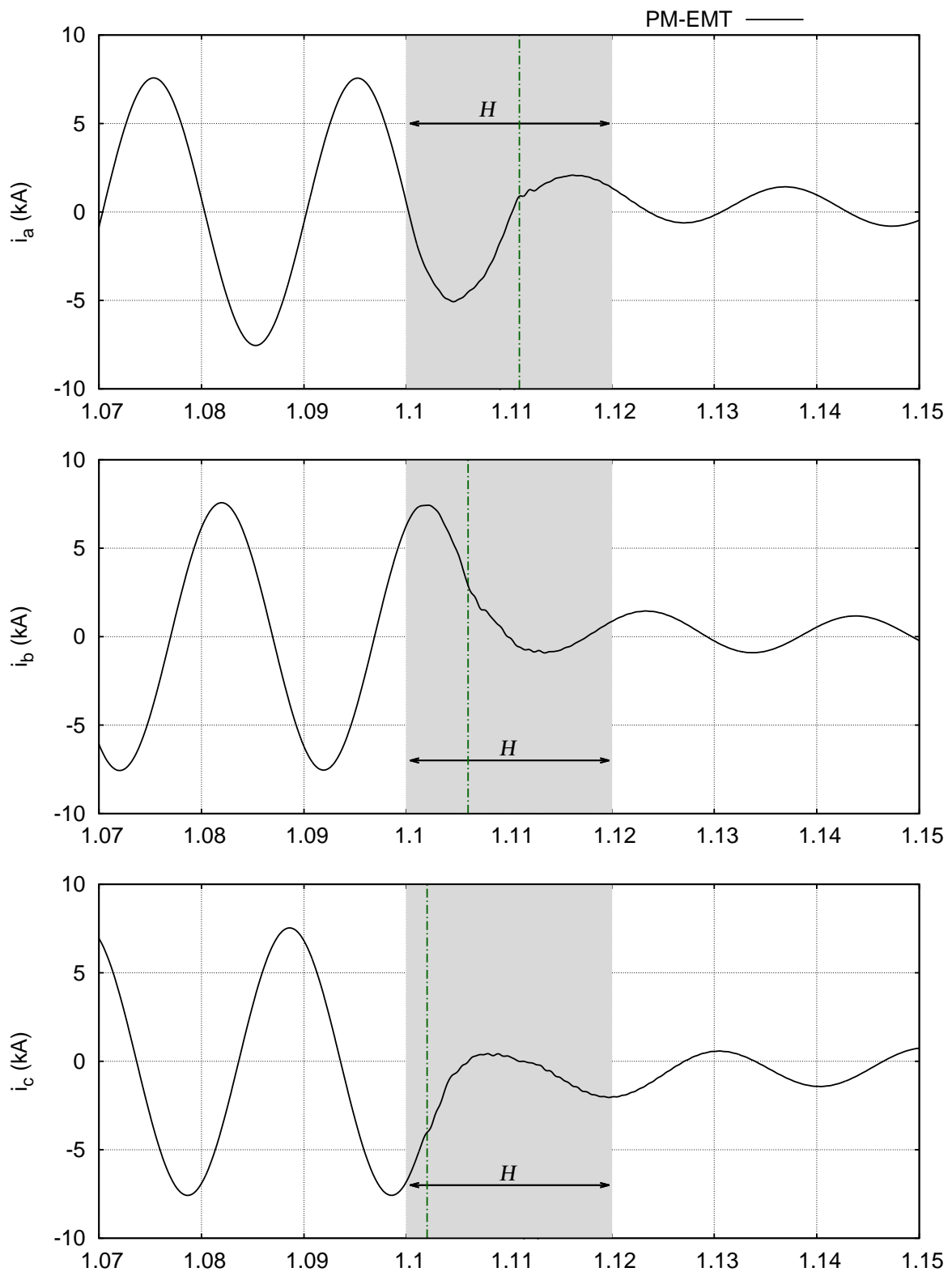
Figure 4.28: Waveforms h. Extraction problem at fault elimination time window.

On the contrary, a three-phase instantaneous technique such as PSRA discussed in Section 4.2.2 is likely to perform better. Let us note that the fault elimination may span over two successive time windows (for instance when the phase opening sequence starts in the middle of a time interval).

To conclude, we advise to use PSRA for a single time interval following the fault inception and two time intervals following the fault clearing instants (fault may be eliminated at the end of the time window, thus spanning on two successive time windows), and to fit every boundary single-phase signal to a quasi-cos waveform with exponentially decaying DC (f_4) for all other time intervals. All the results reported in the next chapter have been obtained using this extraction procedure.

Illustrative simulation results

We have presented in Chapter 3 the coupling of PM and EMT solvers and in Chapter 4 the conversion of boundary variables from PM to EMT models, and conversely. Some simulation results have been presented in Section 3.7. The test-system was small and characterized by a PM sub-system containing a Thévenin model only (see for instance Figure 3.25).

We present in this chapter simulation results produced with the Nordic system (see Figure 2.8) for the cases of single and multiple boundary buses interfaces (Sections 5.1 and 5.2 respectively). Three-phase (cases 1 and 3) and single-phase (cases 2 and 4) faults in the EMT sub-system are considered, with stable and unstable cases. A generator tripping in the PM sub-system is also considered (case 5) to demonstrate a case with a large frequency change (reaching $0.35\,\mathrm{Hz}$). The results presented in Section 5.5 deal with the convergence of the relaxation process. Section 5.6 is focused on simulations with a single evaluation of the EMT sub-system. Finally, complementary results are provided, for all test-cases, in Section 5.7.

5.1 Single boundary bus

5.1.1 Test system

We first report on tests performed with a small EMT sub-system, connected to the rest of the Nordic system through a single boundary bus. The PM and EMT sub-systems are shown in Figure 5.1. The EMT sub-system is identical to the one previously shown in Figure 2.10, and used for validation of our MATLAB-EMT solver. The detailed EMT sub-system includes six buses, two loads and two synchronous machines represented in detail. It is connected to the rest of the system through a single interface bus (4043).
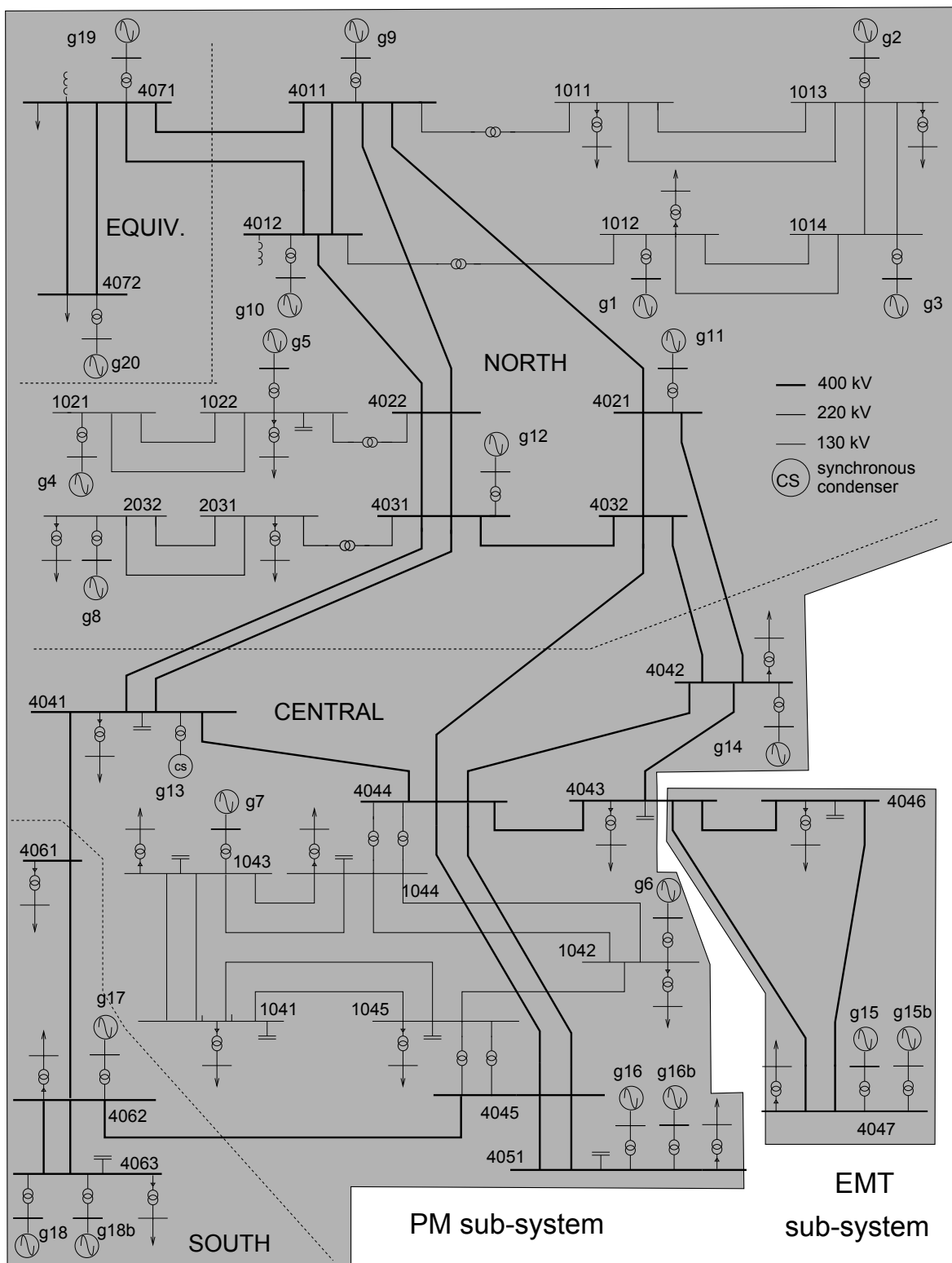
Figure 5.1: Nordic test system decomposed into a "large" PM and a "small" EMT sub-system.
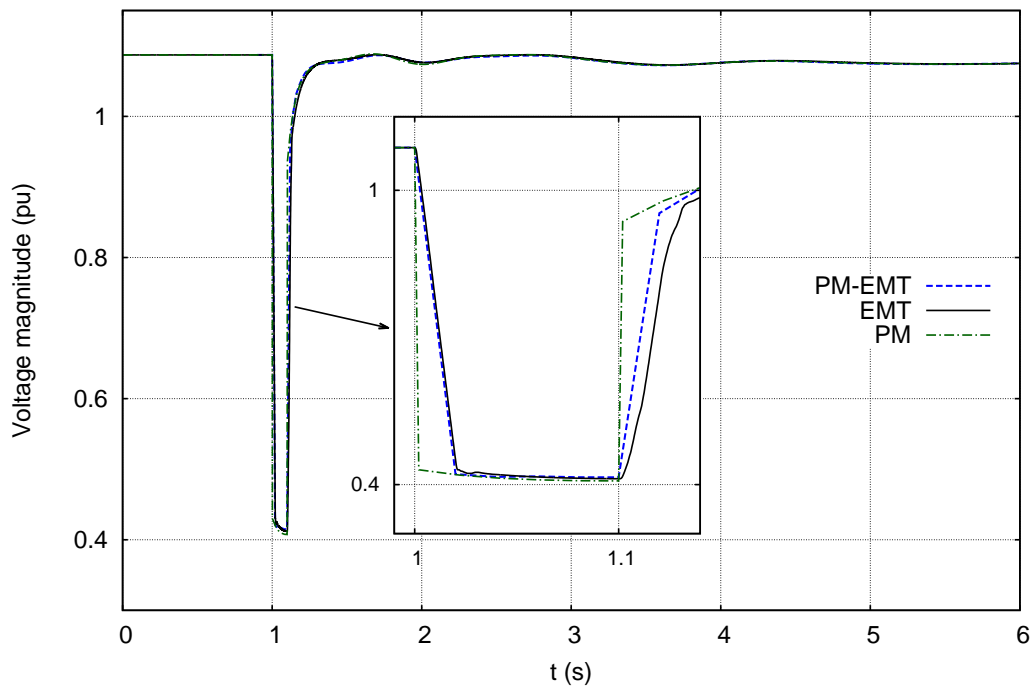
Figure 5.2: Case 1. Boundary bus voltage magnitude.

5.1.2 Case 1: Three-phase five-cycle short-circuit very near bus 4047

In this first test case, a solid three-phase fault is applied at $t = 1\,$s on line 4046-4047, very near bus 4047. It is eliminated at $t = 1.1\,$s, i.e. after 5 cycles.

The time evolution of the boundary bus voltage is shown in Figure 5.2. The algebraic, i.e. instantaneous, modeling of the network in the PM solver is observed by the abrupt (1ms time-step) change in the boundary voltage at fault inception and clearing. A very good match is observed between PM-EMT and EMT solutions. As expected, the co-simulation solution is situated between the PM and the EMT ones.

No major difference being observed between the PM and the EMT solutions, the boundary voltage may not be the best variable to check the accuracy of the coupling in this test-case. We show in addition the evolutions of the active and reactive powers injected at the boundary bus, see Figures 5.3 and 5.4, respectively. In the EMT solver (EMTP-RV), the active and reactive powers are computed from a running one-cycle window. In the PM-EMT solver, active and reactive powers are computed directly from the extracted current and voltage phasors. A reduced accuracy of the PM-EMT solution is observed particularly at the fault inception and clearing instants. This can be explained by the change of extraction technique at these instants from the least-squares fitting of a quasi-cosine waveform including an exponentially decaying DC component to the PSRA projection, which is less precise. Another factor influencing the accuracy of the results is the fact that the boundary is very close to the fault, which was chosen on purpose to push the co-simulation towards its limit. As can be seen from the evolutions of the boundary currents shown
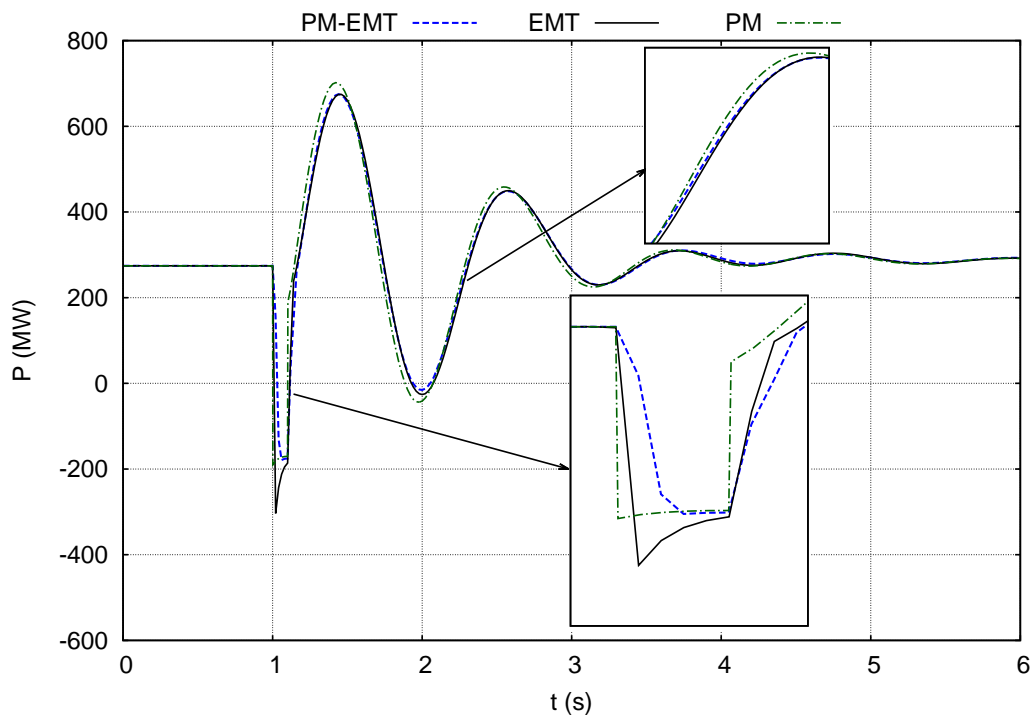
Figure 5.3: Case 1. Active power injected at boundary bus 4043.
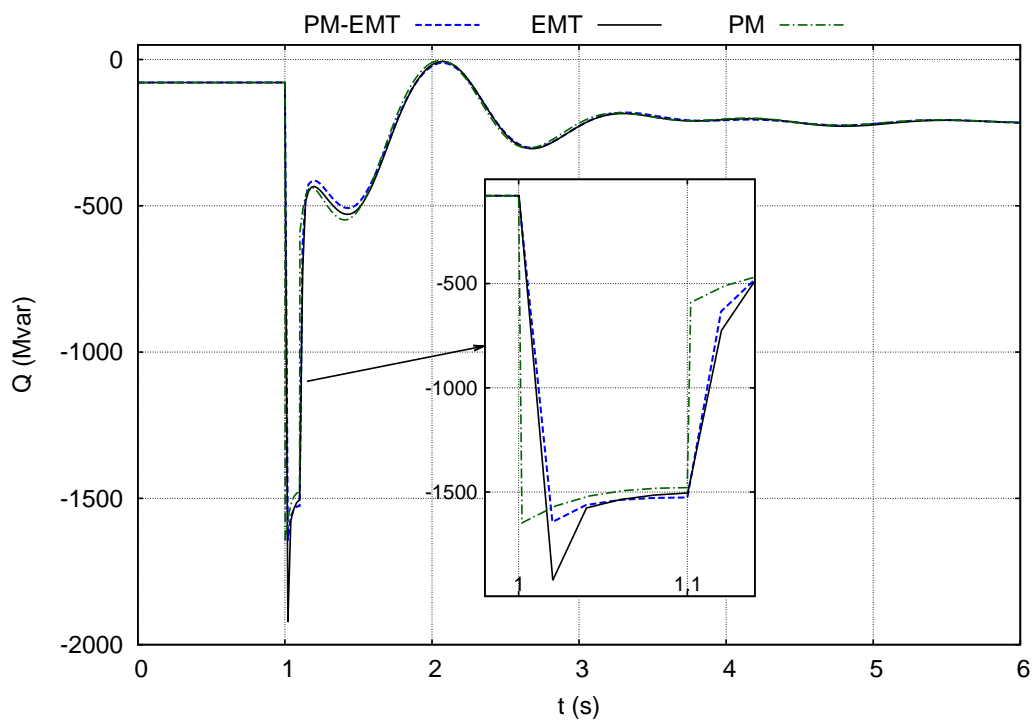
Figure 5.4: Case 1. Reactive power injected at boundary bus 4043.

in Figure 5.5, a DC component is present at the boundary. In the co-simulation, this component cannot be transmitted to the PM side of the boundary. These two factors explain the reduced accuracy during the fault-on period and, to a lower extent, over a few cycles after the fault clearing.

The evolution of the rotor speed of machine g15 is shown in Figure 5.6. The curves show a backswing, correctly reproduced by the co-simulation. This backswing and the higher-frequency oscillations are not reproduced with the simplified models of the PM simulation. The electrome- chanical oscillations are correctly reproduced by the PM-EMT simulation.

5.1.3   Case 2: Single-phase five-cycle short-circuit very near bus 4047

In this second case, a solid short-circuit is applied at $t = 1$ s to phase a only, very near bus 4047. It is eliminated by opening all three phases of line 4046-4047, after 5 cycles. The phase currents at the boundary bus are very imbalanced, as shown in Figure 5.7.
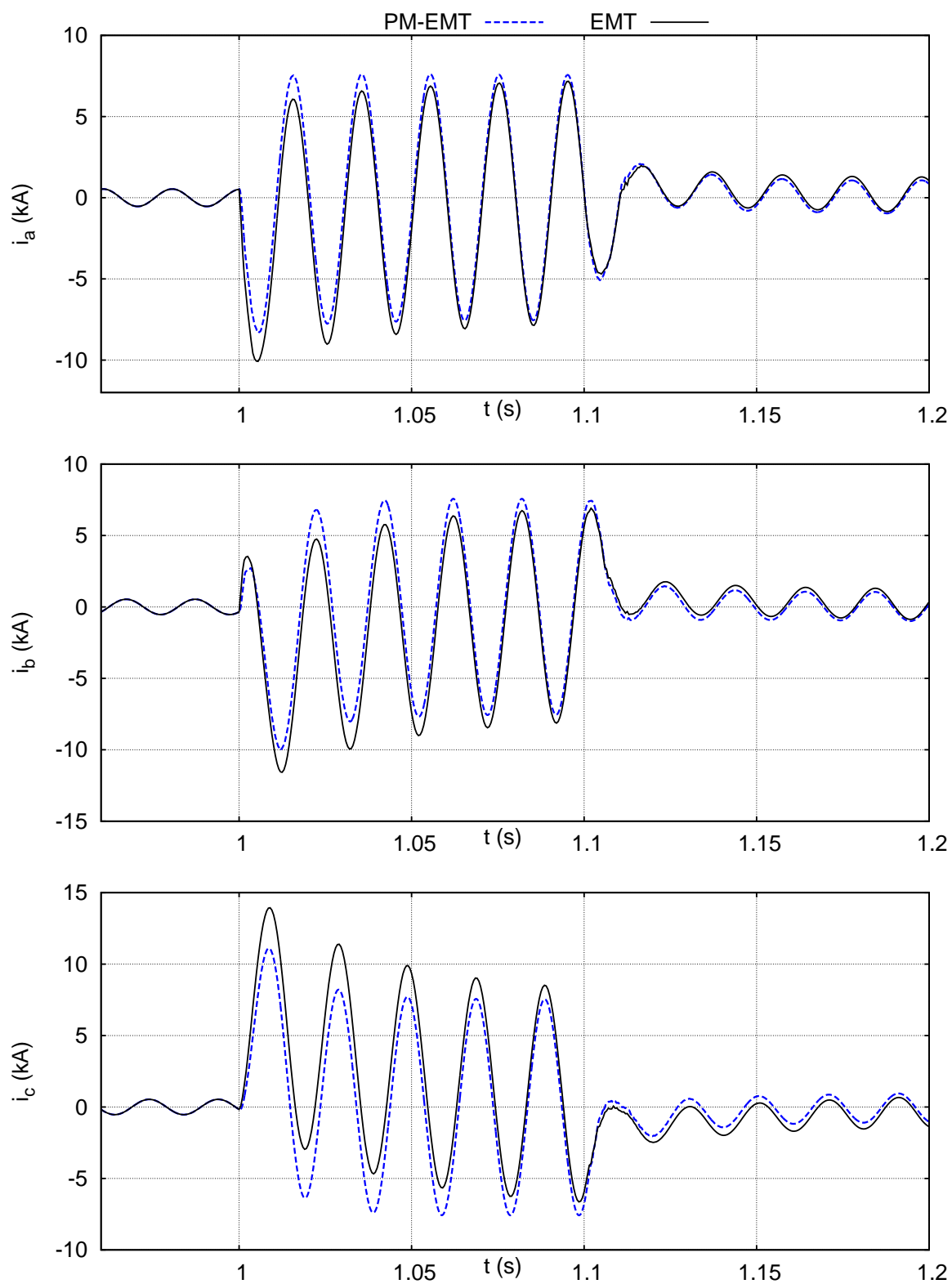
Figure 5.5: Case 1. Phase currents injected at boundary bus 4043.
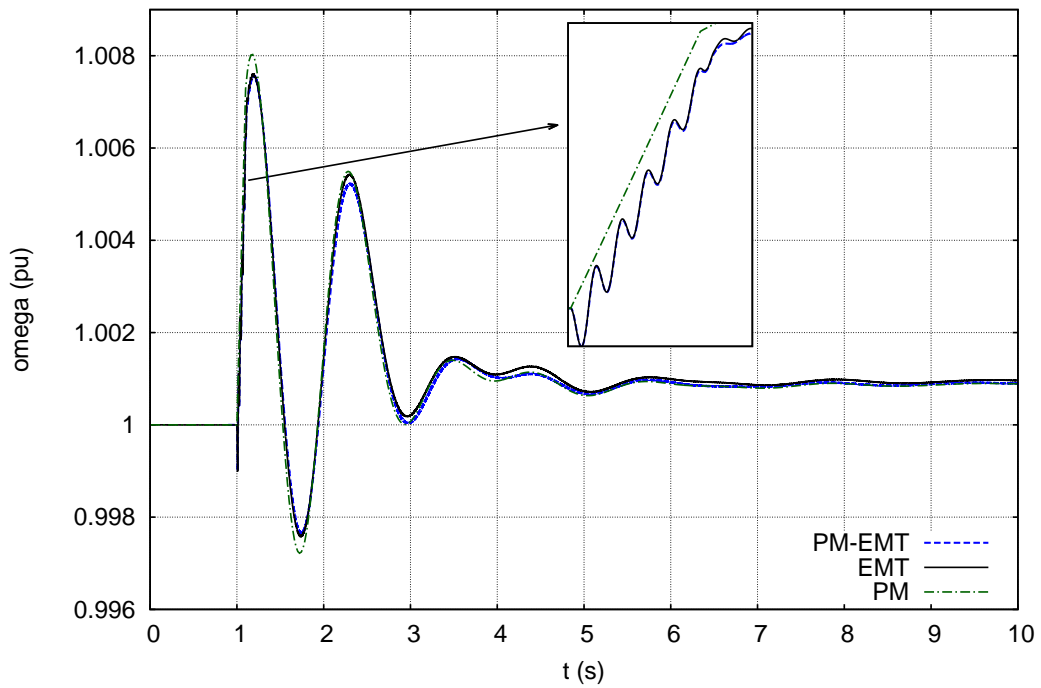
Figure 5.6: Case 1. Speed of machine g15.
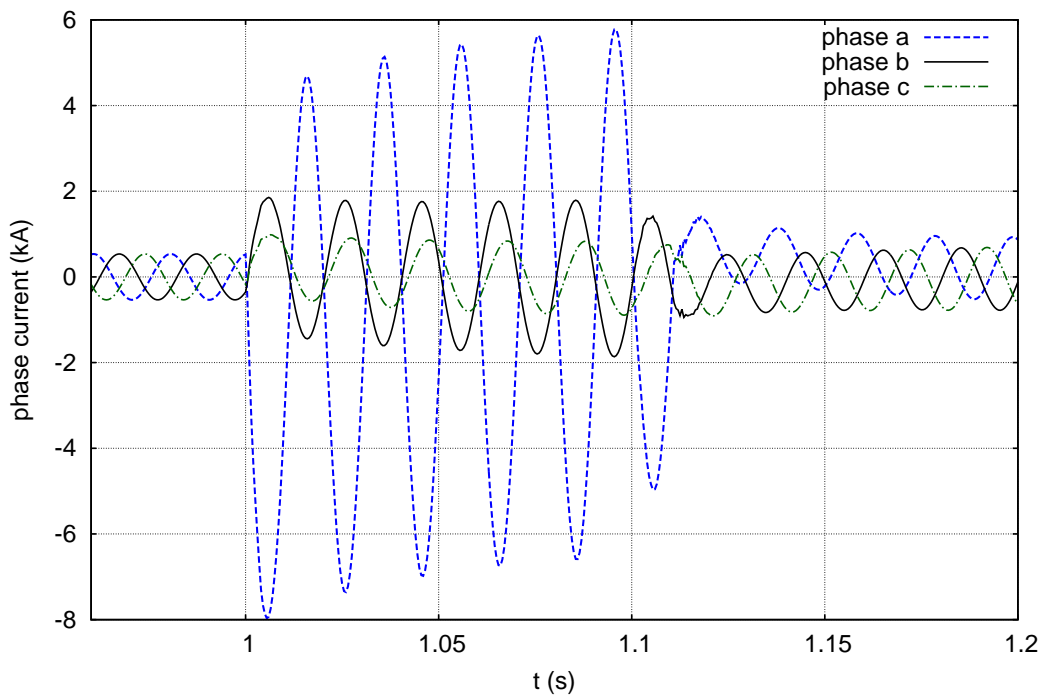
Figure 5.7: Case 2. Phase currents at boundary bus 4043.
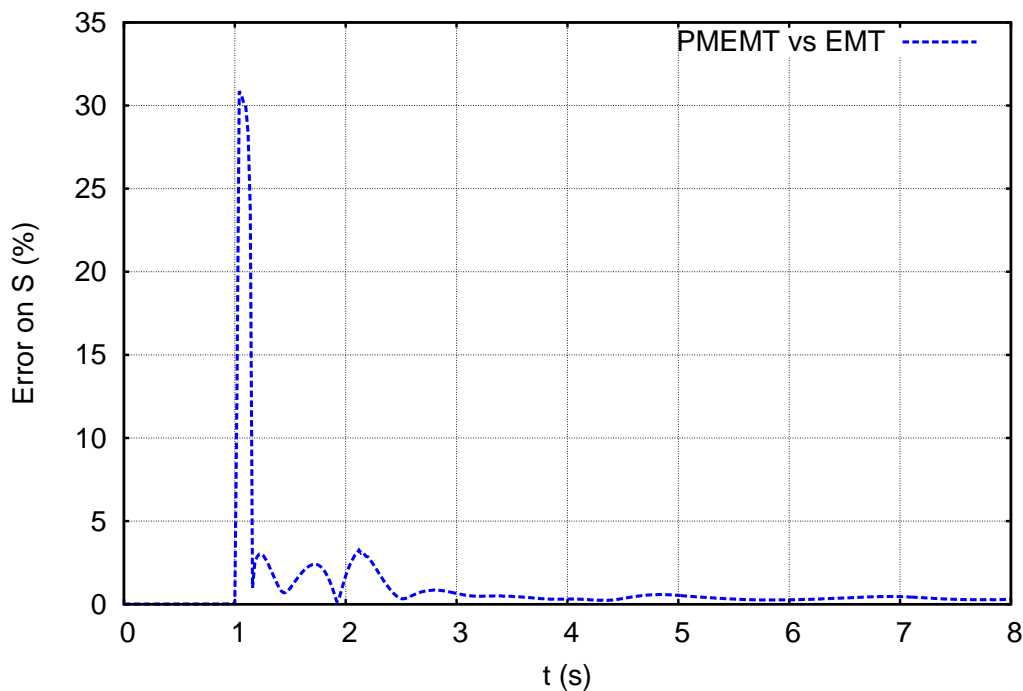
Figure 5.8: Case 2. Relative error on the complex power flowing through the boundary bus 4043.

Clearly, the boundary bus is too close to the disturbance to have a valid PM-EMT simulation (let us recall that only positive-sequence voltages and currents can be processed by the PM solver). This is confirmed by Figure 5.8 showing the relative error on the complex power, of the PM-EMT co-simulation with respect to the EMT benchmark. This is computed as follows at each time of the simulation:

$$relative\ error = \frac{|S_{PM-EMT} - S_{EMT}|}{|S_{EMT}|}, \tag{5.1}$$

where S_{PM-EMT} and S_{EMT} are the complex powers, flowing through the boundary buses, computed by PM-EMT and EMT simulations respectively. This error reaches as much as 30 percent during the fault-on period and a couple of percents in the subsequent seconds. Ideally, to be more accurate, the relative error should not only take into account the amplitude of the difference between the complex powers, but also the time shift [FVC11].

The time evolution of the rotor speed of machine g15, located inside the EMT sub-system, reveals nonetheless a fairly good match between the PM-EMT and the EMT simulations, as shown in Figure 5.9.
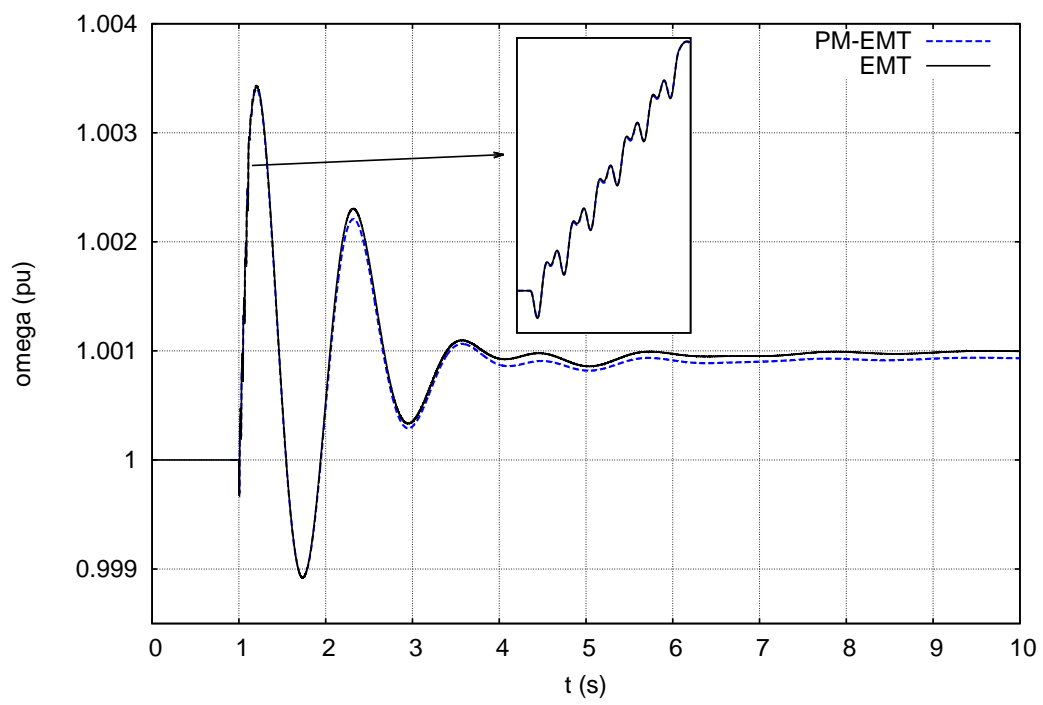
Figure 5.9: Case 2. Speed of machine g15.

5.2   Multiple boundary buses

5.2.1   Test system decomposition

In order to test the co-simulation in the presence of multiple boundary buses, the system has been decomposed as shown in Figure 5.10. The PM sub-system contains the Equivalent and North regions with hydro power plants taking care of primary frequency control. The EMT sub-system, on the other hand, is made up of the Central and South regions with the largest part of the load and thermal power plants, not participating in frequency control. The PM and EMT sub-systems are connected through three 400-kV buses, namely: 4041, 4044 and 4042. When building the Thévenin and Norton equivalents, the impedance and admittance matrices are non-diagonal, i.e. the couplings between boundary buses are taken into account. In steady-state, the active and reactive powers flowing from the PM into the EMT sub-system are given in Table 5.1. They add up to a total of 2600 MW and 160 Mvar flowing from the PM into the EMT sub-system.

5.2.2   Case 3: Three-phase fault at bus 1042

In this scenario, a three-phase, solid fault is applied at $t = 1$ s, to one of the two circuits connecting buses 1044 and 1042, very near the latter, in the EMT sub-system. The fault is cleared by opening all three phases of the faulted line. The nearby machines contribute to imbalance of the system response.

This severe contingency could lead to transient (angle) instability. Thus, two cases have been considered. In case 3a, the fault is cleared in 10.5 cycles, just before the critical clearing time is reached. In case 3b, the fault is cleared in 12.5 cycles, which is higher than the critical clearing time. Clearly, the latter is aimed at testing more severe conditions.

5.2.2.1   Case 3a: Fault cleared before critical time

Boundary voltages magnitude are shown in Figure 5.11. As expected, a very good match is observed between the PM-EMT and the EMT curves.

Bus	4041	4044	4042	**Total**
P (MW)	1091	571.1	937.0	**2599.1**
Q (Mvar)	-0.6	53.9	106.4	**159.7**

Table 5.1: Power flows from the PM into the EMT sub-system.

PM sub-system
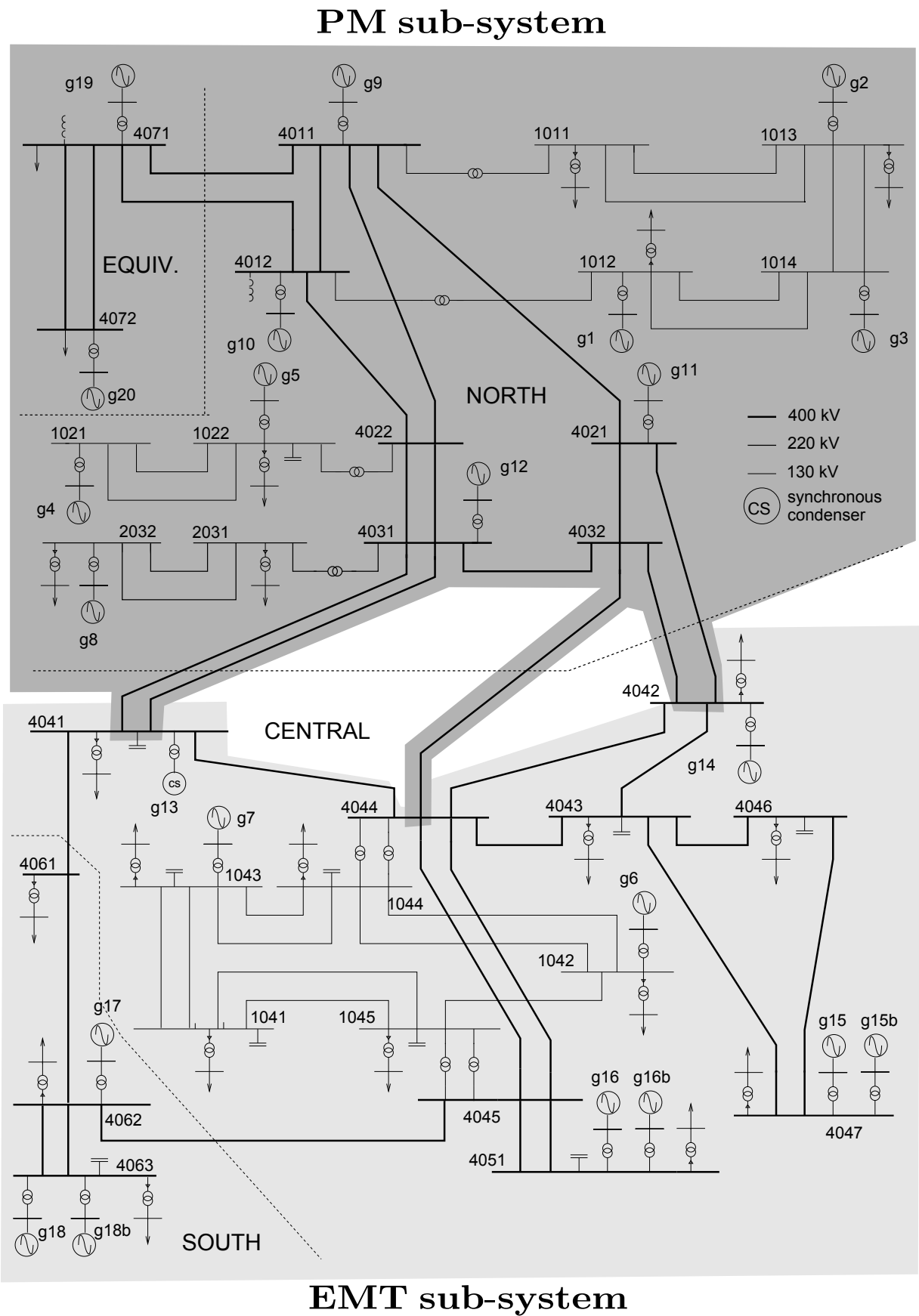
Figure 5.10: System decomposition with multiple boundary buses.

EMT sub-system
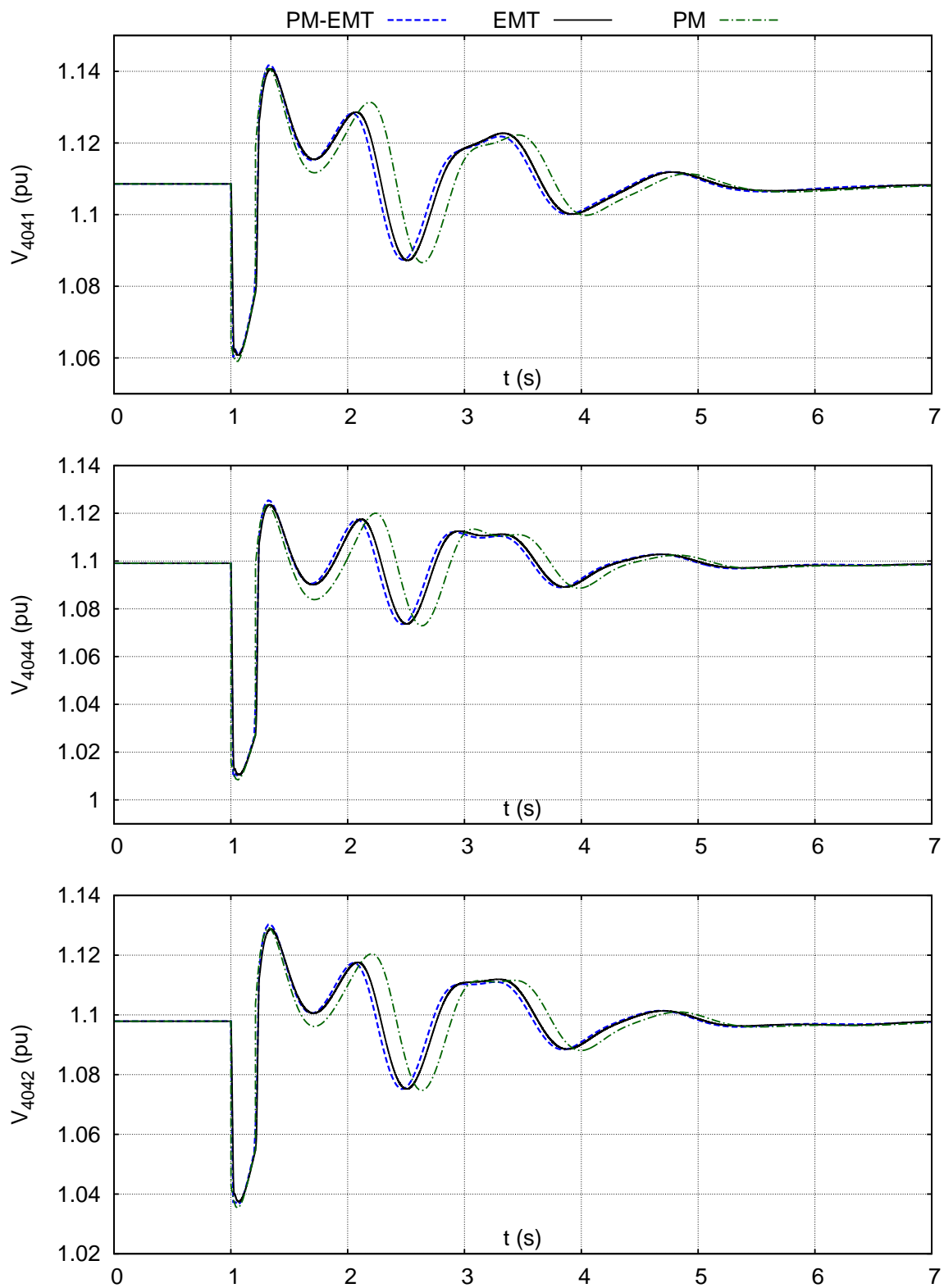
Figure 5.11: Case 3a: Boundary voltages.
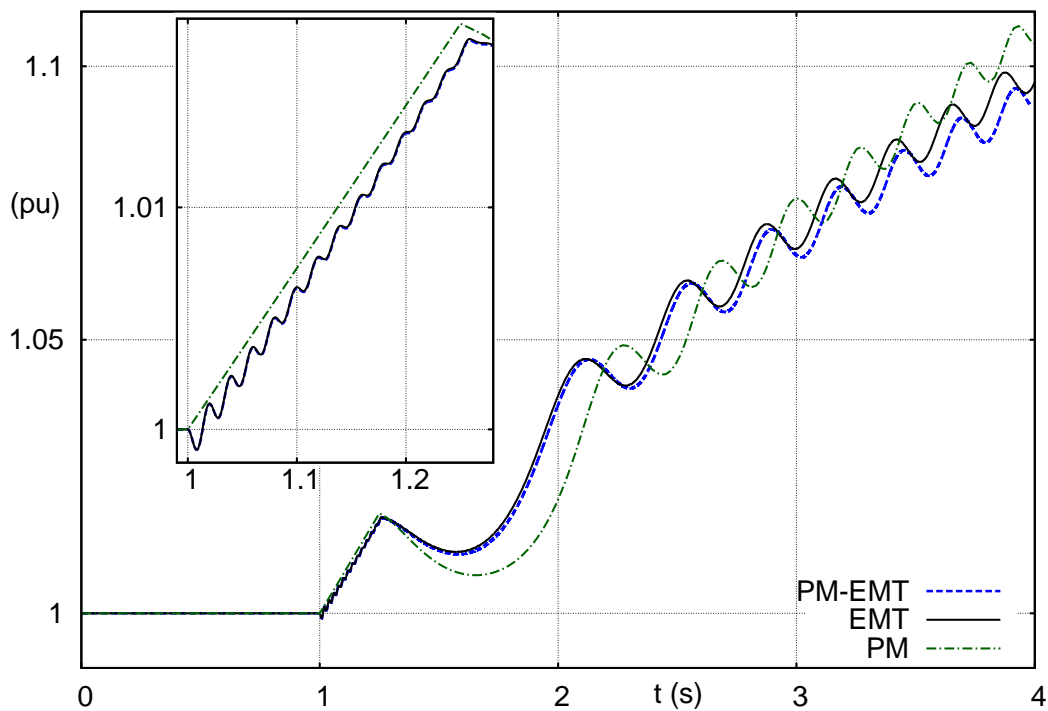
Figure 5.12: Case 3b: Rotor speed of generator g6.

5.2.2.2   Case 3b: Fault cleared after critical time

Due to the delayed fault elimination in this scenario, machine g6 (located next to the fault) loses synchronism and separates with respect to the rest of the system. This marginally unstable scenario is a severe test, since small initial deviations can evolve into large final excursions. Figure 5.12 shows the evolution of the rotor speed of g6. Note that the simulation has been run, for comparison purposes, until the speed reaches 1.1 pu while the machine would be tripped by protections before that in practice. A zoom on the on-fault period reveals, as expected, an almost linear increase in the PM response, while the PM-EMT and EMT evolutions show oscillations due to additional, fast decaying torque components [Kun94].

Figure 5.13 shows the corresponding evolution of the voltage magnitude at the boundary bus 4044, given by the three solvers. A good match is observed between the PM-EMT and the EMT responses, but not with the PM one.

5.2.3   Case 4: Single-phase 10.5-cycle fault on bus 1042

This case is interesting since it involves an imbalanced fault and corresponds to a real, typical application of PM-EMT co-simulations. In this case, to limit the amount of imbalance remaining at the boundary of the PM sub-system, the PM-EMT interface had to be put far enough from the fault location. In this fourth case, the evolutions of the boundary voltage magnitudes are shown in Figure 5.14. The PM simulation cannot handle directly such a case. Hence, the figure only shows the PM-EMT and EMT solutions. A very good match is observed between the PM-EMT and the
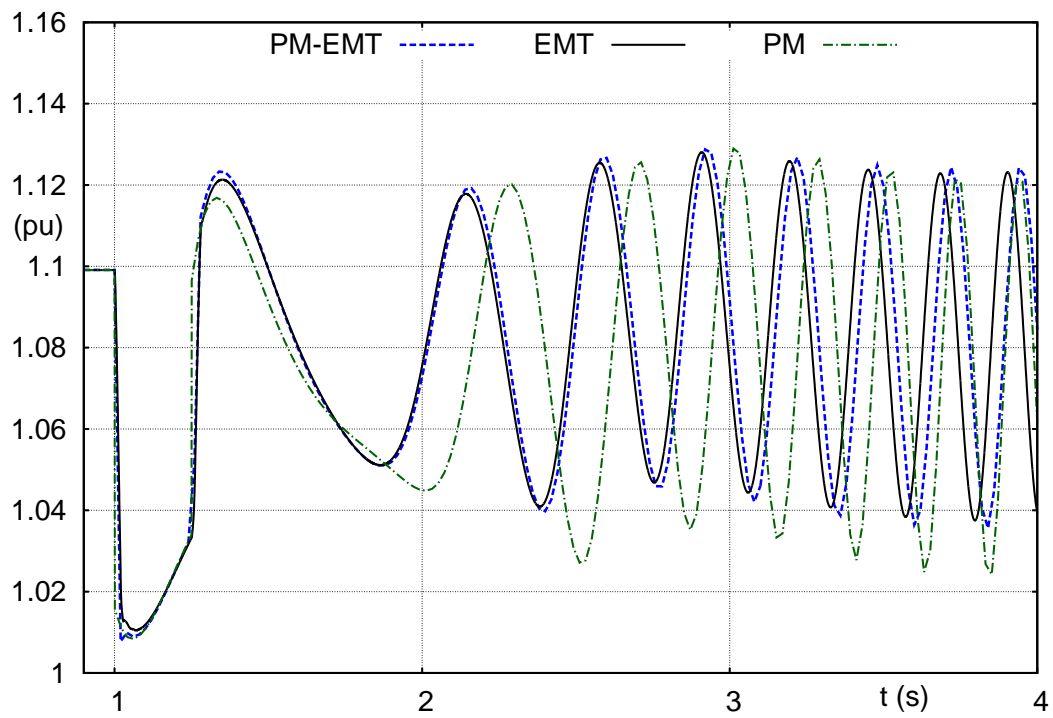
Figure 5.13: Case 3b: Voltage magnitude at bus 4044.

EMT curves in Figure 5.14, emphasizing the high quality of the proposed PM-EMT co-simulation.
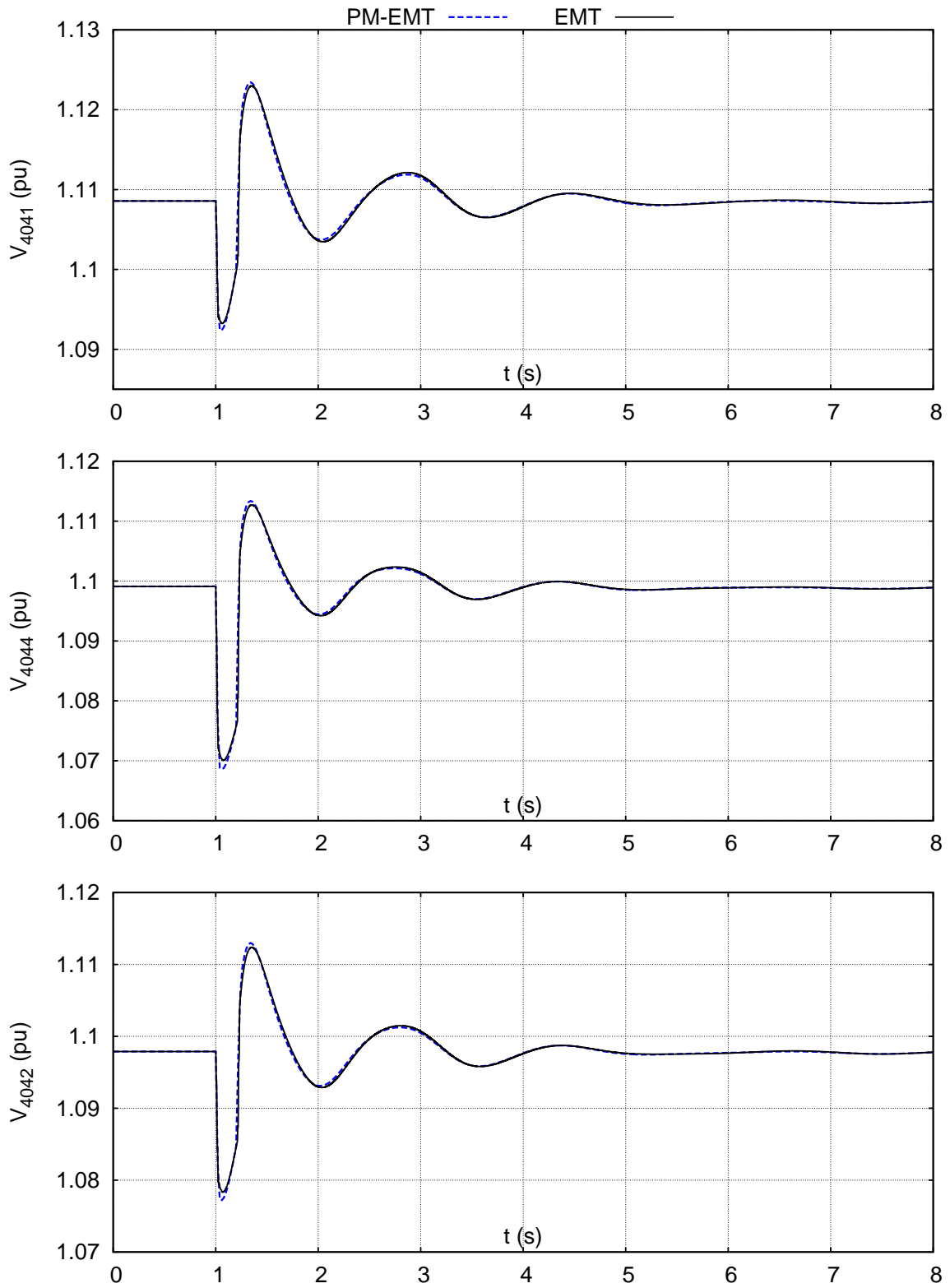
Figure 5.14: Case 4: Boundary voltages.
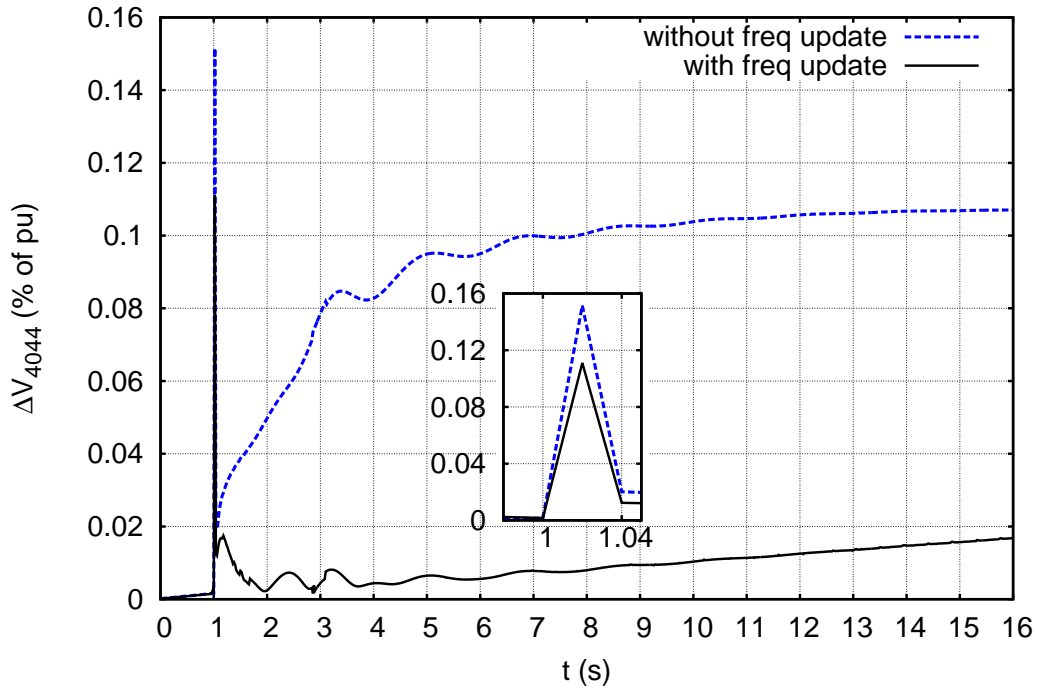
Figure 5.15: Case 5: evolution of $||\bar{V}_{4044}^{k+1} - \bar{V}_{4044}^{k+1/2}||$ with and without update of the Thévenin equivalent with frequency.

5.2.4   Case 5: Tripping g9 in PM sub-system

This last case is aimed at checking the accuracy of the PM-EMT co-simulation in the presence of large frequency deviations. To this purpose, the disturbance consists of tripping, at $t = 1$ s, the 1000-MVA generator g9 located in the PM sub-system. Note that most cases of practical interest involve disturbances located in the sub-system represented in greater detail, i.e. the EMT one. For checking purposes, however, the reverse was considered in this scenario.

Figure 5.15 shows the influence of updating the Thévenin equivalent with frequency, as discussed in Section 3.8. The plot shows the voltage difference at interface bus 4044, $\triangle V_{4044} = ||\bar{V}_{4044}^{k+1} - \bar{V}_{4044}^{k+1/2}||$, where the $k+1$ and $k+1/2$ superscript symbols are those defined in Figure 3.23, and where k corresponds to the last iteration, accepted at the end of the relaxation procedure performed for a given time step. The lower value obtained when updating with frequency indicates that the results of the coupled EMT and PM simulations are more consistent by approximately one order of magnitude.

The evolutions of the rotor speed of machine g13, located near the boundary bus 4041, are shown in Figure 5.16, focusing on the time interval until frequency reaches its minimum. In this case, due to PM approximations in the area near the tripped generator g9, the PM-EMT evolution is comparatively less accurate and closer to the PM rather than the EMT solution. Nevertheless, all three methods are in good agreement.
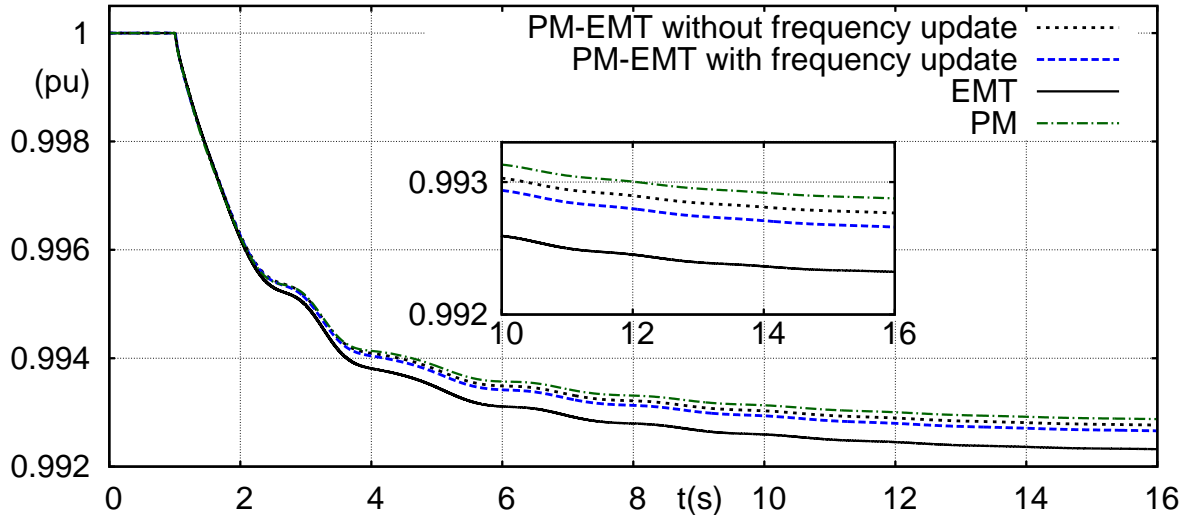
Figure 5.16: Case 5: Rotor speed of generator g13.

5.3   Accuracy of the multiple boundary buses cases

In this section, we examine the accuracy of the multiple boundary buses test cases presented in Section 5.2. The relative error (5.1) on the complex power flowing through the boundary bus 4044 is shown in Figure 5.17. For case 3a, we observe that the relative error is around or below 1 percent, except at fault elimination. For case 3b, the relative error is similar to the one for case 3a, except when the system starts to oscillate. However, the error increase between $t = 3$ and $t = 4$s is overestimated due to the fact that the time-shift between the two responses was not taken into account into the estimation of the error [FVC11]. Case 4 presents a negligible relative error, while case 5 is characterized by a bigger error. This is due to the fact that in case 5, generator g9 has been tripped inside the PM sub-system, which is characterized by simplified models. The relative errors shown have been estimated at the boundary bus 4044. The relative error observed on variables inside the EMT sub-system should be even smaller.

5.4   Evolution of the voltage of the Thévenin source

All test-cases have been simulated with double-sided boundary conditions of the kind shown in Figures 3.16.d (see also the relaxation algorithm in Figure 3.23). Considering the dynamically updated Thévenin equivalent representing the PM sub-system in the EMT simulation, it is of interest to observe the evolution of the voltage of the Thévenin source at a particular boundary bus and compare it to the evolution of the corresponding boundary voltage. Instead of considering the complex value of the Thévenin source $\bar{E}_{pm}$, we consider the relative variation of its magnitude $\left\| \bar{E}_{pm} \right\|$, computed as:

$$\frac{\triangle \left\| \bar{E}_{pm} \right\|}{\left\| \bar{E}_{pm} \right\|} = \frac{\left\| \bar{E}_{pm}\left(t+H\right) \right\| - \left\| \bar{E}_{pm}\left(t\right) \right\|}{\left\| \bar{E}_{pm}\left(t+H\right) \right\|} \tag{5.2}$$
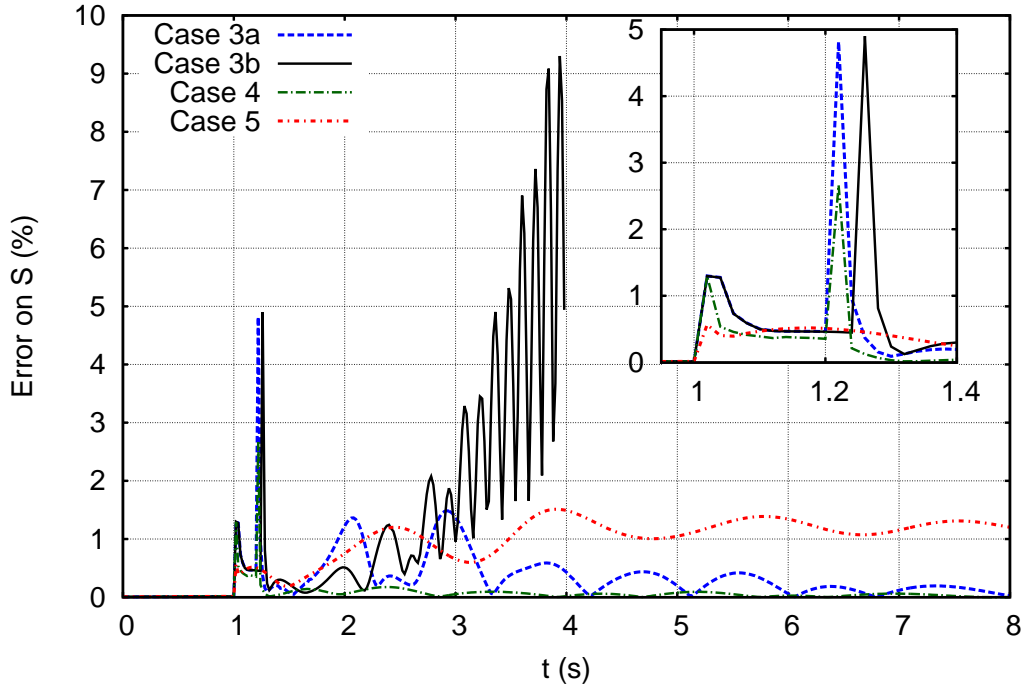
Figure 5.17: Relative error on the complex power, comparing PM-EMT to EMTP-RV at boundary bus 4044, for test cases involving multiple boundary buses.

and similarly for the amplitude of the voltage $\bar{V}$ at the same boundary bus:

$$\frac{\triangle \left\| \bar{V} \right\|}{\left\| \bar{V} \right\|} = \frac{\left\| \bar{V}\left(t+H\right) \right\| - \left\| \bar{V}\left(t\right) \right\|}{\left\| \bar{V}\left(t+H\right) \right\|} . \tag{5.3}$$

These two indices make the comparison between $\bar{E}_{pm}$ and $\bar{V}$ easier since both of them start from zero in pre-disturbance steady-state conditions, while $\left\| \bar{E}_{pm} \right\|$ and $\left\| \bar{V} \right\|$ differ significantly.

The curves for cases 1 and 2 are shown in Figures 5.18 and 5.19 respectively. In these two figures, it is observed that at fault application and clearing times, $\dfrac{\triangle \left\| \bar{E}_{pm} \right\|}{\left\| \bar{E}_{pm} \right\|}$ is smaller than $\dfrac{\triangle \left\| \bar{V} \right\|}{\left\| \bar{V} \right\|}$, which was to be expected.

Observing such small variations of $\left\| \bar{E}_{pm} \right\|$ in Figures 5.18 and 5.19, we may question the real need to use a PM model for the PM sub-system rather than merely a *static Thévenin equivalent* of the latter sub-system, computed once and for all. Figures 5.20 and 5.21 show the relative error on the complex power, computed as in (5.1), when using a static Thévenin equivalent rather than a PM-EMT co-simulation. In Figure 5.20, note that the peak at $t = 2\,$s is due to a value of the apparent power close to zero at the denominator of (5.1) and does not give any valuable information. For other time instants, the zooms show that the maximum error is on the order of 75 to $175\,$percents. This large error justifies the need for PM-EMT co-simulation in this case, rather than a mere static Thévenin equivalent. The error curve, corresponding to case 2, in Figure 5.21,

Figure 5.18: Case 1. Relative variation of the magnitudes of $\bar{E}_{pm}$ and $\bar{V}$ at bus 4043.

Figure 5.19: Case 2. Relative variation of the magnitudes of $\bar{E}_{pm}$ and $\bar{V}$ at bus 4043.
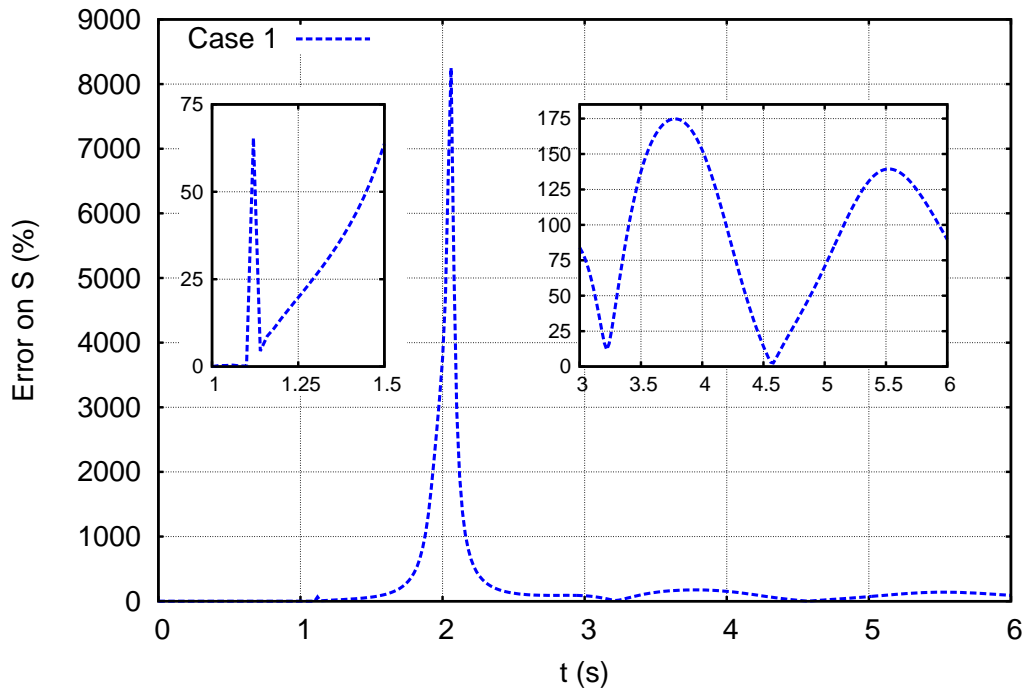
Figure 5.20: Case 1: Relative error on the complex power at bus 4043 when using a static Thévenin equivalent.

presents a large error at $t = 2\,\text{s}$, also due to an apparent power close to zero at the denominator of (5.1). The maximum values of the error go from 20 to 55 percents at other times. These large values proove the need to use PM-EMT co-simulation.

The curves for cases 3a, 3b and 4 are shown in Figures 5.22, 5.23 and 5.24 respectively. In these cases, the boundary is located further away from the disturbance which is in the EMT sub-system. This means that the influence of Z_{pm} (or equivalently R_{pm}^{abc} and L_{pm}^{abc}; see Figure 3.23) is likely to be higher than in cases 1 and 2. This is indeed observed in Figures 5.22, 5.23 and 5.24 where the relative variation of $\left\|\bar{E}_{pm}\right\|$ at bus 4044 is much smaller than the relative variation of $\left\|\bar{V}_{4044}\right\|$.

In Figures 5.22, 5.23 and 5.24, the variation of $\left\|\bar{E}_{pm}\right\|$ is observed to be very small, questioning the need for PM-EMT co-simulation when placing the PM-EMT interface further away from the disturbance. Figure 5.25 shows that the use of a static equivalent in cases 3a, 3b and 4 would lead to an error on the complex power in the order of magnitude of 5 to 30 percents. Even when the PM-EMT interface is far from the disturbance, a static Thévenin equivalent is not sufficient to correctly represent the dynamics of the PM sub-system.

Case 5, shown in Figure 5.26 is different. Note that the relative variations of $\left\|\bar{E}_{pm}\right\|$ and $\left\|\bar{V}_{4044}\right\|$ are both comparatively much smaller, in the order of a few tenths of a percent. However, we observe here that the Thévenin voltage has a larger variation than the boundary voltage. This is most likely due to the fact that the triggering event (outage of generator g9) is located in the PM sub-system. In fact, the EMT sub-system evolves under the effect of this changing $\bar{E}_{pm}$
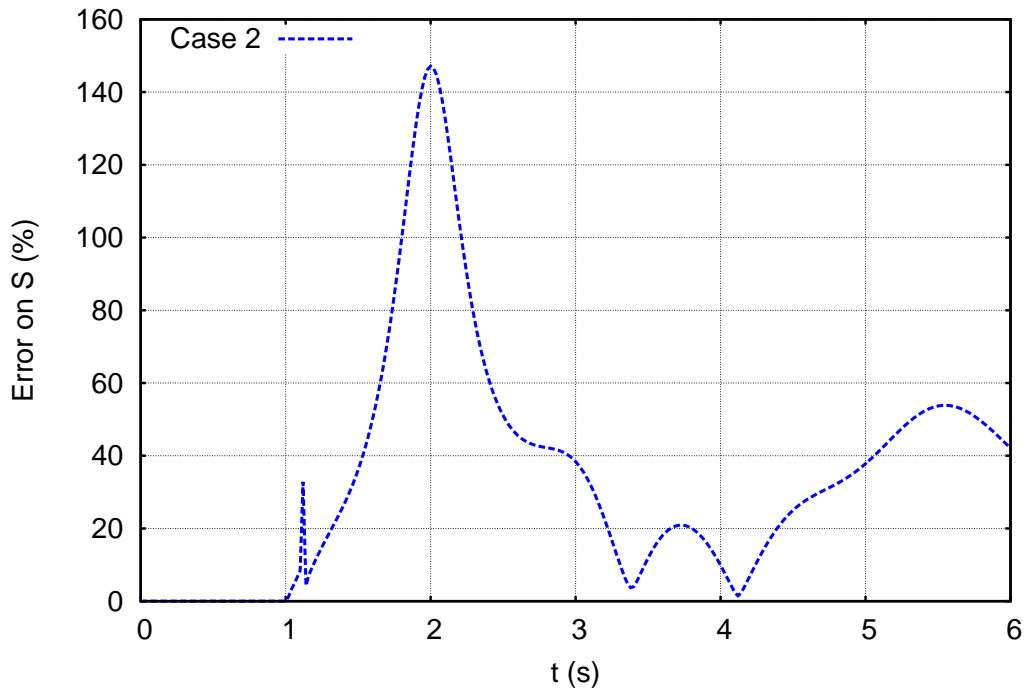
Figure 5.21: Case 2: Relative error on the complex power at bus 4043 when using a static Thévenin equivalent.
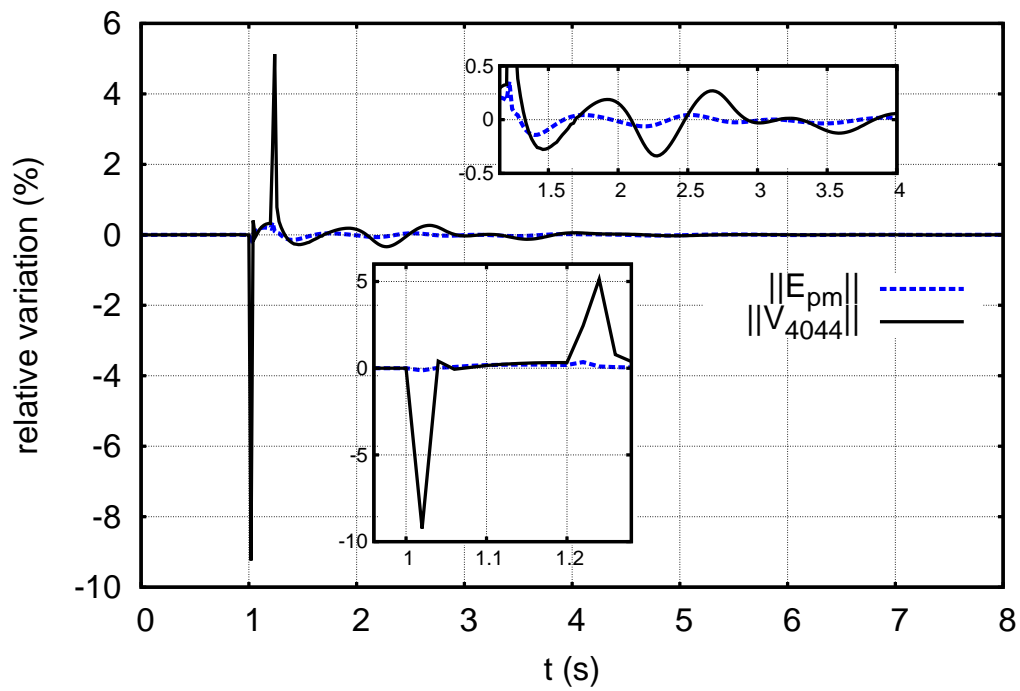
Figure 5.22: Case 3a. Relative variation of the magnitudes of $\bar{E}_{pm}$ and $\bar{V}$ at bus 4044.
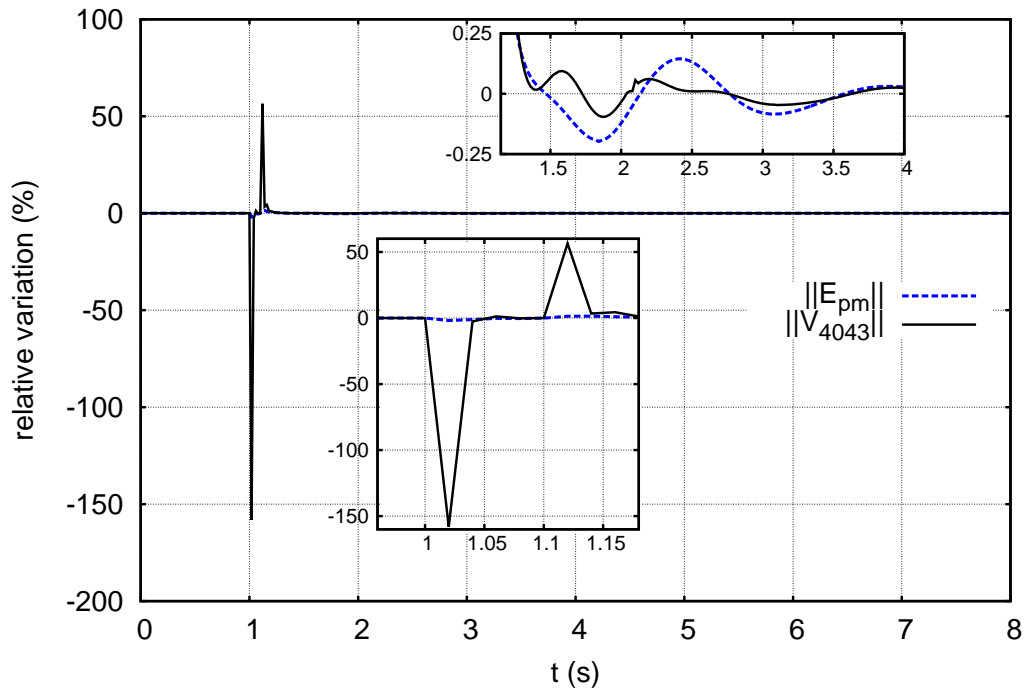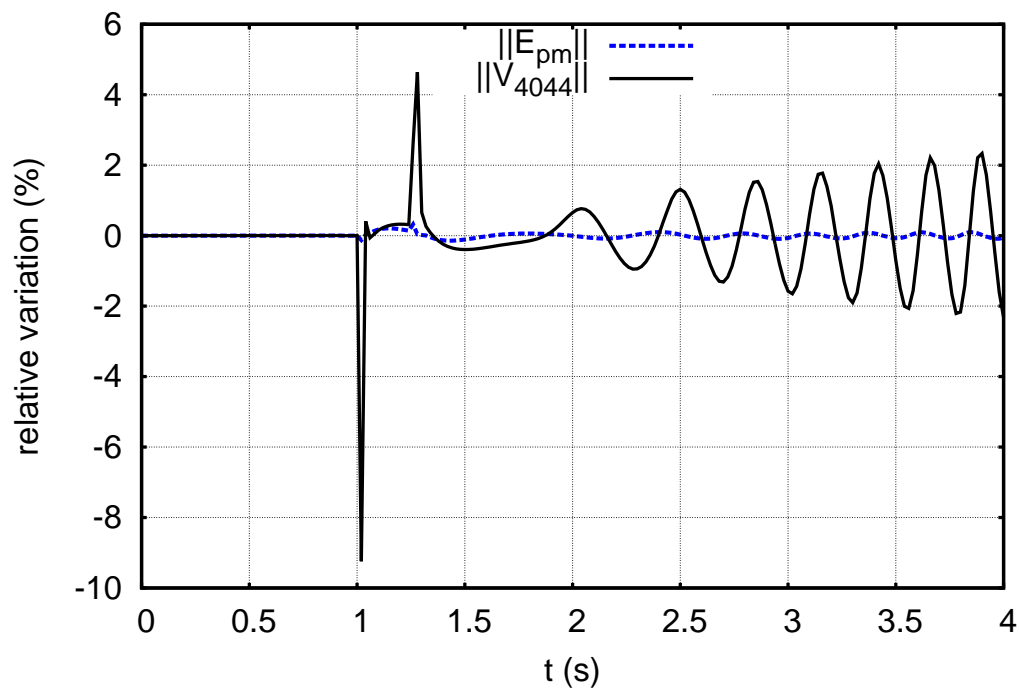
Figure 5.23: Case 3b. Relative variation of the magnitudes of $\bar{E}_{pm}$ and $\bar{V}$ at bus 4044.
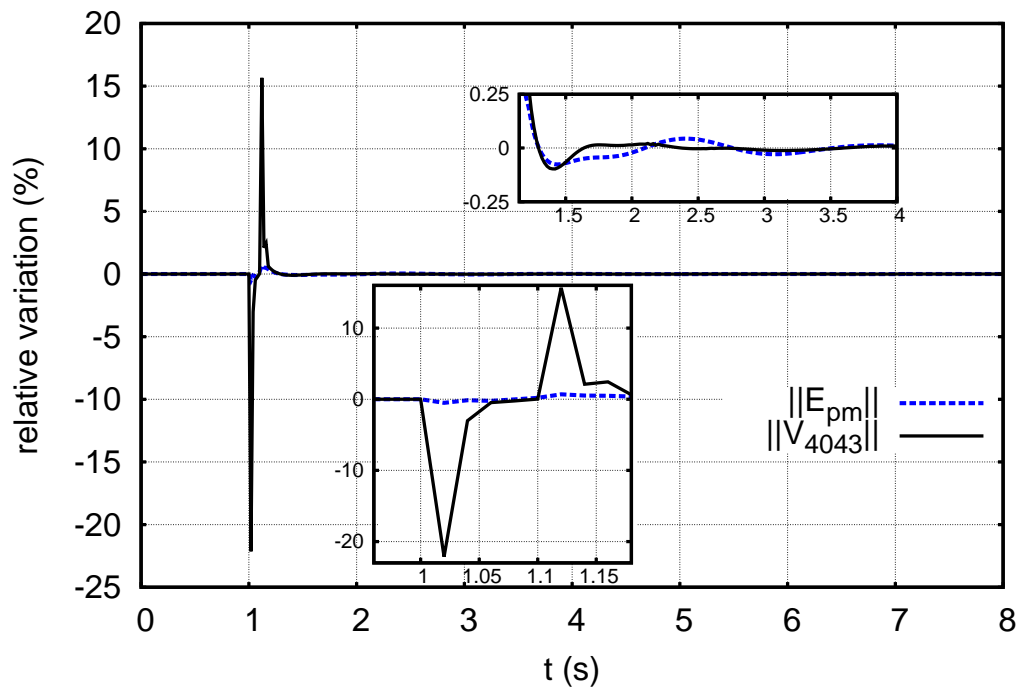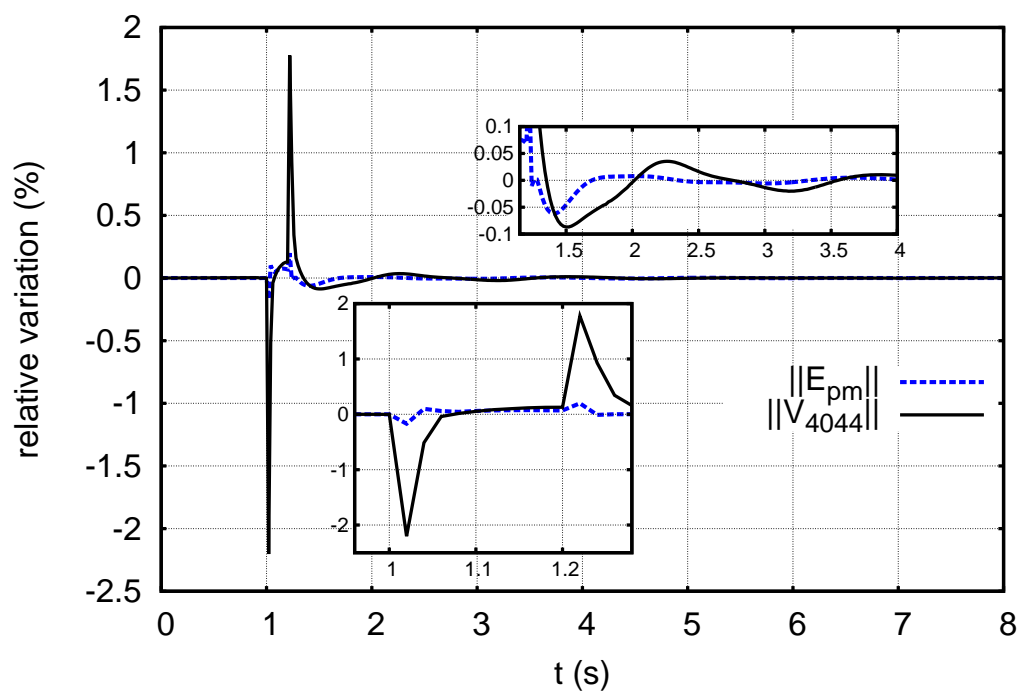

Figure 5.24: Case 4. Relative variation of the magnitudes of $\bar{E}_{pm}$ and $\bar{V}$ at bus 4044.
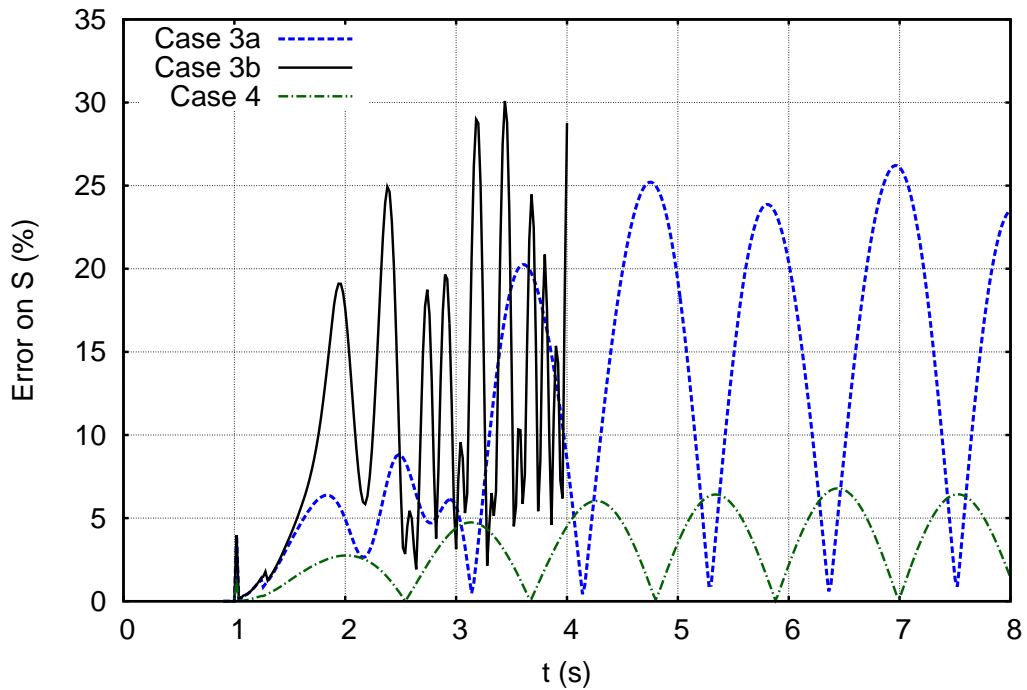
Figure 5.25: Case 3a, 3b and 4: Relative error on the complex power at bus 4044 when using a static Thévenin equivalent.

voltage. For case 5, since the disturbance takes place inside the PM sub-system, a static Thévenin representation would be meaningless. That is why no comparison between a static Thévenin equivalent and a PM-EMT co-simulation is presented for this test case.
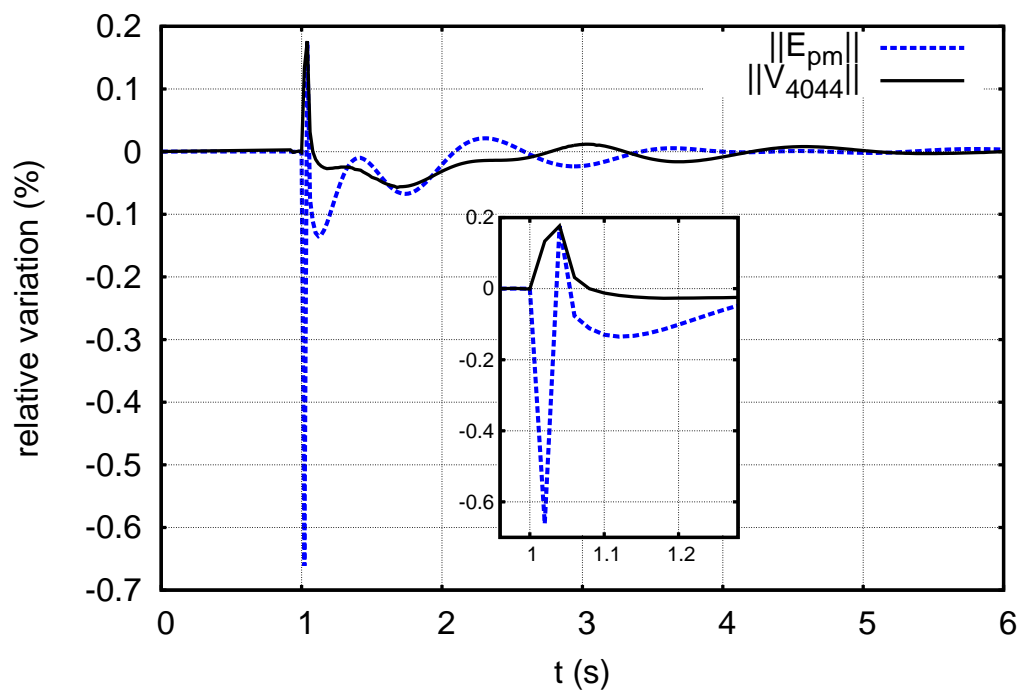
Figure 5.26: Case 5. Relative variation of the magnitudes of $\bar{E}_{pm}$ and $\bar{V}$ at bus 4044.

5.5 Convergence of the relaxation process

Table 5.2 provides the number of iterations of the relaxation procedure, i.e. the number of cycles in Figure 3.23 until convergence is reached. For a given simulation, the numbers of iterations were recorded at all time steps; the median and the maximum of all values are shown in the table. A second-order prediction has been considered in all cases. The results relate to various boundary conditions, identified by the letters in Figure 3.16. It was found that the conditions of type (a) did not allow the iterations to converge (even in steady-state conditions). All other boundary conditions led to convergence, and yielded the same dynamic response (see Section 3.7.3). The performances of type (c) vary too much from one case to another; type (d) is consistently the best.

Table 5.2: Nb. of relaxation iterations for various boundary conditions. "Med" designates the median, and "max" the maximum value.

| Case | Boundary conditions (see Fig. 3.16) | | | | | | |
| | (a) | (b) | | (c) | | (d) | |
		Med	Max	Med	Max	Med	Max
1	no conv.	2	21	3	17	2	17
2	no conv.	2	18	3	16	2	16
3-a	no conv.	2	9	3	25	2	4
3-b	no conv.	3	9	4	25	3	4
4	no conv.	1	4	3	5	2	4
5	no conv.	2	13	3	6	2	4

Table 5.3 shows the median and maximum number of iterations needed when zero-order, first-order or second-order predictions are used (see Section 3.4.1). The number of iterations have been evaluated on a 2 second simulation time interval after the event. The median is then computed over 100 consecutive time steps, each of $H = 20\,\text{ms}$. For all the results in this table, boundary conditions of type (d) have been used. It is observed that the second-order prediction consistently gives the least number of iterations, as expected.

Table 5.3: Nb. of relaxation iterations for various predictions.

| Case | Prediction: | | | | | |
| | zero-order | | first-order | | second-order | |
	Med	Max	Med	Max	Med	Max
1	3	17	3	17	2	17
2	3	16	2	16	2	16
3-a	3	4	3	4	2	4
3-b	3	4	3	4	3	4
4	3	4	2	4	2	4
5	3	4	3	4	2	4

5.6   Impact of restricting to a single EMT evaluation per time step H

For computational efficiency and in applications such as hardware-in-the-loop simulations, it is of interest to perform a single iteration of the relaxation process, involving thus a single EMT simulation per time step H (see Section 3.2.3.2). Limiting the number of iterations to a single one obviously introduces some approximation, which is illustrated in Figures 5.27, 5.28 and 5.29.

Figure 5.27 relates to case 3b, with zero-order prediction and boundary conditions of type (b), (c) and (d), respectively. It shows the relative error on the complex power at the boundary bus 4044, when performing a single iteration, compared to a fully converged co-simulation. The results further confirm the superiority of boundary conditions of type (d).

Figures 5.28 and 5.29 show the same relative error, in the various test cases (single and multiple interface buses), using boundary conditions of type (d) and second-order prediction. It is observed that a single iteration yields very good accuracy.

In order to check if the latter error is significant, it is compared to the error of a converged PM-EMT co-simulation with respect to the EMT benchmark. The most severe case is considered regarding the error introduced by a single EMT sub-system evaluation, at the fault inception and clearing instants. From Figure 5.29, this case is found to be case 3a. The curves in Figure 5.30 show that the relative error on the complex powers between the PM-EMT co-simulation and the benchmark (EMTP-RV) rises up to a few percents at fault inception and clearing instants and is in the order of one percent outside the fault-on period. In this case, there is no added value in iterating until convergence in the PM-EMT co-simulation. Let us stress, however, that this holds true only if the boundary conditions used are of type (d). Figure 5.27 showed indeed that boundary conditions (b) and (c) lead to an error in the order of magnitude of 1 percent, which is not negligible at all compared to the relative error of the converged solution with respect to the benchmark.
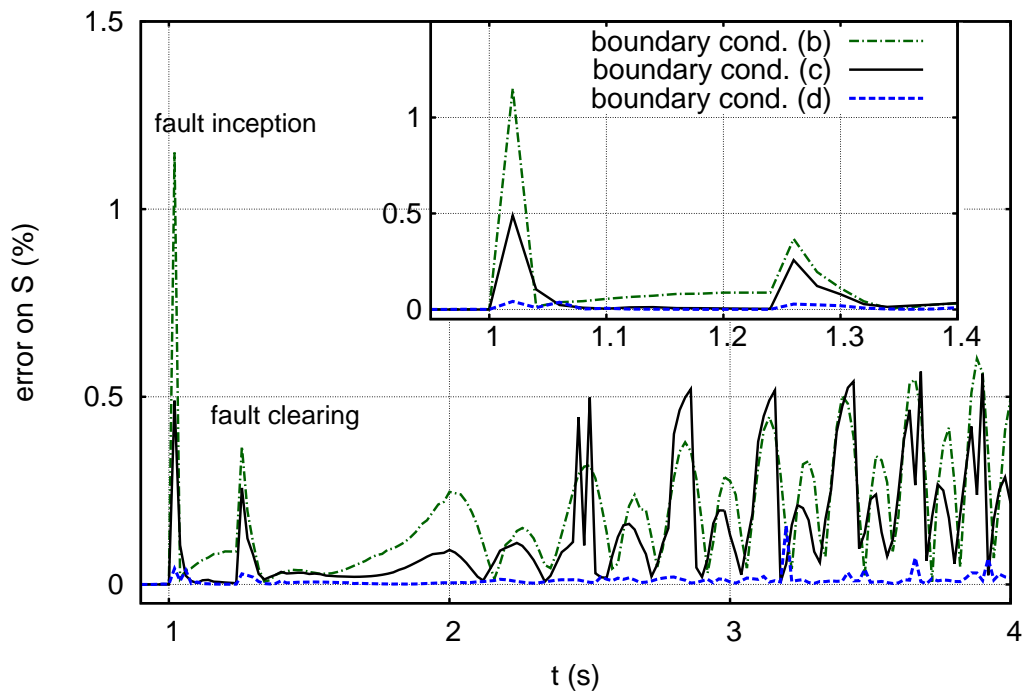
Figure 5.27: Case 3b: Relative error on complex power at bus 4044 when performing a single co-simulation iteration, with zero-order prediction and for various boundary conditions.
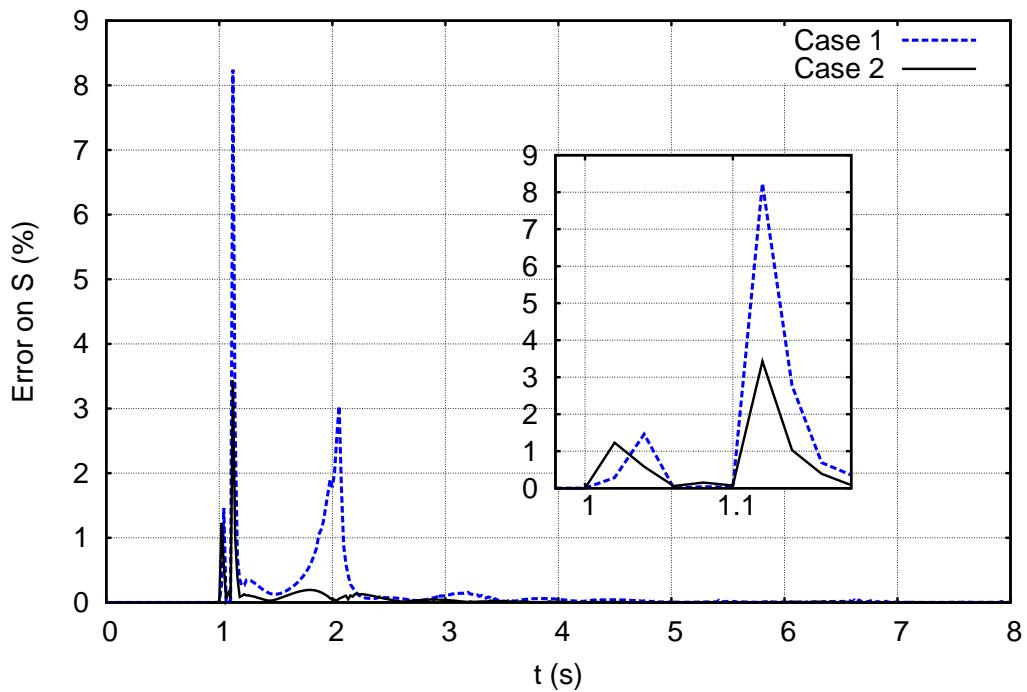
Figure 5.28: Cases 1 and 2: Relative error on complex power at bus 4043 when performing a single co-simulation iteration, using boundary conditions of type (d) and second-order prediction.
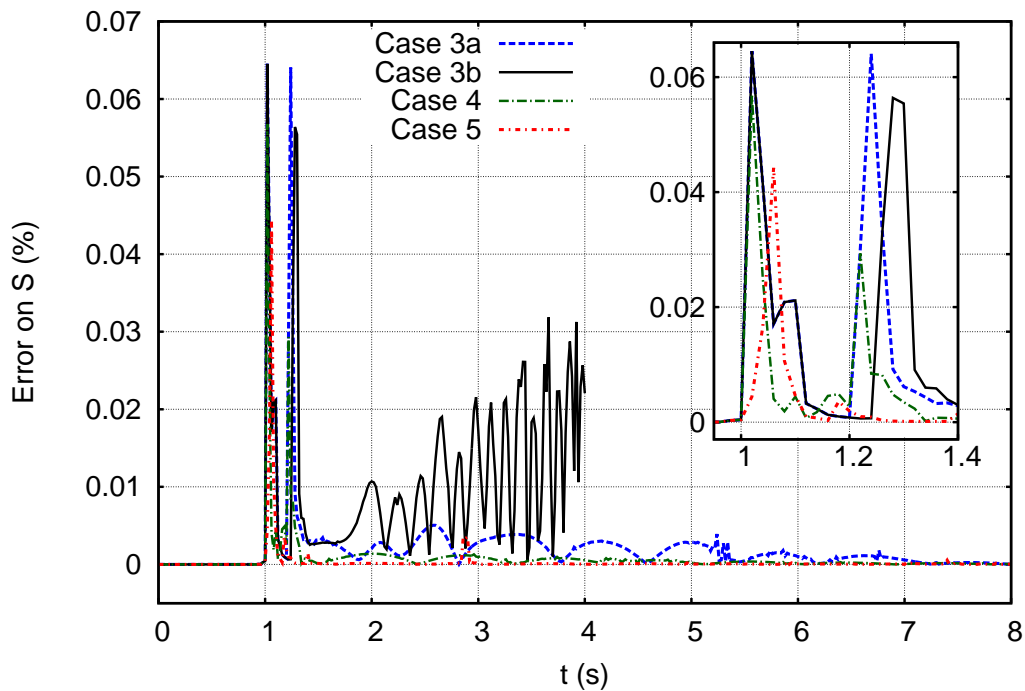
Figure 5.29: Relative error on complex power at bus 4044 when performing a single co-simulation iteration, using boundary conditions of type (d) and second-order prediction.
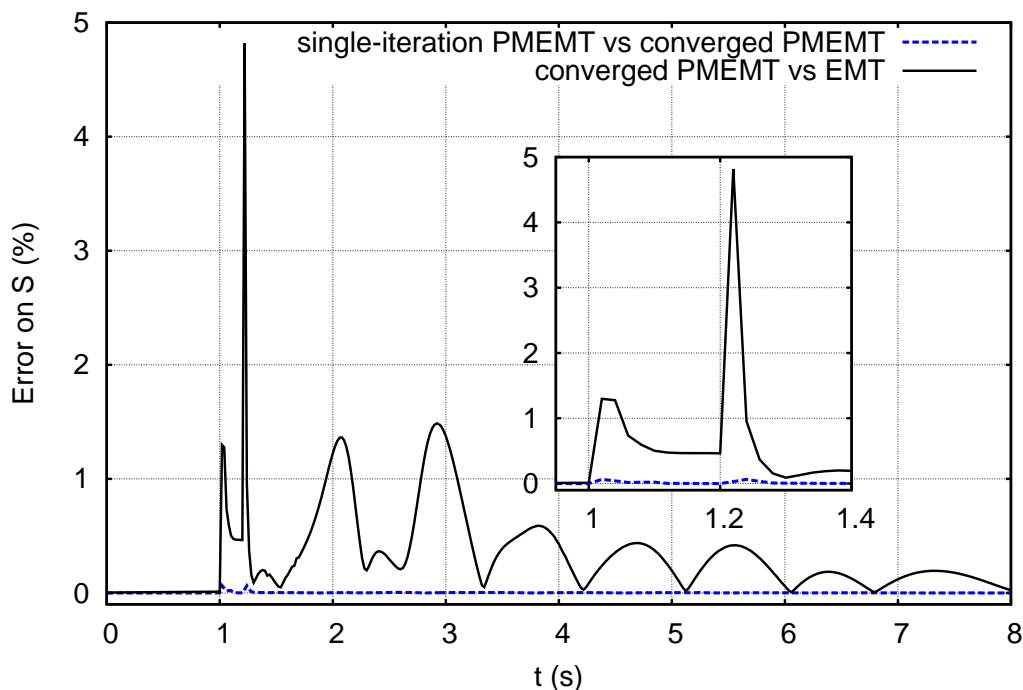
Figure 5.30: Case 3a: Relative error on complex power at bus 4044 when performing a single co-simulation iteration, using boundary conditions of type (d) and second-order prediction, compared to the error of the fully converged solution with respect to the reference solution (EMTP-RV).

5.7 Complementary simulation results

The results in this section have been added to confirm the results presented earlier in this chapter. In a fast reading of the thesis, this section can be skipped.

5.7.1 Case 1: Three-phase five-cycle short-circuit very near bus 4047

The boundary currents generated from the EMT simulation are shown in Figure 5.31. Note the presence of imbalance in the case of this three-phase fault. Exponentially decaying DC components are observed, as expected, during the fault-on time but also after the fault clearing. Machine g15 currents generated by the EMT simulation and the PM-EMT co-simulation, are shown in Figure 5.32. The latter figure shows that, after the fault is cleared, a small discrepancy between the PM-EMT curve and the EMT benchmark can be observed. For the fault-on duration, a negligible discrepancy could also be observed between these two curves. This might come from the fact that in general, a 50μs time step size h has been used in the EMT solver for stability reasons, while $h = 100\mu$s has been used in the MATLAB-EMT solver.
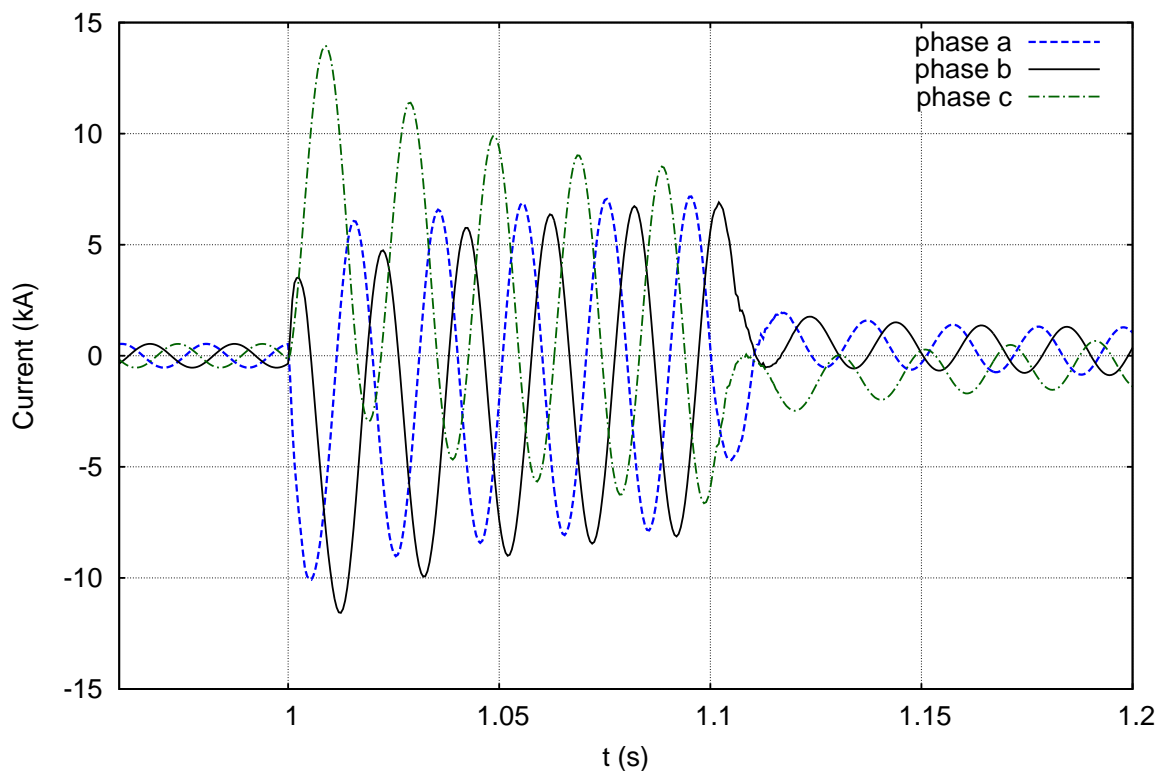
Figure 5.31: Case 1: Currents at boundary bus 4043 (EMTP-RV).
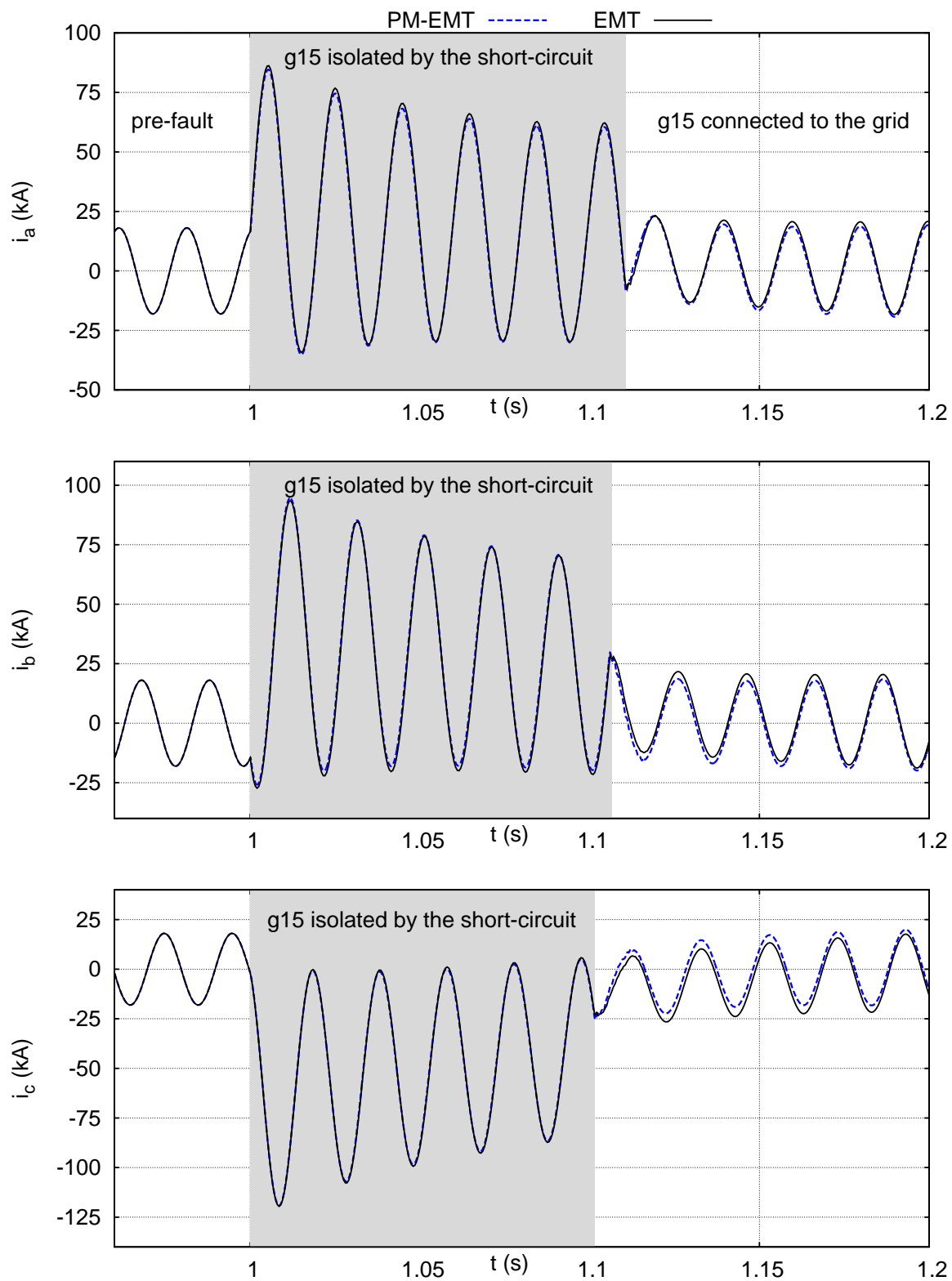
Figure 5.32: Case 1. Machine g15 phase currents.
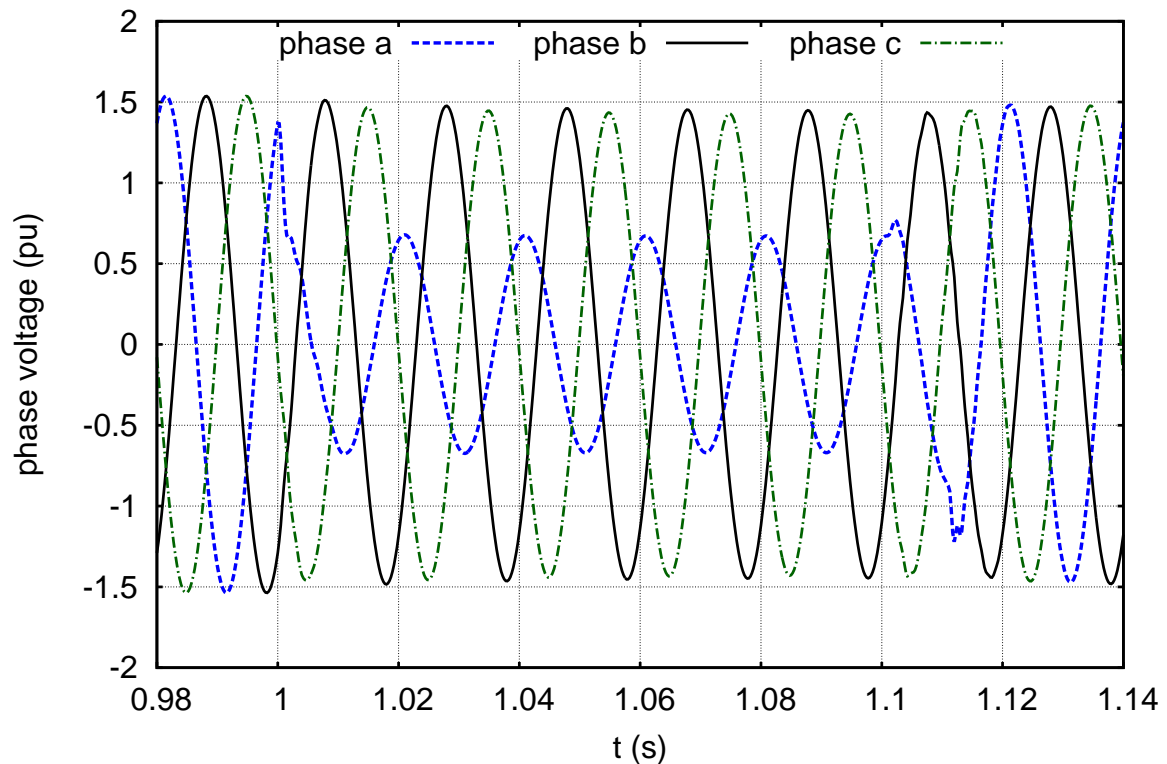
Figure 5.33: Case 2. Three-phase voltages at the boundary bus 4043.

5.7.2 Case 2: Single-phase five-cycle short-circuit very near bus 4047

EMT waveforms of the three-phase boundary voltages, showing the imbalance during the on-fault period, are shown in Figure 5.33. This is a complementary plot to Figure 5.7, where the currents flowing through the boundary bus could be observed. A relatively good match between the PM-EMT co-simulation and the EMT simulation is observed in the boundary voltage magnitudes (see Figure 5.34), which is not the case for the active and reactive powers flowing through the boundary bus 4043 (see Figures 5.35 and 5.36). While the electromechanical oscillations are observed to be correctly reproduced from the latter P and Q curves, the fault-on period reveals quite a large difference between PM-EMT and EMT curves. Finally, the phase currents flowing through the boundary bus 4043 are shown in Figure 5.37, and the ones injected into the grid by machine g15 are shown in Figure 5.38.
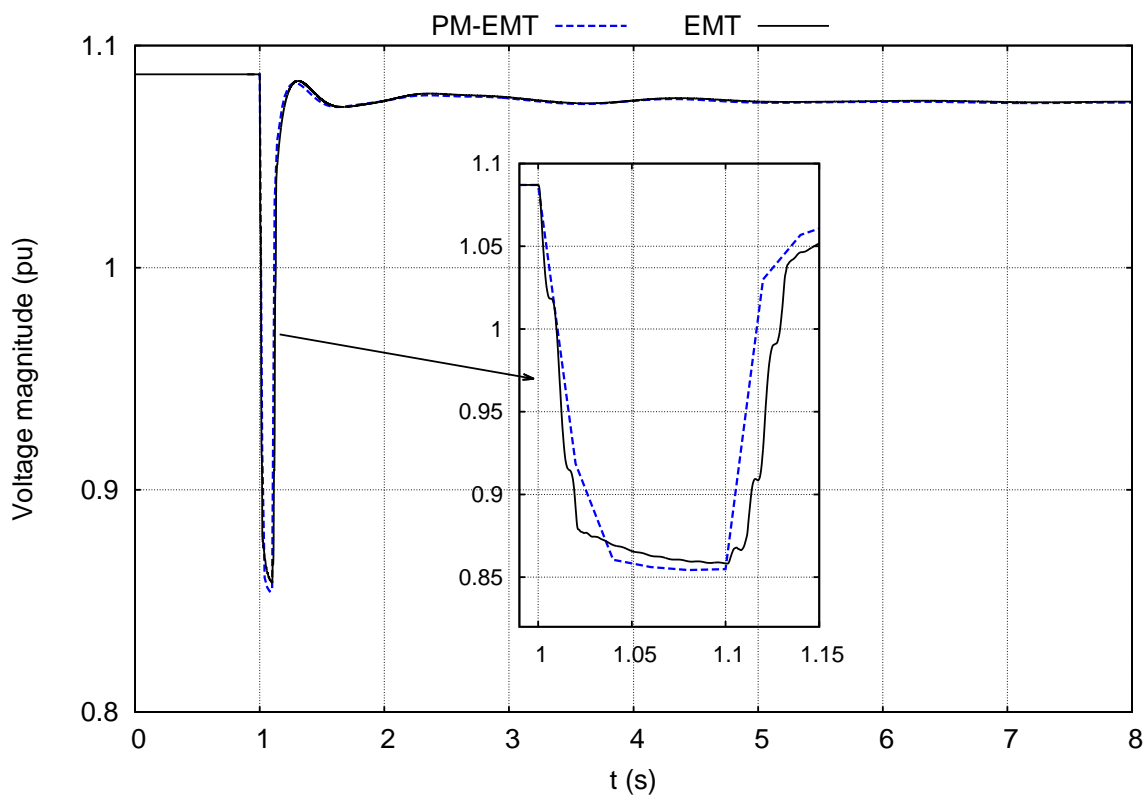
Figure 5.34: Case 2. Boundary bus voltage magnitude.
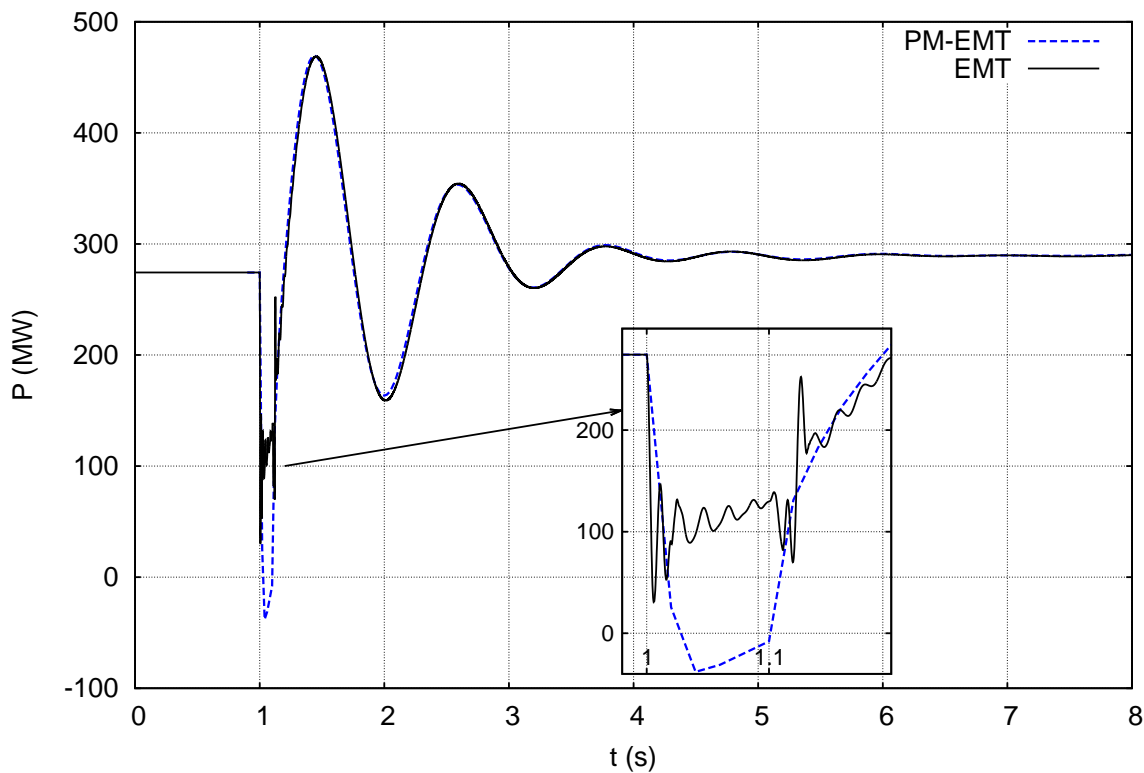
Figure 5.35: Case 2. Active power injected at boundary bus 4043.
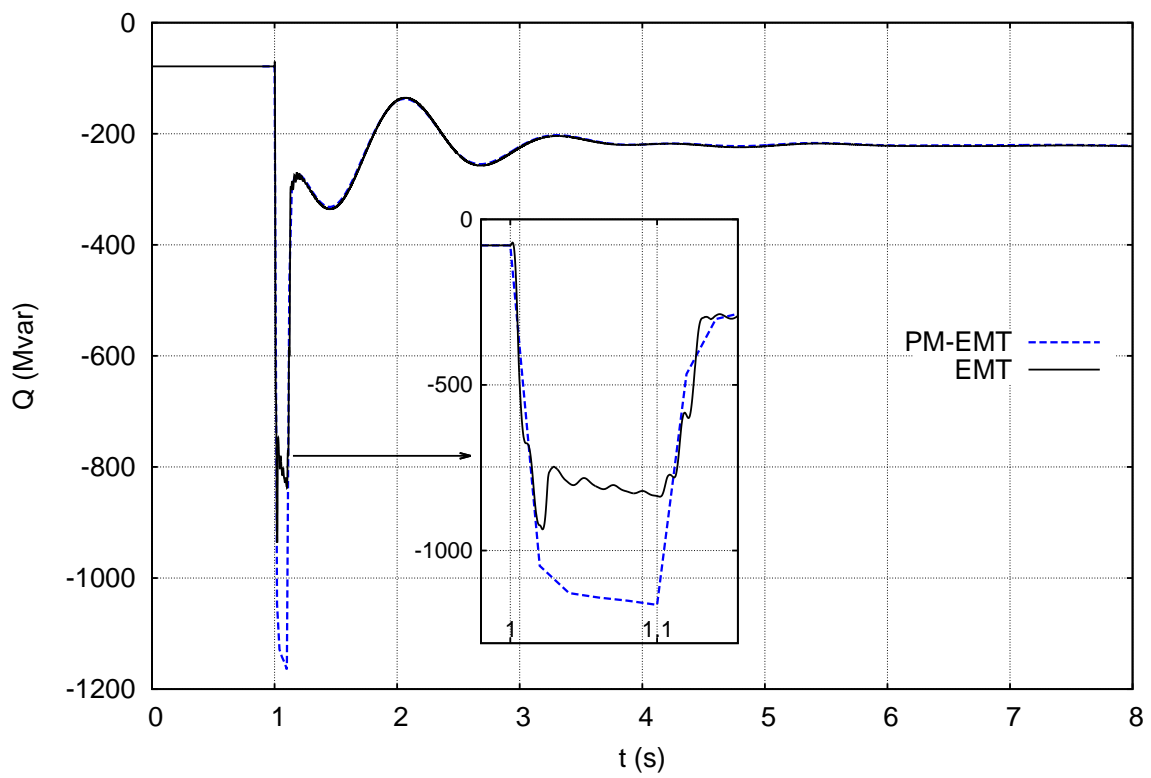
Figure 5.36: Case 2. Reactive power injected at boundary bus 4043.
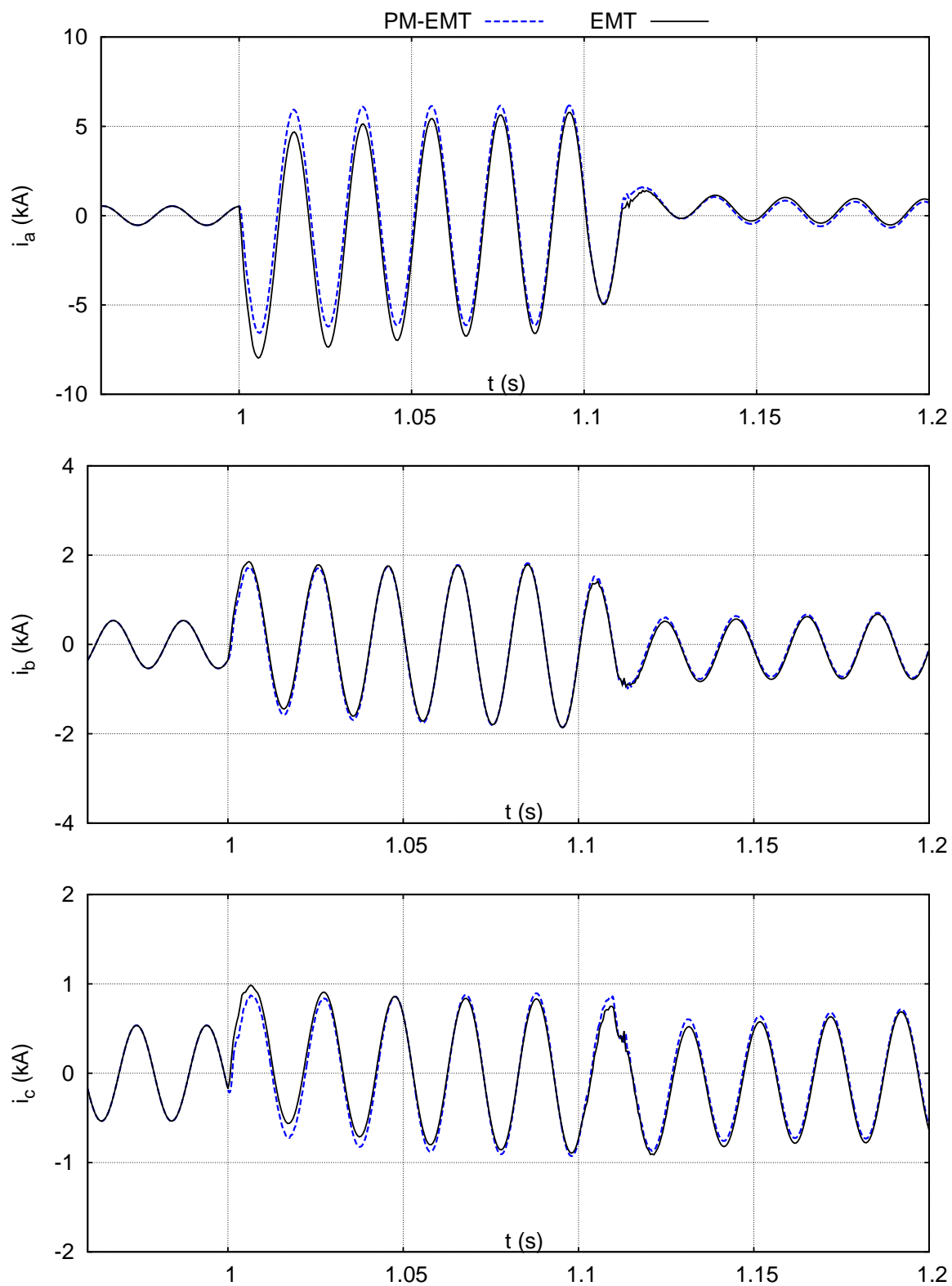
Figure 5.37: Case 2. Phase currents injected at boundary bus 4043.
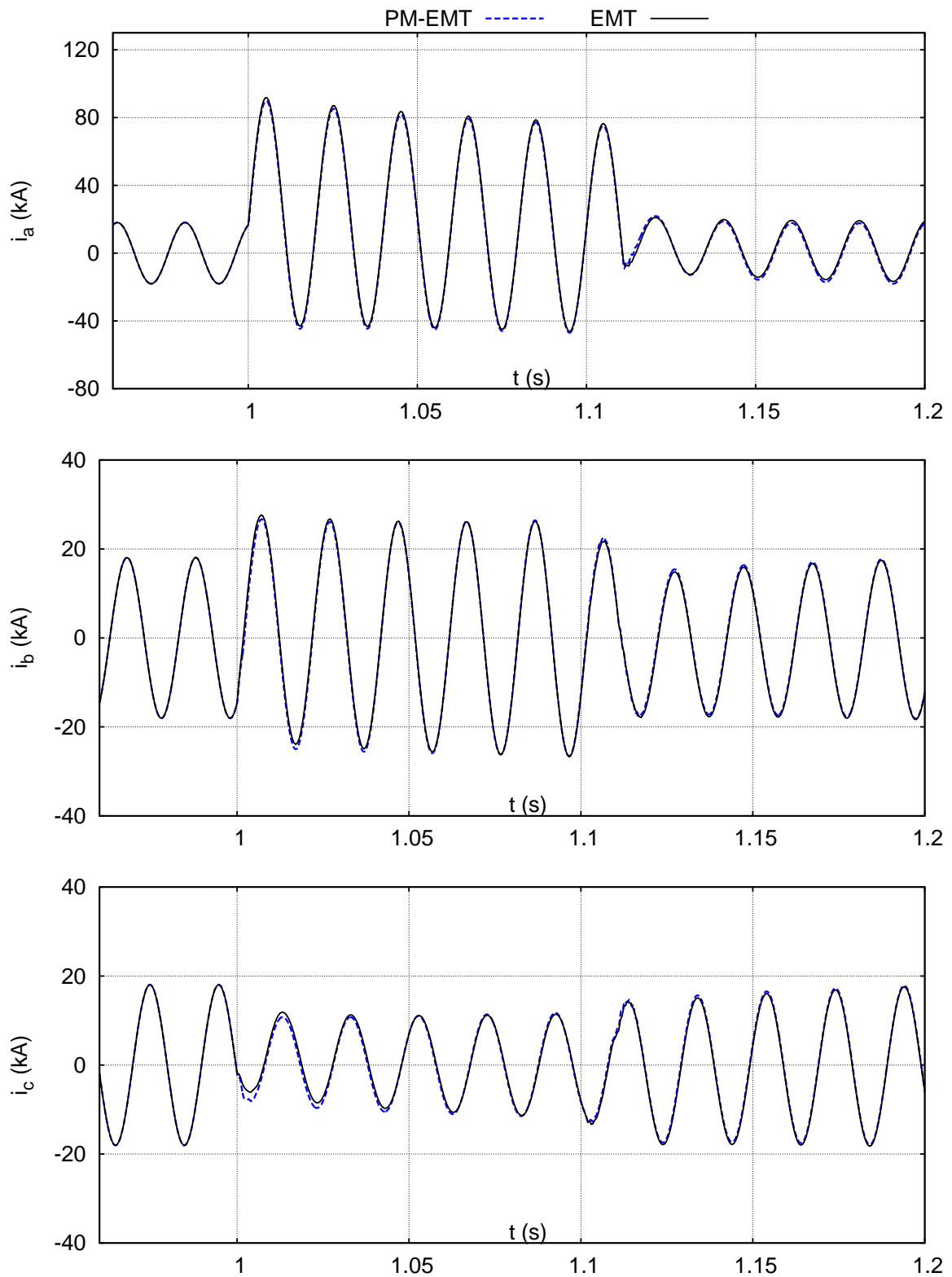
Figure 5.38: Case 2. Machine g15 phase currents.

5.7.3   Case 3a: Three-phase fault at bus 1042 cleared before critical time

Active and reactive powers injected at the three boundary buses are shown in Figure 5.39 and 5.40 respectively.   A fairly good match is observed between the PM-EMT and the EMT curves, while the PM solver introduces some delay at approximatively $t = 1.5$s. In the phase currents at boundary bus 4044, shown in Figure 5.41, an almost perfect match is observed for the faut-on period, spanning from $t = 1$s to $t = 1.21$s. Figures 5.42 and 5.43 present a zoom on a time interval near the fault inception and the fault clearing times, respectively.

Figures 5.44 and 5.45 show the relative error on the complex power transmitted at the boundary buses when restraining the number of evaluation of the EMT sub-system to a single evaluation, shown for zero and second-order predictions respectively. As explained in Section 5.6, the latter relative error is computed by comparison to a fully converged PM-EMT co-simulation. The comparison of the latter two figures illustrates the superiority of second-order prediction. The peaks at fault inception and clearing times are present in the two figures, since no prediction (or equivalently zero-order prediction) is used for the three time steps consecutive to those instants, i.e. zero-order predictions are used for both curves. However, the peaks between $t = 1.5$ and $t = 2$s, observed in Figure 5.44, are not present in Figure 5.45. After $t = 2$s, the error is too small compared to the simulation accuracy (10^{-4}) to observe any remarkable reduction. However, examining the curves with care shows that the maximum values observed around $t = 3$s, $t = 3.9$s, $t = 4.7$s, etc. are reduced through the use of a second-order prediction.   In this case, a non-iterative co-simulation is observed to be almost as accurate as a fully converged simulation, since the maximum relative error is below 0.1 percent.
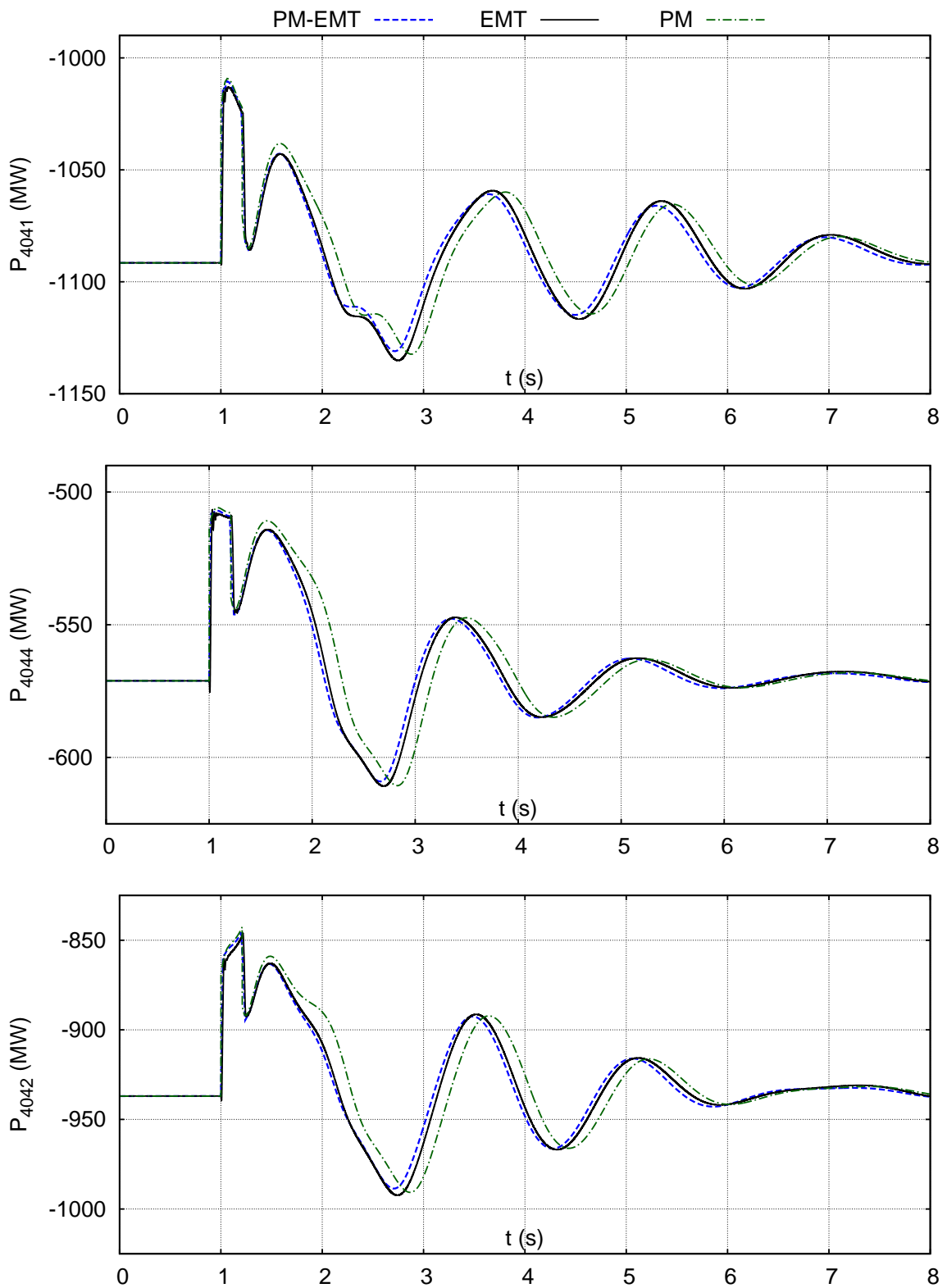
Figure 5.39: Case 3a: Active powers injected at the boundary buses.
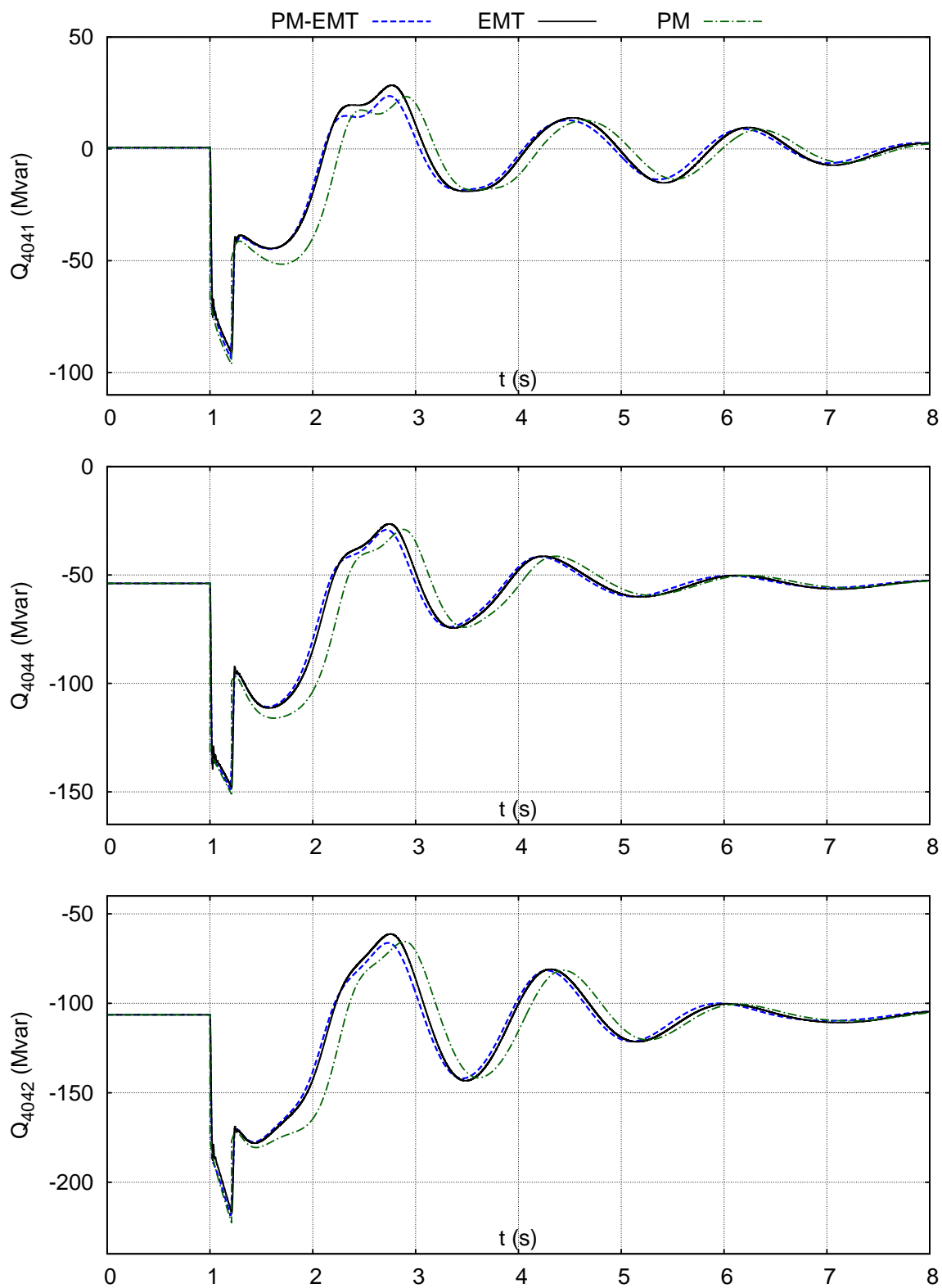
Figure 5.40: Case 3a: Reactive powers injected at the boundary buses.
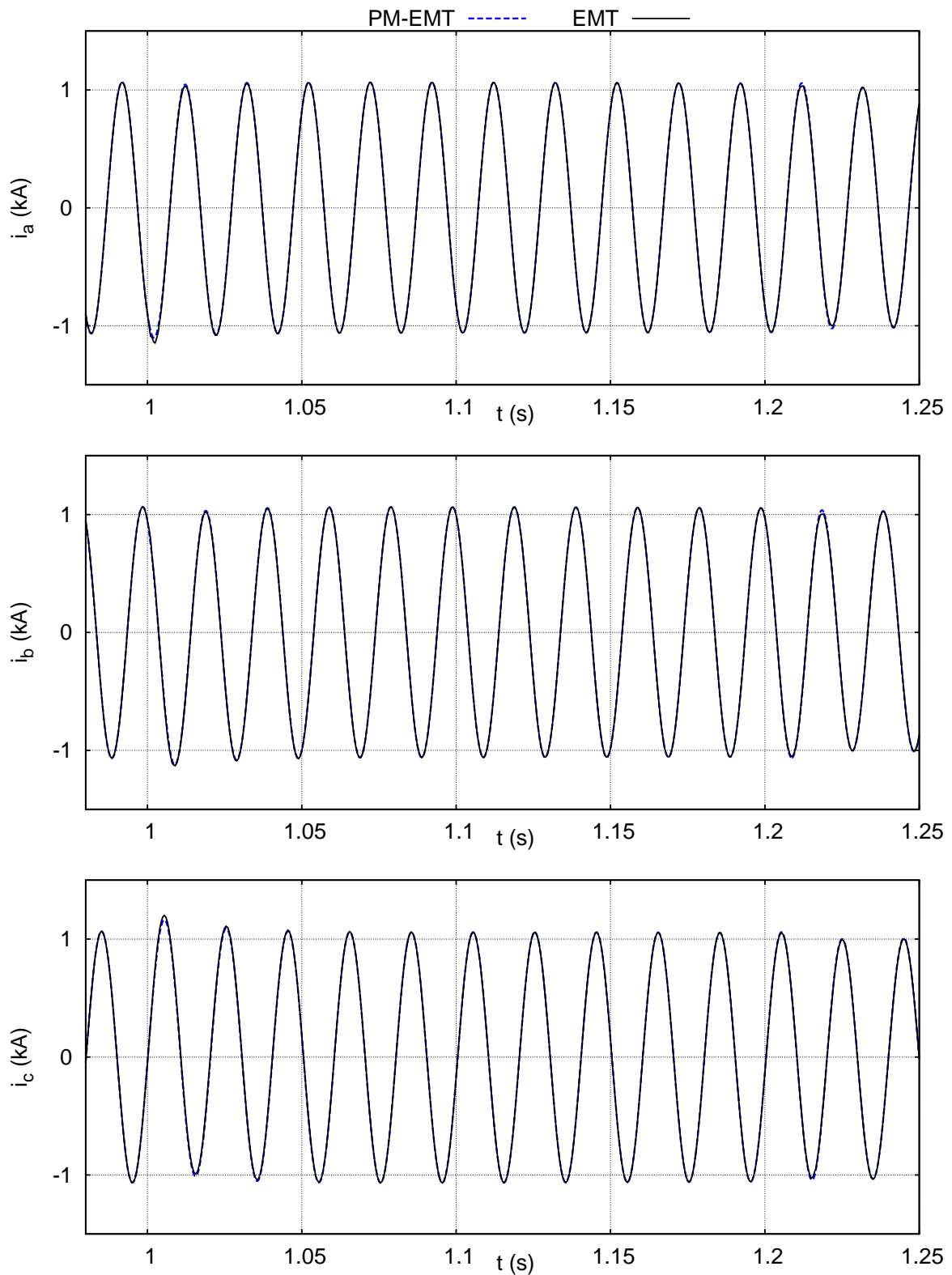
Figure 5.41: Case 3a: Phase currents at boundary bus 4044.
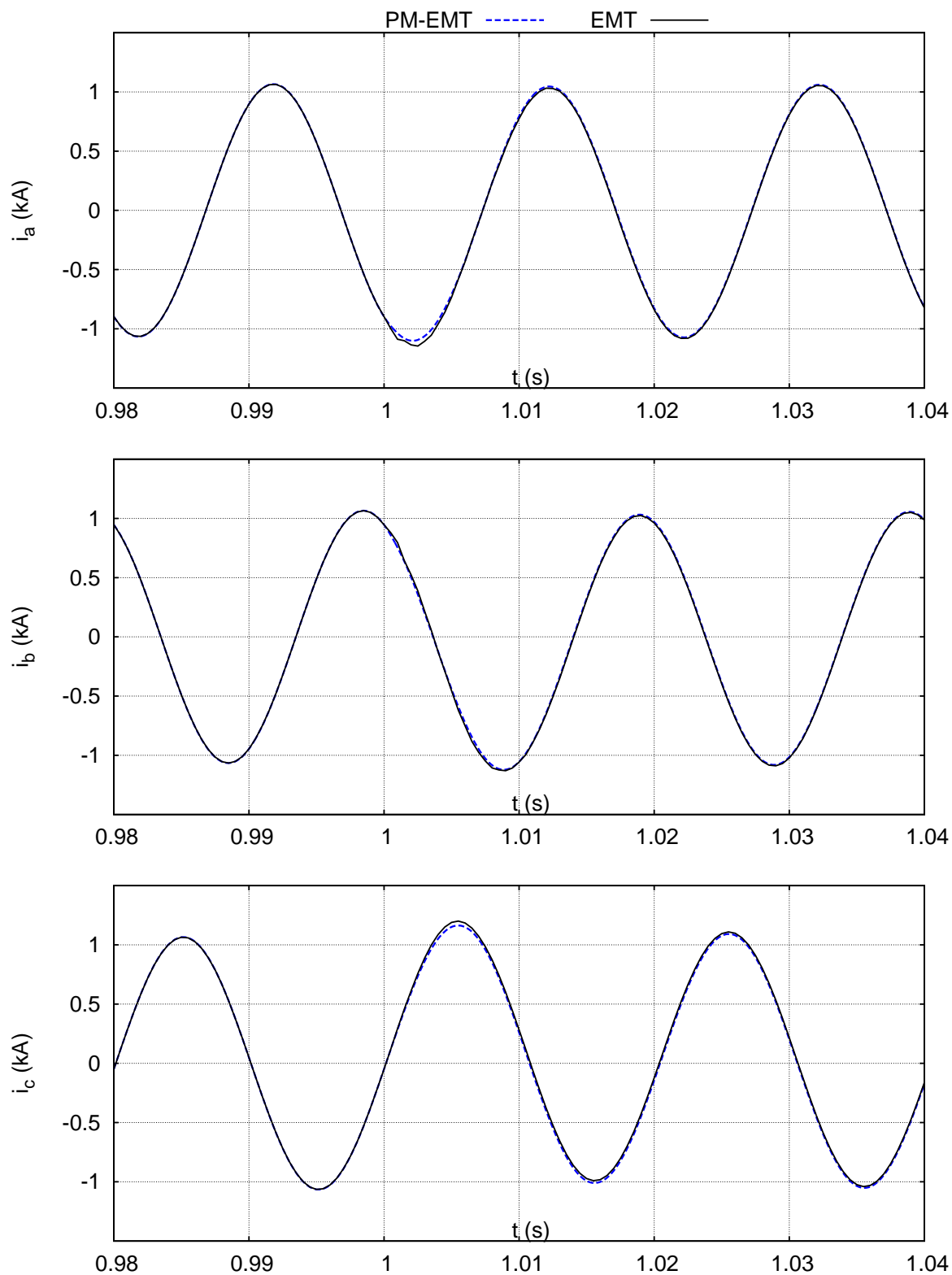
Figure 5.42: Case 3a: Zoom at fault inception ($t = 1\,$s) for the phase currents at boundary bus 4044.
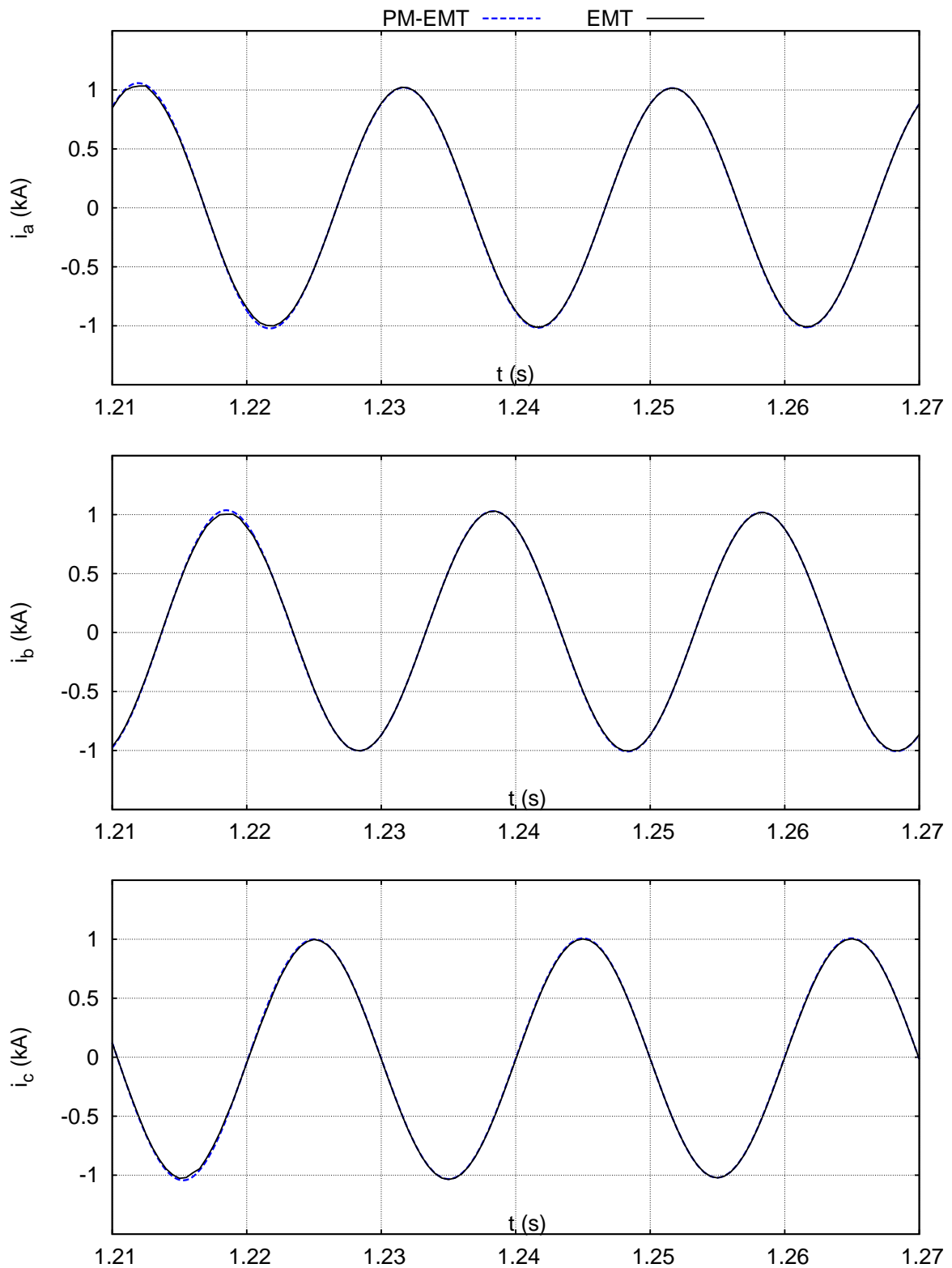
Figure 5.43: Case 3a: Zoom at fault clearing ($t = 1.21\,\text{s}$) for the phase currents at boundary bus 4044.
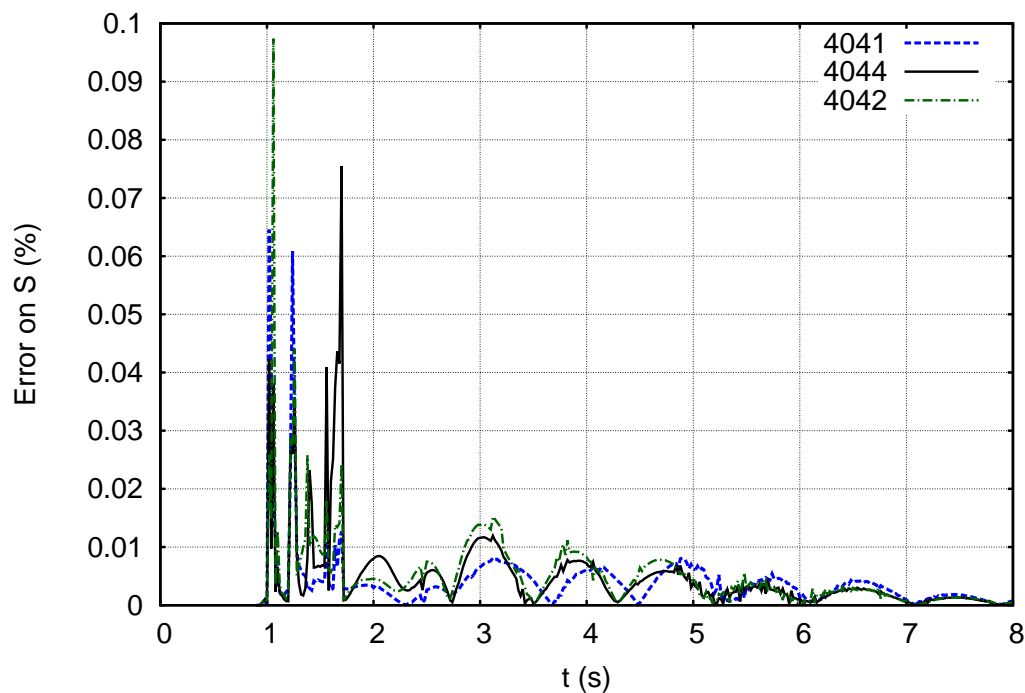
Figure 5.44: Case 3a: Relative error on complex power at the boundary buses when performing a single co-simulation iteration, with zero-order prediction and boundary conditions of type (d).
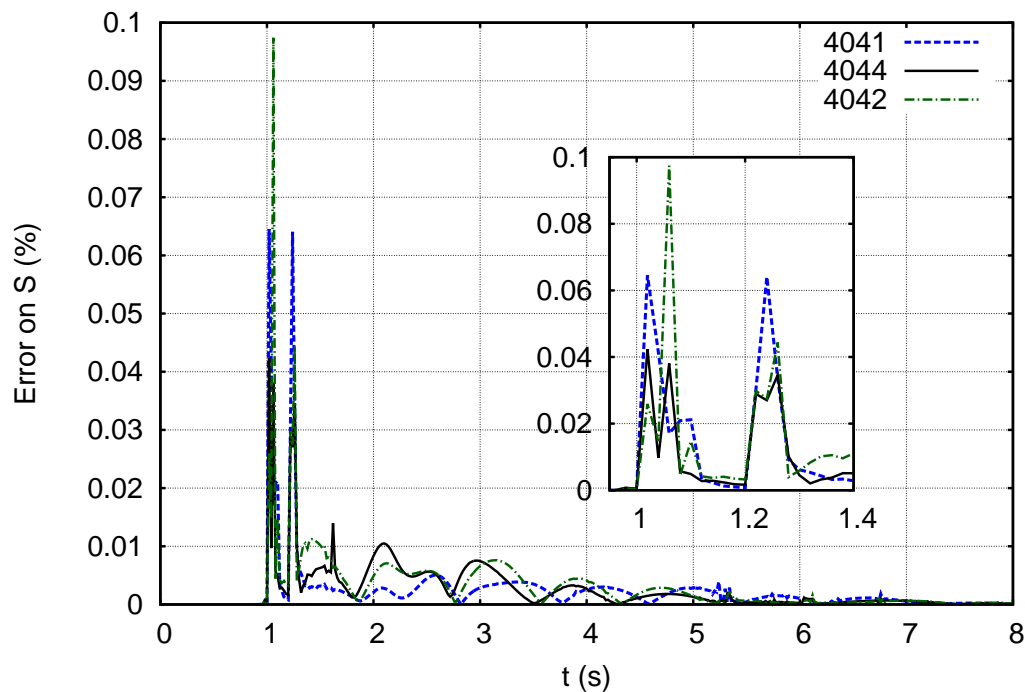
Figure 5.45: Case 3a: Relative error on complex power at the boundary buses when performing a single co-simulation iteration, with second-order prediction and boundary conditions of type (d).
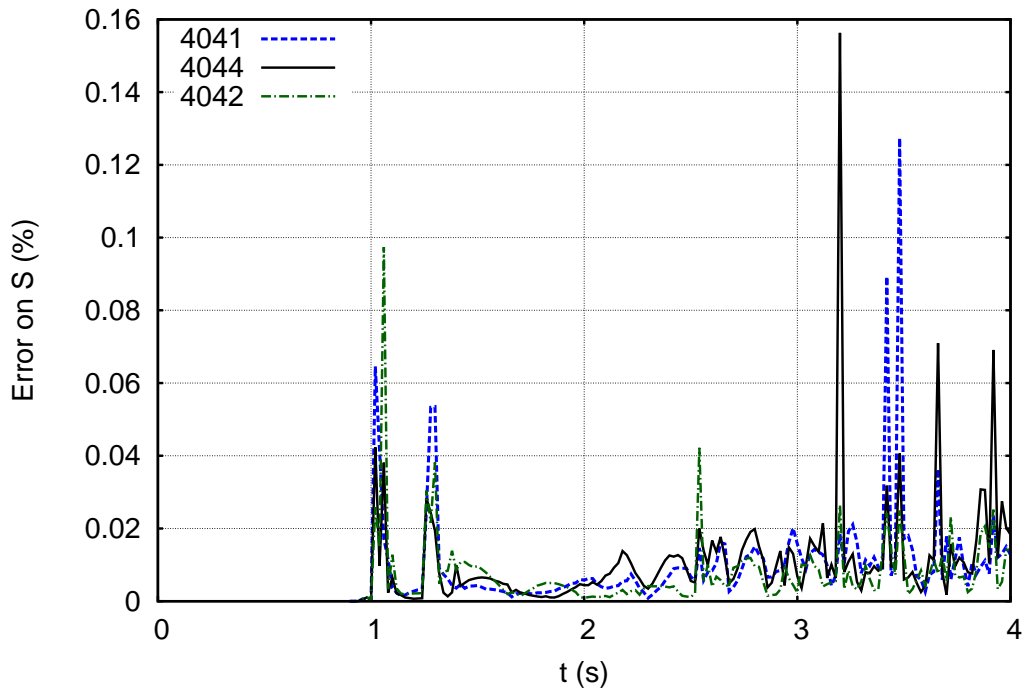
Figure 5.46: Case 3b: Relative error on complex power at the boundary buses when performing a single co-simulation iteration, with zero-order prediction and boundary conditions of type (d).

5.7.4 Case 3b: Three-phase fault at bus 1042, cleared after critical time

Figures 5.46 and 5.47 show the relative error on the complex power transmitted at the boundary buses, when performing a single co-simulation iteration, for zero and second-order predictions respectively. The comparison of the two figures, for which we kept the same graduations, illustrates the improved accuracy gained by using a second-order prediction on the boundary variables.
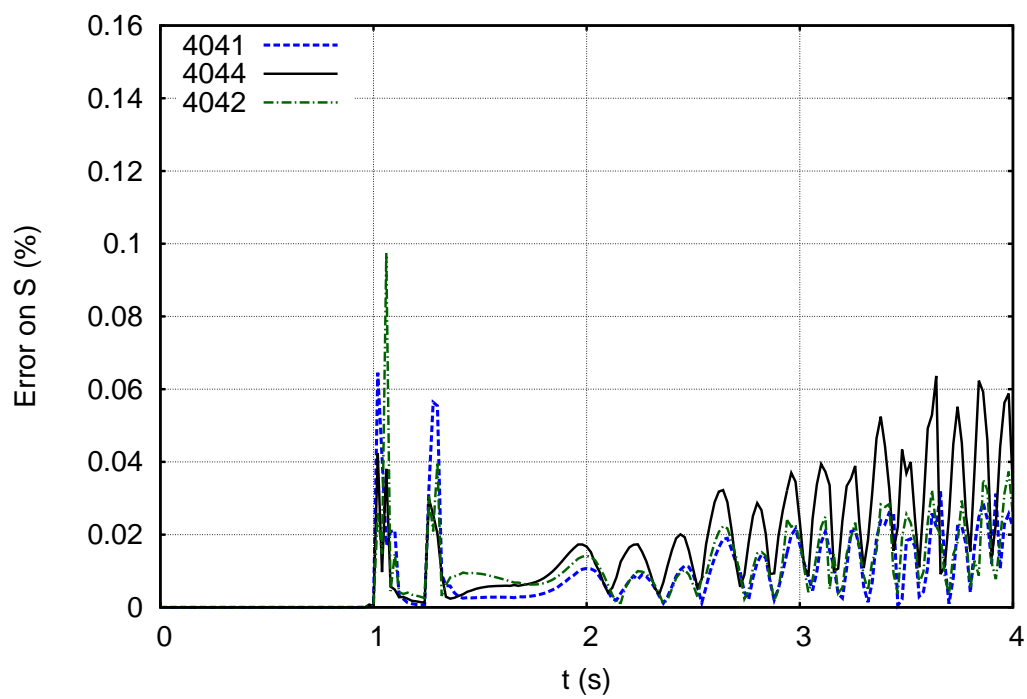
Figure 5.47: Case 3b: Relative error on complex power at the boundary buses when performing a single co-simulation iteration, with second-order prediction and boundary conditions of type (d).

5.7.5 Case 4: Single-phase 10.5-cycle fault on bus 1042

Active and reactive powers passing through the boundary buses are shown in Figure 5.48 and 5.49 respectively. A fairly good match is observed between the PM-EMT and the EMT curves.

Figure 5.50 shows the relative error on the complex power transmitted through the boundary buses, when performing a single co-simulation iteration, for second-order prediction.[1] We observe that apart from the fault inception and clearing times, the relative error is under $1/100$ percent, for all boundary buses. At fault inception and clearing, this error is under 0.25 percent. This is very low and should make it possible to use non-iterative PM-EMT co-simulation under the given conditions of prediction, boundary conditions, along with high quality PM-to-EMT and EMT-to-PM conversions.

5.7.6 Case 5: Tripping g9 in PM sub-system

Figures 5.51 and 5.52 show the relative error on the complex power transmitted through the boundary buses, when performing a single co-simulation iteration, for zero and second-order predictions respectively. Both figures involve boundary conditions of type (d).

In Figure 5.51, as expected, the error increases with time and stabilizes, with a sawtooth evolution. Such a sawtooth evolution of the error seems normal in non-dissipative simulation.

In Figure 5.52, an interesting case is shown where a "bad" (less accurate) step (around 12.5s), due to non-iterating the relaxation process, induces a reduced accuracy for the following time-steps. Note that co-simulation characterized by a single evaluation of the EMT sub-system however remains almost as accurate as the fully converged co-simulation.

---

[1]The error obtained with a zero-order prediction was almost identical and is not be shown here.
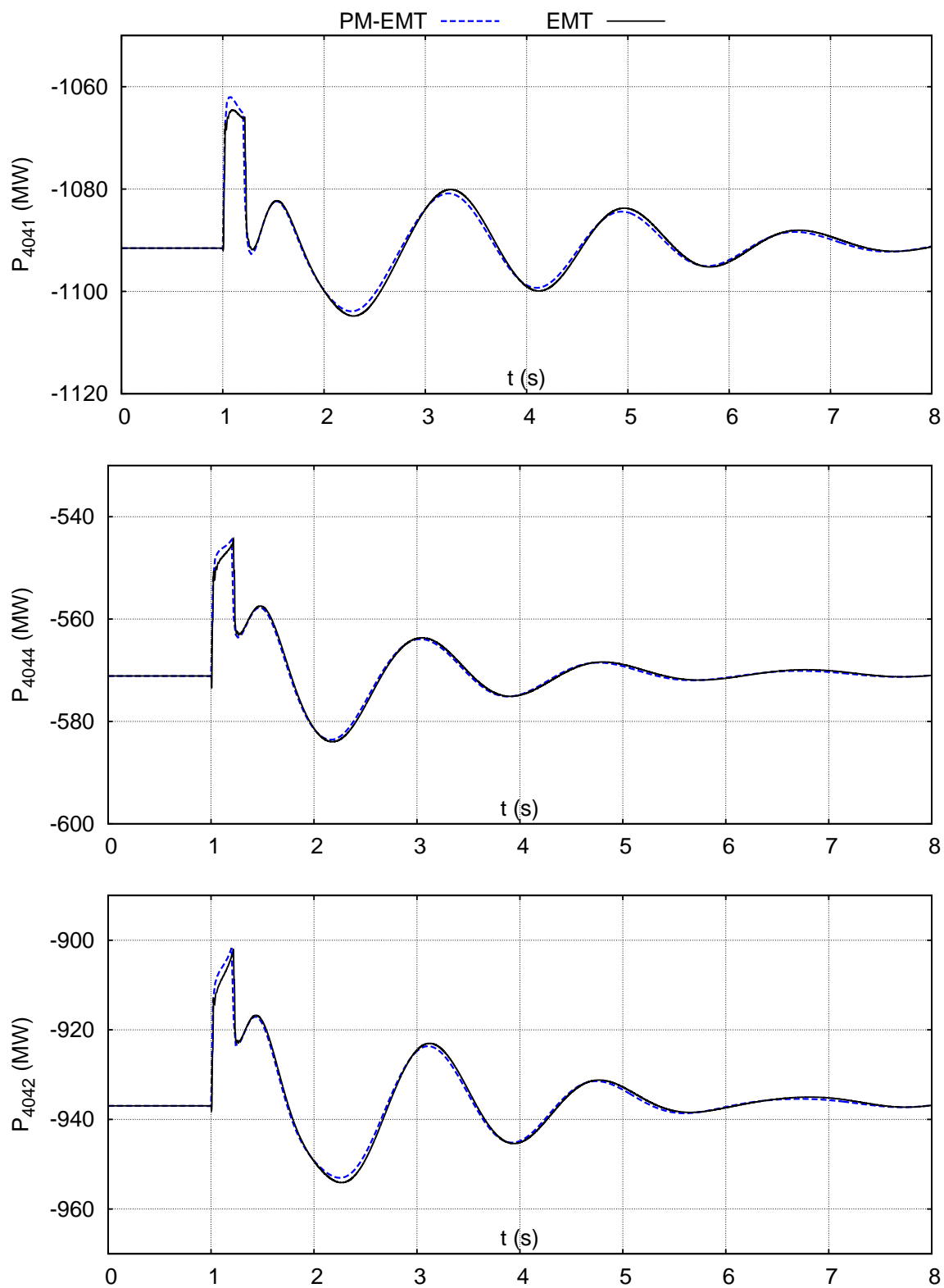
Figure 5.48: Case 4: Active powers injected at the boundary buses.
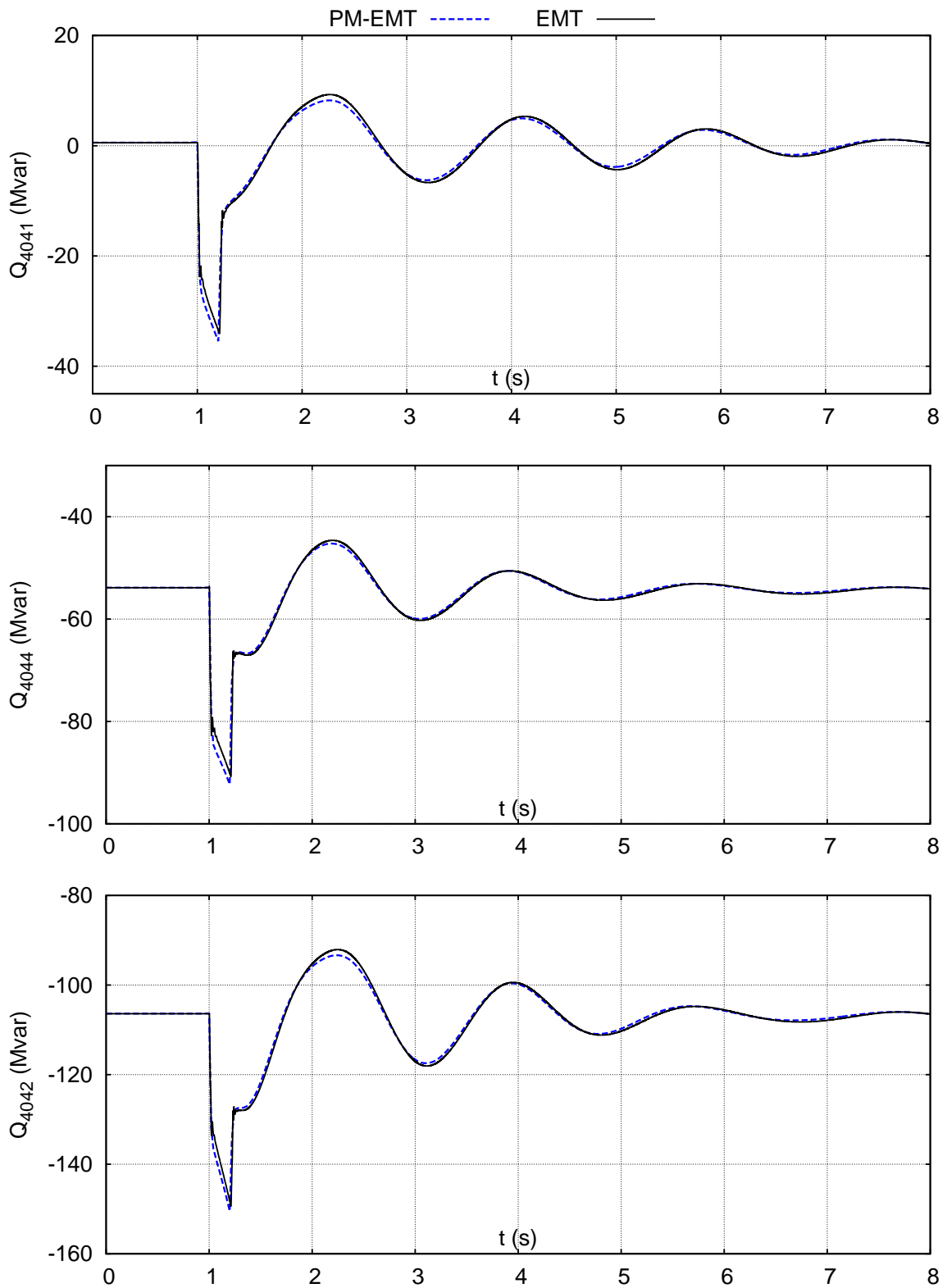
Figure 5.49: Case 4: Reactive powers injected at the boundary buses.
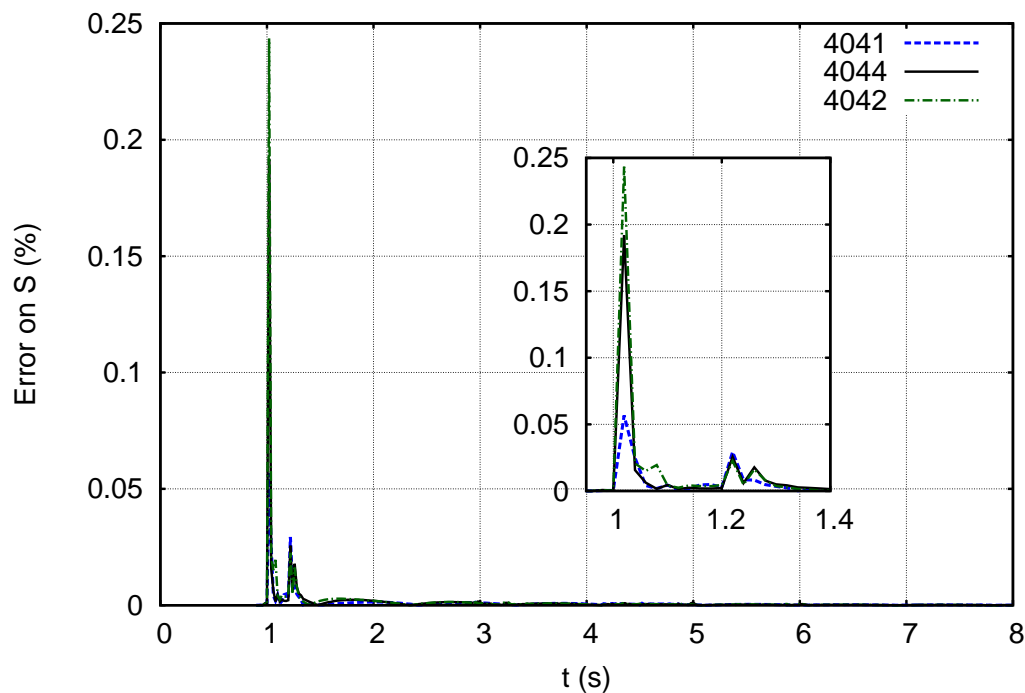
Figure 5.50: Case 4: Relative error on complex power at the boundary buses when performing a single co-simulation iteration, with second-order prediction and boundary conditions of type (d).
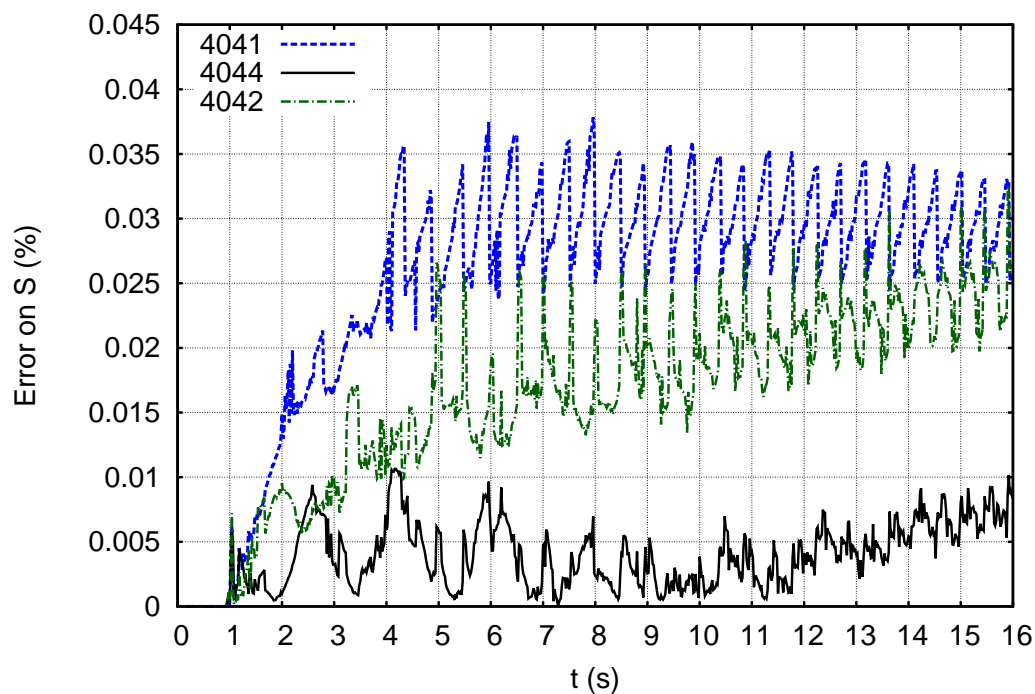
Figure 5.51: Case 5: Relative error on complex power at the boundary buses when performing a single co-simulation iteration, with zero-order prediction and boundary conditions of type (d).
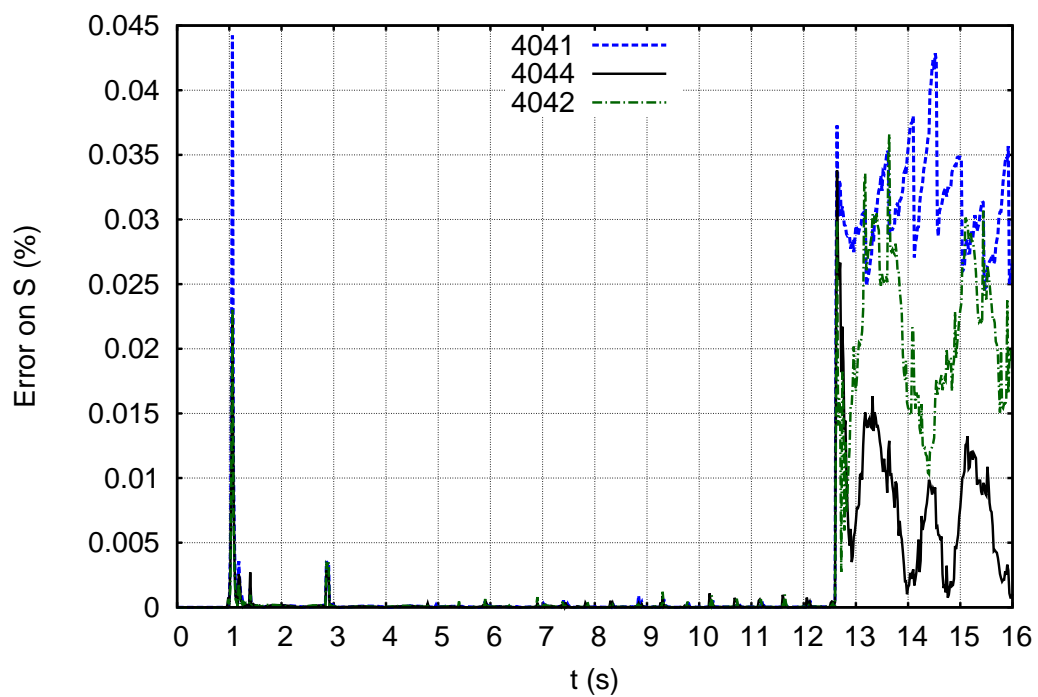
Figure 5.52: Case 5: Relative error on complex power at the boundary buses when performing a single co-simulation iteration, with second-order prediction and boundary conditions of type (d).

Conclusions and perspectives

6.1   Summary of work and contributions

In this thesis the coupling of PM and EMT simulations has been investigated. From the point of view of the EMT sub-system, the coupled PM solver can be considered as a high accuracy dynamic equivalent in the $[0 \ldots 5]$ Hz frequency range. From the point of view of the PM sub-system, the coupled EMT solver can be considered as an accurate model of a subnetwork together with the connected equipment. The PM-EMT co-simulation as a whole can be viewed as a time-domain simulation faster than a full EMT simulation of the same system, while being more accurate or more appropriate in terms of modeling than a full PM simulation of the same system. Moreover, a wider range of time evolutions (e.g. overvoltages, unbalanced waveforms, decaying DC component, ...) are revealed in the PM-EMT solution, which could not be obtained from a pure PM simulation.

We have studied several techniques to efficiently and accurately couple PM and EMT solvers. In Chapter 3, the coupling of PM and EMT solvers has been presented. The system topology has been treated first. It has been shown that all configurations of PM or EMT sub-systems could virtually be treated as a single PM sub-system connected to a single EMT sub-system (through multiple interface buses).

Various iterative schemes have been considered and it has been shown that, in the general case where the PM simulation is much faster than the EMT one, the most accurate and efficient iterative scheme is the Gauss-Seidel sequential coupling of the two solvers (see Section 3.2.3), with the PM solver being executed first. This last point is one of our contributions, which shows to be very important for the case where the EMT solver would be executed once per time step only. Dealing with the PM sub-system first gives the opportunity to solve the PM sub-system twice per time step (see Figure 3.10), which greatly enhances the accuracy (see Section 5.6).

Various boundary conditions for coupling the PM and the EMT models have been reviewed in Section 3.3. The literature has been thoroughly examined to evaluate which boundary conditions have been contemplated (see Table 3.2). A physical interpretation of the boundary conditions has been given (see Figure 3.15. Overlapping sub-systems have been proposed for completeness only

(see Section 3.3.2) but this option was not retained in the work. A comparison of the convergence obtained with different boundary conditions has been given. It was illustrated through simulation results in Section 3.7. For correctness of the boundary conditions and accuracy of the coupling, it is recommended to update with frequency the impedances used in the model of the PM sub-system in the EMT simulation (see Section 3.8). The frequency of concern is obtained from the interface current at each boundary bus.

In order to further improve the accuracy obtained from a non-iterative scheme (or equivalently to reduce the number of iterations in a full relaxation scheme), extrapolation techniques have been considered, in Section 3.4. Second-order prediction in time was shown to give a noticeable convergence improvement, at a negligible computational cost (see Section 3.4.1). Prediction between iterations of the same time step is not relevant due to the small number of iterations required to reach convergence (see Section 3.4.2).

A summary of the presented coupling techniques has been proposed in Table 3.3. This is a key table since it summarizes the characteristics of the relaxation algorithm developed in this research.

In Chapter 4, the techniques for interfacing PM and EMT results have been thoroughly analyzed. The PM-to-EMT conversion, called "interpolation" has been presented in Section 4.1, after a literature review (see Table 4.1). Linear interpolation of the magnitude and phase angles of the Thévenin voltage sources involved in the PM boundary conditions has been shown to be adapted to all practical cases of interest (pre-fault, fault inception, fault-on, ...). Attention has been drawn on a problem that may arise when interpolating phase angles crossing the π value.

Section 4.2 has been devoted to the positive-sequence phasor extraction from the evolutions of the three-phase voltages and currents at the boundary buses. First, a series of small cases has been explored, with increasing complexity. On these examples, the most accurate method has been identified to be the least-squares fitting of a quasi-cosine waveform including an exponentially decaying DC component. By its principle, this method produces no delay at all between the phasors extracted from the EMT simulation and the PM ones. The latter method relying on a time interval, it has been shown that it is not suited to phasor extraction from "broken" waveforms. Such waveforms arise for instance at fault inception, elimination, or in general after discrete events. In this case, a method such as the projection on synchronously rotating axes, where the extracted phasor is obtained from a single point of the waveforms (see Section 4.2.2), is recommended. Our subsequent simulation results have been produced by a combination of two extraction methods: the projection on synchronously rotating axes at fault inception and elimination time-steps, and the least-squares fitting of a quasi-cosine waveform including an exponentially decaying DC component, for the rest of the time.

Finally, in Chapter 5 simulation results have been presented. They have been obtained from the Nordic test system, with respectively a single and multiple boundary buses. When the number of boundary buses was increased, a reduction of the number of iterations to reach convergence was observed. Two factors may explain this observation. The first one is the quality of the multi-

port Thévenin/Norton equivalents used for the boundary conditions and the fact that first-order boundary conditions were used on both PM and EMT sides. The second factor is the increased electrical distance between the PM-EMT boundary and the disturbance, located in the EMT sub-system. A comparison of four different boundary conditions has been carried out for all test cases. The best boundary conditions, in terms of convergence speed and accuracy, are consistently the both-sided first-order (multiport Thévenin/Norton equivalent) ones. The zero-, first- and second-order prediction in time have been also tested. A comparison of the convergence speed is in favour of the second-order predictions, as expected (second-order predictions are used through the whole simulation, except at fault inception and elimination, where a zero-order prediction is used).

6.2 Directions for future work

Several directions for future work are suggested hereafter.

- An intermediate layer with three-phase phasor models in PM simulation could be added as sketched in Figure 6.1, to better take into account the phase imbalance still present at the boundary. Alternatively, the whole PM sub-system could be represented with a three-phase model, as suggested in Figure 6.2. Such a simulation has been recently considered in [HV15]. In such a model, the rotor dynamics of synchronous generators are considered only in the positive-sequence while the negative- and zero-sequence are modeled by impedances only. The other components, such as lines and loads, are represented in three-phases.

- A hybrid PM-Dynamic Phasor simulation could be contemplated, with the DP simulation performed in three-phase (see Section 2.3.1). While keeping almost full EMT accuracy on the detailed sub-system, the DP has the advantage over EMT that it directly gives voltage and
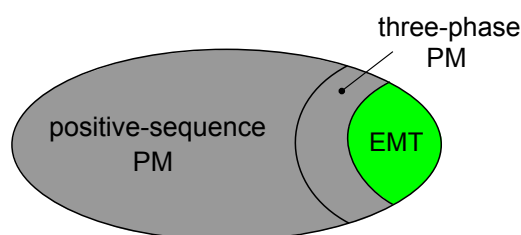
Figure 6.1: Intermediate three-phase PM layer in PM sub-system.
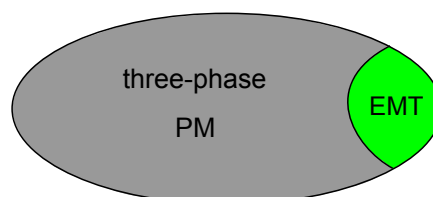
Figure 6.2: Three-phase PM sub-system coupled to EMT sub-system.

current phasor solutions at the boundary. Boundary voltage and current phasor extraction (from boundary abc voltage and current waves) would not be needed anymore in such an approach, or at least it would become very simple.

- In this work, the PM-EMT boundary has been chosen beforehand and the test cases have been selected for the given PM and EMT sub-systems. It would be of interest to search for strategies to identify automatically the PM and EMT sub-systems suitable for a given event, in a given network. Enlarging the EMT sub-system will generally mean increasing the number of interface buses. Further investigations are needed to check the convergence properties in the case of many interface buses, say for instance 20 buses. In our opinion, increasing the number of interface buses should not lead to convergence problems.

- In [Abh11] the author proposed to switch to PM-only simulation after the system has come back to (three-phase balanced) steady state operation. This is not applicable in all cases. For instance, it is not applicable when the PM model of a component has not yet been established or validated, while an EMT model is available. Furthermore, this requires changing the model of the detailed sub-system from EMT to PM and may entail a complex initialization procedure. However, from a research point of view, the idea of switching to PM-only simulation some time after a disturbance should not be put aside. The advantages of such an approach should be studied in greater detail on several application scenarios. Strategies to determine the appropriate switching time should also be investigated.

- It could be interesting to use a coarse EMT solver (same EMT solver with bigger time step size and/or lower order time-stepping method and/or limited number of iterations of the Newton solver[1]) for a first, rough, evaluation of the EMT solution (as is done in Parareal techniques [GDP+15, CM11]). This could yield a high accuracy at the first evaluation of the fine EMT solver. A possible interaction protocol is shown in Figure 6.3 where the first evaluation of the fine EMT solver is referred by the arrow numbered 6. A parallel implementation could use the coarse EMT and the PM solver for the first iteration in order to give the first boundary condition to both EMT and PM solvers as shown in Figure 6.4. The whole procedure would be repeated at each next time step H.

- Finally, concerning phasor extraction, automatic switching between least-squares fitting (of a quasi-cosine waveform including an exponentially decaying DC component) could be designed and implemented based on the residuals of the least-squares curve-fitting procedure. This would allow taking advantage of the high accuracy of the least-squares fitting technique. Also, an automatic procedure could be devised to process the proper number of previous EMT time intervals in case the PM time step size is chosen much smaller than a period at fundamental frequency (see Figure 4.7). Note that for efficiency reasons, reducing the PM

---

[1]In general, a coarse solver may involve solving models based on simplified underlying physics. This solution does not seem practical for a coarse EMT solver.
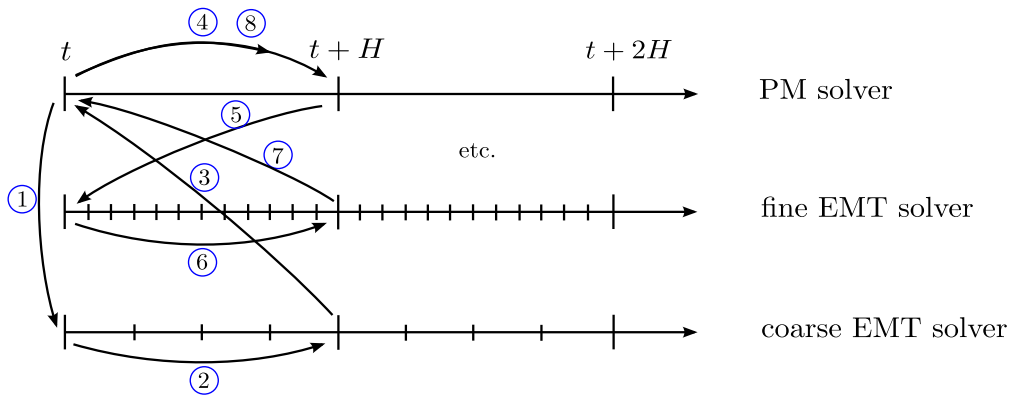
Figure 6.3: Serial PM-EMT simulation. Use of a coarse EMT solver.
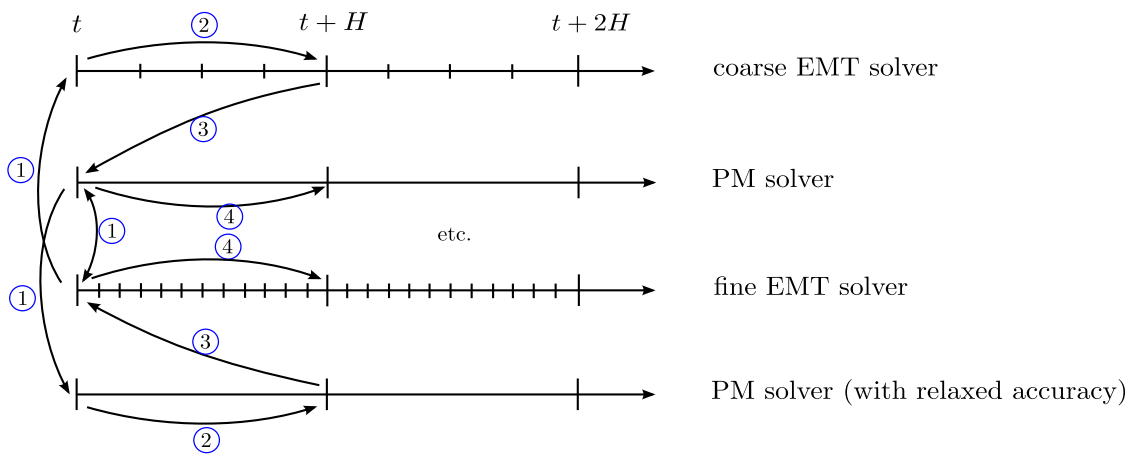
Figure 6.4: Parallel PM-EMT simulation. Use of coarse PM and EMT solvers.

time step size is generally not desired in PM-EMT co-simulation since it increases the number of PM sub-system evaluations, without significantly improving the simulation accuracy. However, this feature could easily be added to the PM-EMT co-simulation protocol.

Models used

A summary of the models used in PM and in EMT sub-systems is presented in Table A.1.

Table A.1: Main characteristics of the implemented models.

	EMT	PM
Synchronous machines	2 d-axis and 2 q-axis rotor windings	same model with transformer voltages neglected
	simplification: saturation ignored	
Transformers	transformer ratio & leakage inductance	
	simplifications: no copper losses, no saturation	
Lines	constant pi model	
Loads	constant impedance model	
Breakers	open each phase at zero-crossing	no distinction between phases

The loads are modeled as constant impedances and the lines with nominal PI section model, for simplicity and without lack of generality.

A.1 Electromagnetic transients models

A.1.1 Transformers

Three-phase transformers are modeled using a Ygyg connection of three single-phase models, such as the one represented in Figure A.1.

A.1.2 Loads

Loads are modeled using the representation of Figure A.2.
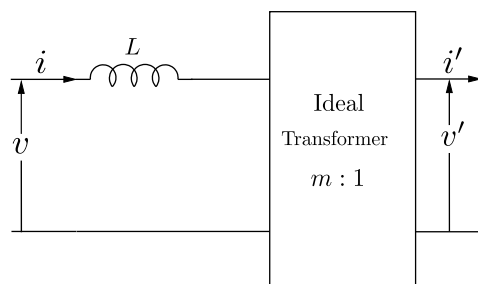
Figure A.1: Equivalent circuit of a two-winding transformer, without magnetising branch [WA03].
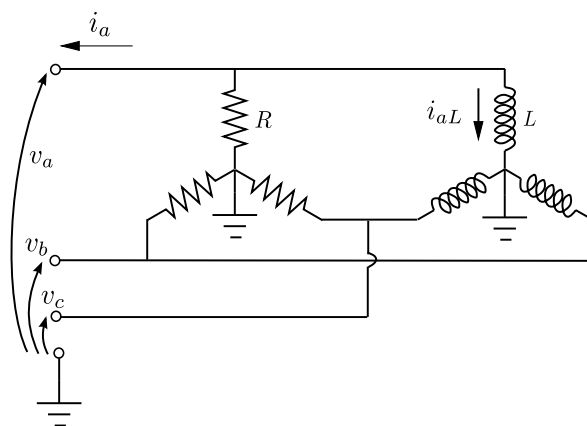
Figure A.2: Impedance load.

A.1.3 Breakers and short-circuits

Three-phase breakers and short-circuits are modeled using three models such as the one of Figure A.3.
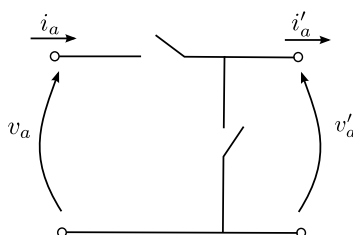
Figure A.3: Single-phase breaker and short-circuit.

A.1.4 Shunts

Shunts are modeled using the configuration of Figure A.4.
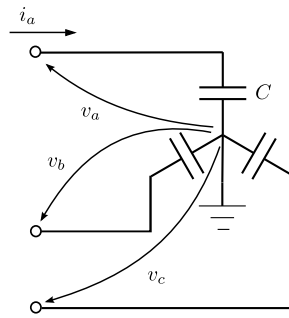
Figure A.4: Shunt.

A.1.5 Synchronous Machines

In order to have a single model, whatever the number of rotor windings, we use "model switches", i.e. integer parameters such as $S_{d1} = 1$ if there is a damper winding $d1$, $S_{d1} = 0$ otherwise, and similarly for $q1$ and $q2$.

The table below shows usual models and their corresponding values of switches:

model	switches
detailed, round rotor	$S_{d1} = 1$, $S_{q1} = 1$, $S_{q2} = 1$
detailed, salient pole	$S_{d1} = 1$, $S_{q1} = 1$, $S_{q2} = 0$
simplified, no damper	$S_{d1} = 0$, $S_{q1} = 0$, $S_{q2} = 0$

Synchronous machines in EMT sub-system are all round-rotor machines, except the synchronous condenser $g13$ [IEE15]. They are represented with four rotor windings (f, $d1$, $q1$, $q2$), i.e. $Sd1 = Sq1 = Sq2 = 1$.

Stator Park equations

$$\frac{d\psi_d}{dt} = \omega_s \left(-v_d - R_a\, i_d - \dot{\theta}\psi_q \right) \tag{A.1}$$

$$\frac{d\psi_q}{dt} = \omega_s \left(-v_q - R_a\, i_q + \dot{\theta}\psi_d \right) \tag{A.2}$$

$$\frac{d\psi_o}{dt} = \omega_s \left(-v_o - R_a\, i_o \right) \tag{A.3}$$

Rotor flux-currents relations

$$\frac{d\psi_f}{dt} = \omega_s \left(K_f v_f - R_f \frac{\psi_f - \psi_{ad}}{L_{lf}} \right) \tag{A.4}$$

$$\frac{d\psi_{d1}}{dt} = -\omega_s R_{d1} \frac{\psi_{d1} - S_{d1}\psi_{ad}}{L_{ld1}} \tag{A.5}$$

$$\frac{d\psi_{q1}}{dt} = -\omega_s R_{q1} \frac{\psi_{q1} - S_{q1}\psi_{aq}}{L_{lq1}} \tag{A.6}$$

$$\frac{d\psi_{q2}}{dt} = -\omega_s R_{q2} \frac{\psi_{q2} - S_{q2}\psi_{aq}}{L_{lq2}} \tag{A.7}$$

where ψ_{ad} and ψ_{aq} are the air-gap fluxes.

A.1.5.1   Relationships between magnetic flux linkages and currents

All currents were eliminated except i_d, i_q and i_o which is coherent with the fact that we want to get i_a, i_b, i_c

$$0 = -\psi_d + L_l i_d + \psi_{ad} \tag{A.8}$$

$$0 = -\psi_q + L_l i_q + \psi_{aq} \tag{A.9}$$

$$0 = -\psi_o + L_{oo} i_o \tag{A.10}$$

A.1.5.2   Saturation model

$$0 = \psi_{ad} \left(\frac{1 + m \left(\sqrt{\psi_{ad}^2 + \psi_{aq}^2} \right)^n}{M_d^u} + \frac{1}{L_{lf}} + \frac{S_{d1}}{L_{ld1}} \right) - i_d - \frac{1}{L_{lf}}\psi_f - \frac{S_{d1}}{L_{ld1}}\psi_{d1} \tag{A.11}$$

$$0 = \psi_{aq} \left(\frac{1 + m \left(\sqrt{\psi_{ad}^2 + \psi_{aq}^2} \right)^n}{M_q^u} + \frac{S_{q1}}{L_{lq1}} + \frac{S_{q2}}{L_{lq2}} \right) - i_q - \frac{S_{q1}}{L_{lq1}}\psi_{q1} - \frac{S_{q2}}{L_{lq2}}\psi_{q2} \tag{A.12}$$

A.1.5.3   Rotor motion

$$\frac{d\theta}{dt} = \omega_s\, \omega \tag{A.13}$$

$$\frac{d\omega}{dt} = \frac{1}{2H} \left(K_m T_m - \psi_{ad} i_q + \psi_{aq} i_d \right) \tag{A.14}$$

A.1.5.4   Park transform for the currents and voltages at the connected bus

$$0 = -i_a + \sqrt{3}\sqrt{\frac{2}{3}}\left(\cos\theta\, i_d + \sin\theta\, i_q + \frac{1}{\sqrt{2}}\, i_o\right)$$

$$0 = -i_b + \sqrt{3}\sqrt{\frac{2}{3}}\left(\cos\left(\theta - \frac{2\pi}{3}\right) i_d + \sin\left(\theta - \frac{2\pi}{3}\right) i_q + \frac{1}{\sqrt{2}}\, i_o\right)$$

$$0 = -i_c + \sqrt{3}\sqrt{\frac{2}{3}}\left(\cos\left(\theta + \frac{2\pi}{3}\right) i_d + \sin\left(\theta + \frac{2\pi}{3}\right) i_q + \frac{1}{\sqrt{2}}\, i_o\right)$$

$$0 = -v_d + \frac{1}{\sqrt{3}}\sqrt{\frac{2}{3}}\left(\cos\theta\, v_a + \cos\left(\theta - \frac{2\pi}{3}\right) v_b + \cos\left(\theta + \frac{2\pi}{3}\right) v_c\right)$$

$$0 = -v_q + \frac{1}{\sqrt{3}}\sqrt{\frac{2}{3}}\left(\sin\theta\, v_a + \sin\left(\theta - \frac{2\pi}{3}\right) v_b + \sin\left(\theta + \frac{2\pi}{3}\right) v_c\right)$$

$$0 = -v_o + \frac{1}{\sqrt{3}}\frac{1}{\sqrt{3}}\left(v_a + v_b + v_c\right)$$

A.1.5.5   Unknowns-equations balance

The 14 unknowns are the stator currents i_d, i_q, i_o, stator flux components ψ_d, ψ_q, ψ_o, rotor flux components ψ_f, ψ_{d1}, ψ_{q1}, ψ_{q2}, air gap flux ($d-$and $q-$axis) ψ_{ad} and ψ_{aq}, rotor angle θ and speed ω.

They are balanced by:

- 9 differential equations: (A.1)-(A.7), (A.13)-(A.14)

- 5 algebraic equations: (A.8)-(A.12)

A.2   Phasor models

A.2.1   Transformers

Transformers are modeled with a single-phase equivalent such as the one shown in Figure A.1, but in phasor notation.

A.2.2   Loads and shunts

The phasor model of a constant impedance load is represented in Figure A.5. It is modeled through the following equation:

$$V_x + jV_y = -\left(R + jX\right)\left(I_x + jI_y\right)$$

where $Z = R + jX$ is the constant load impedance.

The load impedance is initialized such as to match the initial active power P_0 and reactive power Q_0 at initial bus voltage effective value V_0, making use of the following relations:

$$S = \bar{V}\,\bar{I}^*$$

where $\bar{I}^*$ is the complex conjugate of the current $\bar{I}$.
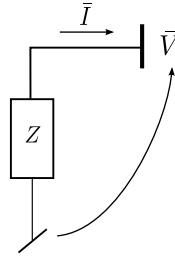
Figure A.5: Phasor model of a constant impedance load.

A.2.3 Synchronous Machines

The model used is the same as the one presented in Appendix A.1.5, neglecting in the stator Park equations (A.1)-(A.3) the transformation EMF $\frac{d\psi_{dq0}}{dt}$, as previously noted in Section 2.4.1. These fast dynamics being neglected, the ODEs (A.1)-(A.3) are being considered infinitely fast and are converted into the following AEs:

$$0 = \omega_s \left(-v_d - R_a\, i_d - \dot{\theta}\psi_q \right) \tag{A.15}$$

$$0 = \omega_s \left(-v_q - R_a\, i_q + \dot{\theta}\psi_d \right) \tag{A.16}$$

$$0 = \omega_s \left(-v_o - R_a\, i_o \right) \tag{A.17}$$

The fluxes ψ_{dq} change instantly due to a change in currents i_{dq}. The current i_o is considered to be instantly modified by a change in the voltage v_o.

More details about the implementation of the phasor model of synchronous machine in the Ramses software used for PM simulation may be found in [Fab12].

A.3 Models common to electromagnetic transients models and phasor approximation

A.3.1 Exciter, automatic voltage regulator and power system stabilizer

The bloc diagram represented in Figure A.6 combines the models of the exciter, the AVR and the PSS.

The exciter is the electrical machine needed to supply current to the field winding of a synchronous generator. Let us call v_i the input signal of the exciter block while its output signal is called v_{fd}. One has:

$$v_{fd} = \frac{1}{1 + \frac{1}{10}s} v_i \tag{A.18}$$

which means the exciter is represented by a $1/10$s time constant, with its output voltage limited to a 0 Volt lower limit and an L_2 upper limit where the values for L_2 may be found in [IEE15].

The AVR computes the error between the measured output RMS voltage V of the considered synchronous generator and its voltage setpoint V^o. The error signal $\epsilon = V^o - V + V_{PSS}$ passes

through a gain G and a transient gain reduction transfer function $\frac{1+sT_a}{1+sT_b}$. Again, the values for G, T_a and T_b for every generator of the Nordic test system are given in [IEE15]. A positive value of the error ϵ corresponds to a low voltage condition and will gives rise to an increased field voltage v_{fd}, which will in turn increase the voltage at the boundary of the synchronous generator.
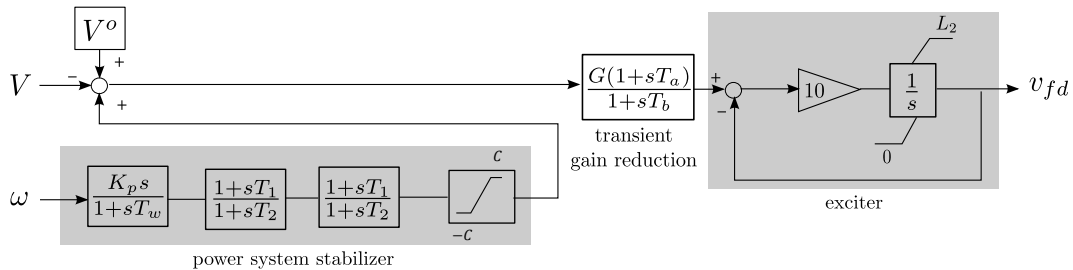
Figure A.6: Model of exciter, AVR and PSS.

Some disturbance in a large power system may lead to machines or groups of machines oscillating against each other for what concerns their synchronous speeds. The power system stabilizer role is to stabilize these inter-area oscillations.

A.3.2 Speed governor

The bloc diagram of the speed controller used for hydro-turbines is shown in Figure A.7. The inputs of the speed controller are the speed of the turbine ω and the mechanical power P given by the turbine. The speed controller output is the gate opening z set by the servomotor.
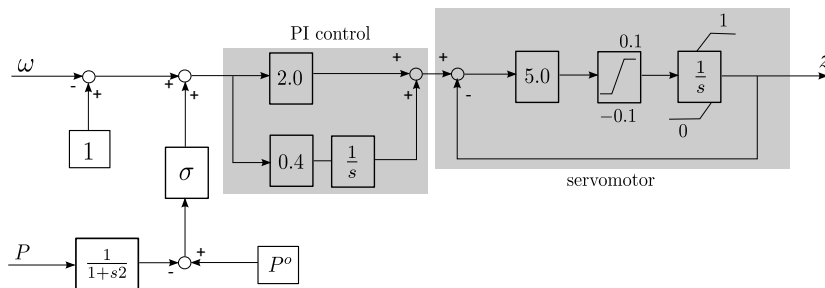
Figure A.7: Speed controller.

A.3.3 Turbine

While a constant mechanical torque is assumed for the machines of thermal plants, the hydraulic turbines are represented by the model of Figure A.8. In this model, the input z is the gate opening tuned by the servomotor ($0 \leq z \leq 1$), q the water flow, H the head, T_w the water time constant, P_m the mechanical power, ω the rotor speed in pu and T_m the mechanical torque.
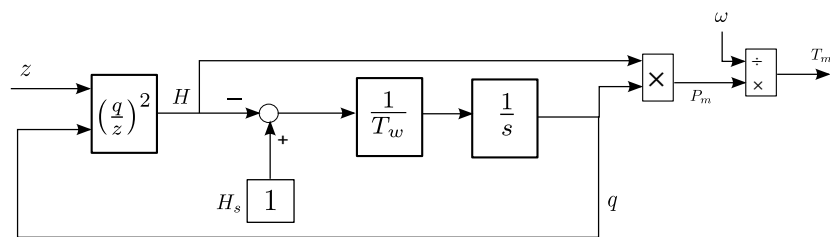
Figure A.8: Hydro turbine model.

Implemented MATLAB-EMT solver and Co-simulation layer

Our goal was to keep the compatibility with the parameter file format used by the PM solver. The parameter file with all the model information is first read and the equations are assembled. All variables are initialized, as schematically represented in Figure B.1. The parameter file containing all the information concerning the EMT sub-system is first analyzed and used to create all the necessary model information in the structure *allmodels*. The possible models are represented in Figure B.2. The names correspond to the following:

- "buses": buses characteristics,

- "tfos": transformers,

- "br_Rshorts": breakers and short-circuits

- lines: three-phase pi-model lines

- PMmodel: dynamically updated Thévenin equivalent of the PM sub-system

- KCLa: Kirchhoff Current Laws (phase a)

- loads: RL three-phase star-shape impedance loads

- gens: synchronous generators

- Cshunts: star-shape model of shunts

A file describing the observables to keep track of during the simulation, called for instance *obs_-EMT.dat*, is then read and interpreted by the procedure. A third file named for instance *methods.dat* containing information about the methods to use, e.g. the kind of boundary conditions or of extraction method or the tolerance of the EMT solver, is then read and the information is
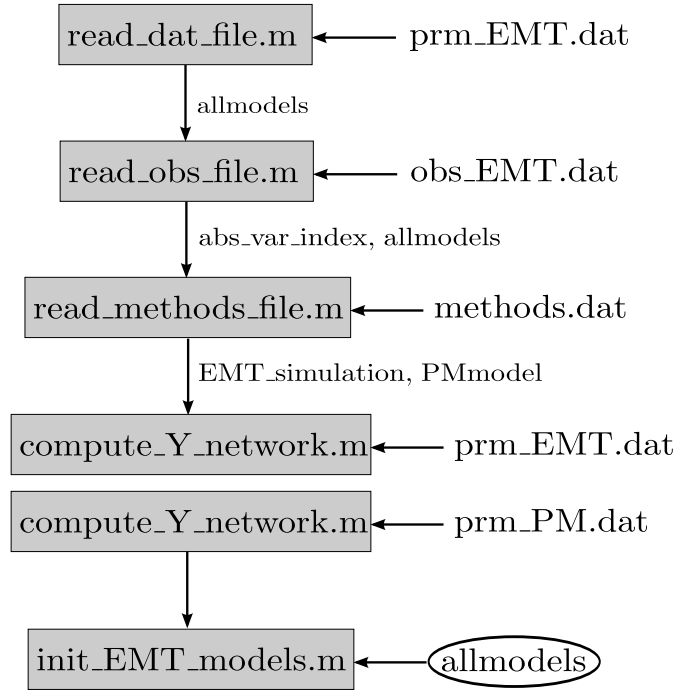
Figure B.1: Initialization procedure.
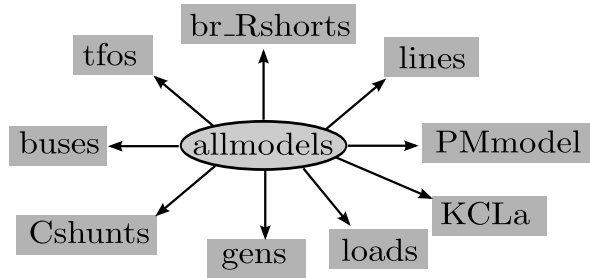
Figure B.2: Models implemented in the developed EMT solver.

kept in the *EMT_simulation* structure. The admittance matrix of both the EMT and the PM sub-systems is computed, as detailed in Appendix C, and the impedance (or similarly admittance) matrix seen from the boundary buses is derived, as previously explained in Section 3.3.3. Finally, all the EMT models are initialized based on the load flow information processed from the file *prm_EMT.dat*.

The coupling layer is represented in Figure B.3. After loading the updated boundary variables from the PM solver, namely $\bar{\mathbf{V}}^{k+\frac{1}{2}}(t+H)$ and $\bar{\mathbf{I}}^{k+\frac{1}{2}}(t+H)$, the coupling layer updates the multiport Thévenin equivalent of the PM sub-system. The EMT solver then computes the EMT sub-system over the time interval $[t \quad t+H]$. The extraction procedure may then be called to produce the updates values of the boundary voltage and current phasors, namely $\bar{\mathbf{V}}^{k+1}(t+H)$ and $\bar{\mathbf{I}}^{k+1}(t+H)$ (see Figure 3.23). The equivalent of the EMT sub-system is then updated and the new one is given to the PM solver, which may resume its simulation. Since the EMT solver is implemented in

```
┌─────────────────────┐
│    read updated     │
│  boundary variables │
│    from PM solver   │
└─────────────────────┘
          │  $\bar{\mathbf{V}}^{k+\frac{1}{2}}$
          │  $\bar{\mathbf{I}}^{k+\frac{1}{2}}$
          ▼
┌─────────────────────┐
│      update         │          TIME
│   equivalent of     │       INTERPOLATION
│   PM sub-system     │
└─────────────────────┘
          │
          ▼
┌─────────────────────┐              EMT
│   simul_interval    │            SOLVER
└─────────────────────┘
          │
          ▼
┌─────────────────────┐
│     extract         │           PHASOR
│  boundary currents  │         EXTRACTION
│    & voltages       │
└─────────────────────┘
          │  $\bar{\mathbf{V}}^{k+1}$
          │  $\bar{\mathbf{I}}^{k+1}$
          ▼
┌─────────────────────┐
│      update         │
│   equivalent of     │
│   EMT sub-system    │
└─────────────────────┘
          │
          ▼
┌─────────────────────┐        PREDICTION
│      predict        │          IN TIME
└─────────────────────┘
          │
          ▼
┌─────────────────────┐
│    give updated     │
│  boundary variables │
│    to PM solver     │
└─────────────────────┘
```
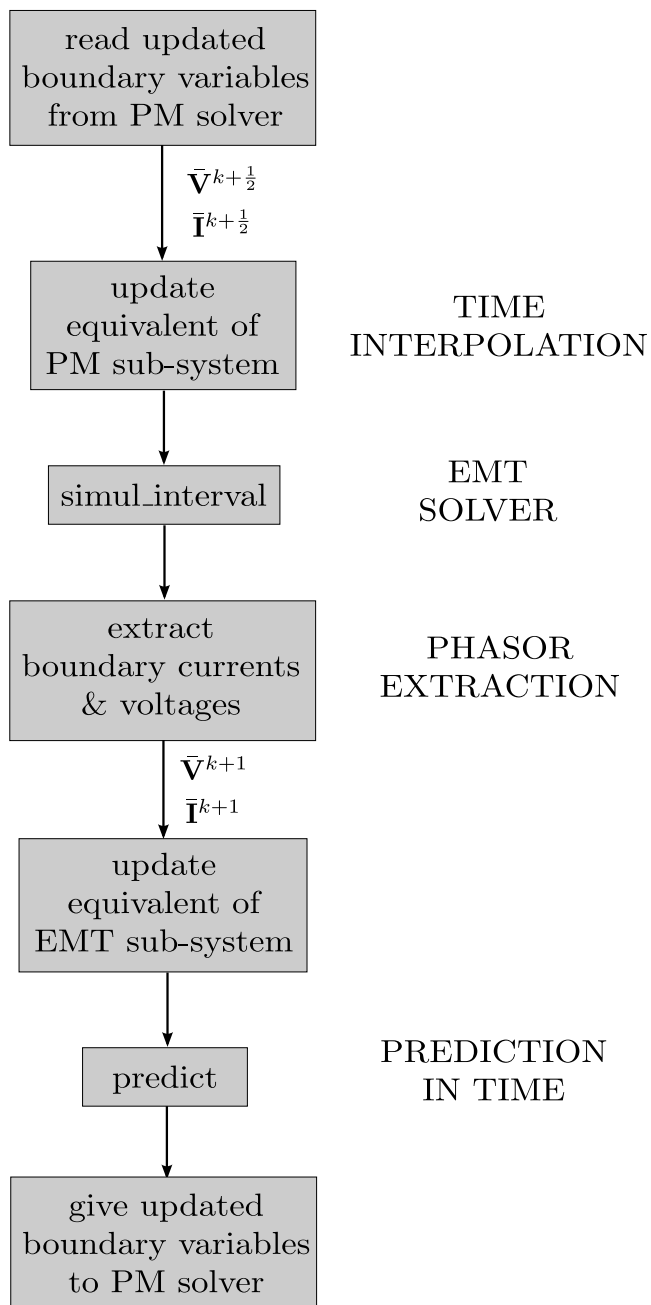
Figure B.3: Coupling layer.

MATLAB, which is an interpreted language, the solver remains slow.A tentative speed comparison with EMTP-RV (same duration -100ms (500ms)-, same time step size, same tolerance, same data kept, same laptop, same power system simulated with the same models - Central and South regions of the Nordic system) gave a simulation time of 94s (716.8s) for MATLAB-EMT versus 1.1s (4.13) for EMTP-RV. This gives a ratio of 85.45 (173.56).

The Jacobian is partially updated since most models do keep the same jacobian during the whole duration of the simulation. The Jacobian of *PMmodel* will be updated at every change of $\mathbf{R}_{pm}$ or $\mathbf{L}_{pm}$ matrices. A particular *br_Rshorts* model will be updated whenever its state changes (opened breaker or short-circuited, ...). The Jacobians of all the synchronous generators are updated at every EMT time-step change or whenever the number of Newton iterations to compute a time step exceed a limit. A representation of the sparse Jacobian matrix is shown in Figure B.4.
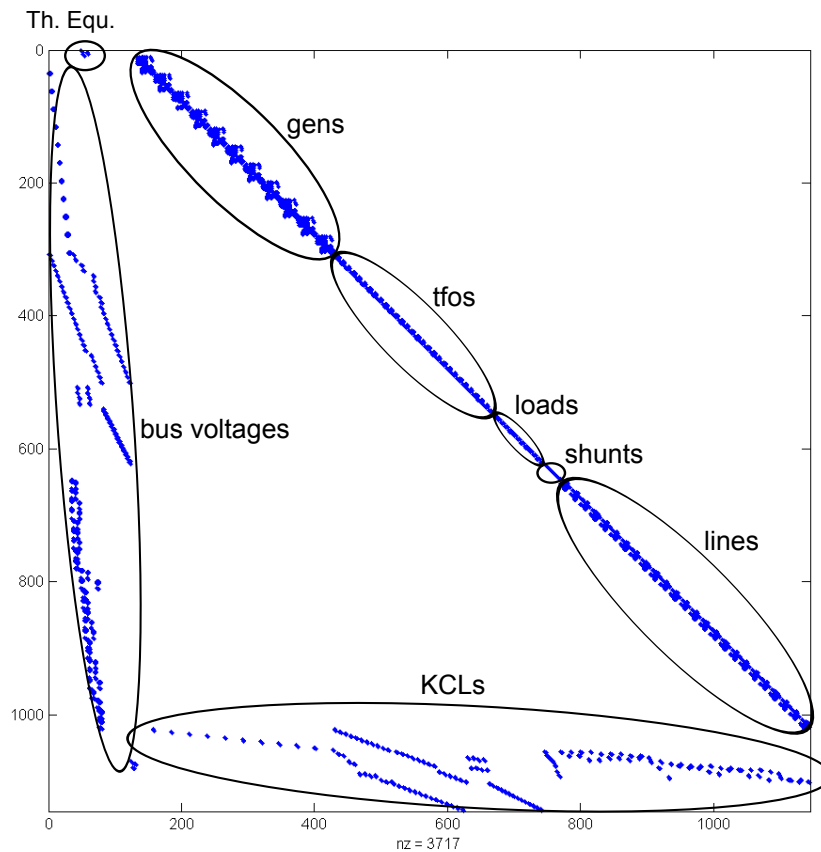
Figure B.4: Jacobian matrix.

A technical flowchart of the PM-EMT algorithm is shown in Figure B.5.

Start

Init Ramses from prm_PM.dat file:
P, Q, V_x, V_y, I_x, I_y

total
current
injected

Pass to matlab:
$nb\_of\_connections$, $Sbases$,
$omega$, V_{x0}, V_{y0}, I_{x0}, I_{y0}

call "init.m"

Read from matlab:
g, b, I_{xinj}, I_{yinj}, $mbratype$

$t = t + 1$

V_x, V_y

solve PM red. network

solve PM injectors

out of the loop
I_{xin}, I_{yin},
gil, bil
bij, ...
CONSTANT

N

PM
converged

Y V_{x_n}, V_{y_n}

copy to matlab: V_x, V_y
V_{x_n}, V_{y_n}, $omega$, t_start

call "eval_f.m"

Get from matlab:
g, b, I_{xinj}, I_{yinj}, $mconv$
I_{xp}, I_{yp}, V_{xp}, V_{yp}, t_setp

matlab & PM
converged

N

Y

N

horizon
reached

Y

Stop

Figure B.5: Detailed flowchart.
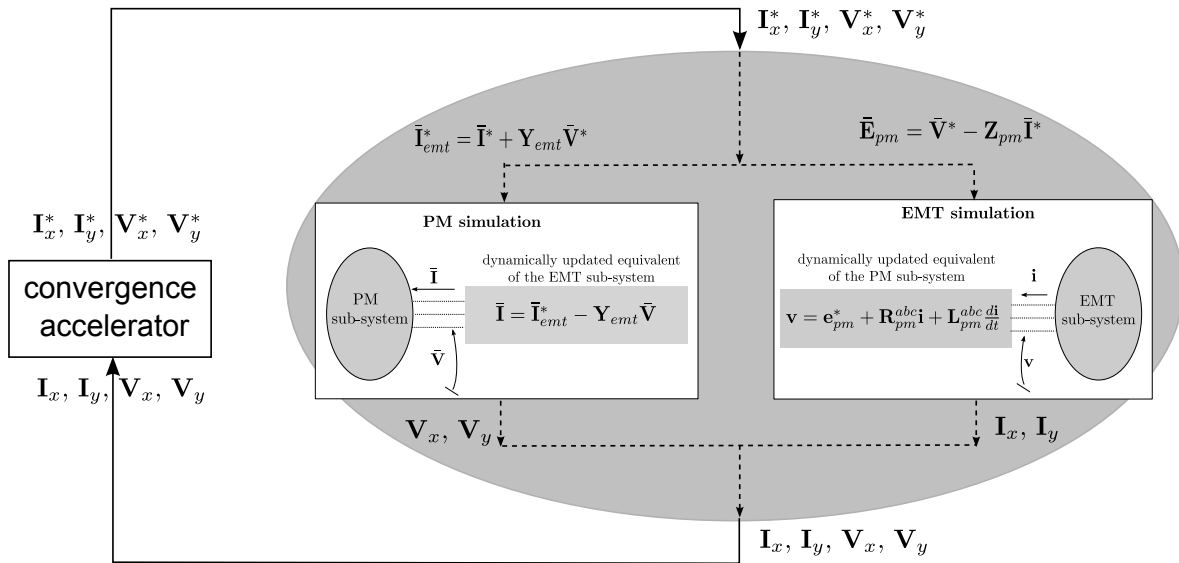
Figure B.6: Jacobi accelerated co-simulation scheme.

Figures B.6 and B.7 presents acceleration schemes (see Section 3.4.2), of respectively the Jacobi and the Gauss-Seidel type, that should be used if the number of co-simulation iterations would increase, for example due to a larger number of boundary buses. In Jacobi scheme, a given co-simulation iteration outputs phasors of the interface currents $\bar{\mathbf{I}} = \mathbf{I}_x + j\mathbf{I}_y$ and voltages $\bar{\mathbf{V}} = \mathbf{V}_x + j\mathbf{V}_y$, as sketched in Figure B.6. However, unlike a classical Jacobi scheme, the interface variables are not directly input to the next iteration. They are rather modified by a convergence accelerator that produces the modified interface variables $\mathbf{I}_x^*$, $\mathbf{I}_y^*$, $\mathbf{V}_x^*$ and $\mathbf{V}_y^*$ intended to be closer to the fixed-point of the given time step. The Gauss-Seidel scheme presented in Figure B.7 uses the same technique, applied to the Norton source currents $\mathbf{I}_{emt}^x$ and $\mathbf{I}_{emt}^y$

$$\mathbf{I}_{emt}^{x*}, \mathbf{I}_{emt}^{y*}$$

$$\bar{\mathbf{I}}_{emt}^* = \mathbf{I}_{emt}^{x*} + j\mathbf{I}_{emt}^{y*}$$

PM simulation

dynamically updated equivalent
of the EMT sub-system

$\bar{\mathbf{I}}$

PM
sub-system

$$\bar{\mathbf{I}} = \bar{\mathbf{I}}_{emt}^* - \mathbf{Y}_{emt}\bar{\mathbf{V}}$$

$\bar{\mathbf{V}}$

$$\mathbf{I}_{emt}^{x*}, \mathbf{I}_{emt}^{y*}$$

convergence
accelerator

$$\mathbf{I}_{emt}^{x}, \mathbf{I}_{emt}^{y}$$

$$\bar{\mathbf{E}}_{pm} = \bar{\mathbf{V}}^{k+\frac{1}{2}} - \mathbf{Z}_{pm}\bar{\mathbf{I}}^{k+\frac{1}{2}}$$

EMT simulation

dynamically updated equivalent
of the PM sub-system

$$\mathbf{v} = \mathbf{e}_{pm} + \mathbf{R}_{pm}^{abc}\mathbf{i} + \mathbf{L}_{pm}^{abc}\frac{d\mathbf{i}}{dt}$$

$\mathbf{i}$

EMT
sub-system

$\mathbf{v}$

$$\bar{\mathbf{I}}_{emt} = \bar{\mathbf{I}}^{k+1} + \mathbf{Y}_{emt}\bar{\mathbf{V}}^{k+1}$$

$$\mathbf{I}_{emt}^{x}, \mathbf{I}_{emt}^{y}$$
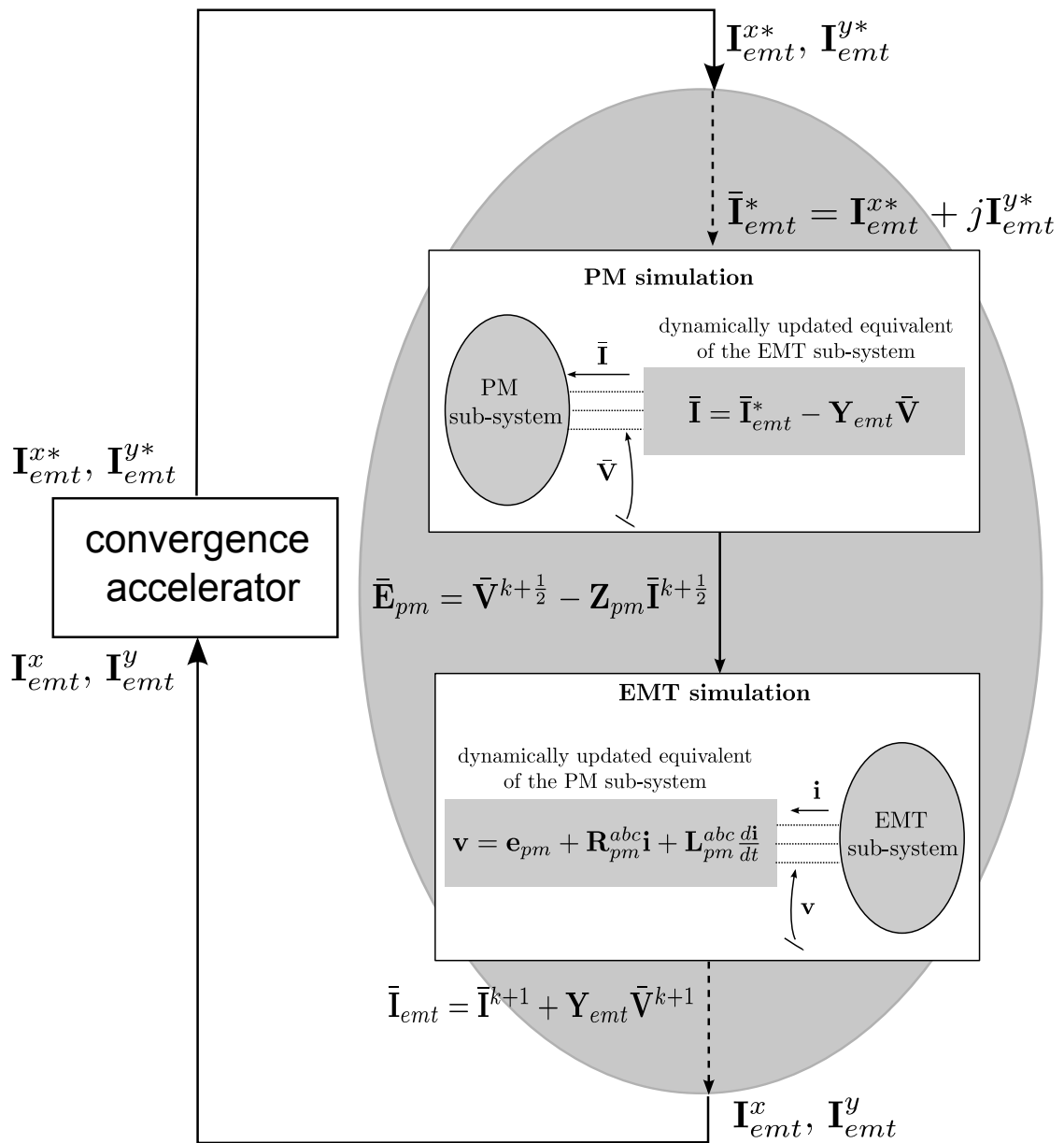
Figure B.7: Gauss-Seidel accelerated co-simulation scheme.

Nodal admittance matrix computation

In this work, to build the nodal admittance matrix $\mathbf{Y}_{network\,abc}$ of size $3N \times 3N$, where N is the number of buses of the considered network (see Figure 3.19), we first build the $\mathbf{Y}_d$, $\mathbf{Y}_i$ and $\mathbf{Y}_o$ matrices (each of size $N \times N$) for the direct (or positive-sequence), inverse (or negative-sequence) and homopolar (zero-sequence) components respectively. These components have been introduced in Section 2.4.3.

C.1 Conversion of elementary 3-by-3 nodal admittance matrix from abc to dio form, and conversely

For a single bus, the elementary 3-by-3 matrix $\mathbf{Y}_{dio}$ is written:

$$\mathbf{Y}_{dio} = \begin{bmatrix} y_d & 0 & 0 \\ 0 & y_i & 0 \\ 0 & 0 & y_0 \end{bmatrix},$$

where y_d, y_i, and y_0 are the direct, inverse and zero-sequence components of the nodal admittance at the considered bus. The following formula allows for the conversion of every elementary 3-by-3 matrix $\mathbf{Y}_{dio}$ into the 3-by-3 matrix $\mathbf{Y}_{abc}$:

$$\mathbf{Y}_{abc} = \mathbf{S}\mathbf{Y}_{dio}\mathbf{S}^{-1},$$

where transformation matrix $\mathbf{S}$ is given by:

$$\mathbf{S} = \begin{pmatrix} 1 & 1 & 1 \\ a^2 & a & 1 \\ a & a^2 & 1 \end{pmatrix},$$

where $a = e^{j\frac{2\pi}{3}}$ had been defined in (2.50). A recursive procedure, treating sequentially each elementary 3-by-3 matrix $\mathbf{Y}_{dio}$, allows for the conversion of the complete nodal admittance matrix $\mathbf{Y}_{network\,dio}$ into $\mathbf{Y}_{network\,abc}$ (or conversely, depending on the needed form).

C.2   Initialization

The three nodal admittance matrices $\mathbf{Y}_d$, $\mathbf{Y}_i$ and $\mathbf{Y}_o$ of size $N \times N$, first need to be initialized to zero matrices:

$$\mathbf{Y}_d = \mathbf{Y}_i = \mathbf{Y}_o = \begin{pmatrix} 0 & \cdots & 0 \\ \vdots & \ddots & \vdots \\ 0 & \cdots & 0 \end{pmatrix}.$$

C.3   Contribution of each component

The contributions of all components need to be added to the initial zero matrices. The components are classified in one-port components (impedance loads, shunts and synchronous machines), or two-ports ones (transformers and lines).

C.3.1   One-port components

These components are supposed to be connected to bus k.

Impedance load Z_{load}

$$
\begin{aligned}
Y_d\,(k,k) &= Y_d\,(k,k) + \frac{1}{Z_{load}}\,, \\
Y_i\,(k,k) &= Y_i\,(k,k) + \frac{1}{Z_{load}}\,, \\
Y_o\,(k,k) &= Y_o\,(k,k) + \frac{1}{Z_{load}}\,.
\end{aligned}
$$

To simplify, in what follows, if the contribution to the three matrices Y_d, Y_i and Y_o are similar, we will write in condensed form:

$$Y_{dio}\,(k,k) = Y_{dio}\,(k,k) + \frac{1}{Z_{load}}\,.$$

Shunt jB_{shunt}

$$Y_{dio}\,(k,k) = Y_{dio}\,(k,k) + jB_{shunt}\,.$$

Synchronous machine

Assuming an armature resistance R_a, a leakage reactance X_l and subtransient reactances $X_d'' = X_q''$, one has:

$$
\begin{aligned}
Y_{di}(k,k) &= Y_{di}(k,k) + \frac{1}{R_a + X_d''}\,, \\
Y_o(k,k) &= Y_o(k,k) + \frac{1}{R_a + X_l}\,.
\end{aligned}
$$

C.3.2 Two-ports components

Two-ports components are supposed to be connected to buses f (from) and t (to).

Ygyg Transformer jX_{tfo}; m

For such a transformer with a Yy connection having both neutral connections grounded, one has:

$$\begin{aligned}
Y_{dio}(f,f) &= Y_{dio}(f,f) + \frac{1}{jX_{tfo}}, \\
Y_{dio}(t,t) &= Y_{dio}(t,t) + \frac{1}{jX_{tfo}m^2}, \\
Y_{dio}(f,t) &= Y_{dio}(f,t) - \frac{1}{jX_{tfo}m}, \\
Y_{dio}(t,f) &= Y_{dio}(t,f) - \frac{1}{jX_{tfo}m}.
\end{aligned}$$

Pi-line

The EMT model of this line was presented in Section 2.2.2. The phasor model was the object of Section 2.4.4. Let us denote Y_s the direct admittance of the series branch of the model of Figure 2.28:

$$Y_s = \frac{1}{R_{pos} + j\omega L_{pos}},$$

and Y_p the direct admittance of each parallel branch on the left or right-hand sides of Figure 2.28:

$$Y_p = \frac{jC_{pos}}{2}.$$

The value for the inverse-sequence are identical to the ones for the direct-sequence.

The contributions of this model to direct and inverse-sequence components of the admittance matrix are:

$$\begin{aligned}
Y_{di}(f,f) &= Y_{di}(f,f) + Y_p + Y_s, \\
Y_{di}(t,t) &= Y_{di}(t,t) + Y_p + Y_s, \\
Y_{di}(f,t) &= Y_{di}(f,t) - Y_s, \\
Y_{di}(t,f) &= Y_{di}(t,f) - Y_s.
\end{aligned}$$

For the zero-sequence, if we do not have the corresponding data, we may assume:

$$\begin{aligned}
R_o &= R_{pos}, \\
L_o &= 3L_{pos}, \\
C_o &= C_{pos}/2.
\end{aligned}$$

Using these values, we define:

$$\begin{aligned}
Y_{so} &= \frac{1}{R_o + j\omega L_o}, \\
Y_{po} &= \frac{jC_0}{2}.
\end{aligned}$$

The contributions of the pi-line model to the zero-sequence component of the nodal admittance matrix are:

$$
\begin{aligned}
Y_o\left(f,f\right) &= Y_o\left(f,f\right) + Y_{po} + Y_{so}\,, \\
Y_o\left(t,t\right) &= Y_o\left(t,t\right) + Y_{po} + Y_{so}\,, \\
Y_o\left(f,t\right) &= Y_o\left(f,t\right) - Y_{so}\,, \\
Y_o\left(t,f\right) &= Y_o\left(t,f\right) - Y_{so}\,.
\end{aligned}
$$

C.4 Fault inception very near bus k

For simplicity, fault inception is performed on the three-phase abc admittance matrix rather than on the dio components one.

In case of a single-phase solid fault very near bus k, one has:

$$
Y_a(k_a, k_a) = Y_a(k_a, k_a) + 10^6\,.
$$

Similarly, for a three-phase solid fault very near bus k, one has:

$$
Y_{abc}(k_{abc}, k_{abc}) = Y_{abc}(k_{abc}, k_{abc}) + 10^6\,.
$$

C.5 Fault clearing by opening line between buses f and t

$$
\begin{aligned}
Y_{dio}\left(f,f\right) &= Y_{dio}\left(f,f\right) - 10^6\,, \\
Y_{dio}\left(t,t\right) &= Y_{dio}\left(t,t\right) - 10^6\,, \\
Y_{dio}\left(f,t\right) &= Y_{dio}\left(f,t\right) + 10^6\,, \\
Y_{dio}\left(t,f\right) &= Y_{dio}\left(t,f\right) + 10^6\,.
\end{aligned}
$$

Data of the Nordic-B system

For the PM simulation, all data are available in [IEE15].

A few additional parameters were needed for the EMT simulation.

For synchronous machines, the needed parameters are the resistances and inductances of every of the four windings (two on d-axis and two on q-axis) of the rotor model, while the parameters available are the reactances and time constants. The parameter L_{oo} needed in (A.10) has been considered equal to the leakage inductance, denoted L_l. The conversion is made through the function *XT2RL.m*

For lines, negative-sequence parameters are considered to be equal to positive-sequence ones. Zero-sequence parameters are computed as follows:

$$
\begin{aligned}
R_o &= R_d \\
L_o &= 3L_d \\
\frac{C_o}{2} &= 0.5\frac{C_d}{2}
\end{aligned}
$$

Bibliography

[19992]   "Reader's guide to subsynchronous resonance," *IEEE Transactions on Power Systems*, vol. 7, no. 1, pp. 150–157, Feb 1992.

[20111]   "IEEE standard for synchrophasor measurements for power systems," *IEEE Std C37.118.1-2011 (Revision of IEEE Std C37.118-2005)*, pp. 1–61, Dec 2011.

[AAALM02]   E. Acha, V. G. Agelidis, O. Anaya-Lara, and T. J. E. Miller, *Power Electronic Control in Electrical Systems.* Newnes, 2002.

[Abh11]   S. Abhyankar, "Development of an implicitly coupled electromechanical and electromagnetic transients simulator for power systems," Ph.D. dissertation, Illinois Institute of Technology, December 2011.

[AF12]   S. Abhyankar and A. Flueck, "An implicitly-coupled solution approach for combined electromechanical and electromagnetic transients simulation," in *Power and Energy Society General Meeting, 2012 IEEE*, july 2012, pp. 1 –8.

[AF13]   ——, "Parallel-in-space-and-time scheme for implicitly coupled electromechanical and electromagnetic transients simulation," in *Proceedings of International Conference on Power System Transients (IPST)*, 2013.

[AF14]   S. Abhyankar and A. J. Flueck, "Multiphysics solvers for implicitly coupled electromechanical and electromagnetic transients simulation," in *T D Conference and Exposition, 2014 IEEE PES*, April 2014, pp. 1–5.

[AFV14]   P. Aristidou, D. Fabozzi, and T. Van Cutsem, "Dynamic simulation of large-scale power systems using a parallel schur-complement-based decomposition method," *IEEE Transactions on Parallel and Distributed Systems*, vol. 25, pp. 2561–2570, 2014.

[AG01]   M. Arnold and M. Günther, "Preconditioned dynamic iteration for coupled differential-algebraic systems," *BIT Numerical Mathematics*, vol. 41, no. 1, pp. 1–25, 2001.

[AK02]   M. Al-Khaleel, "optimized waveform relaxation methods for rc type circuits," Ph.D. dissertation, Department of Methematics and Statistics, McGill University, Montreal, 2002.

[And95]   G. W. Anderson, "Hybrid simulation of AC-DC power systems," Ph.D. dissertation, University of Canterbury, Christchurch, New Zealand, 1995.

[ANL+12]   U. Annakkage, N. K. C. Nair, Y. Liang, A. Gole, V. Dinavahi, B. Gustavsen, T. Noda, H. Ghasemi, A. Monti, M. Matar, R. Iravani, and J. Martinez, "Dynamic system equivalents: A survey of available techniques," *IEEE Transactions on Power Delivery*, vol. 27, no. 1, pp. 411–420, Jan 2012.

[AP98]   U. M. Ascher and L. R. Petzold, *Computer Methods for Ordinary Differential Equations and Differential-Algebraic Equations*, 1st ed. Philadelphia, PA, USA: Society for Industrial and Applied Mathematics, 1998.

[Ast04]   P. Astrid, "Reduction of process simulation models: a proper orthogonal decomposition approach," Ph.D. dissertation, Technische Universiteit Eindhoven, 2004.

[BBGS13]   A. Bartel, M. Brunk, M. Günther, and S. Schöps, "Dynamic iteration for coupled problems of electric circuits and distributed devices," *SIAM J. Sci. Comput.*, vol. 35, no. 2, pp. B315–B335, 2013.

[BBS13]   A. Bartel, M. Brunk, and S. Schöps, "On the convergence rate of dynamic iteration for coupled problems with multiple subsystems," *JCAM*, p. accepted, 2013.

[BH14]   B. Badrzadeh and A. Halley, "Challenges associated with assessment and testing of fault ride-through compliance of variable power generation in australian national electricity market," *IEEE Transactions on Sustainable Energy*, vol. PP, no. 99, pp. 1–9, 2014.

[But30]   S. Butterworth, "On the theory of filter amplifiers," *Wireless Engineer*, vol. 7, 1930.

[CA70]   A. Chang and M. Adibi, "Power system dynamic equivalents," *IEEE Transactions on Power Apparatus and Systems*, vol. PAS-89, no. 8, pp. 1737–1744, Nov 1970.

[Cha84]   T. F. Chan, "An approximate newton method for coupled nonlinear systems," INRIA, Tech. Rep. RR-0294, 1984. [Online]. Available: http://opac.inria.fr/record=b1011374

[Chu00]   S.-K. Chung, "A phase tracking system for three phase utility interface inverters," *IEEE Transactions on Power Electronics*, vol. 15, no. 3, pp. 431 –438, may 2000.

[CI90]   M. Crow and M. Ilic, "The parallel implementation of the waveform relaxation method for transient stability simulations," *IEEE Transactions on Power Systems*, vol. 5, no. 3, pp. 922–932, Aug 1990.

[CM11]   T. Cadeau and F. Magoules, "Coupling parareal and waveform relaxation methods for power systems," in *2011 International Conference on Electrical and Control Engineering (ICECE 2011)*, vol. 4. Yichang, China: IEEE Computer Society, Sep. 2011, pp. –. [Online]. Available: https://hal.archives-ouvertes.fr/hal-00803332

[CS$^+$02]   K. W. Chan, , L. A. Snider, R. C. Dai, and B. M. Zhang, "Transient stability simulation with embedded electromagnetic transient SVC model," in *Proceedings of International Conference on Power System Transients (IPST)*, 2002.

[Dem08]   T. H. Demiray, "Simulation of power system dynamics using dynamic phasor models," Ph.D. dissertation, Swiss Federal Institute of Technology Zurich, 2008.

[Dom69]   H. Dommel, "Digital computer solution of electromagnetic transients in single- and multiphase networks," *IEEE Transactions on Power Apparatus and Systems*, vol. PAS-88, no. 4, pp. 388–399, April 1969.

[EKS02]   I. Erlich, Z. Kasztel, and P. Schegner, "Enhanced modal based technique for construction of power system dynamic equivalents," in *Proceedings of the 14th Power System Computation Conference*, 2002.

[emt]   EMTP-RV. Accessed February 2015. [Online]. Available: http://www.empt-rv.com

[ENT11]   ENTSO-E Sub Group "System Protection and Dynamics" under - Regional Group Continental Europe -, "Technical background and recommendations for defence plans in the continental europe synchronous area," ENTSO-E, Tech. Rep., 2011.

[EOBE14]   H. Elmqvist, H. Olsson, V. Belsky, and B. Engelmann, "Co-simulation procedures using full derivatives of output variables," Patent, Jan. 1, 2014, eP Patent App. EP20,130,173,462. [Online]. Available: http://www.google.com/patents/EP2680157A1?cl=en

[ES13]   M. Eremia and M. Shahidehpour, Eds., *Handbook of Electrical Power System Dynamics: Modeling, Stability, and Control*. John Wiley & Sons, 2013.

[Eur]   EUROSTAG and FAST. Accessed February 2015. [Online]. Available: http://www.eurostag.be/

[Fab12]   D. Fabozzi, "Decomposition, localization and time-averaging approaches in large-scale power system dynamic simulation," Ph.D. dissertation, 2012.

[FD12]   S. Fan and H. Ding, "Time domain transformation method for accelerating EMTP simulation of power system dynamics," *IEEE Transactions on Power Systems*, vol. 27, pp. 1778–1787, 2012.

[FLCW06]   D. Fang, W. Liwei, T. Chung, and K. Wong, "New techniques for enhancing accuracy of EMTP/TSP hybrid simulation," *International Journal of Electrical Power and Energy Systems*, vol. 28, pp. 707 – 711, 2006.

[FVC11]   D. Fabozzi and T. Van Cutsem, "Assessing the proximity of time evolutions through dynamic time warping," *IET Generation, Transmission & Distribution*, vol. 5, p. 1268, 2011.

[GDP+15]   G. Gurrala, A. Dimitrovski, S. Pannala, S. Simunovic, and M. Starke, "Parareal in time for fast power system dynamic simulations," *Power Systems, IEEE Transactions on*, vol. PP, no. 99, pp. 1–11, 2015.

[GP84]   C. W. Gear and L. R. Petzold, "Ode methods for the solution of differential/algebraic systems," *SIAM Journal on Numerical Analysis*, vol. 21, no. 4, pp. 716–728, 1984.

[GS94]   J. Grainger and W. Stevenson, *Power system analysis*. McGraw-Hill, 1994.

[GS09]   F. Gao and K. Strunz, "Frequency-adaptive power system modeling for multiscale simulation of transients," *IEEE Transactions on Power Systems*, vol. 24, no. 2, pp. 561–571, May 2009.

[GTD08]   D. Guibert and D. Tromeur-Dervout, "A Schur Complement Method for DAE/ODE Systems in Multi-Domain Mechanical Design," *Domain Decomposition Methods in Science and Engineering XVII*, pp. 535–541, 2008.

[Gup75]   S. C. Gupta, "Phase-locked loops," *Proceedings of the IEEE*, vol. 63, no. 2, pp. 291–306, Feb 1975.

[Hay68]   E. V. Haynsworth, "On the Schur complement," Basel Mathematical Notes, June 1968.

[HCSC14]   S. Huang, Y. Chen, C. Shen, and L. Chen, "A novel hybrid dynamic simulation algorithm based on iterative coordination," in *Innovative Smart Grid Technologies Conference Europe (ISGT-Europe), 2014 IEEE PES*, Oct 2014, pp. 1–5.

[Hen99]   S. Henschel, "Analysis of electromagnetic and electromechanical power system transients with dynamic phasors," Ph.D. dissertation, University of British Columbia, 1999.

[HH96]   G.-C. Hsieh and J. Hung, "Phase-locked loop techniques. a survey," *Industrial Electronics, IEEE Transactions on*, vol. 43, no. 6, pp. 609–615, Dec 1996.

[HKLS05]   H.Su, K.W.Chan, L.A.Snider, and J.-C. Soumagne, "Advancements on the integration of electromagnetic transients simulator and transient stability simulator," in *Proceedings of the international conference on power system transients*, Montreal, QC, Canada, june 2005, pp. 1–6.

[HTAA81]   M. Heffernan, K. Turner, J. Arrillaga, and C. Arnold, "Computation of AC-DC system disturbances - Part I, II and III. interactive coordination of generator and converter transient models," *IEEE Transactions on Power Apparatus and Systems*, vol. 100, no. 11, pp. 4341 – 4363, 1981.

[HV15]   Q. Huang and V. Vittal, "Application of electromagnetic transient-transient stability hybrid simulation to fidvr study," *Power Systems, IEEE Transactions on*, vol. PP, no. 99, pp. 1–13, 2015.

[IAKW12]   G. Irwin, C. Amarasinghe, N. Kroeker, and D. Woodford, "Parallel processing and hybrid simulation for hvdcnsc pscad studies," in *AC and DC Power Transmission (ACDC 2012), 10th IET International Conference on*, Dec 2012, pp. 1–6.

[IC96]   I. V. Ionova and E. A. Carter, "Error vector choice in direct inversion in the iterative subspace method." 1996, pp. 1836–1847.

[IEE15]   IEEE PES Task Force on Test Systems for Voltage Stability Analysis and Security Assessment, "Test Systems for Voltage Stability Analysis and Security Assessment," Tech. Rep. PES-TR19, 2015. [Online]. Available: http://resourcecenter.ieee-pes.org/publications/ test-systems-for-voltage-stability-analysis-and-security-assessment-2015-pdf/

[IFHI03]   H. Inabe, T. Futada, H. Horii, and K. Inomae, "Development of an instantaneous and phasor analysis combined type real-time digital power system simulator," in *Proceedings of the international conference on power system transients (IPST)*, New Orleans, USA, 2003, pp. 1–6.

[IT69]   B. M. Irons and R. C. Tuck, "A version of the aitken accelerator for computer iteration," *International Journal for Numerical Methods in Engineering*, vol. 1, no. 3, pp. 275–277, 1969. [Online]. Available: http://dx.doi.org/10.1002/nme.1620010306

[JDP09]   M. M. Joosten, W. G. Dettmer, and D. Peric, "Analysis of the block gauss-seidel solution procedure for a strongly coupled model problem with reference to fluid-structure interaction," *International Journal for Numerical Methods in Engineering*, vol. 78, pp. 757–778, 2009.

[JMD09]   V. Jalili-Marandi and V. Dinavahi, "Instantaneous relaxation-based real-time transient stability simulation," *IEEE Transactions on Power Systems*, vol. 24, no. 3, pp. 1327 – 1336, 2009.

[JMDS$^+$09] V. Jalili-Marandi, V. Dinavahi, K. Strunz, J. Martinez, and A. Ramirez, "Interfacing techniques for transient stability and electromagnetic transient programs," *IEEE Transactions on Power Delivery*, vol. 24, no. 4, pp. 2385 – 2395, 2009.

[JS68]   L. Johnson and D. Scholz, "On Steffensen's method," *SIAM Journal on Numerical Analysis*, vol. 5 (2), pp. 296–302, 1968.

[JWW13]   X. Jin, F. Wang, and Z. Wang, "A dynamic phasor estimation algorithm based on angle-shifted energy operator," *Science China - Technological Sciences*, vol. 56, pp. 1322–1329, 2013.

[KK00]   B. Kasztenny and M. Kezunovic, "A method for linking different modeling techniques for accurate and efficient simulation," *IEEE Transactions on Power Systems*, vol. 15, no. 1, pp. 65 – 72, 2000.

[KPA$^+$04]   P. Kundur, J. Paserba, V. Ajjarapu, G. Andersson, A. Bose, C. Canizares, N. Hatziargyriou, D. Hill, A. Stankovic, C. Taylor, T. Van Cutsem, and V. Vittal, "Definition and classification of power system stability ieee/cigre joint task force on stability terms and definitions," *IEEE Transactions on Power Systems*, vol. 19, no. 3, pp. 1387–1401, Aug 2004.

[Kun94]   P. Kundur, *Power System Stability and Control*, New York, 1994.

[LCL09]   Y.-Q. Long, S. Cen, and Z.-F. Long, *Advanced Finite Element Method in Structural Engineering*.   Springer, 2009.

[LGY09]   X. Lin, A. Gole, and M. Yu, "A wide-band multi-port system equivalent for real-time digital power system simulators," *IEEE Transactions on Power Systems*, vol. 24, no. 1, pp. 237–249, 2009.

[LL11]   Y. M. Leroy and F. K. Lehner, *Mechanics of Crustal Rocks*.   Springer Science & Business Media, 2011.

[Lou14]   P. H. Lourenço dos Santos, "Hybrid time domain simulation - integration of electromagnetic and electromechanical transient programs," Master's thesis, Universidade Federal do Rio de Janeiro, 2014.

[LRSV82]   E. Lelarasmee, A. E. Ruehli, and A. Sangiovanni-Vincentelli, "The waveform relaxation method for time-domain analysis of large scale integrated circuits," *IEEE Transactions on Computer-Aided Design of Integrated Circuits and Systems*, vol. 1, no. 3, pp. 131–145, July 1982.

[LS73]   S. Lee and F. Schweppe, "Distance measures and coherency recognition for transient stability equivalents," *Power Apparatus and Systems, IEEE Transactions on*, vol. PAS-92, no. 5, pp. 1550–1557, Sept 1973.

[MDBB14]   J. R. Martì, H. W. Dommel, B. D. Bonatto, and A. F. R. Barreto, "Shifted frequency analysis (SFA) concepts for emtp modelling and simulation of power system analysis," in *Proceedings of the 18th Power System Computation Conference, Wroclaw, Poland*, 2014.

[Mie89]   U. Miekkala, "Dynamic iteration methods applied to linear DAE systems," *Journal of Computational and Applied Mathematics*, vol. 25, no. 2, pp. 133 – 151, 1989. [Online]. Available: http://www.sciencedirect.com/science/article/pii/0377042789900447

[MKQ93a]   P. Maragos, J. F. Kaiser, and T. F. Quatieri, "Energy separation in signal modulations with application to speech analysis," *Signal Processing, IEEE Transactions on*, vol. 41, no. 10, pp. 3024–3051, 1993.

[MKQ93b]   ——, "On amplitude and frequency demodulation using energy operators," *Signal Processing, IEEE Transactions on*, vol. 41, no. 4, pp. 1532–1550, 1993.

[MN87]   U. Miekkala and O. Nevanlinna, "Convergence of dynamic iteration methods for initial value problems," vol. 8, no. 4, pp. 459–482, Jul. 1987.

[MN96]   ——, "Iterative solution of systems of linear differential equations," *Acta Numerica*, vol. 5, pp. 259–307, 1 1996. [Online]. Available: http://journals.cambridge.org/article_S096249290000266X

[MNS06]   H. G. Matthies, R. Niekamp, and J. Steindorf, "Alinteraction strong coupling procedures," *Computer Methods in applied mechanics and engineering*, vol. 195, pp. 2028–2049, 2006.

[Mos13]   K. P. P. J. Mosterman, Ed., *Real-Time Simulation Technologies: Principles, Methodologies, and Applications*.   CRC Press, 2013.

[MV11]   F. Ma and V. Vittal, "Right-sized power system dynamic equivalents for power system operation," *Power Systems, IEEE Transactions on*, vol. 26, no. 4, pp. 1998–2005, Nov 2011.

[MV15]   J. A. Martinez-Velasco, Ed., *Transient Analysis of Power Systems: Solution Techniques, Tools and Applications*.   Wiley-IEEE Press, January 2015.

[Ope15]   (2015) Openhybridsim. Accessed October 2015. [Online]. Available: https://github.com/OpenHybridSim/OHM-release/

[OS89]   A. V. Oppenheim and R. W. Schafer, *Discrete-time signal processing*.   Prentice-Hall, 1989.

[Paa00]   G. Paap, "Symmetrical components in the time domain and their application to power network calculations," *IEEE Transactions on Power Systems*, vol. 15, no. 2, pp. 522 –528, may 2000.

[PAGV14]   F. Plumier, P. Aristidou, C. Geuzaine, and T. Van Cutsem, "A relaxation scheme to combine phasor-mode and electromagnetic transients simulations," in *Proceedings of the 18th Power System Computation Conference*, Wroclaw, Poland, August 2014.

[PAGV15]   ——, "Co-simulation of electromagnetic transients and phasor models: a relaxation approach," *submitted for publication in IEEE Transactions on Power Delivery*, 2015.

[PBN11]   M. Paolone, A. Borghetti, and C. A. Nucci, "a synchrophasor estimation algorithm for the monitoring of active distribution networks in steady state and transient conditions," in *Proceedings of the 17th Power System Computation Conference*, 2011.

[PGV13]   F. Plumier, C. Geuzaine, and T. Van Cutsem, "A multirate approach to combine electromagnetic transients and fundamental-frequency simulations," in *Proceedings of International Conference on Power System Transients (IPST)*, 2013.

[PGV14]   ——, "On the convergence of relaxation schemes to couple phasor-mode and electromagnetic transients simulations," in *Proceedings of IEEE PES General Meeting*, Washington D.C., July 2014. [Online]. Available: http://hdl.handle.net/2268/163099

[PGV15]   L. Papangelis, X. Guillaud, and T. Van Cutsem, "Frequency support among asynchronous AC systems through VSCs emulating power plants," in *Proceedings of the 11th IET Conference on AC and DC Power Transmission*, 2015.

[PT08]   A. Phadke and J. Thorp, *Synchronized Phasor Measurements and Their Applications*.   Springer US, 2008.

[RA88a]   J. Reeve and R. Adapa, "A new approach to dynamic analysis of ac networks incorporating detailed modeling of dc systems. part i and ii." *IEEE Transactions on Power Delivery*, vol. 3, 1988.

[RA88b]   ——, "A new approach to dynamic analysis of ac networks incorporating detailed modeling of dc systems. part i: principles and implementation," *IEEE Transactions on Power Delivery*, vol. 3, no. 4, pp. 2005 – 2011, 1988.

[RA88c]   ——, "A new approach to dynamic analysis of ac networks incorporating detailed modeling of dc systems. part ii: application to interaction of dc and weak ac systems," *IEEE Transactions on Power Delivery*, vol. 3, no. 4, pp. 2012 – 2019, 1988.

[RPB$^+$07]   P. Rodriguez, J. Pou, J. Bergas, J. Candela, R. Burgos, and D. Boroyevich, "Decoupled double synchronous reference frame PLL for power converters control," *IEEE Transactions on Power Electronics*, vol. 22, no. 2, pp. 584–592, March 2007.

[Saa03]   Y. Saad, *Iterative methods for sparse linear systems*, 2nd ed. Society for Industrial and Applied Mathematics, 2003.

[SBE$^+$14]   S. Sicklinger, V. Belsky, B. Engelmann, H. Elmqvist, H. Olsson, R. Wüchner, and K.-U. Bletzinger, "Interface jacobian-based co-simulation," *International Journal for Numerical Methods in Engineering*, vol. 98, no. 6, pp. 418–444, 2014.

[SBG04]   B. F. Smith, P. E. Bjorstad, and W. D. Gropp, *Domain Decomposition: Parallel Multilevel Methods for Elliptic Partial Differential Equations*. Cambridge Univ. Press, 2004.

[SCS05]   H. Su, K. Chan, and L. Snider, "Evaluation study for the integration of electromagnetic transients simulator and transient stability simulator," *Electric Power Systems Research*, vol. 75, pp. 67 – 78, 2005.

[SCSS05]   H. Su, K. Chan, L. Snider, and J.-C. Soumagne, "Advancements on the integration of electromagnetic transients simulator and transient stability simulator," in *Proceedings of the international conference on power system transients*, Montreal, QC, Canada, june 2005, pp. 1–6.

[SDGB10]   S. Schöps, H. De Gersem, and A. Bartel, "A cosimulation framework for multirate time-integration of field/circuit coupled problems," *IEEE Transactions on Magnetics*, vol. 46, no. 8, pp. 3233–3236, 7 2010.

[SDS14]   A. Stankovic, S. Dukic, and A. Saric, "Approximate bisimulation-based reduction of power system dynamic models," *IEEE Transactions on Power Systems*, vol. PP, no. 99, pp. 1–9, 2014.

[SJ13]   S. Sommer and H. Johannsson, "Real-time thevenin impedance computation," in *Innovative Smart Grid Technologies (ISGT), 2013 IEEE PES*, Feb 2013, pp. 1–6.

[SLA99]   A. Stankovic, B. Lesieutre, and T. Aydin, "Modeling and analysis of single-phase induction machines with dynamic phasors," *IEEE Transactions on Power Systems*, vol. 14, no. 1, pp. 9–14, Feb 1999.

[SRA98]   M. Sultan, J. Reeve, and R. Adapa, "Combined transient and dynamic analysis
             of hvdc and facts systems," *IEEE Transactions on Power Delivery*, vol. 13, no. 4,
             pp. 2005 – 2011, 1998.

[SS04]   A. Stankovic and A. Saric, "Transient power system analysis with measurement-
             based gray box and hybrid dynamic equivalents," *IEEE Transactions on Power
             Systems*, vol. 19, no. 1, pp. 455–462, Feb 2004.

[SSA02]   A. Stankovic, S. Sanders, and T. Aydin, "Dynamic phasors in modeling and
             analysis of unbalanced polyphase ac machines," *IEEE Transactions on Energy
             Conversion*, vol. 17, no. 1, pp. 107–113, Mar 2002.

[SSCZ03]   H. Su, A. Snider, K. W. Chan, and B. Zhou, "A new approach for integration
             of two distinct types of numerical simulator," in *Proceedings of International
             Conference on Power System Transients (IPST)*, 2003.

[SSG06]   K. Strunz, R. Shintaku, and F. Gao, "Frequency-adaptive network modeling for
             integrative simulation of natural and envelope waveforms in power systems and
             circuits," *IEEE Transactions on Circuits and Systems I: Regular Papers*, vol. 53,
             no. 12, pp. 2788–2803, December 2006.

[THW09]   M. Trcka, J. Hensen, and M. Wetter, "Co-simulation of innovative integrated
             hvac systems in buildings," *Journal of Building Performance Simulation*, vol. 2,
             pp. 209–230, 2009.

[TYZZ05]   F. Tian, C. Yue, W. Zhongxi, and X. Zhou, "Realization of electromechanical
             transient and electromagnetic transient real time hybrid simulation in power sys-
             tem," in *Proceedings of IEEE/PES Transmission and Distribution Conference &
             Exhibition: Asia and Pacific*, 2005.

[UT71]   J. Undrill and A. E. Turner, "Construction of power system electromechanical
             equivalents by modal analysis," *IEEE Transactions on Power Apparatus and Sys-
             tems*, vol. PAS-90, no. 5, pp. 2049–2059, Sept 1971.

[VCV98]   T. Van Cutsem and C. Vournas, *Voltage stability analysis of electric power sys-
             tems*.   Kluwer Academic Publishers, 1998.

[vdMGvdM+14] A. van der Meer, M. Gibescu, A. van der Meijden, W. Kling, and J. Ferreira, "Ad-
             vanced hybrid transient stability and EMT simulation for VSC-HVDC systems,"
             IEEE Transactions on Power Delivery, vol. PP, no. 99, pp. 1–1, 2014.

[vdMRK10]   A. van der Meer, R.L.Hendriks, and W. Kling, "Combined stability and electro-
             magnetic transients simulation of offshore wind power connected through multi-
             terminal vsc-hvdc," in *Proceedings of Power and Energy Society General Meeting*,
             July 25-29 2010.

[vHGK11] A. van der Meer, R. Hendriks, M. Gibescu, and W. Kling, "Interfacing methods for combined stability and electro-magnetic transient simulations applied to vsc-hvdc," in *Proceedings of International Conference on Power System Transients (IPST)*, Delft, The Netherlands, 2011.

[WA03] N. Watson and J. Arrillaga, *Power Systems Electromagnetic Transients Simulation*, ser. IEE power and energy series. Institution of Engineering and Technology, 2003.

[WSV87] J. K. White and A. Sangiovanni-Vincentelli, *Relaxation Techniques for the Simulation of VLSI Circuits*. Kluwer Academic Publishers, 1987.

[XyHTPH14] L. Xu, yong Hong Tang, W. Pu, and Y. Han, "Hybrid electromechanical-electromagnetic simulation to svc controller based on adpss platform," *Journal of Energy in Southern Africa*, vol. 25, pp. 112–122, 2014.

[YBA11] T. Yang, S. Bozhko, and G. Asher, "Assessment of dynamic phasors modelling technique for accelerated electric power system simulations," in *Power Electronics and Applications (EPE 2011), Proceedings of the 2011-14th European Conference on*, Aug 2011, pp. 1–9.

[YLD09] A. Yeckel, L. Lun, and J. J. Derby, "An approximate block newton method for coupled iterations of nonlinear solvers: Theory and conjugate heat transfer applications." *J. Comput. Physics*, vol. 228, no. 23, pp. 8566–8588, 2009. [Online]. Available: http://dblp.uni-trier.de/db/journals/jcphy/jcphy228.html#YeckelLD09

[ZDKS09] E. Zhijun, D.Z.Fang, K.W.Chan, and S.Q.Yuan, "Hybrid simulation of power systems with svc dynamic phasor model," *International Journal of Electrical Power and Energy Systems*, vol. 31, pp. 175 – 180, 2009.

[ZFA14] X. Zhang, A. Flueck, and S. Abhyankar, "Equivalent models for implicitly-coupled electromechanical and electromagnetic transient analysis," in *North American Power Symposium (NAPS), 2014*, Sept 2014, pp. 1–6.

[ZFLZ14] S. Zhao, D. Z. Fang, W. Li, and L. G. Zhao, "An interface model for accurate TSP-EMTP hybrid simulation of power systems," *Applied Mechanics and Materials*, vol. 448, pp. 2439–2446, 2014.

[ZGW+13] Y. Zhang, A. Gole, W. Wu, B. Zhang, and H. Sun, "Development and analysis of applicability of a hybrid transient simulation platform combining TSA and EMT elements," *IEEE Transactions on Power Systems*, vol. 28, no. 1, pp. 357–366, 2013.

[zLxHT$^+$11]   W. zhuo Liu, J. xian Hou, Y. Tang, L. Wan, X. li Song, and S. tao Fan, "An electromechanical/electromagnetic transient hybrid simulation method that considers asymmetric faults in an electromechanical network," in *Proceedings of the Power Systems conference and exposition (PSCE)*, Phoenix, USA, March 20-23 2011.

[ZMD07]   P. Zhang, J. R. Marti, and H. Dommel, "Synchronous machine modeling based on shifted frequency analysis," *IEEE Transactions on Power Systems*, vol. 22, no. 3, pp. 1139–1147, Aug 2007.

[ZMD09]   ——, "Induction machine modeling based on shifted frequency analysis," *IEEE Transactions on Power Systems*, vol. 24, no. 1, pp. 157–164, Feb 2009.